Fall 11-11-2016

# Reduced-Order Monte Carlo Modeling of Radiation Transport in Random Media

Aaron J. Olson
*University of New Mexico*

Aaron Olson
_____
*Candidate*

Nuclear Engineering
_____
*Department*


This dissertation is approved, and it is acceptable in quality and form for publication:

*Approved by the Dissertation Committee:*


Dr. Anil Prinja    , Chairperson
_____


Dr. Cassiano de Oliveira
_____


Dr. Mohammad Motamed
_____


Dr. Brian Franke
_____


_____


_____


_____


_____


_____

# Reduced-Order Monte Carlo Modeling of Radiation Transport in Random Media

by

Aaron OLSON

B.S., Nuclear Engineering, Missouri University of Science and Technology, 2011

M.A., Pastoral Counseling, John Brown University, 2013

DISSERTATION

*Submitted in partial fulfillment of the requirements*
*for the degree of Doctor of Philosophy in*

Engineering

The University of New Mexico
Albuquerque, New Mexico

December 2016

# *Acknowledgements*

Many others have contributed to my personal and professional development and supported me throughout my graduate research endeavor whom I must thank. Preeminently, I thank my Lord Jesus for hemming me in before and behind in every aspect of life, and for giving me grace to face each day, some of which have included the enjoyment of success and others perseverance through failure. I thank my wife Ashley for enduring six and a half years married to a seemingly perpetual student and everything that entails including sporadic schedules and limited income. Thank you to my kiddos Josiah and Titus for being constant reminders, through both cuteness and tantrums, that life is more than research, and to Josiah for all the times he sat on Daddy's lap watching Netflix on one monitor while I scrambled to reach a good stopping point for the day on the other. I thank also my parents, Jeff and Kathy Olson, for providing every opportunity they could for me to experience and excel, for teaching me to work hard, and for encouraging the three-year-old curiosity in me since before I can remember. The professional foundation on which my development in graduate school has been built is due in no small part to their love, worry, tears, countless hours of reading, playing games, and working together, discussions and quizzes in the car, and never lacking in posing or entertaining "what if" questions–I cannot thank them enough.

# *Abstract*

The ability to perform radiation transport computations in stochastic media is essential for predictive capabilities in applications such as weather modeling, radiation shielding involving non-homogeneous materials, atmospheric radiation transport computations, and transport in plasma-air structures. Due to the random nature of such media, it is often not clear how to model or otherwise compute on many forms of stochastic media. Several approaches to evaluation of transport quantities for some stochastic media exist, though such approaches often either yield considerable error or are quite computationally expensive. We model stochastic media using the Karhunen-Loève (KL) expansion, seek to improve efficiency through use of stochastic collocation (SC), and provide higher-order information of output values using the polynomial chaos expansion (PCE). We study and demonstrate method convergence and apply the new methods to both spatially continuous and spatially discontinuous stochastic media. New methods are shown to produce accurate solutions for reasonable computational cost for several problem when compared with existing solution methods.

Spatially random media are modeled using transformations of the Gaussian-distributed KL expansion–continuous random media with a lognormal transformation and discontinuous random media with a Nataf transformation. Each transformation preserves second-order statistics for the quantity–atom density or material index, respectively–being modeled. The Nyström method facilitates numerical solution of the KL eigenvalues and eigenvectors, and a variety of methods are investigated for sampling KL eigenfunctions as a function of solved eigenvectors. The infinite KL expansion is truncated to a finite number of terms each containing a random variable, and material realizations are created by either randomly or deterministically sampling from the random variables. Deterministic sampling is performed with either isotropic or anisotropic stochastic collocation (SC), the latter of which takes advantage of the monotonic decay of KL terms. Transport quantities are solved on realizations using Monte Carlo particle transport with Woodcock sampling (WMC). Surrogate models of system responses are constructed from SC solutions using the polynomial chaos expansion (PCE) from which probability density functions (PDFs) of response quantities are constructed. The error convergence of solution methods is examined as a validation of the choice of methods, a verification of method implementation, and to give insight towards parameter selection for efficient computation. Solutions are compared against benchmark values generated in a variety of ways including analytic solutions, computational solutions of simpler models, expensive benchmark computations, and published benchmark values.

# Contents

# List of Figures

# List of Tables

# Abbreviations

| | |
|---|---|
| **aPCE** | **a**nisotropic **p**olynomial **c**haos **e**xpansion |
| **AM** | **a**tomic **m**ix |
| **aSC** | **a**nisotropic **s**tochastic **c**ollocation |
| **GH** | **G**auss-**H**ermite |
| **GL** | **G**auss-**L**egendre |
| **iPCE** | **i**sotropic **p**olynomial **c**haos **e**xpansion |
| **iSC** | **i**sotropic **s**tochastic **c**ollocation |
| **KL** | **K**arhunen-**L**oève |
| **LHS** | **l**eft-**h**and **s**ide |
| **LP** | **L**evermore-**P**omraning |
| **MC** | **M**onte **C**arlo method of particle simulation |
| **MP** | **m**id**p**oint integration rule |
| **NM** | **N**yström **m**ethod |
| **PCE** | **p**olynomial **c**haos **e**xpansion |
| **PDF** | **p**robability **d**ensity **f**unction |
| **QoI** | **q**uantity **o**f **i**nterest |
| **RHS** | **r**ight-**h**and **s**ide |
| **RS** | **r**andom **s**ampling |
| **SC** | **s**tochastic **c**ollocation |
| **SC-PCE** | **s**tochastic **c**ollocation-**p**olynomial **c**haos **e**xpansion |
| **TOL** | **Tol**erance |
| **WMC** | **W**oodcock **M**onte **C**arlo |

# Physical Constants

Avogadro's Constant $\quad N_A \quad = \quad 0.602\ 214\ 09 \times 10^{24}\ \text{mol}^{-1}$

# Symbols

| | | |
|---|---|---|
| $a$ | lower bound for integration over finite space | |
| $a_{\mathbf{i}}$, $a_{\mathbf{j}}$ | orthogonality coefficient for term $\mathbf{i}$, $\mathbf{j}$ | |
| $A_k$ | normalization constant of KL mode $k$ | |
| $b$ | higher bound for integration over finite space | |
| $B_k$ | temporary constant in analytic KL eigenmode solution | |
| $\mathbf{B}$ | temporary matrix in Nyström solve | |
| $c$ | scattering ratio, $c := \Sigma_s / \Sigma_t$ | |
| $c_g$ | relative Gaussian process autocovariance | |
| $c_{N_{at}}$ | relative atom density process autocovariance | |
| $\mathbf{C}$ | covariance matrix in Nyström solve | |
| $C_{ij}$ | entry $i$, $j$ of matrix $\mathbf{C}$: $C_{ij} = C_{xx}(x_i, x_j)$ | |
| $C_g$ | Gaussian process autocovariance | |
| $C_{N_{at}}$ | atom density process autocovariance | |
| $C_Z$ | normalized material index process autocovariance | |
| $D$ | number of stochastic dimensions | |
| $d_b$ | distance to boundary | cm |
| $d_c$ | distance to collision | cm |
| $d_c^*$ | distance to potential collision, paired with $\Sigma_t^*$ | cm |
| $\mathbb{E}[]$ | expectation operator | |
| $f$ | arbitrary function | |
| $g$ | random process | |
| | arbitrary function | |
| $g_K$ | random process modeled with $K$-order KL expansion | |
| $g^*$ | cutoff value used in Nataf transformation | |
| $h()$ | function in Nataf transformation | |

| | | |
|---|---|---|
| $H_i, H_j$ | Hermite (probabilists') polynomial of order $i$ or $j$ | |
| $i$ | index of chord length in binary stochastic media | |
| | index of particle interaction number in particle history | |
| | index of Nyström method quadrature | |
| | index of random sampling realization | |
| | index of solution method for tolerance splitting parameter | |
| | order of polynomial | |
| $i_x$ | order tally subscript for PCE coefficients, $x \in \{0, \ldots, I\}$ | |
| $\mathbf{i}$ | multi-index of PCE orders $i_n$ | |
| $I$ | truncation order of polynomial chaos expansion | |
| $I_t$ | (one less than) number of PCE terms | |
| $j$ | index of tally cell | |
| | index of Nyström method quadrature | |
| | index of material cell | |
| | order of polynomial | |
| $\mathbf{j}$ | multi-index of PCE orders $j_n$ | |
| $J$ | particle current | cm$^{-2}$ |
| $J^\pm$ | particle current heading right $(+)$ or left $(-)$ | cm$^{-2}$ |
| $k, k'$ | index of a Karhunen-Loève eigenmode | |
| $K$ | truncation order of KL expansion | |
| $L$ | length of slab | cm |
| $m$ | arbitrary integer used in moment notation | |
| $M$ | gram atomic weight | g mol$^{-1}$ |
| $n$ | index of stochastic dimension | |
| $n$ | index of particle history | |
| $n_{te}$ | index for a tally event within a particle history | |
| $N$ | number of particle histories | |
| $N_{at}$ | atom density | cm$^{-3}$ |
| $N_{Ny}$ | quadrature order of Nyström method | |
| $N_{te}^\pm$ | number of $J^\pm$ tally events over all histories | |
| $p, p'$ | basis function, may be a probability space | |
| $p_g$ | bivariate Gaussian distribution | |
| $p_z$ | probability of material $z$ | |

| | | |
|---|---|---|
| $P_i$, $P_j$ | Legendre polynomial of order $i$ or $j$ | |
| $q$ | index of quadrature node | |
| $q_n$ | index of SC dimension $n$ | |
| $Q$ | quadrature order of stochastic collocation | |
| $Q_n$ | quadrature order of SC for dimension $n$ | |
| $Q_x$ | quadrature order integration of physical domain | |
| $\mathbf{Q}$ | multi-index of SC quadrature orders | |
| $r$ | distance in covariance function | cm |
| | placeholder for cross section type | |
| $R$ | slab reflectance: $R = J^-(0)$ | cm$^{-2}$ |
| | number of random samples | |
| $R_{SC}$ | number of realizations in SC scheme | |
| $R_p$, $R_n$, $R_{p+n}$ | number of samples in previous, new, or combined set | |
| $s_\varphi$ | sample standard deviation of tally $\varphi$ | |
| $s_{\langle\varphi\rangle}$ | sample standard error of the mean of tally $\varphi$ | |
| $t$, $t'$ | variable for integration operations | |
| $T$ | slab transmittance: $T = J^+(L)$ | cm$^{-2}$ |
| $\widehat{u}$ | coefficient of PCE term | |
| $\mathbf{u}_k$ | eigenvector of KL mode $k$ | |
| $\mathbf{u}_k^*$ | intermediate eigenvector $k$ in Nyström KL solve | |
| $\mathbf{u}_{k,j}^*$ | entry $j$ of $\mathbf{u}_k^*$ | |
| $u_k$ | eigenfunction $k$ of Karhunen-Loève expansion | |
| $v_g$ | variance of process $g$ | |
| $\mathbb{V}[]$ | expectation of variance operator | |
| $\mathbf{W}$ | weight matrix in Nyström method | |
| $w_j$ | weight of Nyström node $j$ | |
| $w^{(q)}$, $w'^{(q)}$ | weight of quadrature node $q$ | |
| $w_n^{(q_n)}$ | weight of SC node $q_n$ in dimension $n$ | |
| $x$, $x'$ | variation in physical space | |
| $x_i$, $x_{i-1}$ | position of particle: current, previous | cm |
| $x_i$ | node $i$ in Nyström method | |
| $x_j$, $x_{j+1}$ | position of cell $j$ left, right boundary | cm |
| | node $j, j+1$ in Nyström method | |

| | | |
|---|---|---|
| $x_n$, $x_{n+1}$ | position of left/right edge of material $n$ | cm |
| $\widehat{x}$, $\widehat{x}'$ | length of particle streaming track-length | cm |
| $\widehat{x}_i$ | length of particle streaming track-length in event $i$ | cm |
| $\widehat{x}_{i,n_{te}}$ | portion of $\widehat{x}_i$ allocated to $n_{te}$ | cm |
| $z$ | material index | |
| $z$, $z_1$, $z_2$ | Gaussian-distributed, pseudo-random number | |
| $z'$ | integration variable | |
| | | |
| $\alpha_k$ | root of KL transcendental equation mode $k$ | |
| $\gamma_k$ | eigenvalue of Karhunen-Loève mode $k$ | |
| $\Gamma_i$, $\Gamma_j$ | orthogonal polynomial of order $i$ or $j$ | |
| $\delta_{ij}$ | Dirac delta function | |
| $\Delta x_j$ | length of material segment in material cell $j$ | cm |
| $\Delta x_n$ | length of material segment in material $n$ | cm |
| $\epsilon_K^2$ | mean squared error for $K$-order KL expansion | |
| $\varepsilon$ | angle below which surface flux tallies are treated specially | |
| | error of solution method | |
| $\varepsilon_{\bar{x}}$, $\varepsilon_s$ | error in mean/standard deviation | |
| $\eta$, $\eta_1$, $\eta_2$ | uniformly-distributed, pseudo-random number | |
| $\theta$ | angle of particle travel | rad. (deg.) |
| | tolerance splitting parameter | |
| $\theta_i$ | tolerance splitting parameter for method $i$ | |
| $\iota$ | term of PCE corresponding to unique set of values **i** | |
| $\kappa$ | term of PCE corresponding to unique set of values **j** | |
| $\lambda_z$ | chord length in material $z$ | cm |
| $\lambda_{z,i}$ | chord length $i$ of material $z$ | cm |
| $\lambda_c$ | correlation length in random process | cm |
| $\Lambda_z$ | average chord length of material $z$ | cm |
| $\mu$, $\mu'$ | direction of particle travel: $\mu = cos(\theta)$ | |
| $\mu_i$, $\mu_{i-1}$ | direction of particle travel: current, previous | |
| $\mu_{inc}$ | direction of incident particle beam source | |
| $\mu_{n_{te}}$ | direction of particle for tally event $N_{te}$ | |
| $\xi_k$ | random variable KL mode $k$ | |

| | | |
|---|---|---|
| $\rho$ | material density | g cm$^{-3}$ |
| $\sigma_r$ | microscopic nuclear cross section of type "r" | b (cm$^2$) |
| $\Sigma_r$ | macroscopic nuclear cross section of type "r" | cm$^{-1}$ |
| $\Sigma_{r,z}$ | macroscopic nuclear cross section of type "r" in material "z" | cm$^{-1}$ |
| $\Sigma_t^*$ | macroscopic fictitious total cross section | cm$^{-1}$ |
| $\widehat{\Sigma_{t,n}}$ | range of variation in macrosopic total cross section $n$ | |
| $\tau$ | optical thickness | |
| $\phi$ | scalar particle flux | cm$^{-2}$ |
| $\boldsymbol{\Phi}$ | multi-dimensional Askey polynomial | |
| $\varphi$ | quantity of interest | |
| $\xi_k$, $\xi_d$ | random variable in KL mode $k$, dimension $d$ | |
| $\xi^{(q)}$, $\xi'^{(q)}$ | node of $\xi$ for quadrature node $q$ | |
| $\xi_n^{(i)}$, $\xi_n^{(q_n)}$ | node of $\xi$ in dimension $n$ for realization $i$, SC node $q_n$ | |
| $\boldsymbol{\xi}$ | multi-index of PCE random variables $\xi_n$ | |
| $\boldsymbol{\xi}^{(\boldsymbol{q})}$ | matrix of SC nodes over $\boldsymbol{\xi}$ | |
| $\psi$ | angular particle flux | cm$^{-2}$ sr$^{-1}$ |
| $\omega$ | sample of the stochastic domain | |

# Chapter 1

# Introduction

Modeling and computation of physical systems involving at least one uncertain parameter provides a unique challenge: how to characterize the effects of uncertainty in the input on uncertainty in the outputs of interest. A particularly challenging form of uncertain input is that for which system properties are variable as a function of physical space. For example, radiation calculations involving planetary and stellar atmospheres are performed in a system for which nuclear material properties vary greatly as a function of gas density, a quantity constantly in flux and often varying in non-predictable ways. Materials used in radiation shielding, such as concrete, are often comprised of multiple materials with no clear structure for mixing such that the dose received on the "safe" side is variable. Understanding of such variability can ensure safety, cost-effectiveness, and at times may determine design feasibility. Inertial confinement fusion relies on a precise knowledge of the implosion properties of fuel pellets while being compressed by photon beams; the level of knowledge of the effects of randomly mixed plasma and gas on photon beams during implosion greatly affects yield of the induced fusion and may be the difference in meeting yield goals. The challenge of radiation transport computations in stochastic media also occurs in scenarios such as nuclear reactor fuel, Boiling Water Reactor moderators, and meteorological modeling of sunlight through clouds.

Several qualities are desirable in solution methods of the stochastic transport equation, especially accuracy and efficiency, though further qualities like higher-order characterization of output values, the ability to estimate solution error, and the ability to generalize to other statistical mixings or multiple dimensions are valuable. A most basic approach

to characterization of transport quantities in stochastic media is to assume the material is mixed homogeneously, or equivalently that mixing is on a very small (atomic) scale. This "atomic mix" (AM) approach is efficient, requiring the solution of only one basic transport equation, but only accurate in special cases such as highly scattering media or extremely fine material mixing [1, 2]. In addition, it provides no information on the spread of resulting transport quantities–only a mean value–and no estimate of the error in that mean. Another approach is to describe the stochastic transport equation as a system of coupled equations representing various material property states. Such an approach for spatially discontinuous materials with Markovian statistical mixing is the Levermore-Pomraning (LP) closure [1–4]. The closure is computationally cheap, exact in purely scattering materials, and generally more accurate than the atomic mix approximation. The method can produce higher-order information on transport quantity responses, though an additional closure on the system of equations is required introducing additional error [5, 6]. The method provides no effective means for estimating output error. A more reliable, but expensive, approach is to sample from possible realizations of stochastic media many times [1, 2]. This method, often used as a benchmark solution, provides values for all moments of desired output values and allows for the construction of output probability density functions (PDFs) with a number of entries equal to the number of transport computations run. Convergence of values can be characterized and therefore the remaining error estimated. This method requires, however, knowledge of how to create realizations of stochastic media. In some cases, such as spatially discontinuous stochastic media with Markovian mixing, methods are known for construction of realizations [1, 2], whereas in other cases such as spatially discontinuous stochastic media with other statistical mixing or spatially continuous stochastic media, it may not be known how to construct realizations.

We present use of the Karhunen-Loève (KL) expansion [7–9] for modeling spatially continuous stochastic media (using a lognormal transformation [10]) and a related method for modeling spatially discontinuous stochastic media (using a Nataf transformation [11–13]), each utilizing the Nyström method [14, 15] for numerical solution KL quantities, that seeks to perform better across method goals than existing methods. The only fundamental assumption of the method limiting its accuracy–one introduced through the second-order nature of the KL expansion [9]–is the assumption that the stochastic media can be well represented through its second-order statistics: mean, variance, and

autocovariance. The method seeks to be efficient through smart choice of KL expansion truncation level and use of a deterministic sampling method, stochastic collocation (SC) [10, 16, 17], over the uncertain domain. Efficiency is further improved through use of anisotropic collocation orders by resolving the effects of weightier KL terms more than those less weighty [17]. The method solves an arbitrary number of moments of output values and creates a polynomial chaos expansion (PCE) model [18–21] of the response that, once constructed, can be sampled from cheaply to provide PDFs of output values [10, 22]. Method error convergence can be tracked allowing an estimation of the error of output quantities. We have only applied the methods to stochastic media with exponential covariance functions in a one-dimensional physical domain in this work, but the method lends to extension in modeling of materials with non-exponential covariance functions and application in multi-dimensional physical domains.

The rest of the dissertation is organized as follows:

- Chapter 2: Introduction to the stochastic transport equation and Monte Carlo (MC) particle transport techniques for solving transport quantities on material realizations

- Chapter 3: Discussion of reduced-order methods including the Karhunen-Loève (KL) expansion, random sampling (RS), stochastic collocation (SC), and the polynomial chaos expansion (PCE)

- Chapter 4: Establishment of an error analysis framework and demonstration of the framework on a stochastic transport problem with random nuclear cross section values and deterministic material boundaries

- Chapter 5: Use of a lognormal transformation of the KL expansion to model spatially continuous random media

- Chapter 6: Use of a Nataf transformation of the KL expansion to model spatially discontinuous random media

- Chapter 7: Conclusions and future work

- Appendices A-D: Generation of Gaussian-distributed random samples, use of numerical quadrature, discussion of orthogonal polynomials, and an example benchmark value generation script

# Chapter 2

# Problem Statement and Transport Methods

In this chapter the stochastic transport equation is described along with a solution method for deterministic realizations of the equation. The stochastic transport equation is first discussed along with quantities of interest in this work. Three different sources of uncertainty within this equation are described. The solution method used in this work for deterministic realizations of the stochastic transport equation, the Monte Carlo (MC) method of particle simulation, is then discussed. The discussion includes a description of MC computational mechanics, MC tallies and statistics, and a rejection method called Woodcock Monte Carlo (WMC).

## 2.1    Random Transport Equation

The stochastic, one-dimensional, mono-energetic, neutral-particle, steady-state, and isotropically scattering transport equation that we will focus on is written:

$$\mu \frac{\partial \psi(x,\mu,\omega)}{\partial x} + \Sigma_t(x,\omega)\psi(x,\mu,\omega) = \frac{\Sigma_s(x,\omega)}{2} \int_{-1}^{1} d\mu' \psi(x,\mu',\omega), \qquad (2.1a)$$

$$0 \leq x \leq L; \qquad -1 \leq \mu \leq 1, \qquad (2.1b)$$

where $\mu = cos(\theta)$ is the cosine of the angle of particle travel with respect to the forward direction, $\omega$ represents one realization stochastic domain, $\Sigma_t(x,\omega)$ and $\Sigma_s(x,\omega)$

4

are the total and scattering stochastic macroscopic nuclear interaction cross sections, and $\psi(x, \mu, \omega)$ is the spatially, angularly, and stochastically dependent response function known as angular particle flux. The nuclear cross sections $\Sigma_t(x, \omega)$ and $\Sigma_s(x, \omega)$ are sources of randomness and $\psi(x, \mu, \omega)$ is the random response. The spatial domain extends from the "left" boundary of $x = 0$ to the "right" boundary of $x = L$. In the one-dimensional "slab" geometry used in this work, direction of particle travel spans $\mu \in [-1, 1]$. Depending on the application, "isotropic source" boundary conditions–

$$\psi(0, \mu) = 2, \quad \mu > 0; \qquad \psi(L, \mu) = 0, \quad \mu < 0 \tag{2.2}$$

–or "beam source" boundary conditions–

$$\psi(0, \mu) = \delta(\mu_{inc} - \mu)/\mu_{inc}, \quad \mu > 0; \qquad \psi(L, \mu) = 0, \quad \mu < 0 \tag{2.3}$$

–are chosen. Isotropic source boundary conditions (Eq. (2.2)) impose an isotropically distributed source of strength two. Beam source boundary conditions (Eq. (2.3)) impose a source of strength $\frac{1}{\mu_{inc}}$ at incident angle $\mu_{inc}$. Each set of boundary conditions produces an incident current of magnitude one. Both sets of boundary conditions impose a vacuum condition on the right boundary such that no particles enter the problem from this domain boundary. Both sets of boundary conditions implicitly enforce that any particles traveling out of the domain are lost to the system. We assume the incident boundary source to be nonrandom.

In addition to using the angular particle flux $\psi(\mu, x, \omega)$ as the quantity of interest (QoI) we are interested at various times in either of two QoIs derived from this response function: scalar particle flux $\phi(x, \omega)$ and particle current $J(x, \omega)$. The scalar flux is the particle flux irrespective of, or integrated over, direction of particle travel:

$$\phi(x, \omega) = \int_{-1}^{1} d\mu' \psi(x, \mu', \omega). \tag{2.4}$$

Scalar flux is of interest since many other quantities are independent of the direction of particle travel and can be derived from the scalar flux. Additionally, various approximations and acceleration methods to particle transport problems take advantage of the reduced dimensionality of the scalar flux. The net particle current is the net flux

traveling normally incident through a surface:

$$J(x,\omega) = \int_{-1}^{1} d\mu' \mu' \psi(x,\mu',\omega). \tag{2.5}$$

The net current can be split into the partial currents traveling in each direction through a surface:

$$J(x,\omega) = J^{+}(x,\omega) - J^{-}(x,\omega), \tag{2.6}$$

where the superscripts "+" and "−" denote the right and left direction of particle travel. These particle currents are more fully described as

$$J^{+}(x,\omega) = \int_{0}^{1} d\mu' \mu' \psi(x,\mu',\omega); \qquad J^{-}(x,\omega) = \int_{-1}^{0} d\mu' |\mu'| \psi(x,\mu',\omega). \tag{2.7}$$

In this work we will use $\varphi$ to refer to an arbitrary quantity of interest. The QoI in this work is always derived from the response of Eq. (2.1): $\psi(x,\mu,\omega)$.

Both sets of boundary conditions, Eq. (2.2) and Eq. (2.3), impose an incoming particle current on the left boundary of the slab equal to one, $J^{+}(0,\omega) = 1$, and an incoming particle current on the right boundary of the slab equal to zero, $J^{-}(L,\omega) = 0$.

## 2.2 Types of Random Media

In all problem types we investigate, the uncertainty in Eq. (2.1) originates in the macroscopic nuclear cross sections $\Sigma_r(x,\omega)$, where "$r$" is either equal to "$t$" for total cross section or "$s$" for scattering cross section. Non-stochastic macroscopic nuclear cross sections $\Sigma_r(x)$ are calculated as the product of material atom density $N_{at}(x)$–equal to the material density $\rho(x)$ times Avogadro's Constant $N_A$ divided by gram atomic weight $M(x)$–and microscopic cross section $\sigma_r(x)$, vis.,

$$\Sigma_r(x) = N_{at}(x)\sigma_r(x). \tag{2.8}$$

We investigate three unique stochastic transport problems based on uncertainty originating in cross sections $\Sigma_r(x,\omega)$.

Random variables $\boldsymbol{\xi} = \{\xi_1,\ldots,\xi_D\}$ map the stochastic event space, of which $\omega$ is one event, to a measurable stochastic space $\boldsymbol{\xi}(\omega)$ such that one value of $\omega$ corresponds to a set

of values for all random variables $\boldsymbol{\xi}$. The general expression for stochastic macroscopic cross section "r" may then either be written $\Sigma_r(\omega)$, $\Sigma_r(\boldsymbol{\xi}(\omega))$, or $\Sigma_r(\boldsymbol{\xi})$.

In the first problem type we investigate geometric boundaries and densities for materials are known a priori, but the value of at least one macroscopic cross section for at least one material is uncertain and varied according to independent uniformly distributed random variables:

$$\Sigma_r(x,\omega) = \Sigma_r(x,\boldsymbol{\xi}(\omega)), \quad \xi_n \in \mathcal{U}(-1,1) \ \forall \ n. \tag{2.9}$$

One application of this problem type is quantifying the effects of experimentally determined microscopic cross sections in which, for many cross sections, there is great uncertainty. The microscopic cross sections are often assumed to be Gaussian distributed, though this distribution is chosen somewhat arbitrarily, and the methods examined here can also be performed using Gaussian distributions for the uncertain variables. We investigate modeling and transport through this type of random media in Chapter 4.

The second type of random media we investigate involves continuously varying uncertainty material densities:

$$\Sigma_r(x,\omega) = N_{at}(x,\boldsymbol{\xi}(\omega))\sigma_r(x), \quad \xi_n \in \mathcal{N}(0,1) \ \forall \ n. \tag{2.10}$$

Material density is taken to vary continuously through the slab geometry and is modeled using a transformation of the Karhunen-Loève expansion in which the random variables are Gaussian distributed. Applications of this problem type include transport calculations in fluid density fluctuations such as those in the atmosphere. We investigate modeling and transport through this type of random media in Chapter 5.

The last type of random media we investigate involves two materials which are discontinuously mixed over the physical domain and for which the boundaries between the materials are located randomly. Uncertainty originates in material interface locations $x$, such that for each material $z$ macroscopic cross sections are deterministic:

$$\Sigma_r(x,\omega) = \Sigma_{r,z(x,\boldsymbol{\xi}(\omega))}, \quad z \in \{0,1\}, \quad \xi_n \in \mathcal{N}(0,1), \ \forall n. \tag{2.11}$$

Material index $z$ is a random process modeled using a transformation of the Karhunen-Loève expansion with Gaussian random variables. We focus our investigation on binary, Markovian-mixed materials in which two materials have clearly defined average chord

lengths, vis., $\Lambda_z$, $z \in \{0, 1\}$, and individual chord lengths $\lambda_z$ are distributed according to the exponential distribution:

$$p(\lambda_z)d\lambda_z = \frac{1}{\Lambda_z} \exp\left[-\frac{\lambda_z}{\Lambda_z}\right] d\lambda_z. \qquad (2.12)$$

This sub-class of spatially discontinuous random media is of interest in applications such as pebble-bed nuclear reactors, photon transport through turbulently mixed materials in laser fusion experiments, photon transport through clouds, and neutron transport in mixtures of water and air in boiling water reactors. We limit investigation of spatially discontinuous random media to binary materials with Markovian mixing statistics here, but develop numerical methods which allow the modeling of spatially discontinuous random media obeying other statistical models as well. We investigate modeling and transport through this type of random media in Chapter 6.

## 2.3    Radiation Transport Solver Method: Monte Carlo (MC) Transport

In this section we discuss the use of Monte Carlo particle simulation to solve quantities of interest on realizations of the stochastic transport equation. The radiation transport equation is typically solved for the expectation value of particle flux using either deterministic solvers such as finite elements methods, or using the Monte Carlo method of particle simulation (MC) through random sampling. Though random sampling in the uncertain domain and the differential equation solution method through random sampling of particle tracks are each appropriately called a Monte Carlo method [23], for clarity we will restrict usage of the title "Monte Carlo" in this work to the second–Monte Carlo sampling of particle tracks–and refer to the first simply as "random sampling" (RS). Woodcock sampling is an extension of the Monte Carlo method of interest in this work. We will refer to Monte Carlo particle simulation using Woodcock sampling as Woodcock Monte Carlo (WMC), and discuss it further in Section 2.3.4.

Monte Carlo transport is a method which samples from terms of the Neumann expansion of the second-kind, Fredholm-type integral equation form of the transport equation [24, 25]. The effects of operations such as particle streaming and particle scattering are represented by terms which can be sampled from in the Neumann series. Individual

particle histories are simulated by sampling successively against these terms to "advance" a particle through a series of operations characterized by a Markov process of state changes. Though rigorously the Monte Carlo method samples against terms of the Neumann expansion of the integral form of the transport equation, a non-rigorous but possibly more intuitive way to think of the function of individual sampling operations is presented in the following sections, based on the differential form of the transport equation.

We discuss the theory of the Monte Carlo particle transport method briefly; more detailed accounts can be found in books such as Refs. [24–26].

### 2.3.1 Monte Carlo Particle Simulation Mechanics

Here we describe Monte Carlo transport through a realization of the stochastic, one-dimensional, mono-energetic, neutral-particle, steady-state, and isotropically scattering transport equation:

$$\mu \frac{\partial \psi(x, \mu)}{\partial x} + \Sigma_t(x) \psi(x, \mu) = \frac{\Sigma_s(x)}{2} \int_{-1}^{1} d\mu' \psi(x, \mu'), \tag{2.13a}$$

$$0 \le x \le L; \qquad -1 \le \mu \le 1, \tag{2.13b}$$

with appropriate boundary conditions, e.g., Eq. (2.2) or Eq. (2.3). Particle histories are instantiated according to a source term in the equation, in our cases in the left incident boundary condition, and are simulated according to system probabilities defined by macroscopic cross section values. Before a simulation, "tallies" are set such that events of interest, contributing to any quantities of interest (QoIs), are tallied during the simulation. These tallies are then used to calculate the defined QoIs through statistical analysis.

#### 2.3.1.1 Particle Instantiation

Particle histories are instantiated according to whatever source term(s) are present in the transport equation. In our problems, particles begin according to the left boundary condition in Eq. (2.2) or Eq. (2.3). A new particle history's position is assigned as $x_i = 0$. In the case of an isotropic boundary source, as in Eq. (2.2), the initial particle angle

of travel ($\mu_i$) is set equal to the square root of a pseudo-random number ($\eta$) sampled from a uniform distribution between 0 and 1, $\mu_i = \sqrt{\eta}, \eta \in \mathcal{U}(0, 1)$. This results from choosing a constant flux in each direction,

$$\psi(\mu_i) = 2 = \frac{2}{\mu_i} J(\mu) \therefore J(\mu) = \mu_i, \tag{2.14}$$

and sampling $\mu_i$ pseudo-randomly against the cumulative density function of $J(\mu)$:

$$\eta = \frac{\int_0^{\mu_i} J(\mu) d\mu}{\int_0^1 J(\mu) d\mu} = \frac{\int_0^{\mu_i} \mu d\mu}{\int_0^1 \mu d\mu} = \frac{[\mu^2/2]_0^{\mu_i}}{[\mu^2/2]_0^1} = \mu_i^2 \ \rightarrow \ \mu_i = \sqrt{\eta}. \tag{2.15}$$

The direction of particle travel has been restricted to traveling "rightward", since "leftward" particles on the left slab boundary would not enter the slab. In the case of a beam boundary source, as in Eq. (2.3), the current particle angle of travel ($\mu_i$) is set equal to the incident angle of the beam: $\mu_i = \mu_{inc}$.


### 2.3.1.2 Particle Streaming Operator

The first operation after instantiation of a particle history is a streaming operation in which the particle position is advanced from the now previous position $x_{i-1}$ to the new position $x_i$. The streaming operation samples a distance to collision and computes the distance to the nearest boundary, selecting to stream the particle the smaller of these two distances from the current position. Though the rigorous mathematical basis for this sampling method comes from the Neumann expansion of the integral form of the transport equation, the streaming operation can be viewed as an evaluation of the streaming and collision terms of the transport equation (Eq. (2.13)):

$$\mu \frac{\partial \psi(x, \mu)}{\partial x} + \Sigma_t(x)\psi(x, \mu) = 0. \tag{2.16}$$

In a streaming operation, a particle advances from position $x_{i-1}$ to position $x_i = x_{i-1} + \mu_{i-1}\widehat{x}_i$, where $\widehat{x}_i$ is the distance the particle traveled. In a traditional approach to sampling the distance a particle streams during event $i$, a constant total cross section is required over the flight path of the particle history, vis., $\Sigma_t = \Sigma_t(x) \ \forall \ x \in [x_{i-1}, x_i]$. The probability of non-interaction from $x_{i-1}$ to $x_i$ is equal to $\exp[-\Sigma_t\widehat{x}_i]$, and the differential probability of interaction is $\Sigma_t d\widehat{x}_i$ [26], such that the probability of a particle at $x_{i-1}$

traveling distance $\widehat{x}$ is

$$f(\widehat{x})d\widehat{x} = \Sigma_t \exp[-\Sigma_t\widehat{x}]d\widehat{x}. \tag{2.17}$$

From a pseudo-random $\eta \in \mathcal{U}(0,1)$ a distance to collision value $d_c$ is solved by integrating to create a cumulative probability distribution:

$$\eta = F(d_c) = \int_0^{d_c} \Sigma_t \exp[-\Sigma_t\widehat{x}']d\widehat{x}'. \tag{2.18}$$

The distance to collision $d_c$ is solved and, noting that $1 - \eta$ and $\eta$ share the same distribution, the former is replaced with the latter to minimize computational effort:

$$d_c = -\frac{\ln(1 - \eta)}{\Sigma_t} = -\frac{\ln(\eta)}{\Sigma_t}. \tag{2.19}$$

After sampling a distance to collision $d_c$, distance to the nearest boundary along the flight path $d_b$ is calculated. A boundary can be the point along the flight path for which the total cross section is no longer constant such as a domain boundary, a material interface, or an imposed boundary meant for purposes such as collecting tallies. The new particle position $x_i$ is then chosen according to the distance which is most limiting:

$$x_i = x_{i-1} + \mu_{i-1}\widehat{x}_i, \quad \widehat{x}_i = min(d_b, d_c). \tag{2.20}$$

While the angle of particle travel is not changed, vis., $\mu_i = \mu_{i-1}$, any tallies pertaining to the advancement of the particle history from $x_{i-1}$ to $x_i$ are taken and the next operation for the particle is evaluated. If the particle reached an imposed boundary, a new streaming operation is performed with the same macroscopic cross sections. If the particle reached a location at which the macroscopic cross sections change, a new streaming operation is performed with the now local macroscopic cross section values. If the particle reached a physical domain boundary, the particle history is terminated and a new one is instantiated, beginning a new particle history. If the particle reached a collision event, a collision operation is performed.

### 2.3.1.3 Particle Collision Operator

A collision operation occurs after a streaming operation has resulted in the choice of a collision event. The collision operation determines what type of collision event the particle will undergo. In our simple physics, the two outcomes are either particle absorption or scattering. If the particle scatters, this operation will select a new direction of particle travel. The mathematical basis for this operation is a sampling from terms in the Neumann expansion of the integral form of the transport equation, though a comparison of the collision and scattering terms in Eq. (2.13) may add intuition:

$$\Sigma_t(x)\psi(x,\mu) = \frac{\Sigma_s(x)}{2}\int_{-1}^{1}d\mu'\psi(x,\mu') \quad \Rightarrow \quad \psi(x,\mu) = \frac{\Sigma_s(x)}{\Sigma_t(x)}\frac{1}{2}\int_{-1}^{1}d\mu'\psi(x,\mu'). \quad (2.21)$$

To evaluate this relationship, a pseudo-random number $\eta \in \mathcal{U}(0,1)$ is compared against the local scattering ratio $c(x_i) = \Sigma_s(x_i)/\Sigma_t(x_i)$ to determine if a particle is absorbed or scattered. In either case the particle position remains unchanged, vis., $x_i = x_{i-1}$. If the particle is determined to be absorbed, $\eta > c(x_i)$, any appropriate tallies are taken and the particle history is terminated. If the particle is determined to be scattered, $\eta < c(x_i)$, the particle survives and a new particle direction $\mu_i$ is sampled, evaluating the integral in Eq. (2.21).

Since our scattering physics is chosen to be isotropic, the new direction of particle travel is simply chosen using another pseudo-random number:

$$\mu_i = 2\eta - 1, \eta \in \mathcal{U}(0,1). \quad (2.22)$$

Any appropriate tallies are taken and a new streaming operation begins based on the current position $x_i$ and direction $\mu_i$ of particle travel.

### 2.3.2 Monte Carlo Particle Simulation Tallies

We calculate three different types of quantities of interest (QoIs) in our one-dimensional geometry using Monte Carlo particle simulation tallies. For each tally type we typically tally both the QoI and its square over each history. This information is sufficient to yield a sample mean and standard deviation for the tally. We calculate current over a surface at point $x$, $J^+(x)$ or $J^-(x)$, scalar flux over a surface at point $x$, $\phi(x)$, and scalar

flux over a cell defined between $x_j$ and $x_{j+1}$, $\phi_j = \phi(x_j, x_{j+1})$. Here we briefly discuss each.

For all three tally types defined here, we must sum the contributions from each tally event for each particle history. Since we have only utilized current tallies on the boundaries of the domain, each of our current tallies is only able to have one tally event per particle history. If there was a possibility of more than one tally event per particle history for our current tallies, they would require summing over the tally events in each particle history. Examples of such multiple tally events would be particles crossing a surface heading in the forward or backward direction more than once or multiple tallies per particle history arising from secondary particles.

### 2.3.2.1 Boundary Current Tallies

We calculate the total current over a boundary at $x$ headed in either the positive-facing direction $\mu > 0$ on the right boundary of the slab, $J^+(L)$, or the negative-facing direction $\mu < 0$ on the left boundary of the slab, $J^-(0)$. These quantities are called the transmittance

$$T = J^+(L) \tag{2.23}$$

and reflectance

$$R = J^-(0), \tag{2.24}$$

respectively. Since particles which exit the slab are lost to the system and our physics does not include secondary particles, each particle history can contribute a tally of either 0 or 1 to each of these leakage current tallies. We tally the number of particle histories which end in a transmittance or reflectance event and divide by the number of particle histories simulated to calculate the mean and second moment of transmittance and reflectance:

$$\langle T \rangle = \langle T^2 \rangle = \frac{N_{te}^+(L)}{N}, \tag{2.25a}$$

$$\langle R \rangle = \langle R^2 \rangle = \frac{N_{te}^-(0)}{N}, \tag{2.25b}$$

where $N_{te}^\pm(x)$ is the number of transmittance or reflectance tally events. Since each tally has a value of 1, the sample mean and second moment of the current are the same.

#### 2.3.2.2 Surface Flux Tallies

We calculate the flux on a surface at point $x$ in a similar manner as we calculate current, but we care about the direction of travel of the particles crossing the surface. To calculate statistics on flux values we must calculate first and second moments separately. Each time a particle crosses a surface, we call this a tally event and tally the absolute value of the inverse of the direction of particle travel, $|\mu_{n_{te}}^{-1}|$. We sum all tally events for each tally on each particle history. We use this sum to find the sample mean and second moment of the flux at a surface located at $x$:

$$\langle \phi(x) \rangle = \frac{1}{N} \sum_{n=1}^{N} \left( \sum_{n_{te}} \frac{1}{|\mu_{n_{te}}|} \right)_n ; \quad \langle \phi^2(x) \rangle = \frac{1}{N} \sum_{n=1}^{N} \left( \sum_{n_{te}} \frac{1}{|\mu_{n_{te}}|} \right)_n^2 . \tag{2.26}$$

This flux estimator is unbounded: as $\mu \to 0$, $\frac{1}{|\mu_{n_{te}}|} \to \infty$. We have not addressed the unbounded nature of the surface flux estimator in any special way. Though we are not aware of skewed statistics in any of our tallies due to this unbounded estimator, we cannot rule out the possibility with the current implementation. One common treatment of this phenomenon, as discussed in Dupree and Fraley [25], is to supply a value $\varepsilon$ such that any surface flux tally made by a particle traveling at a direction $|\mu| < \varepsilon$ is accounted for as traveling at some averaged value $|\mu|$. A permutation on this approach is to simply disregard any tallies for particles with direction $|\mu| < \varepsilon$.

#### 2.3.2.3 Cell Flux Tallies

We calculate the flux in cell $j$ using track-length estimators. A particle's track-length is calculated as the absolute value of a particle's change in $x$ over a streaming operation from $x_{i-1}$ to $x_i$ divided by the direction of particle travel for that streaming operation:

$$\widehat{x}_i = \left| \frac{x_i - x_{i-1}}{\mu_{i-1}} \right| . \tag{2.27}$$

We calculate the flux sample mean and second moment in cell $j$ by tallying the sum of the track-lengths from all tally events in cell $j$ for a history and that quantity's square.

We then divide by the number of particle histories simulated and the size of the cell:

$$\langle \phi_j \rangle = \frac{1}{x_{j+1} - x_j} \frac{1}{N} \sum_{n=1}^{N} \left( \sum_{n_{te}} \widehat{x}_{i,n_{te}} \right)_n ; \qquad \langle \phi_j^2 \rangle = \frac{1}{x_{j+1} - x_j} \frac{1}{N} \sum_{n=1}^{N} \left( \sum_{n_{te}} \widehat{x}_{i,n_{te}} \right)_n^2 .$$
$$(2.28)$$

We note that the computation of $\widehat{x}_i$ using Eq. (2.26) includes the potential to divide by zero or a number very close to zero. This can cause computational errors and may cause Eq. (2.28) to be unbounded. Though we are not aware of use of Eq. (2.27) having caused any issues in our computations, it is possible. A simple solution to this problem is to use $\widehat{x}_i$ as calculated by the minimum of the distance to boundary and distance to collision as in Equation 2.20 instead of computation of $\widehat{x}_i$ as calculated in Equation 2.27. The subtle, but important, difference in the two approaches is that use of Eq. (2.20) does not require division, and thus cannot require division by zero or a number close to zero.

When using cell flux tallies, we allocate track-length tally events to cells in one of two ways. In one approach, we allocate a tally event to each cell in which a particle track-length traveled with a magnitude equal to the distance traveled while in that cell. This is probably the most intuitive method. In another approach we allocate one tally event per track-length to one of the cells over which the track-length spanned, and contribute the full magnitude of the distance traveled to that cell. The cell is chosen by statistically sampling from the cells over which the track-length spanned according to the relative distances traveled in each cell. Fully converged, these two methods are equivalent. The first method is likely to converge a tally to a smaller error for the same number of particles simulated $N$, but the second method simulates each particle with less computational effort. It is difficult to know a priori which is more efficient.

### 2.3.3 Monte Carlo Tally Statistics

We have demonstrated calculation of a quantity of interest's sample mean and second moment, $\langle \varphi \rangle$ and $\langle \varphi^2 \rangle$, using tallies in Section 2.3.2. Here we briefly discuss batch statistics and demonstrate use of these quantities for calculation of the sample mean, standard deviation, and standard error of the mean of a quantity of interest $\varphi$.

Sometimes in Monte Carlo particle simulation implementations, batches are used in which a collection of particle histories provides sample values for a tally and the following

statistical procedures are performed over batch values. Using batch tally values instead of history tally values can reduce computational effort for tally statistics and provides a natural point for parallel code synchronization. Our implementation does not use batch statistics but performs the statistical analysis for a tally directly on quantities arising from individual particle history tallies. Performing statistics over particle histories can be viewed as using batch statistics with a batch size of one particle history; Eqs. (2.26) and (2.28) solve batch statistical quantities if index $n$ sums over $N$ batches and all tally events $n_{te}$ for every particle history in each batch are summed. Eq. (2.25) could be similarly reformatted.

In Section 2.3.2 we calculated the sample mean and second moment of QoIs according to

$$\langle\varphi\rangle = \frac{1}{N}\sum_{n=1}^{N}\varphi_n; \qquad \langle\varphi^2\rangle = \frac{1}{N}\sum_{n=1}^{N}\varphi_n^2, \tag{2.29}$$

where $\varphi_n$ was the sum of all tally events for a QoI in particle history $n$. We have already attained the sample mean, $\langle\varphi\rangle$, but now use the sample mean and second moment of $\varphi$ to calculate the sample standard deviation and standard error of the mean.

The sample variance of $\varphi$ is

$$s_\varphi^2 = \frac{1}{N-1}\sum_{n=1}^{N}(\varphi_n - \langle\varphi\rangle)^2 \tag{2.30a}$$

$$= \frac{1}{N-1}\left[\sum_{n=1}^{N}\varphi_n^2 - 2\langle\varphi\rangle\sum_{n=1}^{N}\varphi_n + \sum_{n=1}^{N}\langle\varphi\rangle^2\right] \tag{2.30b}$$

$$= \frac{1}{N-1}\left[\sum_{n=1}^{N}\varphi_n^2 - 2N\langle\varphi\rangle^2 + N\langle\varphi\rangle^2\right] \tag{2.30c}$$

$$= \frac{N}{N-1}\left[\frac{1}{N}\sum_{n=1}^{N}\varphi_n^2 - \langle\varphi\rangle^2\right] \tag{2.30d}$$

$$= \frac{N}{N-1}\left[\langle\varphi^2\rangle - \langle\varphi\rangle^2\right]. \tag{2.30e}$$

It is clear from Eqs. (2.29) and (2.30e) that the sample standard deviation $s_\varphi$ for any QoI is calculable from nothing more than the sum of tallies for a quantity and the sum of the square of tallies for the quantity across particle histories. This is convenient computationally and as a result the sum of a tally and the sum of squares of the tally are often all that is stored in computer memory for a given tally.

Following the Central Limit Theorem, the sample standard error of the mean $s_{\langle\varphi\rangle}$ is calculated

$$s_{\langle\varphi\rangle} = \frac{s_\varphi}{\sqrt{N}}. \tag{2.31}$$

The sample standard error of the mean, using $N$ samples from the population, provides, with about 68% confidence, that the true mean of the sample is within a standard error of the mean from the mean.

In the case that tallies contain only values of either 0 or 1, the second moment need not be tallied to calculate the solution standard deviation or standard error of the mean. Each solution value is equal to its square, $\varphi_i = \varphi_i^2$, such that the first and second moments are equal: $\langle\varphi\rangle = \langle\varphi^2\rangle$. Calculation of standard devation (and thus standard error of the mean) thus only requires tallying of the first moment:

$$s_{\langle\varphi\rangle}^2 = \frac{N}{N-1}\Big[\langle\varphi\rangle - \langle\varphi\rangle^2\Big]. \tag{2.32}$$

### 2.3.4 Woodcock Monte Carlo (WMC)

Woodcock sampling is a rejection method developed within Monte Carlo particle simulation which allows for sampling a distance to collision $d_c$ (Eq. (2.19)) over a portion of a problem domain in which the macroscopic total cross section $\Sigma_t(x)$ in that portion of the domain need not be constant. Woodcock sampling is sometimes also called "delta-tracking" or "pseudo-scattering-tracking". We will call evaluation of Monte Carlo particle simulation using Woodcock sampling simply Woodcock Monte Carlo (WMC).

Woodcock Monte Carlo was developed to reduce the runtime required in a multi-D Monte Carlo simulation problem by allowing particle tracks to stream over potentially many material interfaces before requiring the often expensive calculation of determining which material cell the particle track is in [27, 28]. WMC was more mathematically-rigorously presented soon thereafter [29, 30], then extended for application involving spatially continuously varying macroscopic total cross sections [31].

There seems to be renewed interest in WMC in recent years: WMC is an option in several production-level Monte Carlo codes including MONK and MCBEND [32], MORET 5 [33], and Serpent 2 [34]. Schemes involving when and how to implement WMC for greatest efficiency have been investigated [33–39], and when implemented effectively

WMC can show significant computational savings over the more traditional approach to MC. For at least one modern problem, application of WMC without any special schemes has yielded significantly more efficient Monte Carlo transport results than MC without Woodcock sampling [40].

Woodcock Monte Carlo is our method of choice for handling Monte Carlo transport over spatially continuous cross sections, though other options exist. In the early 2000's Brown and Martin [41, 42] proposed a method of sampling optical depth, rather than distance to collision, by integrating total cross section seen by the particle. Though accurate, this method provides implementation challenges, i.e., the total cross section field must be known well enough to integrate to a value. At best this is little more than a minor modification of Eq. (2.18). At worst it requires a transcendental solve for the optical thickness to be traveled by a particle, which is computed numerically over values that must be extracted from a multi-D geometry.

Another option is to discretize the domain into cells for which an average total cross section value is solved in each bin. Distance to collision operations can then be performed over each bin. Alternatively, the optical thickness traveled can be sampled and the distance to collision computed using the discrete total cross section values over potentially many cells. In either of these approaches, discretizing spatially introduces an avoidable discretization error. In the first, many small cells, requiring many streaming operations which almost always end in the particle streaming through the cell, make the MC simulation process computationally inefficient. Whereas the optical thickness evaluation over a grid reduces the computational burden, it still requires summing optical thickness over cells, requires a way to average cross section values over the local cell, and introduces a discretization error.

### 2.3.4.1 WMC Formulation

Woodcock Monte Carlo adds a fictitious macroscopic total cross section $\Sigma_t^*$ to the transport equation (Eq. (2.13)):

$$\mu\frac{\partial\psi(x,\mu)}{\partial x} + \frac{\Sigma_t(x)}{\Sigma_t^*}\Sigma_t^*\psi(x,\mu) = \frac{\Sigma_s(x)}{2}\int_{-1}^{1}d\mu'\psi(x,\mu'), \tag{2.33a}$$

$$0 \le x \le L; \qquad -1 \le \mu \le 1, \tag{2.33b}$$

again with appropriate boundary conditions, e.g., Eq. (2.2) or Eq. (2.3). This ficti-
tious cross section is sometimes also referred to as the "ceiling", "delta-scatterer", or
"majorant" cross section, though we will simply call it the fictitious total cross section.

In our implementation we have chosen $\Sigma_t^*$ as the maximum total cross section from a
particle's current position $x_i$ to the end of the slab in the direction of particle travel.
The simplest implementation would be to choose $\Sigma_t^*$ as the maximum total cross section
over the entire slab; we have chosen to reduce the frequency of interaction rejection by
choosing $\Sigma_t^*$ only as a function of the total cross section values a particle may interact
with for a given particle flight. Since the fictitious cross section need only be equal to
or larger than the total cross section for a given particle flight path, we could further
reduce rejection frequency by smartly imposing boundaries to each particle flight path.
Some have investigated savings through such imposed boundaries [34, 37, 38].

### 2.3.4.2   WMC Mechanics: Modified Streaming Operator

Woodcock sampling is a modification of the particle streaming operation (Section 2.3.1.2).
The mathematical basis for evaluating all Monte Carlo operations in the Monte Carlo
method is a sampling against terms of the Neumann series of the integral form of the
transport equation, though it may add intuition to think of WMC as a sampling of the
streaming operation governed by

$$\mu\frac{\partial\psi(x,\mu)}{\partial x} + \frac{\Sigma_t(x)}{\Sigma_t^*}\Sigma_t^*\psi(x,\mu) = 0. \tag{2.34}$$

When using Woodcock sampling in Monte Carlo transport operations, a distance to
potential collision $d_c^*$ is sampled. This operation can be thought of as an evaluation of

$$\mu\frac{\partial\psi(x,\mu)}{\partial x} + \Sigma_t^*\psi(x,\mu) = 0, \tag{2.35}$$

and $d_c^*$ is sampled according to

$$d_c^* = -\frac{\ln(\eta)}{\Sigma_t^*}, \quad \eta \in \mathcal{U}(0,1). \tag{2.36}$$

The particle is advanced to a new position $x_i$:

$$x_i = x_{i-1} + \mu_{i-1}\widehat{x}_i, \quad \widehat{x}_i = min(d_b, d_c^*). \tag{2.37}$$

Any tallies pertaining to the advancement of the particle history from $x_{i-1}$ to $x_i$ are taken.

If the distance to potential collision $d_c^*$ was the limiting factor in determining the length of the particle flight $\widehat{x}_i$, vis., $\widehat{x}_i = d_c^*$, the ratio between the macroscopic total cross section and the fictitious total cross section governs whether the potential collision event becomes a collision event or a streaming event. If a newly chosen pseudo-random number $\eta \in \mathcal{U}(0,1)$ is less than the ratio of the total cross section to the fictitious cross section,

$$\eta < \frac{\Sigma_t(x)}{\Sigma_t^*}, \tag{2.38}$$

the event is chosen to be a collision event. Any appropriate tallies are taken and the particle undergoes a particle scattering event. If $\eta$ is greater than the ratio, the potential collision is chosen to be a non-collision. Any appropriate tallies are taken and the particle undergoes another Woodcock-sampling-modified streaming event beginning from the new value of $x_i$ and maintaining the same direction of particle travel $\mu_i = \mu_{i-1}$.

### 2.3.4.3 WMC Efficiency

Woodcock Monte Carlo is most efficient with well-chosen fictitious cross section values over well-chosen flight path domains. Assuming the cost of determining optimal fictitious cross section values and flight path domains is zero, fictitious cross section values will be chosen for each particle flight path such that the fictitious cross section is exactly equal to the maximum total cross section in the flight path. Likewise, an optimal algorithm will impose a boundary on the length of the flight path such that the maximum total cross section is not too disparate from the minimum and average total cross sections. This reduces the additional computational cost of sampling many potential distances to collision for which another streaming operation was chosen.

For example, if the total cross section in a flight path domain was generally very small, but very large for a small portion of the domain, $d_c^*$ would be sampled over $d_b$ on average many times, and for most of them the particle would continue streaming on its initial

path. This would cause many essentially meaningless potential collision interactions. A more efficient choice would be to impose a boundary immediately before and another after the small section of the flight path domain for which the total cross section was large. The flight path would be broken up into three segments for which WMC is efficient on each, and on average considerable computational time would be saved.

When available a search for the most efficient location or locations for imposed flight path domains should be made as an analysis of a physical system before particle simulation, though searches can be made on the fly. If searches for efficient flight path domains are made during particle simulation, careful consideration must be made in selecting the searching algorithm so that its net effect is computational savings. Whether WMC flight path domains are solved for before or during particle simulation, the challenge is to spend less time analyzing the physical problem for placement of imposed boundaries than is saved though the use of the imposed boundaries.

# Chapter 3

# Stochastic Solution Methods

In Chapter 2 we introduced the stochastic transport equation and described the use of Monte Carlo particle simulation for the solution of a realization of the stochastic equation. Here we discuss methods used to solve quantities of interest over the stochastic variation of the input.

The Karhunen-Loève (KL) expansion and the polynomial chaos expansion (PCE) are two spectral models of a field. In general, use of the KL expansion is preferred as its terms belong to a single eigenspectrum expansion of monotonically decreasing magnitude. The number of terms required in a truncation of the KL expansion to attain desired accuracy is generally less than the number required from the PCE and the truncation scheme is more straightforward. Modeling a field using the KL expansion, however, requires knowledge of the field covariance, which is not always known. The PCE can be used even when the field covariance is not known.

We use the KL expansion to model random media. In Chapter 5 we use the KL expansion to model spatially continuous random media and in Chapter 6 we use the KL expansion to model spatially discontinuous random media. In both cases we assume the covariance of the random field of material cross sections and use the KL expansion to reduce an uncountably infinite number of random variables–one at each location in $x$–to a countably infinite number of random variables. Through truncation we further reduce the stochastic dimensionality to a finite number of random variables.

We resolve the effects of stochastic variation in input parameters on our quantities of interest through random sampling (RS), stochastic collocation (SC), and construction

of the response field through use of the PCE. In Chapter 4 we examine a problem which has a finite number of random variables. In Chapters 5 and 6 we examine problems for which random cross section fields have been modeled using the KL expansion, reducing the number of random variables to a finite number. In each case, we solve quantities of interest over realizations of the stochastic transport equation at nodes of a RS or SC method. Random sampling provides moments of a quantity of interest and allows construction of a response probability density function (PDF). Stochastic collocation, a form of deterministic sampling, solves moments of a quantity of interest, for some problems more efficiently than RS, but does not provide calculation of response PDFs. We therefore use SC nodes and solutions to build a PCE model of the stochastic response. From this PCE model we solve moments of the quantity of interest and sample cheaply to construct PDFs of the response.

## 3.1 Random Geometry Modeling: Karhunen-Loève (KL) Expansion

The Karhunen-Loève expansion is the optimal spectral expansion of a second order random process [7–9]. For random process $g(x, \omega)$ it is written:

$$g(x, \omega) = \langle g \rangle + \sum_{k=1}^{\infty} \sqrt{\gamma_k} u_k(x) \xi_k(\omega), \tag{3.1}$$

where $\langle g \rangle$ is the average value of the process, often in literature assumed to be equal to zero; $\gamma_k$, $u_k$, and $\xi_k$ are the eigenvalue, eigenfunction or eigenvector, and random coefficient for expansion term $k$; $x$ represents dependence in the physical domain; and $\omega$ represents a realization in the stochastic domain. Eigenfunctions $u_k(x)$ provide variation across the physical domain and random variables $\xi_k(\omega)$ provide variation across the stochastic domain. Eigenvalues $\gamma_k$ provide a magnitude for the contribution of each term $k$, and the process average $\langle g \rangle$ provides a value about which the rest of the expansion adds variation.

The eigenspectrum is purely discrete, characterized by a countably infinite ordered set of eigenvalues and orthogonal eigenfunctions (Eq. (3.1)) which can be normalized yielding

$$\big( u_k(x), u_{k'}(x) \big) = \delta_{kk'}, \tag{3.2}$$

where $\big(f(x), g(x)\big) \equiv \int_x f(x)g(x)dx$.

The expansion coefficients $\xi_k(\omega)$ are uncorrelated (Eq. (3.3a)), zero-mean (Eq. (3.3b)), and unit variance (Eq. (3.3c)) random variables:

$$\mathbb{E}[\xi_k(\omega)\xi_{k'}(\omega)] = \int_{\xi_k}\int_{\xi_{k'}} \xi_k\xi_{k'}p(\xi_k,\xi_{k'})d\xi_k d\xi_{k'} = \delta_{kk'}, \qquad (3.3a)$$

$$\mathbb{E}[\xi_k(\omega)] = \int_{\xi_k} \xi_k p(\xi_k)d\xi_k \qquad\qquad = 0, \qquad (3.3b)$$

$$\mathbb{V}[\xi_k(\omega)] = \int_{\xi_k} (\mathbb{E}[\xi_k] - \xi_k)^2 p(\xi_k)d\xi_k \qquad = 1. \qquad (3.3c)$$

Eigenvalue and eigenfunction or eigenvector pairs for eigenmode $k$ in the KL expansion are generated by solving the Fredholm integral equation

$$\int_D C_g(x, x')u(x')dx' = \gamma u(x), \qquad (3.4)$$

in which $C_g(x, x')$ is the autocovariance of process $g(x, \omega)$. KL eigenvalues decrease monotonically in magnitude, and KL eigenfunctions are spatially smooth functions. If the Fredholm equation is solved numerically, KL eigenvectors approximate spatially smooth eigenfunctions.

In practice evaluation of the KL expansion, Eq. (3.1), must be truncated to a finite number of eigenmodes $K$. The number of terms which must be kept to represent the process variance within a tolerance is governed by the rate at which the eigenvalues decrease. In general, highly correlated processes require fewer eigenmodes to accurately represent a process, whereas processes with weak correlation require more eigenmodes. In application it is generally hoped that few eigenmodes will be required. Using a truncation of the KL expansion discretizes a continuous random process and allows for dimension reduction in correlated systems.

For some calculations it may be beneficial to approach $g(x, \boldsymbol{\xi}(\omega))$ as a function spanning a physical and a stochastic dimension. Often it is advantageous to sample values from the stochastic domain and solve QoIs over realizations of $g(x, \omega)$. Sampling realizations of random process $g(x, \omega)$ allows codes which solve QoIs in the physical domain to be used as black-box solvers that are unaware of stochastic variation. For this reason, solution methods to problems involving a random field are often selected which only

require QoI values at various realizations of the process. Since they require no, or very little, modification to the black-box solver, these solution methods are called non-intrusive methods. Two such non-intrusive solution methods are random sampling and the stochastic collocation approach.

### 3.1.1 KL Random Variable PDF Generation

In the case that the random variable distribution is not known or wished to be assumed a priori and realizations of the process to be modeled are acquirable, probability density functions of the random variable distributions can be numerically constructed. This may be advantageous, for example, when creating a KL model from experimental data which provides realizations of a process or if it is known how to numerically construct realizations of the process using a method other than the KL expansion. We start with the KL expansion, use eigenfunction orthonormality (Eq. (3.3a)) to solve for the random variable $\xi_{k'}$, and re-index back to $k$:

$$g(x,\omega) = \langle g \rangle + \sum_{k=1}^{\infty} \sqrt{\gamma_k} u_k(x) \xi_k(\omega)$$

$$\Rightarrow \int_0^L (g(x,\omega) - \langle g \rangle) u_{k'}(x) dx = \int_0^L \sum_{k=1}^{\infty} \sqrt{\gamma_k} u_k(x) \xi_k(\omega) u_{k'}(\omega) dx$$

$$\Rightarrow \frac{1}{\sqrt{\gamma_{k'}}} \int_0^L (g(x,\omega) - \langle g \rangle) u_{k'}(x) dx = \xi_{k'}(\omega)$$

$$\Rightarrow \xi_k(\omega) = \frac{1}{\sqrt{\gamma_k}} \int_0^L (g(x,\omega) - \langle g \rangle) u_k(x) dx.$$

(3.5)

We solve the RHS of Eq. (3.5) for various values of $\boldsymbol{\xi}$, and from these values construct a probability density function for each random variable $\xi_k(\omega)$.

### 3.1.2 KL Truncation Error

We make use of the random variable orthogonality condition (Eq. (3.3a)) to solve for the variance maintained at $x$ in the slab in the KL expansion as a result of truncation

at term $K$:

$$g_K(x, \omega) = \langle g \rangle + \sum_{k=1}^{K} \sqrt{\gamma_k} u_k(x) \xi_k(\omega)$$

$$\Rightarrow \int_{-\infty}^{\infty} \cdots \int_{\infty}^{\infty} (g_K(x, \omega) - \langle g \rangle)^2 d\boldsymbol{\xi} = \int_{-\infty}^{\infty} \cdots \int_{-\infty}^{\infty} \left( \sum_{k=1}^{K} \sqrt{\gamma_k} u_k(x) \xi_k(\omega) \right)^2 d\boldsymbol{\xi} \tag{3.6}$$

$$\Rightarrow \mathbb{E}[(g_K(x) - \langle g \rangle)^2] = \sum_{k'=1}^{K} \sqrt{\gamma_{k'}} \sqrt{\gamma_{k'}} u_{k'}(x) u_{k'}(x)$$

$$\Rightarrow \mathbb{V}[g_K(x)] = \sum_{k=1}^{K} \gamma_k u_k^2(x).$$

We can transform this into the percentage of variance maintained at $x$ with KL truncation order $K$ by dividing by the process variance:

$$\% \text{ variance maintained} = \frac{\mathbb{V}[g_K(x)]}{v_g} = \frac{\mathbb{V}[g_K(x)]}{\mathbb{V}[g_{K=\infty}(x)]} = \frac{1}{v_g} \sum_{k=1}^{K} \gamma_k u_k^2(x). \tag{3.7}$$

We integrate the variance maintained (Eq. (3.6)) over the domain and utilize the orthonormality of the eigenfunctions (Eq. (3.3a)) to reduce:

$$\int_0^L \mathbb{V}[g_K(x)] dx = \int_0^L \sum_{k=1}^{K} \gamma_k u_k^2(x) dx = \sum_{k=1}^{K} \gamma_k. \tag{3.8}$$

We note that if all eigenmodes are kept and the process is therefore perfectly represented ($K = \infty$), the solution to this integral is exact and known:

$$\int_0^L \mathbb{V}[g_{K=\infty}(x)] dx = \sum_{k=1}^{\infty} \gamma_k = v_g \int_0^L dx = v_g L. \tag{3.9}$$

We use Eqs. (3.8) and (3.9) to represent the truncated KL's mean square error over the domain:

$$\epsilon_K^2 = v_g L - \sum_{k=1}^{K} \gamma_k. \tag{3.10}$$

Noting that $v_g L$ is equal to the non-truncated sum of the eigenvalues (Eq. (3.9)) it can be seen that this formulation of the mean squared error is equivalent to that often given in the literature:

$$\epsilon_K^2 = \sum_{k > K} \gamma_k. \tag{3.11}$$

As long as the variance of the process is known a priori, the form in Eq. (3.10) is more useful computationally, as it provides the mean squared error of the process as a function of terms kept in the KL truncation instead of the infinite number of terms which are truncated.

### 3.1.3   KL Eigenmode Solutions

Karhunen-Loève eigenvalues and eigenfunctions or eigenvectors are solved from

$$\int_D C_g(x, x') u_k(x') dx' = \gamma_k u_k(x),\tag{3.12}$$

which is a re-statement of Eq. (3.4). If the covariance $C_g(x, x')$ is such that the integral can be analytically solved, an analytic solution of the eigenvalues and eigenfunctions is likely preferred. We present an analytic solution of the KL eigenfunctions and eigenvalues for the exponential covariance in Section 3.1.3.1. A similar analytic solve for the triangular covariance function is available in Ref. [43]. Many covariance functions, including those defined by a discrete vector only, do not lend to an analytic solve. As a result we solve Eq. (3.12) numerically using the Nyström method in Section 3.1.3.2.

#### 3.1.3.1   Analytic Solve for Covariance Function: Exponential Covariance

The exponential autocovariance function

$$C_g(x, x') = v_g \exp\left[\frac{-\left|x - x'\right|}{\lambda_c}\right],\tag{3.13}$$

where $\lambda_c$ is a correlation length between points in an isotropic, weakly stationary field, represents the autocovariance of a medium with Markovian mixing statistics and is sometimes of interest in modeling random processes [10, 44, 45]. We note that as the correlation length increases, $\lambda_c \to \infty$, the process becomes fully correlated and has no variation in the spatial domain. As the correlation length decreases, $\lambda_c \to 0$, the process is not correlated with itself and takes on a spatially sporadic structure.

Inserting the exponential covariance (Eq. (3.13)) into the Fredholm equation (Eq. (3.4)) for a problem of domain $x, x' \in [0, L]$ produces

$$\int_0^L v_g \exp\left[\frac{-|x - x'|}{\lambda_c}\right] u(x')dx' = \gamma u(x). \tag{3.14}$$

We differentiate Eq. (3.13) twice with respect to $x$ and reorganize to form the differential equation

$$u''(x) + \alpha^2 u(x) = 0, \quad \alpha^2 = \frac{2v_g - \frac{\gamma}{\lambda_c}}{\lambda_c \gamma}. \tag{3.15}$$

We evaluate Eq. (3.13) and its derivative with respect to $x$ at $x = 0$ and $x = L$ and arrange the resulting equations to yield boundary conditions:

$$\lambda_c u'(0) - u(0) = 0 \tag{3.16a}$$

$$\lambda_c u'(L) + u(L) = 0. \tag{3.16b}$$

Noting that Eq. (3.13) represents a simple harmonic oscillator, we present the solution

$$u(x) = A\sin(\alpha x) + B\cos(\alpha x) \tag{3.17}$$

and utilize boundary conditions (Eq. (3.16)) to form the transcendental equation

$$\tan\left(\frac{\alpha L}{\lambda_c}\right) = \frac{2\alpha\lambda_c}{\lambda_c^2 \alpha^2 - 1}, \tag{3.18}$$

with roots $\alpha_k$. We update our differential equation to a set of differential equations and solutions arising from the values of $\alpha_k$:

$$u_k''(x) + \alpha_k^2 u_k(x) = 0, \quad \alpha_k^2 = \frac{2v_g - \frac{\gamma_k}{\lambda_c}}{\lambda_c \gamma_k}, \tag{3.19}$$

and

$$u_k(x) = A_k\sin(\alpha_k x) + B_k\cos(\alpha_k x). \tag{3.20}$$

We insert Eq. (3.20) into Eq. (3.19) and solve for eigenvalues $\gamma_k$:

$$\gamma_k = \frac{2v_g\lambda_c}{\lambda_c^2 \alpha_k^2 + 1}. \tag{3.21}$$

We use Eq. (3.16a) to relate $A_k$ and $B_k$,

$$B_k = \lambda_c \alpha_k A_k, \tag{3.22}$$

and simplify Eq. (3.20):

$$u_k(x) = A_k[\sin(\alpha_k x) + \lambda_c \alpha_k \cos(\alpha_k x)]. \tag{3.23}$$

Finally we solve $A_k$ by normalizing the already orthogonal eigenfunctions $u_k(x)$:

$$\int_0^L u_k^2(x)dx = 1 \tag{3.24a}$$

$$\Rightarrow A_k = \sqrt{\frac{1}{\frac{L}{2}(\lambda_c^2 \alpha_k^2 - 1) + \lambda_c}}. \tag{3.24b}$$

Figure 3.1 plots eigenvalues and eigenfunctions produced using the exponential covariance function and a slab length $L = 5$. We note the monotonic decrease in eigenvalue magnitudes and that this decrease is sharper for more correlated processes (when $\lambda_c$ is larger). This means that for more correlated processes, a smaller truncation order $K$ can be chosen in order to maintain the same amount of statistical information.
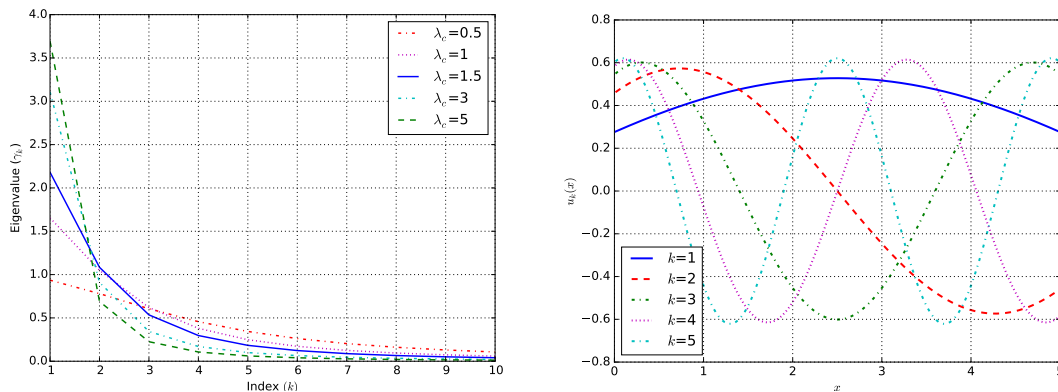


FIGURE 3.1: Example Eigenvalues and Eigenfunctions for Exponential Variance

#### 3.1.3.2 Numeric Solve of Covariance Function: Nyström Method

To solve the Fredholm integral equation that defines Karhunen-Loève eigenvalues and eigenvectors (Eq. (3.4)), we employ the Nyström method (NM) [14, 15]. The Nyström

method applies a quadrature of order $N_{Ny}$ over the domain to integrate the LHS integral,

$$\sum_{j=1}^{N_{Ny}} w_j C_g(x, x_j) u_k(x_j) = \gamma_k u_k(x), \tag{3.25}$$

with nodes at $x_j$, $j \in \{1, \ldots, N_{Ny}\}$, and weights of $w_j$. The integral is solved for each value of $x_i$:

$$\sum_{j=1}^{N_{Ny}} w_j C_g(x_i, x_j) u_k(x_j) = \gamma_k u_k(x_i), \quad k = 1, \ldots, N_{Ny}. \tag{3.26}$$

We rewrite the eigenvalue problem in Eq. (3.26) in matrix notation:

$$\mathbf{CW}\mathbf{u}_k = \gamma_k \mathbf{u}_k. \tag{3.27}$$

Matrix $\mathbf{C}$ is a symmetric positive semi-definite matrix with elements $C_{ij} = C_g(x_i, x_j)$. Matrix $\mathbf{W}$ is a diagonal matrix with values $w_j$. Vector $\mathbf{u}_k$ spans the physical domain for each KL eigenvalue $k$. The quadrature order $N_{Ny}$ is equal to the number of eigenmodes that are solved for, and the variance of the problem is normalized based on the number of KL eigenmodes solved. To minimize the bias of normalizing the total process variance to that given by $N_{Ny}$ Karhunen-Loève terms, quadrature order $N_{Ny}$ should be somewhat larger than the number of KL terms kept, $K$. What order of $N_{Ny}$ is sufficient is best determined through a convergence study.

We reformulate Eq. (3.27) to

$$\mathbf{W}^{\frac{1}{2}}\mathbf{C}\mathbf{W}^{\frac{1}{2}}\mathbf{W}^{\frac{1}{2}}\mathbf{u}_k = \gamma_k \mathbf{W}^{\frac{1}{2}}\mathbf{u}_k, \tag{3.28}$$

where $\mathbf{W}^{\frac{1}{2}}$ is a diagonal matrix with values $\sqrt{w_j}$. Through substitutions

$$\mathbf{B} = \mathbf{W}^{\frac{1}{2}}\mathbf{C}\mathbf{W}^{\frac{1}{2}}, \tag{3.29a}$$

$$\mathbf{u}_k^* = \mathbf{W}^{\frac{1}{2}}\mathbf{u}_k, \tag{3.29b}$$

we simplify:

$$\mathbf{B}\mathbf{u}_k^* = \gamma_k \mathbf{u}_k^*. \tag{3.30}$$

We solve Eq. (3.30) for $\mathbf{u}_k^*$ and eigenvalues $\gamma_k$, and finally solve for eigenvectors $\mathbf{u}_k$:

$$\mathbf{u}_k = \mathbf{W}^{-\frac{1}{2}}\mathbf{u}_k^*. \tag{3.31}$$

The simplest way to evaluate eigenfunction $u_k(x)$ using eigenvector $\mathbf{u}_k$ is to return the eigenvector value which corresponds to the eigenvector node $x_i$ closest to $x$: $\mathbf{u}_{k,i}$. We call this the "discrete" eigenfunction interpolation scheme. This interpolation scheme produces an eigenfunction comprised of spatially discontinuous and discrete values. It requires one evaluation of the $\mathbf{u}_k$ per term in the KL expansion.

An alternative method for evaluation of $u_k(x)$ comes from the Nyström theory:

$$u_k(x) = \frac{1}{\gamma_k} \sum_{j=1}^{N_{Ny}} \sqrt{w_j} \mathbf{u}_{k,j}^* C_g(x, x_j). \tag{3.32}$$

This "Nyström" interpolation scheme provides interpolation/extrapolation for $u_k(x)$, such that the shape of the eigenfunction is not discontinuous and more closely represents the true eigenfunction. The "Nyström" interpolation scheme requires $N_{Ny}$ evaluations of eigenvector $\mathbf{u}_k^*$ per term in the KL expansion along with computation which evaluates Eq. (3.32). Though the "Nyström" interpolation scheme produces a more accurate representation of the eigenfunction than the "discrete" interpolation scheme, it is about $N_{Ny}$ times more expensive.

We introduce a third interpolation scheme we call the "linear" interpolation scheme. The "linear" interpolation scheme linearly interpolates between the nearest eigenvector values corresponding to nodes $x_j$ and $x_{j+1}$ when $x$ exists between nodes and defers to the "Nyström" interpolation method when $x$ is not located between two nodes (when $x$ is near an edge of the slab). If eigenfunctions are sampled equally at values through space, the "linear" interpolation scheme requires $1 + 2\frac{N_{Ny}-1}{N_{Ny}}$–roughly three–evaluations of $\mathbf{u}_k$ or $\mathbf{u}_k^*$ per term in the KL expansion along with some computation. The "linear" interpolation scheme is nearly as accurate as the "Nyström" interpolation scheme and much less expensive. Though the "linear" interpolation scheme is about 3 times more expensive than the "discrete" interpolation scheme, unless the Nyström discretization order $N_{Ny}$ is very large, we expect the additional accuracy of the "linear" interpolation scheme to be worth the additional cost. We compare the performance of the "discrete" and "linear" interpolation schemes for a problem in Sections 5.4.2 and 5.4.3.

## 3.2 Stochastic Equation Solution Methods

We present several means for acquiring a solution to a quantity of interest (QoI) which results from solution of the stochastic transport equation. We presented means for solving the problem in the physical domain using the Monte Carlo method described in Section 2.3. We presented means for modeling random geometries using the Karhunen-Loève expansion described in Section 3.1. The KL expansion reduces an uncountably infinite number of random variables to a countably infinite number and with truncation to a finite number of random variables. In problems using the KL expansion, techniques still must be used to acquire results of the solutions of the QoIs in terms of the finite number of random variables. The same is true for problems involving random variables inherent in the problem, i.e., not originated through use of the KL expansion.

In this section we present three tools for solving a QoI over the uncertain domain: random sampling (RS), stochastic collocation (SC), and the polynomial chaos expansion (PCE). The first two sample from the stochastic domain at randomly and deterministically chosen nodes, respectively. The third is used to create a surrogate model of the response from SC nodes and solutions.

We solve for the expectation of moment $m$ of QoI $\varphi$ by integrating the solution for that moment over the probability density $p(\xi_1, \ldots, \xi_D)$:

$$\langle \varphi^m \rangle = \int_{\xi_D} \cdots \int_{\xi_1} \varphi^m(\xi_1, \ldots, \xi_D) p(\xi_1, \ldots, \xi_D) d\xi_1 \ldots \xi_D, \tag{3.33}$$

where $D$ is the number of stochastic dimensions.

In each of our applications, we know or assume the uncertain distributions to be fully independent, a property which allows a factorization of the joint probability into a product of one-dimensional probability distributions, vis.,

$$p(\xi_1, \ldots, \xi_D) = \prod_{n=1}^{D} p(\xi_n). \tag{3.34}$$

### 3.2.1 Random Sampling (RS)

Our first solution method for solving the expectation of a moment of the QoI is through random sampling (RS). In the RS approach, we choose nodes $\xi_n^{(i)}$ randomly, but according to the probability distribution $p(\xi_n)$, in each dimension $n$ and for each realization $i$. After choosing nodes $\xi_n^{(i)}$, the QoIs for each realization $i$ are solved using Monte Carlo particle transport. QoI data is used to either solve for moments of a particular QoI, or to generate a probability density function (PDF) of the QoI. This method of random sampling is correctly called a "Monte Carlo" method, but we call it random sampling for the duration of this work to avoid confusion in terminology.

If we are seeking a moment of a QoI, we evaluate Eq. (3.33) as

$$\langle \varphi^m \rangle \approx \frac{1}{R} \sum_{i=1}^{R} \varphi^m(\xi_1^{(i)}, \ldots, \xi_N^{(i)}), \tag{3.35}$$

where $R$ is the total number of realizations and $\xi_n^{(i)}$ are sampled from $p(\xi_n)$. A value of $\langle \varphi^m \rangle$ converges according to the Central Limit Theorem as $R^{-\frac{1}{2}}$.

If we are seeking a PDF of the QoI, we store moment values of the QoI for each realization $i$, $\left( \varphi^{(i)} \right)^m$, choose an upper and lower bound and number of cells for the PDF, and generate the PDF. Care should be taken to choose an appropriate number of bins for the PDF. Selecting too many bins for the number of samples $R$ will result in a noisy distribution which is of little use. Selecting too few bins will jeopardize the integrity of the PDF by averaging over regions of the QoI response in which the true PDF may contain important shape features. These features will be "smeared out" by selecting too few bins.

The random sampling method is dimensionally agnostic, meaning the convergence rate of a moment is not affected by the number of random dimensions. For this reason, it is often used to provide a benchmark solution using many realizations $R$. For problems with few random variables there are other methods such as stochastic collocation which are expected to converge more quickly than RS. For problems with a large number of random variables, however, RS may remain the most efficient stochastic solution method.

In this work we use either uniformly distributed or Gaussian-distributed probability densities. Since most random number generators provide numbers uniformly distributed

from zero to one, generation of random samples over a uniform probability distribution is a trivial mapping of the probability distribution. Depending on the software being used, generation of Gaussian-distributed random samples may be less trivial. We therefore examine methods for generating Gaussian-distributed random samples in Appendix A.

### 3.2.2 Stochastic Collocation (SC)

Our second method for solving the expectation of a moment of the quantity of interest is a deterministic sampling method called stochastic collocation (SC). In the SC approach, we choose nodes $\xi_n^{(q_n)}$ according to a $Q_n$-order quadrature in dimension $n$. With realizations defined through node values $\xi_n^{(q_n)}$ using quadrature index $q_n \in \{q_1, \ldots, q_D\}$ for each dimension $n$, solutions to QoIs are solved on each realization using Monte Carlo particle transport. QoI data is used to solve for moments of the QoIs. This method does not, of itself, produce a PDF of the QoI. We choose, however, to use this method to solve the coefficients of a polynomial chaos expansion representation of the QoIs which can be used to produce PDFs of the QoIs. Simply put, the SC method applies a cubature over the stochastic dimensions.

We solve the expectation of a moment of a QoI, $\varphi^m$, through application of a cubature over the multi-dimensional integral in Eq. (3.33):

$$\langle \varphi^m \rangle \approx \sum_{q_D}^{Q_D} \cdots \sum_{q_1}^{Q_1} w_1^{(q_1)} \ldots w_D^{(q_D)} \varphi^m(\xi_1^{(q_1)}, \ldots, \xi_D^{(q_D)}), \tag{3.36}$$

where $w_n^{(q_n)}$ are the cubature weights.

The most direct approach to stochastic collocation applies the same quadrature order $Q$ in each dimension $n$, vis., $Q = Q_n \forall n \in \{1, \ldots, D\}$. This is called isotropic stochastic collocation (iSC). The number of realizations for iSC is

$$R_{SC} = Q^D. \tag{3.37}$$

Often some stochastic inputs contribute considerably more to the response than others. It such a case it may be advantageous to apply an anisotropic cubature, in which the quadrature order in each dimension $n$ is not uniform [17]–we call this anisotropic

stochastic collocation (aSC). The number of realizations for aSC is

$$R_{SC} = \prod_n^D Q_n. \tag{3.38}$$

It is easy to see that Eq. (3.38) reduces to Eq. (3.37) when all quadrature orders have the same value.

Other methods exist for choosing an efficient cubature grid. Sparse collocation grids reduce the number of cubature nodes [10, 16, 17]. Sparse, anisotropic collocation grids reduce the number of cubature nodes preferentially resolving the effects of stochastic inputs which are considered of greater importance to the response [17]. Adaptive methods exist in which quadrature orders are successively increased according to an estimate of the error in the response which would be reduced in each dimension by increasing the quadrature order [16, 17]. Each of these approaches integrates to solve the response over an integral of the entire stochastic domain; methods also exist for applying cubature over portions of the stochastic domain such that regions of higher significance can be resolved more than others. Another way to increase the efficiency of a SC solve is to apply sensitivity methods [16] which assess the sensitivity of stochastic inputs or input combinations and allow certain stochastic inputs to be ignored in analysis due to negligible contribution to the response.

In this work we use iSC and aSC. We have chosen aSC for several of our applications because our stochastic inputs are the random variables of the Karhunen-Loève expansion, which are known to decrease in contribution to the response monotonically. This provides a natural opportunity for collocation anisotropy [17]. In problems not using the KL expansion, we resolve all stochastic inputs, considering them significant contributors to the response. In problems involving the KL expansion, we decrease the number of stochastic inputs by choosing our KL truncation order, but apply no other sensitivity analysis for dimensional reduction.

Various quadratures are available, and may be preferred for different applications. We examine several quadrature rules in Appendix B. In this work, we use Gauss-Legendre (GL) quadrature when integrating over a closed support, and Gauss-Hermite (GH) quadrature when integrating over an open support. Gauss-Hermite quadrature is defined over a Gaussian basis which is not normalized $\left( \exp\left[ -\xi^2 \right] \right)$, whereas we apply

GH quadrature over the standard normal basis function $\left( \frac{1}{\sqrt{2\pi}} \exp\left[ -\frac{\xi^2}{2} \right] \right)$. We discuss mapping of GH quadrature from the first basis to the second (probability density) in Appendix B.

### 3.2.3 The Polynomial Chaos Expansion (PCE)

The polynomial chaos expansion (PCE) creates a surface using orthogonal random polynomials. We use it to build a surrogate model of system response. It was first introduced as homogeneous chaos by Wiener in 1938 [18] using Gaussian-random variables and Hermite polynomials. In 1985 Askey and Wilson [46] identified orthogonal (and hypergeometric) polynomials over other basis functions. These orthogonal polynomials are now commonly called Askey-scheme polynomials or simply Askey polynomials. In 2002 Xiu and Karniadakis [19] generalized the existing Gaussian-based homogeneous chaos using Askey polynomials over their corresponding basis functions to produce generalized polynomial chaos. Selected Askey polynomials and their associated basis functions are presented in Appendix C. Generalized polynomial chaos is sometimes known by our name for it: the polynomial chaos expansion (PCE). In 2003 Mathelin and Hussaini [20] used a cubature over the Askey polynomials of the PCE, creating Askey-based stochastic collocation-polynomial chaos. This method is discussed more rigorously in [21], and has been used widely in recent years, especially in engineering applications such as [10, 16, 22, 44, 47–51]. This is the method for constructing the PCE we use in this work. Another approach to stochastic collocation for construction of a PCE uses Lagrange polynomials. It is rigorously presented in [52] and has been used widely in recent years as well in works such as [17, 53–58]. Both approaches to the PCE are available in Sandia's Dakota [59] uncertainty quantification code, and at least one investigation has compared the performance of the two [60].

The PCE is an infinite expansion of Askey polynomials which define a surface. We use the PCE to build a surrogate model of the system response spanning the stochastic domain. In practice we must truncate the infinite expansion. We solve expansion coefficients using stochastic collocation, though other methods such as integration using random sampling or the stochastic Galerkin method [20, 22, 47] exist. A PCE model built from SC results (SC-PCE) is as accurate to the system response as the results

of the numerical integration of the stochastic collocation with an additional error introduced through PCE truncation. We find the PCE model advantageous, however, primarily in that it uses SC to produce a response surface which can be sampled from to produce PDFs of the system response–a capability SC in itself lacks. The PCE model can also be used for response prediction. Once a physical problem has been solved enough times to build a PCE model, the model can predict the response throughout the stochastic domain. This can be useful when analyzing a physical model's response across the stochastic domain for results such as maximum and minimum responses, and is especially useful when solution of the physical model is expensive.

The PCE requires a somewhat smooth response in the stochastic domain, as it approximates a response surface using polynomials. This is a constraint of any surrogate model which uses continuous functions, and is similar to the smoothness limitation of stochastic collocation.

The infinite-dimensional, infinite-order PCE for a quantity of interest $\varphi$ is written

$$
\begin{aligned}
\varphi(\omega) =& \widehat{u}_0 \Gamma_0 + \sum_{i_1=1}^{\infty} \widehat{u}_{i_1} \Gamma_1(\xi_{i_1}) + \sum_{i_1=1}^{\infty} \sum_{i_2=1}^{i_1} \widehat{u}_{i_1 i_2} \Gamma_2(\xi_{i_1}, \xi_{i_2}) \\
&+ \sum_{i_1=1}^{\infty} \sum_{i_2=1}^{i_1} \sum_{i_3=1}^{i_2} \widehat{u}_{i_1 i_2 i_3} \Gamma_3(\xi_{i_1}, \xi_{i_2}, \xi_{i_3}) + \cdots ,
\end{aligned}
\tag{3.39}
$$

where $\Gamma_j$ are $j$-order Askey polynomials, $\widehat{u}_{i_1 \ldots i_I}$ are PCE coefficients, and $\xi_n$ denote polynomial dependence in dimension $n$ [43]. For a $D$-dimensional problem with an $I$-order truncation the PCE reduces to

$$
\begin{aligned}
\varphi(\omega) =& \widehat{u}_0 \Gamma_0 + \sum_{i_1=1}^{D} \widehat{u}_{i_1} \Gamma_1(\xi_{i_1}) + \sum_{i_1=1}^{D} \sum_{i_2=1}^{i_1} \widehat{u}_{i_1 i_2} \Gamma_2(\xi_{i_1}, \xi_{i_2}) + \cdots \\
&+ \sum_{i_1=1}^{D} \cdots \sum_{i_{I-1}=1}^{i_1} \widehat{u}_{i_1 \cdots i_{I-1}} \Gamma_{I-1}(\xi_{i_1}, \ldots, \xi_{i_I}).
\end{aligned}
\tag{3.40}
$$

The first term of the PCE, $\widehat{u}_0 \Gamma_0$, is the zeroth-order term of the PCE, comprised of one coefficient and a zeroth-order polynomial ($\Gamma_0 = 1$).

The set of PCE terms after the first term, $\sum_{i_1=1}^{\infty} \widehat{u}_{i_1} \Gamma_1(\xi_{i_1})$, contains all PCE terms of total polynomial order one. This consists of multivariate polynomials which are first-order in dimension $i_1$ and zeroth-order in all other dimensions. The subscript $i_1$ on

the coefficient $\widehat{u}_{i_1}$ denotes which multivariate polynomial it pairs with: the first-order polynomial with dependence on $\xi_{i_1}$.

The next set of PCE terms, $\sum_{i_1=1}^{\infty} \sum_{i_2=1}^{i_1} \widehat{u}_{i_1 i_2} \Gamma_2(\xi_{i_1}, \xi_{i_2})$, contains all PCE terms of total polynomial order two. It consists of multivariate polynomials which are first-order in each of two dimensions while being zeroth-order in all other dimensions and multivariate polynomials which are second-order in one dimension while being zeroth-order in all other dimensions. The subscripts on the $\xi$ terms in the polynomial $\Gamma$ denote the order of the polynomial in each dimension, i.e., $\Gamma_2(\xi_{i_1}, \xi_{i_2})$ is first-order in dimension $i_1$ and first-order in dimension $i_2$ while being zeroth-order in all other dimensions, unless $i_1 = i_2$. In that case $\Gamma_2(\xi_{i_1}, \xi_{i_2})$ is second-order in dimension $i_1$ (same as $i_2$) and zeroth-order in all other dimensions. The subscripts of the coefficient $\widehat{u}_{i_1, i_2}$ denote which multivariate polynomial it pairs with: the second-order polynomial with dependence on $\xi_{i_1}$ and $\xi_{i_2}$ respectively.

In each of our applications the underlying probability densities are independent such that the multivariate Askey polynomials simplify to a product of univariate polynomials, i.e.,

$$\Gamma_I(\xi_1, \ldots, \xi_I) = \prod_{n=1}^{D} \Gamma_j(\xi_n). \tag{3.41}$$

Table 3.1 provides examples of the PCE notation for a three-dimensional PCE.

TABLE 3.1: Example PCE Subscript Expansion for D=3

| Set of PCE Terms | Constituent Terms | Orders |
|---|---|---|
| $\widehat{u}_0 \Gamma_0$ | $\widehat{u}_0 \Gamma_0$ | {0,0,0} |
| $\sum_{i_1=1}^{D} \widehat{u}_{i_1} \Gamma_1(\xi_{i_1})$ | $\widehat{u}_1 \Gamma_1(\xi_1)$ | {1,0,0} |
| | $\widehat{u}_2 \Gamma_1(\xi_2)$ | {0,1,0} |
| | $\widehat{u}_3 \Gamma_1(\xi_3)$ | {0,0,1} |
| $\sum_{i_1=1}^{D} \sum_{i_2=1}^{i_1} \widehat{u}_{i_1 i_2} \Gamma_2(\xi_{i_1})$ | $\widehat{u}_{11} \Gamma_2(\xi_1, \xi_1)$ | {2,0,0} |
| | $\widehat{u}_{21} \Gamma_1(\xi_2) \Gamma_1(\xi_1)$ | {1,1,0} |
| | $\widehat{u}_{22} \Gamma_2(\xi_2)$ | {0,2,0} |
| | $\widehat{u}_{31} \Gamma_1(\xi_3) \Gamma_1(\xi_1)$ | {1,0,1} |
| | $\vdots$ | $\vdots$ |

Introducing the multi-indices $\mathbf{i} = \{i_1, \ldots, i_D\}$ and $\boldsymbol{\xi} = \{\xi_1, \ldots, i_D\}$ and the multi-dimensional Askey polynomial $\Phi_{\mathbf{i}}$, we can write the PCE more simply:

$$\varphi(\omega) = \sum_{\iota=0}^{I_t} \widehat{u}_{\mathbf{i}(\iota)} \Phi_{\mathbf{i}(\iota)}(\boldsymbol{\xi}), \tag{3.42}$$

where $\iota$ represents a term of the expansion corresponding to a unique set of values $\mathbf{i}$, and $I_t + 1$ is the total number of PCE terms kept in truncation. The number of terms kept in truncation is solved as a binomial coefficient:

$$I_t + 1 = \frac{(D+I)!}{D!I!}. \tag{3.43}$$

The PCE suffers from the curse of dimensionality as does stochastic collocation. The increase in the number of terms with increased dimensionality is somewhat mitigated compared to the increase in terms for SC, however, since a grid of PCE terms is simplex-shaped whereas a grid of SC terms is hypercube-shaped. We have presented an isotropic, simplex-shaped PCE formulation, as is presented in the original publication of homogeneous chaos [18]. It is possible to truncate in other ways, such as an anisotropic PCE grid, vis., $\exists\, n_1, n_2 \in \{1, \ldots, D\}$ s.t. $I_{n_1} \neq I_{n_2}$, or through the use of a hypercube-shaped PCE formulation [22]. The simplex-shaped PCE formulation carries advantages such as simplicity and a mitigation of the curse of dimensionality, so we have used it in this work.

### 3.2.3.1 Solution of PCE Coefficients using SC (SC-PCE)

There is more than one way to solve for expansion coefficients when using the PCE to model a response surface. We have chosen to solve the expansion coefficients using stochastic collocation, and denote use of the PCE with coefficients solved using SC as SC-PCE.

We begin with the compact version of the PCE in Eq. (3.42):

$$\varphi(\omega) = \sum_{\iota=0}^{I_t} \widehat{u}_{\mathbf{i}(\iota)} \Phi_{\mathbf{i}(\iota)}(\boldsymbol{\xi}). \tag{3.44}$$

We define notation for integration of functions $f$ and $g$ over multi-dimensional probability density $p(\boldsymbol{\xi})$:

$$\left\langle f(\boldsymbol{\xi}), g(\boldsymbol{\xi}) \right\rangle = \int_{\xi_I} \cdots \int_{\xi_1} f(\boldsymbol{\xi}) g(\boldsymbol{\xi}) p(\boldsymbol{\xi}) d\boldsymbol{\xi}. \tag{3.45}$$

We multiply both sides of Eq. (3.44) by a multi-dimensional Askey polynomial and integrate over the probability density:

$$\left\langle \varphi(\omega), \Phi_{\mathbf{j}}(\boldsymbol{\xi}) \right\rangle = \left\langle \sum_{\iota=0}^{I_t} \widehat{u}_{\mathbf{i}(\iota)} \Phi_{\mathbf{i}(\iota)}(\boldsymbol{\xi}), \Phi_{\mathbf{j}}(\boldsymbol{\xi}) \right\rangle, \tag{3.46}$$

where $\mathbf{j} = \{j_1, \ldots, j_D\}$. We pull the expansion coefficients out of the integral on the RHS and evaluate the equation using the Askey polynomial orthogonality condition discussed for selected Askey polynomials in Appendix C. Eq. (3.46) reduces to

$$\left\langle \varphi(\omega), \Phi_{\mathbf{j}}(\boldsymbol{\xi}) \right\rangle = \frac{\widehat{u}_{\mathbf{j}}}{a_{\mathbf{j}}}. \tag{3.47}$$

We rearrange and re-index to yield an expression for each PCE coefficient:

$$\widehat{u}_{\mathbf{i}} = a_{\mathbf{i}} \left\langle \varphi(\boldsymbol{\xi}), \Phi_{\mathbf{i}}(\boldsymbol{\xi}) \right\rangle. \tag{3.48}$$

Since we do not have values for the whole response surface $\varphi(\boldsymbol{\xi})$–that is in fact what we are creating a surrogate model to approximate–we solve the integral in Eq. (3.48) numerically. We could solve this integral using a variety of numerical integration techniques such as random sampling, but choose to solve it using stochastic collocation. We choose a cubature-based on the Askey polynomial over which we integrate with nodes at $\boldsymbol{\xi}^{(\boldsymbol{q})} = \{\{\xi_1^{(q_1)}, \ldots, \xi_D^{(q_1)}\}, \cdots, \{\xi_1^{(q_D)}, \ldots, \xi_D^{(q_D)}\}\}$ with corresponding weights $w_n^{(q_n)}$. Some quadratures corresponding to selected polynomials are discussed in Appendix B. We approximate the integral in Eq. (3.48), as

$$\widehat{u}_{\mathbf{i}} \approx a_{\mathbf{i}} \sum_{q_D=1}^{Q_D} \cdots \sum_{q_1=1}^{Q_1} w_1^{(q_1)} \ldots w_D^{(q_D)} \varphi(\boldsymbol{\xi}^{(\boldsymbol{q})}) \Gamma_{i_1}(\xi_1^{(q_1)}) \ldots \Gamma_{i_D}(\xi_D^{(q_D)}) p(\boldsymbol{\xi}^{(\boldsymbol{q})}). \tag{3.49}$$

It is useful to remember that $p(\boldsymbol{\xi}^{(\boldsymbol{q})})$, for the problems we solve here, is simply the product of the probability densities in each dimension (Eq. (3.34)).

We can now solve the expansion coefficients using only $R_{SC}$ evaluations of the physical problem.

### 3.2.3.2 Anisotropic PCE based on anisotropic SC (aSC-aPCE)

The order of the quadrature used when solving the expansion coefficients in Eq. (3.49) limits the amount of information available for solving the coefficients. Quadrature of order $Q_n$ can solve expansion coefficients of polynomial order $Q_n$. We therefore limit the polynomial order for terms of the PCE to be no greater than the highest order which can be solved for with the quadrature order chosen. Subject to this constraint, we introduce an implementation of anisotropic polynomial chaos.

Our initial truncation is according to the isotropic PCE truncation order of the PCE, such that the number of PCE terms is solved by Eq. (3.43). We further truncate to create an anisotropic PCE implementation by eliminating any terms for which the polynomial order is greater than the SC quadrature order used to solve that coefficient in the corresponding dimension. We accomplish this by setting the expansion coefficient equal to zero, vis., $\widehat{u}_{\mathbf{i}} = 0$, for all terms in which the polynomial order is greater than the collocation order in at least one dimension, vis., $\exists\, n\, \text{s.t.}\, i_n > Q_n$. We denote the method described as use of isotropic stochastic collocation to build a PCE model subject to SC orders (and thus isotropic) as either iSC-iPCE or simply iSC-PCE. Conversely, we denote the method described as use of anisotropic stochastic collocation to build a PCE model subject to SC orders (and thus anisotropic) as either aSC-aPCE or simply aSC-PCE.

Following SC-based truncation of the PCE ,the number of remaining terms is less than or equal to the number given by Eq. (3.43) and less than or equal to the maximum allowed by the truncation due to an underlying aSC. These two constraints on the number of terms are summarized as

$$I_t + 1 \leq \frac{(D+I)!}{D!I!}; \tag{3.50}$$

$$I_t + 1 \leq \sum_{n=1}^{D}(Q_n + 1). \tag{3.51}$$

Two logical choices for PCE truncation order $I$ for a quadrature set are $I = \max(\boldsymbol{Q})$ and $I = \sum_n Q_n$. The first choice for truncation order reduces the number of higher-order

cross terms in the expansion, while capturing the on-axis terms up to the quadrature order in each dimension. When using isotropic stochastic collocation, the number of PCE terms yielded by this choice of PCE order is solved by Eq. (3.50). The second choice of initial PCE truncation order captures all higher-order cross terms for which SC information is available. The number of terms is solved by Eq. (3.51). When evaluating the efficiency of a solve, we compare the convergence of the error as a function of either the number of physical solves or the number of MC particle histories and consider the cost of computation for PCE operations negligible. If the cost of PCE operations is negligible for a particular problem and quantity of interest, the second choice of PCE truncation order should be chosen as it captures all the available information from a SC solve. The first choice of PCE truncation order grows considerably slower with increased stochastic dimensionality, however, and may be preferred to help ensure that the computational cost of performing operations using the PCE is in fact negligible for a problem. Because of the trade-off of increased computation for a larger number of solves, especially in problems with many stochastic dimensions, the best PCE truncation scheme is problem-dependent. We will use the first truncation method, that does not capture as many higher-order cross-terms in this work except as specified.

### 3.2.3.3 Analytic Solution of PCE Response Moments

Using Askey polynomial orthogonality, we can solve the mean and variance of a PCE surface for which we know the expansion coefficients analytically. We solve each in succession starting from Eq. (3.42) restated here:

$$\varphi(\omega) = \sum_{\iota=0}^{I_t} \widehat{u}_{\mathbf{i}(\iota)} \Phi_{\mathbf{i}(\iota)}(\boldsymbol{\xi}). \tag{3.52}$$

To solve the mean of the PCE, $\mathbb{E}[\varphi]$, we integrate over the probability density associated with the Askey polynomials, inserting a zeroth order polynomial ($\Gamma_0 = 1$) in the integral to take advantage of orthogonality:

$$\int_{\xi_1} \cdots \int_{\xi_D} \varphi(\boldsymbol{\xi}(\omega)) \; 1 \; p(\boldsymbol{\xi}) d\boldsymbol{\xi} = \int_{\xi_1} \cdots \int_{\xi_D} \left( \sum_{\iota=0}^{I_t} \widehat{u}_{\mathbf{i}(\iota)} \Phi_{\mathbf{i}(\iota)}(\boldsymbol{\xi}) \right) \left( \Phi_{\{0,\ldots,0\}}(\boldsymbol{\xi}) \right) p(\boldsymbol{\xi}) d\boldsymbol{\xi}$$
$$\Rightarrow \mathbb{E}[\varphi] = \langle \varphi \rangle = \frac{\widehat{u}_{\{0,\ldots,0\}}}{a_{\{0,\ldots,0\}}} \tag{3.53}$$

When using Legendre polynomials, this reduces to simply the zeroth order PCE coefficient:

$$\mathbb{E}[\varphi] = \widehat{u}_{\{0,\dots,0\}}. \tag{3.54}$$

When using Hermite (probablists') polynomials, the solution is almost as simple:

$$\mathbb{E}[\varphi] = \widehat{u}_{\{0,\dots,0\}}(2\pi)^{\frac{D}{2}}. \tag{3.55}$$

We solve the second moment of the QoI in a similar way, but begin by squaring each side of the equation and end by re-indexing:

$$\int_{\xi_1} \cdots \int_{\xi_D} \varphi^2(\boldsymbol{\xi}(\omega))p(\boldsymbol{\xi})d\boldsymbol{\xi} = \int_{\xi_1} \cdots \int_{\xi_D} \left( \sum_{\iota=0}^{I_t} \widehat{u}_{\mathbf{i}(\iota)}\Phi_{\mathbf{i}(\iota)}(\boldsymbol{\xi}) \right) \left( \sum_{\kappa=0}^{I_t} \widehat{u}_{\mathbf{j}(\kappa)}\Phi_{\mathbf{j}(\kappa)}(\boldsymbol{\xi}) \right) p(\boldsymbol{\xi})d\boldsymbol{\xi}$$
$$\Rightarrow \langle \varphi^2 \rangle = \sum_{\iota=0}^{I_t} \frac{\widehat{u}_{\mathbf{i}(\iota)}^2}{a_{\mathbf{i}(\iota)}} \tag{3.56}$$

Finally we solve the the variance of the PCE surface:

$$\mathbb{V}[\varphi] = \quad \langle \varphi^2 \rangle \quad - \quad \langle \varphi \rangle^2; \tag{3.57a}$$

$$\mathbb{V}[\varphi] = \sum_{\iota=0}^{I_t} \frac{\widehat{u}_{\mathbf{i}(\iota)}^2}{a_{\mathbf{i}(\iota)}} - \left( \frac{\widehat{u}_{\{0,\dots,0\}}}{a_{\{0,\dots,0\}}} \right)^2. \tag{3.57b}$$

In general, Eq. (3.57a) is probably the most practical approach to solving for $\mathbb{V}[\varphi]$, vis., solving for each moment and then subtracting. When using Legendre polynomials, however, since $a_{\{0,\dots,0\}} = 1$, we can further reduce Eq. (3.57b) to

$$\mathbb{V}[\varphi] = \sum_{\iota=1}^{I_t} \frac{\widehat{u}_{\mathbf{i}(\iota)}^2}{a_{\mathbf{i}(\iota)}}. \tag{3.58}$$

This form makes it clear that the variance of the Legendre polynomial-based PCE is not influenced by the value of the mean of the PCE.

# Chapter 4

# Stochastic Convergence on Random Coefficients

In this chapter we establish nomenclature and methods for examination of solution method error convergence and demonstrate on a simple problem. We first discuss error bounding and convergence. We then present a stochastic transport problem for which we investigate the error convergence of several methods. We look at the convergence of several methods in isolation and finally solve a problem by resolving quantity of interest (QoI) error below a chosen tolerance using two different stochastic solvers.

## 4.1   Error Convergence

A solution method is appropriate for a problem and QoI if successive changes in a set of parameters for that solution method will towards the correct value of the chosen problem QoI. In this section we define an approach to bound the total QoI error and the contributions to the error from each solver. We then discuss how to approach a study of the solution error convergence. Lastly we discuss the reuse of solution data in Monte Carlo (MC) and random sampling (RS) solves with limited information storage and in cubature solves using nested quadrature.

### 4.1.1 Definition of Error Bounds

We define the error for a QoI $\varphi$ as the magnitude of the difference between the expectation of the model's true solution and the solution yielded by the method. We denote use of a solver in the stochastic domain with a subscript to the expectation operator as in Eq. (4.1a) and use of a solver in the physical domain with a subscript on the QoI as in Eq. (4.1b):

$$\varepsilon_{SC} = \Big| \mathbb{E}[\varphi] - \mathbb{E}_{SC}[\varphi] \Big|, \tag{4.1a}$$

$$\varepsilon_{MC} = \Big| \mathbb{E}[\varphi] - \mathbb{E}[\varphi_{MC}] \Big|. \tag{4.1b}$$

In both cases we include as a subscript of the error term $\varepsilon$ a description of the solver being used.

At times we want to compute the error of one method solved in conjunction with another method at a certain set of method parameters. For example, we may want to compute the error of the Monte Carlo solver for a QoI solved with a certain set of stochastic collocation (SC) quadrature orders. The error we solve for is the difference between the expectation solved using the stochastic collocation scheme with no, or negligible, error in the physical solver, $\mathbb{E}_{SC}[\varphi]$, and the expectation solved using the same stochastic collocation grid with the Monte Carlo physical solver, $\mathbb{E}_{SC}[\varphi_{MC}]$. We denote this error using the subscript $MC(SC)$ to show that this is the Monte Carlo error for a set stochastic collocation solve. The error term is then defined:

$$\varepsilon_{MC(SC)} = \Big| \mathbb{E}_{SC}[\varphi] - \mathbb{E}_{SC}[\varphi_{MC}] \Big|. \tag{4.2}$$

We may use more specific notation by providing the parameter set for the solver which does not change between the two solves. For example, Eq. (4.2) could be rewritten while providing the quadrature orders for the stochastic collocation solver as

$$\varepsilon_{MC(SC,\mathbf{Q}=\{5,4,3\})} = \Big| \mathbb{E}_{SC,\mathbf{Q}=\{5,4,3\}}[\varphi] - \mathbb{E}_{SC,\mathbf{Q}=\{5,4,3\}}[\varphi_{MC}] \Big|. \tag{4.3}$$

Furthermore, at times we are interested in computing a bound on the total error produced from more than one error source in a solution approach. We solve a bound on the error by summing the magnitude of the error contributed from each solution method.

We include in the subscript of the error term the designation for each solution method that contributes to the error, separated by commas. For example, we begin by representing the total error from the MC physical solver and the SC stochastic solver as $\varepsilon_{SC,MC}$. We add and subtract the expectation of the QoI solved with our SC solver $\mathbb{E}_{SC}[\varphi]$. We introduce absolute value signs to acquire the error of the SC solver and the error of the MC solver as a function of the SC solver with a chosen set of parameters. In practice, multiple error sources may serendipitously counteract to produce less total error than the sum of the magnitude of each individual error. We compute a bound on the total error, however, by summing the magnitude of errors introduced by each error source. This process for our example is summarized as

$$\varepsilon_{SC,MC} = \left| \mathbb{E}[\varphi] - \mathbb{E}_{SC}[\varphi_{MC}] \right| \tag{4.4a}$$

$$= \left| \mathbb{E}[\varphi] - \mathbb{E}_{SC}[\varphi] + \mathbb{E}_{SC}[\varphi] - \mathbb{E}_{SC}[\varphi_{MC}] \right| \tag{4.4b}$$

$$\leq \varepsilon_{SC} + \varepsilon_{MC(SC)} = \left| \mathbb{E}[\varphi] - \mathbb{E}_{SC}[\varphi] \right| + \left| \mathbb{E}_{SC}[\varphi] - \mathbb{E}_{SC}[\varphi_{MC}] \right|. \tag{4.4c}$$

We can write equations similar to Eq. (4.4c) by isolating the error contribution of the methods in different ways, e.g.,

$$\varepsilon_{SC,MC} \leq \varepsilon_{MC} + \varepsilon_{SC(MC)} = \left| \mathbb{E}[\varphi] - \mathbb{E}[\varphi_{MC}] \right| + \left| \mathbb{E}[\varphi_{MC}] - \mathbb{E}_{SC}[\varphi_{MC}] \right|. \tag{4.5}$$

Similarly, we can write equations like this for error terms involving more than two solvers. For example, the total error for a QoI solved from a PCE model built using SC and using the MC physical solver at each collocation node can be represented as

$$\begin{aligned}
\varepsilon_{PCE,SC,MC} &\leq \varepsilon_{PCE} + \varepsilon_{SC(PCE)} + \varepsilon_{MC(PCE,SC)}; \\
\varepsilon_{PCE} &= \left| \mathbb{E}[\varphi] - \mathbb{E}_{PCE}[\varphi] \right|, \\
\varepsilon_{SC(PCE)} &= \left| \mathbb{E}_{PCE}[\varphi] - \mathbb{E}_{SC(PCE)}[\varphi] \right|, \\
\varepsilon_{MC(PCE,SC)} &= \left| \mathbb{E}_{PCE,SC}[\varphi] - \mathbb{E}_{PCE,SC}[\varphi_{MC}] \right|.
\end{aligned} \tag{4.6}$$

### 4.1.2 Error Convergence Methodology

An error convergence study changes some solver parameter in a way expected to yield a smaller error. If the method converges for the problem and QoI, the error will decrease as the free parameter(s) of the solver changes in the correct way. A plot of this behavior is a convergence plot.

In order to perform a convergence study, $\mathbb{E}[\varphi]$ must be known or adequately approximated. In practice $\mathbb{E}[\varphi]$ will not usually be known–if it were there would be no need for a solver which produces error. We have chosen a problem for this chapter, however, in which we solve $\mathbb{E}[\varphi]$ analytically. In applications $\mathbb{E}[\varphi]$ can be approximated by solving with a set of parameters for the solver or solvers which is expected to produce an error significantly smaller than the errors of interest in the convergence study. Alternatively, the solution expectation can be approximated by solving $\mathbb{E}[\varphi]$ with another solution method for which the error is expected to be sufficiently small. For example, when using MC in the physical domain $\mathbb{E}[\varphi]$ may be approximated by $\mathbb{E}[\varphi_{MC}]$ with a number of particle histories $N$ greater than any number of histories for which the error is plotted in a convergence study or using a different method like SC with high quadrature orders in each dimension. When desiring to plot error convergence for a number of histories up to $N = 10^8$, $\mathbb{E}[\varphi]$ could be approximated using $N = 10^{10}$ histories: $\mathbb{E}[\varphi] \approx \mathbb{E}[\varphi_{MC,N=10^{10}}]$, $\mathbb{E}[\varphi_{MC}] = \mathbb{E}[\varphi_{MC,N=\{10^2,...,10^8\}}]$.

When solving a problem and using more than one solver method, it can be useful to study the error convergence of each method individually. For the example in Eq. (4.4c), we seek to generate convergence data for the SC solver, then for the MC solver at a selected SC quadrature order set. To gather convergence data for the SC solver, if we do not have an analytical solution for the physical domain, we choose parameters for the MC solver which are expected to yield a minimal error contribution in the physical solver, then increase the SC quadrature orders until we observe convergence in the stochastic domain. We choose a set of quadrature orders for the isotropic SC (iSC) solver which yields an error $\varepsilon_{iSC}$ below a chosen tolerance and perform a convergence study of the MC solver using iSC with our chosen quadrature orders. This process using isotropic stochastic collocation is demonstrated as Algorithm 1.

---

**Algorithm 1** Example Multi-Method Convergence Algorithm

---

* Approximate $\mathbb{E}[\varphi]$,

$$\mathbb{E}[\varphi] \approx \mathbb{E}_{iSC,Q=10}[\varphi_{MC,N=10^{10}}]$$

* Evaluate $\varepsilon_{iSC}$ for various $Q$,

$$\varepsilon_{iSC} \approx \left| \mathbb{E}[\varphi] - \mathbb{E}_{iSC,Q=\{1,...,10\}}[\varphi_{MC,N=10^{10}}] \right|$$

* Plot $\varepsilon_{iSC}$ against $Q$

* Choose a cubature order $Q$

* Evaluate $\varepsilon_{MC(iSC)}$ at your $Q$ and various $N$,

$$\varepsilon_{MC(iSC)} \approx \left| \mathbb{E}_{iSC,Q}[\varphi_{MC,N=10^{10}}] - \mathbb{E}_{iSC,Q}[\varphi_{MC,N=\{10^3,...,10^8\}}] \right|$$

* Plot $\varepsilon_{MC(iSC)}$ against $N$

---

### 4.1.3 Reuse of Data in Convergence Studies

Since convergence studies produce data at several or many different parameter sets, they can be computationally expensive to perform. It is therefore advantageous to reuse data in successive solves if possible. Random and deterministic sampling methods each allow for reuse of solutions at input nodes if the nodes are used again in successive solves. This is somewhat straightforward for random sampling methods, but requires use of nested quadratures in deterministic sampling. We briefly discuss each here.

When performing a convergence study with random sampling (or Monte Carlo sampling), a new estimation of the solution can be attained with each additional sample. Estimating the error with every additional sample may not be desired due to increased computational overhead, but obtaining enough points to discern convergence rates and have a reasonable chance at observing any anomalies is certainly desired. The solution at each node may be kept and the error recalculated for each number of samples at which an error is desired. If the quantity of interest is a moment of the response or a derivative thereof, however, the data at each node does not need to be stored in memory. Instead only the expectation of the moment $\langle \varphi^m \rangle_p$ at the previous number of samples $R_p$ and the expectation of the moment $\langle \varphi^m \rangle_n$ for a new set of $R_n$ samples need to be stored to

calculate an updated expectation for the QoI moment $\langle\varphi^m\rangle_{p+n}$:

$$
\begin{aligned}
(R_p + R_n)\langle\varphi^m\rangle_{p+n} =& (R_p + R_n)\frac{1}{R_p + R_n}\sum_{i=1}^{R_p+R_n}\varphi_i^m \\
=& \sum_{i=1}^{R_p+R_n}\varphi_i^m \\
=& \sum_{i=1}^{R_p}\varphi_i^m + \sum_{i=R_p+1}^{R_p+R_n}\varphi_i^m \\
=& \frac{R_p}{R_p}\sum_{i=1}^{R_p}\varphi_i^m + \frac{R_n}{R_n}\sum_{i=R_p+1}^{R_p+R_n}\varphi_i^m \\
\Rightarrow \langle\varphi^m\rangle_{p+n} =& \frac{R_p\langle\varphi^m\rangle_p + R_n\langle\varphi^m\rangle_n}{R_p + R_n}.
\end{aligned}
\tag{4.7}
$$

We use this method to update expectation of moment values using random sampling in the stochastic domain or Monte Carlo in the physical domain. From these moments we also update our sample standard deviation:

$$
s_{p+n} = \sqrt{\langle\varphi^2\rangle_{p+n} - \langle\varphi\rangle_{p+n}^2}.
\tag{4.8}
$$

Generating convergence plots by reusing samples as described here enables relatively cheap generation of convergence plots. Without reuse of sample solutions, creation of these plots would be much more expensive and require solving an entire set of new samples at each point on a convergence plot. Reuse of data like this does, however, add correlation between successive points on a convergence plot, i.e., $\langle\varphi^m\rangle_{p+n}$ contains the same samples as $\langle\varphi^m\rangle_p$ and differs only by the contribution of the new $R_n$ samples. This correlation does not nullify the validity of a convergence plot constructed in this way. The correlation will, however, tend to create local peaks or valleys across several values of $R$ in a convergence plot, as the value will only change based on $R_n$. This is especially true when $R_n$ is small compared to $R_{n+p}$; the value at $R_{n+p}$ will be nearly the same as the value at $R_n$.

This type of correlation can also play an important role when producing an approximate-as-exact solution. If the solution considered to be exact for a convergence study reuses any of the same samples as the less-converged solutions against which the "exact" solution is compared, the error will be underestimated. The best practice is to approximate

the exact solution using an entirely different set of samples than the set used to generate the "unconverged" solutions. Thus when reusing data as part of a random sampling convergence study, the problem should be solved twice, once for approximating the exact solution with a large number of samples and once for generating unconverged solutions with a maximum number of samples less than that number. If the unconverged solutions are compared against an "exact" solution computed using some of the same samples, the error will be underestimated, especially when the number of samples for an unconverged solution is close the number used to produce the solution considered to be converged.

Solutions can be reused with successively higher quadrature when using nested quadrature. In nested quadrature rules, nodes present in lower quadrature orders are reused in higher quadrature orders. We have not used nested quadrature in this work, though it would be a logical extension of this work. Selected nested quadrature rules are discussed in Appendix B.

### 4.1.4 Optimal Solution for Chosen Efficiency

Demonstrating error convergence for a QoI for a problem is useful for gaining confidence in the applicability of and implementation of a solver method or set of solver methods. In addition, convergence studies can be used to seek an optimal set of parameters for the chosen solution methods for resolving a QoI within a tolerance. We have presented tools to perform convergence studies based on knowledge of the exact solution for a quantity of interest or the QoI solution yielded by computational methods which are expected to be more converged than the solutions in the convergence study. We can use this type of convergence study to seek the optimal set of parameters to solve a problem QoI for error below a chosen tolerance.

When seeking an optimal set of solver parameters for a solution involving one method, we must converge the solution method until the total error is below a tolerance: $\varepsilon \leq TOL$. If the solve requires use of two solution methods, we can require convergence of each method below a portion of the total tolerance by introducing a parameter $\theta$,

$$TOL_1 = TOL\theta; \quad TOL_2 = TOL(1 - \theta), \tag{4.9}$$

and requiring $\varepsilon_1 \leq TOL_1$ and $\varepsilon_2 \leq TOL_2$. For use of more than two solution methods, we can introduce more free parameters to split the total tolerance between more solution methods. For example, for a three-method solve, we can distribute portions of the tolerance,

$$TOL_1 = TOL\theta_1; \quad TOL_2 = TOL\theta_2; \quad TOL_3(1 - \theta_1 - \theta_2), \quad (4.10)$$

and require each error to be converged below its assigned tolerance.

To truly optimize the overall solve, selection of the free parameters $\theta_i$ must be optimized. This introduces complexity into the problem. We investigate optimal solution parameters for several problems in this work for set values of $TOL$ and $\theta_i$. We do not seek the optimal values of $\theta_i$, and consider that beyond the scope of this work.

Some solver approaches seek an optimal solution through use of updated error estimates instead of requiring knowledge of an exact, or approximated-as-exact, solution. These adaptive methods estimate the error that could be resolved by refining one portion of the solve and use knowledge of the increased computation required to refine the solve to choose which method refinement is expected to most efficiently reduce the overall error. This refinement process is followed until the solution error estimates are below the required tolerance. One such method is multi-level Monte Carlo [61, 62] which relies on knowledge of finite element and Monte Carlo convergence rates. Another is an adaptive algorithm developed by Gerstner and Griebel [9, 16, 63, 64] which successively refines fully-nested cubature.

## 4.2 Problem Statement

We present a stochastic transport problem on which to demonstrate method convergence. We choose the stochastic, one-dimensional, mono-energetic, neutral-particle, steady-state, and absorption-only transport equation with a normally incident beam source of

magnitude 1:

$$\mu\frac{\partial\psi(x,\omega)}{\partial x} + \Sigma_t(x,\omega)\psi(x,\omega) = 0, \tag{4.11a}$$

$$0 \leq x \leq L; \qquad -1 \leq \mu \leq 1; \qquad \Sigma_s = 0, \tag{4.11b}$$

$$\psi(0,\mu) = \delta(1-\mu), \quad \mu > 0; \qquad \psi(L,\mu) = 0, \quad \mu < 0. \tag{4.11c}$$

In this problem the geometry is known a priori but the magnitude of the total cross section $\Sigma_{t,n}$ in each material $n$ is assumed to be uniformly distributed about mean $\langle\Sigma_{t,n}\rangle$ with total variation $\widehat{\Sigma_{t,n}}$:

$$\Sigma_{t,n}(x) = \langle\Sigma_{t,n}\rangle + \widehat{\Sigma_{t,n}}\xi_n(\omega) \,\forall\, n, \quad \xi_n \in \mathcal{U}(-1,1) \,\forall\, n. \tag{4.12}$$

The stochastic dimensionality $D$ is then equal to the number of unique materials which have a random cross section.

We choose problem transmittance, $T$, as our QoI, largely because it is easy to calculate analytically for this problem. We choose problem parameters for a two-dimensional (two-material) problem in the stochastic domain such that the average contribution to the attenuation of the particles from each material is equal but the effects of the uncertainty from each material are not equal. This creates an intuitive and anisotropic problem. We allot each material equal length in the slab beginning from the left side of the slab: $\Delta x_1 = \Delta x_2$, where $x_{n-1}$ and $x_n$ are the left and right boundaries of the slab segment for material $n$, the $x$ value at the left side of the slab is equal to zero $x_0 = 0$, the $x$ value at the right end of the slab is equal to the slab lengh $x_D = L$ and

$$\Delta x_n = x_n - x_{n-1}. \tag{4.13}$$

We also choose cross section values and a slab thickness such that the problem is somewhat optically thick, adding shape to the distribution of resulting transmittance values. The problem parameters chosen are summarized in Table 4.1.

TABLE 4.1: Chapter 4 Problem Parameters

| Material Index | n=1 | n=2 |
|:---:|:---:|:---:|
| $\langle \Sigma_{t,n} \rangle$ [cm$^{-1}$] | 1 | 1 |
| $\widehat{\Sigma_{t,n}}$ [cm$^{-1}$] | 0.1 | 0.9 |
| $x_{n-1}$ [cm] | 0 | 2.5 |
| $x_n$ [cm] | 2.5 | 5 |
| $L$ [cm] | | 5 |

To solve transmittance in the physical domain for a set of values $\boldsymbol{\xi}$ we calculate the optical depth $\tau$ of the slab:

$$\tau(\boldsymbol{\xi}) = \sum_{n=1}^{D} \Sigma_{t,n}(\boldsymbol{\xi}) \Delta x_n. \tag{4.14}$$

We then either solve transmittance analytically by evaluating the probability of attenuation,

$$T(\boldsymbol{\xi}) = \frac{J^+(L, \boldsymbol{\xi})}{J^+(0)} = \exp\left[-\tau(\boldsymbol{\xi})\right], \tag{4.15}$$

or through Monte Carlo sampling by comparing pseudo-random numbers $\eta$ against that probability.

We resolve the solution in the stochastic domain either through random sampling (RS), stochastic collocation (SC), or from a polynomial chaos model built with coefficients determined through stochastic collocation (SC-PCE). We choose Gauss-Legendre (GL) quadrature for numerical, deterministic integration and use Legendre polynomials in our PCE models.

The simplicity of the problem we have chosen enables us to solve a collection of quantities analytically, yielding to demonstration of convergence for various solution methods. We solve moments of the transmission analytically establishing the exact solution for any moment of the transmittance. We also solve PCE coefficients analytically, so that convergence of the PCE model with higher orders of truncation can be shown without bias from error in cubature solves for the PCE coefficients.

### 4.2.1 Analytic Solution of Transmittance Flux Moments

Here we solve for moments of the transmittance $\langle T^m \rangle$ for our problem analytically. We begin with the expression for the analytic transmittance in the physical domain (Eq 4.15),

$$T(\xi_1, \xi_2) = e^{-\Delta x_1 \Sigma_{t,1}(\xi_1) - \Delta x_2 \Sigma_{t,2}(\xi_2)}, \tag{4.16}$$

and the definition of the stochastic total cross sections (Eq. (4.12)):

$$\Sigma_{t,1} = \langle \Sigma_{t,1} \rangle + \widehat{\Sigma_{t,1}} \xi_1; \quad \Sigma_{t,2} = \langle \Sigma_{t,2} \rangle + \widehat{\Sigma_{t,2}} \xi_2. \tag{4.17}$$

We integrate the moment of the transmittance we are interested in over the probability density and simplify:

$$\langle T^m \rangle = \int_{-1}^{1} \int_{-1}^{1} T^m(\xi_1, \xi_2) \frac{1}{2} \frac{1}{2} d\xi_1 d\xi_2 \tag{4.18a}$$

$$= \int_{-1}^{1} \int_{-1}^{1} \frac{1}{2} \frac{1}{2} e^{-m\Delta x_1 \Sigma_{t,1}(\xi_1)} e^{-m\Delta x_2 \Sigma_{t,2}(\xi_2)} d\xi_1 d\xi_2 \tag{4.18b}$$

$$= e^{-m\Delta x_1 \langle \Sigma_{t,1} \rangle} e^{-m\Delta x_2 \langle \Sigma_{t,2} \rangle} \int_{-1}^{1} \frac{1}{2} e^{-m\Delta x_1 \widehat{\Sigma_{t,1}} \xi_1} d\xi_1 \int_{-1}^{1} \frac{1}{2} e^{-m\Delta x_2 \widehat{\Sigma_{t,2}} \xi_2} d\xi_2 \tag{4.18c}$$

$$= e^{-m\Delta x_1 \langle \Sigma_{t,1} \rangle} e^{-m\Delta x_2 \langle \Sigma_{t,2} \rangle} \frac{\left[ e^{m\widehat{\Sigma_{t,1}} \Delta x_1} - e^{-m\widehat{\Sigma_{t,1}} \Delta x_1} \right]}{2m\widehat{\Sigma_{t,1}} \Delta x_1} \frac{\left[ e^{m\widehat{\Sigma_{t,2}} \Delta x_2} - e^{-m\widehat{\Sigma_{t,2}} \Delta x_2} \right]}{2m\widehat{\Sigma_{t,2}} \Delta x_2} \tag{4.18d}$$

$$= e^{-m\Delta x_1 \langle \Sigma_{t,1} \rangle} e^{-m\Delta x_2 \langle \Sigma_{t,2} \rangle} \frac{\sinh \left[ m\widehat{\Sigma_{t,1}} \Delta x_1 \right]}{m\widehat{\Sigma_{t,1}} \Delta x_1} \frac{\sinh \left[ m\widehat{\Sigma_{t,2}} \Delta x_2 \right]}{m\widehat{\Sigma_{t,2}} \Delta x_2}. \tag{4.18e}$$

We note that the contribution to the analytic solution of the transmittance moments from each stochastic dimension is entirely independent such that this expression for an arbitrary number of stochastic dimensions is

$$\langle T^m \rangle = \prod_{n=1}^{D} e^{-m\Delta x_n \langle \Sigma_{t,n} \rangle} \frac{\sinh \left[ m\widehat{\Sigma_{t,n}} \Delta x_n \right]}{m\widehat{\Sigma_{t,n}} \Delta x_n}. \tag{4.19}$$

### 4.2.2   Analytic Solution of PCE Coefficients for Transmission Flux

We also solve PCE coefficients for our problem analytically. We represent the slab transmittance using a polynomial chaos expansion of Legendre polynomials:

$$\psi(L,\omega) = T(\xi_1, \xi_2) = \sum_{i_1=0}^{\infty} \sum_{i_2=0}^{\infty} \widehat{u}_{i_1,i_2} P_{i_1,i_2}(\xi_1, \xi_2). \tag{4.20}$$

As before, we note the analytic expression for transmittance (Eq 4.15) and the definition of the stochastic cross sections (Eq. (4.12)):

$$T(\xi_1, \xi_2) = e^{-\Delta x_1 \Sigma_{t,1}(\xi_1) - \Delta x_2 \Sigma_{t,2}(\xi_2)}; \tag{4.21a}$$

$$\Sigma_{t,1} = \langle \Sigma_{t,1} \rangle + \widehat{\Sigma_{t,1}} \xi_1; \quad \Sigma_{t,2} = \langle \Sigma_{t,2} \rangle + \widehat{\Sigma_{t,2}} \xi_2. \tag{4.21b}$$

Since our probability distributions vary independently, we factor the joint polynomials into a product of univariate polynomials:

$$P(\xi_1, \xi_2) = P(\xi_1) P(\xi_2). \tag{4.22}$$

We insert Eqs. (4.21a), (4.21b), and (4.22) into Eq. (4.20), multiply by Legendre polynomials $P_{j_1}$ and $P_{j_2}$, and integrate over the probability density:

$$\frac{1}{2} \cdot \frac{1}{2} e^{-\Delta x_1 \langle \Sigma_{t,1} \rangle - \Delta x_2 \langle \Sigma_{t,2} \rangle} \int_{-1}^{1} e^{-\Delta x_1 \widehat{\Sigma_{t,1}} \xi_1} P_{j_1}(\xi_1) d\xi_1 \int_{-1}^{1} e^{-\Delta x_2 \widehat{\Sigma_{t,2}} \xi_2} P_{j_2}(\xi_2) d\xi_2$$
$$= \sum_{i_1=0}^{\infty} \sum_{i_2=0}^{\infty} \widehat{u}_{i_1,i_2}(x) \int_{-1}^{1} \frac{1}{2} P_{i_1}(\xi_1) P_{j_1}(\xi_1) d\xi_1 \int_{-1}^{1} \frac{1}{2} P_{i_2}(\xi_2) P_{j_2}(\xi_2) d\xi_2. \tag{4.23}$$

We utilize Legendre polynomial orthogonality, re-index back to $i_1$ and $i_2$, and solve for the PCE coefficients:

$$\widehat{u}_{i_1,i_2} = \left( \frac{2i_1 + 1}{2} e^{-\Delta x_1 \langle \Sigma_{t,1} \rangle} \int_{-1}^{1} e^{-\Delta x_1 \widehat{\Sigma_{t,1}} \xi_1} P_{i_1}(\xi_1) d\xi_1 \right) \cdot$$
$$\left( \frac{2i_2 + 1}{2} e^{-\Delta x_2 \langle \Sigma_{t,2} \rangle} \int_{-1}^{1} e^{-\Delta x_2 \widehat{\Sigma_{t,2}} \xi_2} P_{i_2}(\xi_2) d\xi_2 \right). \tag{4.24}$$

We use

$$\int \xi^b e^{a\xi} dx = e^{a\xi} \sum_{r=0}^{b} (-1)^r \frac{b! \; \xi^{b-r}}{(b-r)! \; a^{r+1}}, \tag{4.25}$$

(Formula 29 on pg. 259 of Ref. [65]) to analytically integrate the exponential with each term of the polynomial on the RHS of Eq. (4.24).

We note that the contribution to the PCE coefficient from each dimension is independent such that solving the PCE coefficients for any number of dimensions reduces to

$$\widehat{u}_{i_1,...,i_D} = \prod_{n=1}^{D} \left( \frac{2i_n + 1}{2} e^{-\Delta x_n \langle \Sigma_{t,n} \rangle} \int_{-1}^{1} e^{-\Delta x_n \widehat{\Sigma_{t,n}} \xi_n} P_{i_n}(\xi_n) d\xi_n \right). \tag{4.26}$$

We also note that we can solve for each PCE coefficient $u_{i_1,...,i_D}$ in this manner, allowing calculation of any combination of PCE coefficients including anisotropic PCE schemes.

## 4.3 Demonstration of Error Convergence for Individual Methods

Here we demonstrate convergence for each of our solvers. We investigate use of Monte Carlo in the physical domain as well as random sampling, stochastic collocation, and construction of a polynomial chaos model in the stochastic domain.

### 4.3.1 Monte Carlo Convergence on Nominal Case

We first demonstrate convergence of our Monte Carlo solver for solutions in the physical domain. While we would like to solve the transmittance by simulating particles over the solution to Eq. (4.11) for the entire stochastic domain at once, this is not practical. We instead choose to simulate particles by sampling against Eq. (4.15) using a set of values for $\boldsymbol{\xi}$. We choose a nominal case when $\boldsymbol{\xi} = \{0, 0\}$ such that each cross section is equal to its average value. We solve the transmittance analytically to produce the exact solution against which to compare. We solve exact transmittance moments for the nominal case using the analytic physical transmittance solution in Eq. (4.15) and stochastic collocation in the stochastic domain of orders 1: $\mathbf{Q} = \{1, 1\}$. We then solve transmittance moments on our nominal case at $\mathbf{Q} = \{1, 1\}$ using an increasing number of particle histories. By comparing the solution of our nominal case solved analytically and using Monte Carlo particle simulation, we can generate the error in the mean of the

transmittance,

$$\varepsilon_{\hat{x},MC(SC)} = \Big|\ \ \mathbb{E}_{SC,\boldsymbol{Q}=\{1,1\}}[T] - \ \ \mathbb{E}_{SC,\boldsymbol{Q}=\{1,1\}}[T_{MC}]\Big|; \qquad (4.27)$$

at various numbers of particle histories.

Figure 4.1 provides plots of the convergence of the mean transmittance using two different random number seeds (denoted by $MC_1$ and $MC_2$). Convergence is as $N^{-\frac{1}{2}}$ as expected.
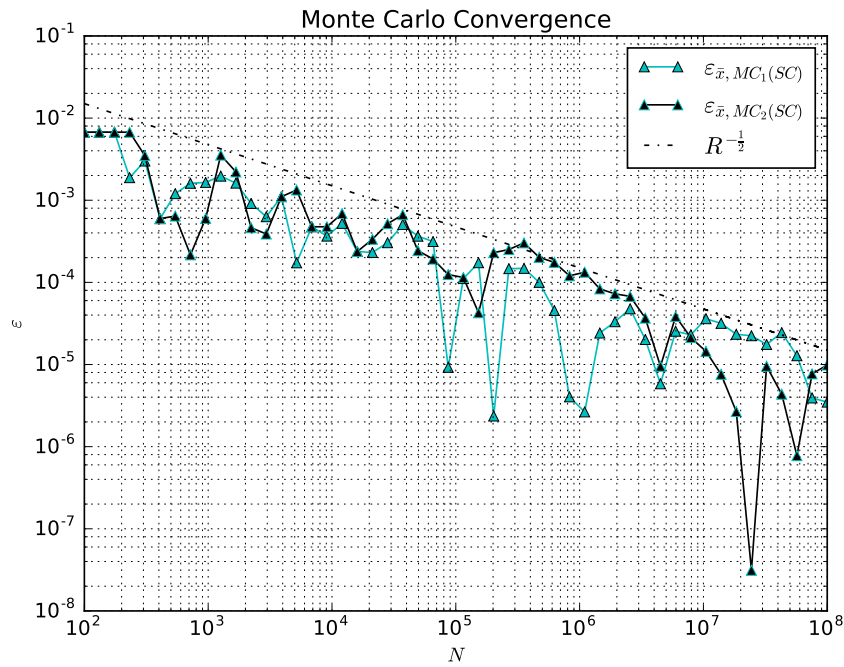


FIGURE 4.1: Convergence of MC Solver

## 4.3.2  Random Sampling Convergence

Here we demonstrate convergence of random sampling in the stochastic domain. We solve the physical problem analytically according to Eq. (4.15) at each randomly sampled point $\boldsymbol{\xi}$ in the stochastic domain. We compare these solutions against the analytic solution generated in Section 4.2.1. Error terms are defined as

$$\varepsilon_{\hat{x},RS} = \Big|\ \ \mathbb{E}[T] - \ \ \mathbb{E}_{RS}[T]\Big|; \qquad (4.28)$$

$$\varepsilon_{s,RS} = \Big|\sqrt{\mathbb{V}[T]} - \sqrt{\mathbb{V}_{RS}[T]}\Big|. \qquad (4.29)$$

We plot the standard error of the mean for random sampling $s_{\langle T \rangle}$ and note that it serves as a decent estimator for the error in the QoI average $\varepsilon_{\hat{x},RS}$. Figures 4.2 and 4.3 each plot the convergence of the mean, the standard error of the mean, the convergence of the standard deviation, and a $R^{-\frac{1}{2}}$ line for reference using different random number seeds. Convergence is as $R^{-\frac{1}{2}}$ as expected.
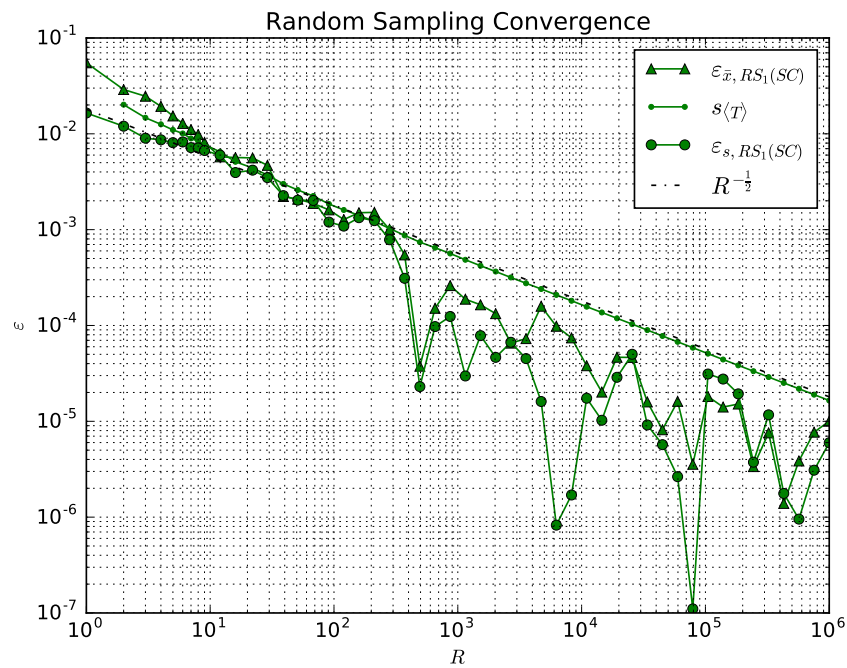


FIGURE 4.2: Convergence of RS Solver
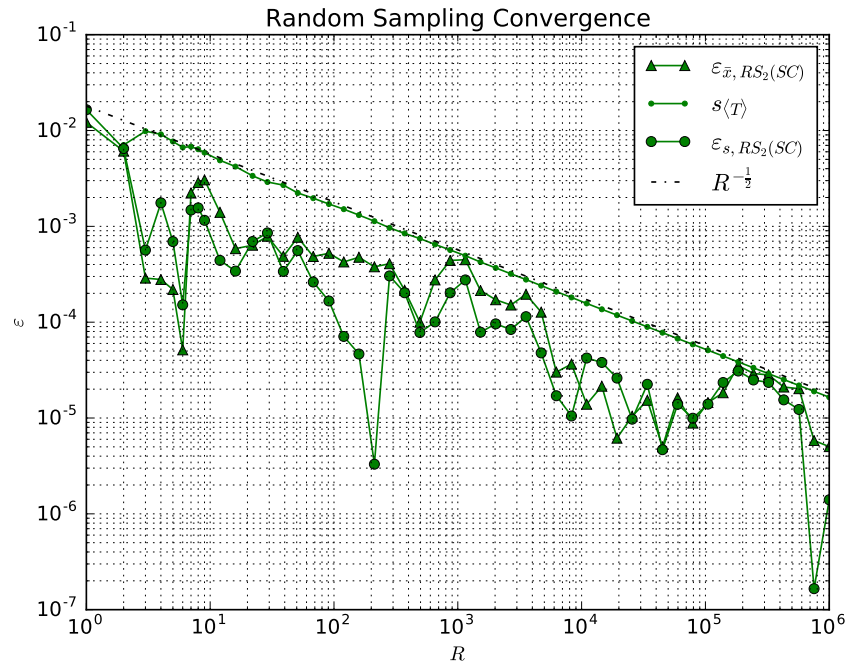
FIGURE 4.3: Convergence of RS Solver

### 4.3.3 Stochastic Collocation Convergence

We next demonstrate convergence of our stochastic collocation solver. We solve the physical problem analytically according to Eq. (4.15) at each deterministically sampled cubature node $\boldsymbol{\xi}^{(q)}$ in the stochastic domain. We compare these solutions against the analytic solution generated in Section 4.2.1. Error terms are defined as

$$\varepsilon_{\hat{x},SC} = \Big| \quad \mathbb{E}[T] - \quad \mathbb{E}_{SC}[T] \Big|; \tag{4.30}$$

$$\varepsilon_{s,SC} = \Big| \sqrt{\mathbb{V}[T]} - \sqrt{\mathbb{V}_{SC}[T]} \Big|. \tag{4.31}$$

We plot convergence of the mean and standard deviation of the solution for our isotropic stochastic collocation (iSC) solver as a function of the number of nodes (solves) in Figure 4.4. We observe the expected exponential convergence of both quantities.
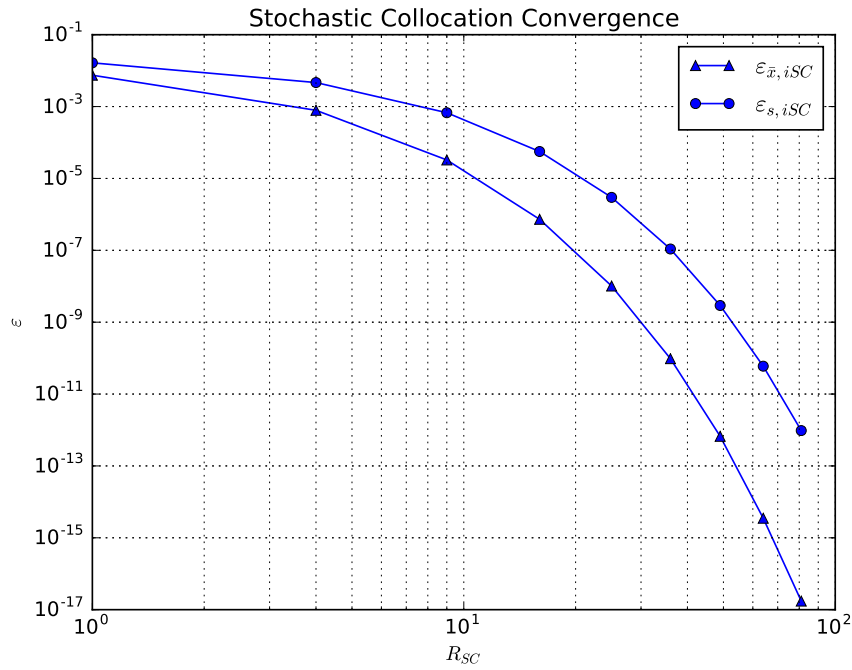
FIGURE 4.4: Convergence of Isotropic Stochastic Collocation Solver

Next we investigate the use of anisotropic stochastic collocation (aSC). We plot the iSC error terms for reference along with select aSC points and allow the notation $[Q_1, Q_2]$ to denote quadrature orders $\boldsymbol{Q} = \{Q_1, Q_2\}$. We plot errors in the quantity of interest mean in Figure 4.5 and the QoI standard deviation in Figure 4.6.
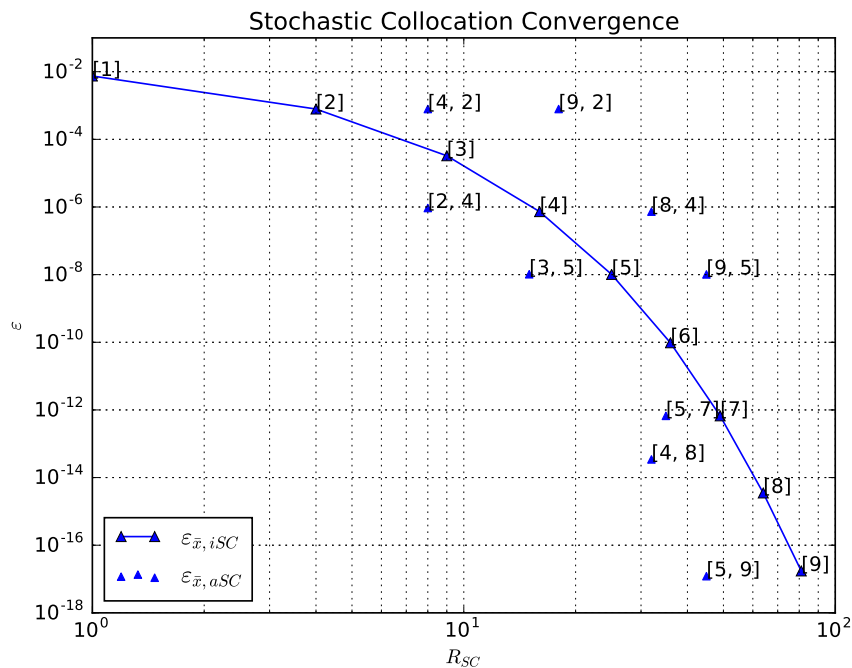


FIGURE 4.5: Convergence of Anisotropic Stochastic Collocation Solver for QoI Mean
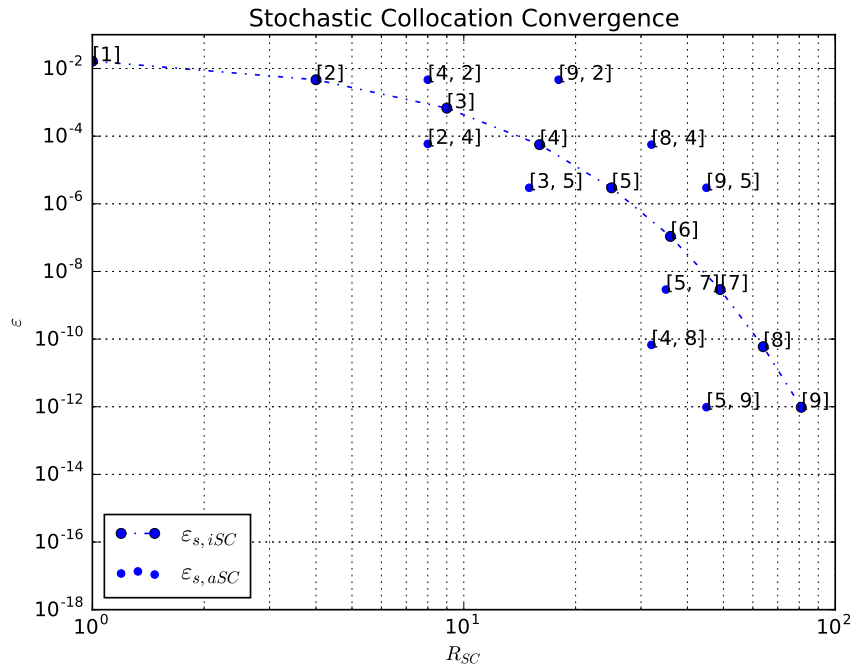
FIGURE 4.6: Convergence of Anisotropic Stochastic Collocation Solver for QoI Standard Deviation

We note that a well-chosen aSC cubature scheme for this anisotropic problem yields smaller errors for the same number of solves than iSC and that the converse is true as well. For a truly isotropic problem the optimal cubature is isotropic. In other cases there is the potential to be more or less efficient than the iSC solve based on the order chosen in each dimension. For example, aSC orders of $\boldsymbol{Q} = \{5, 9\}$ produce errors on par with $\boldsymbol{Q} = \{9, 9\}$ while requiring 45 problem evaluations as opposed to 81. For this problem the variation in the solution due to the variation in the input in the first dimension is well resolved with a 5th-order quadrature. Conversely $\boldsymbol{Q} = \{9, 5\}$ produces errors on par with $\boldsymbol{Q} = \{5, 5\}$, while requiring more problem evaluations. The second dimension appears to be resolved at a quadrature order of nine. This same type of behavior can be observed in the error at other collocation points. The quadrature order in each dimension could be treated as a parameter to be converged to a chosen tolerance. We consider that beyond the scope of this work, but note that such an approach could help identify the most efficient combination of solution methods and method parameters available for a chosen tolerance.

### 4.3.4 Polynomial Chaos Truncation Convergence

Here we demonstrate convergence of a polynomial chaos expansion model of the response with successively higher truncation order. We solve PCE coefficients for our problem analytically as discussed in Section 4.2.2 and evaluate mean and standard deviation of the surface using Eqs. (3.54) and (3.57b). We compare these solutions against the analytic solution generated in Section 4.2.1. Error terms are defined as

$$\varepsilon_{\hat{x},PCE} = \Big| \ \ \mathbb{E}[T] - \ \ \mathbb{E}_{PCE}[T] \Big|; \tag{4.32}$$

$$\varepsilon_{s,PCE} = \Big| \sqrt{\mathbb{V}[T]} - \sqrt{\mathbb{V}_{PCE}[T]} \Big|. \tag{4.33}$$

We plot convergence of the mean and standard deviation of the solution as a function of the number of PCE coefficients in Figure 4.7. Though in Section 4.2.2 we solved an analytic expression for the PCE coefficients, numerical evaluation of Eq. (4.26) begins to introduce non-negligible errors in the PCE coefficient values for this problem after a PCE order of 7. We note that the mean is solved to machine precision with only one coefficient according to Eq. (3.54).
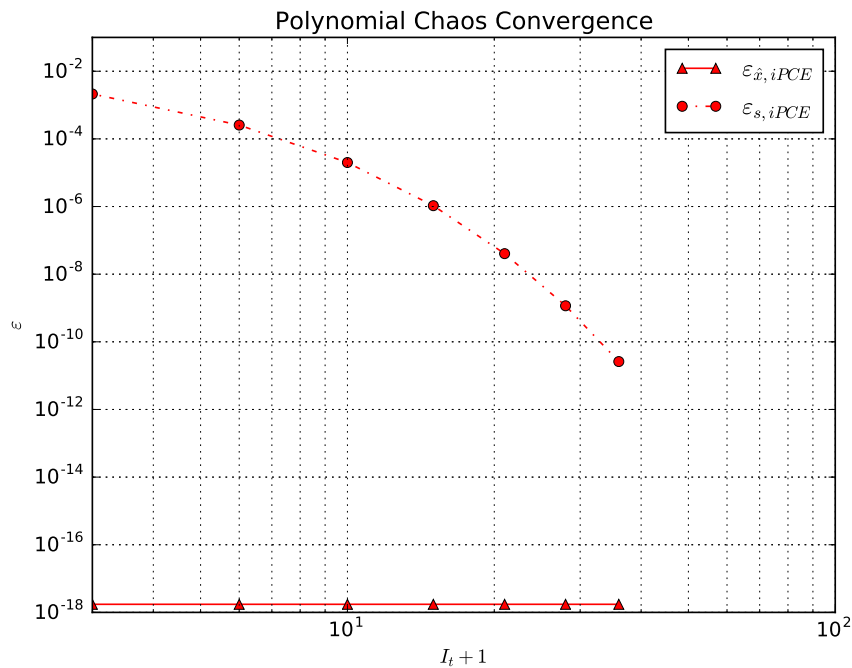


FIGURE 4.7: Convergence of iPCE Truncation

Next we investigate the use of an anisotropic PCE model as described in Section 3.2.3.2. We plot isotropic PCE (iPCE) error terms for reference along with selected anisotropic PCE (aPCE) points. Though we are solving PCE coefficients analytically and not through use of stochastic collocation, we allow the notation $[Q_1, Q_2], I$ to mean an $I$-order iPCE for which terms are further truncated as they would be when solving using aSC with quadrature orders $\boldsymbol{Q} = \{Q_1, Q_2\}$. We do not show the convergence of the mean, as it is fully converged with only the smallest order PCE truncation.
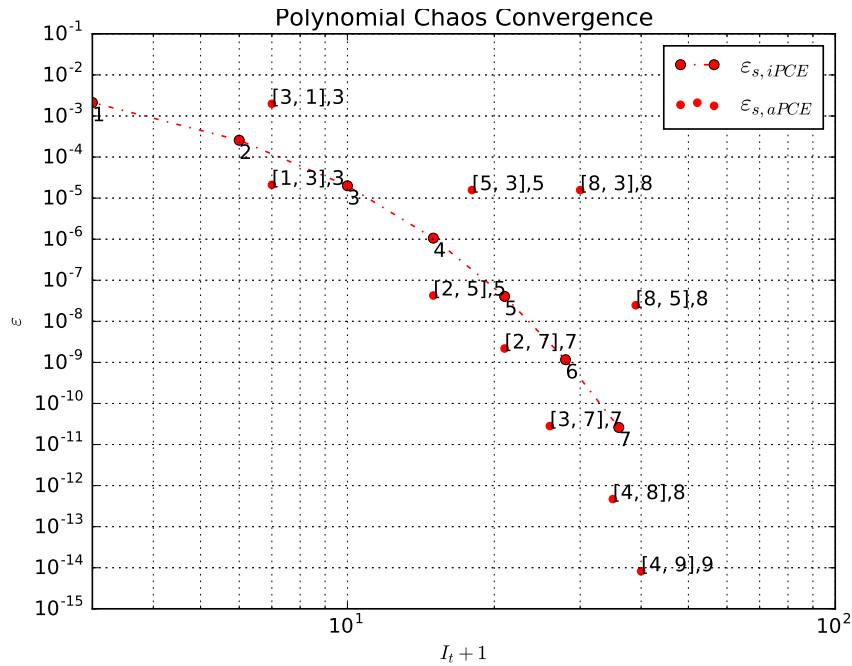


FIGURE 4.8: Convergence of aPCE Truncation

We note that a well-chosen aPCE truncation scheme for this anisotropic problem yields smaller errors for the same number of PCE terms than iPCE and that the converse is true as well. The first dimension seems to be resolved after about a 4th-order truncation, whereas the second dimension seems to not be resolved until at least a 9th-order truncation. We show through comparison of the points $[3, 1], 3$; $[1, 3], 3$; $[5, 3], 5$; and $[8, 3], 8$ that if the error from one dimension dominates, the truncation in that dimension should be increased. Increasing the order of truncation in the right dimension will decrease the error. Increasing the order of truncation in the wrong dimension will not significantly decrease the error, but require more PCE terms.

### 4.3.5 Combination of SC and PCE error as SC-PCE Convergence

Here we make a case for converging the error of the combined SC-PCE solver in the stochastic domain instead of converging the SC and the PCE model solvers individually. Since we solve PCE coefficients using SC, the maximum order of each PCE coefficient is limited by the SC quadrature order used to solve for it. In Section 3.2.3.2 we discussed a version of anisotropic PCE that truncates an isotropic PCE model subject to the constraints of the selected SC quadrature orders. We proposed two different PCE truncation orders, before applying the aPCE truncation, which may be the best choice relative to the underlying SC orders. The first suggested PCE truncation chooses $I$ as the largest quadrature order used in the SC solve. This selection of PCE truncation order ensures that at least one PCE term uses the highest order polynomial available based on the selected SC solves. The second suggested PCE truncation chooses $I$ as the sum of the quadrature orders used in the SC solve. This selection of PCE truncation order includes all PCE terms for which the SC solve provides enough information to solve the coefficient of the term. The second truncation order is more accurate since it keeps more cross-moment terms in the PCE. If the computational overhead of PCE operations is negligible compared to the cost of evaluating the physical solver, the second suggested truncation order should be used. Polynomial chaos expansion operations may not always be negligible, however, especially if the problem has many stochastic dimensions, the SC solve uses large quadrature orders, or the PCE is to be sampled from many times. In these cases the first suggested truncation order may be preferred. Beyond this section, except when specified, we use the first of the two proposed PCE truncations.

Here we plot convergence of the solution yielded by an aPCE model with increasing orders of initial PCE truncation for chosen SC quadrature orders. We demonstrate for this problem that either the higher or lower suggested PCE order, subject to truncation based on the SC solve, is a suitable choice for constructing a joint SC-PCE solver for which only one error needs to be resovled.

Here we demonstrate the error of an aPCE truncation error for a chosen set of aSC quadrature orders. Error terms are defined as

$$\varepsilon_{\hat{x},PCE(SC)} = \Big|\ \ \mathbb{E}_{SC}[T] - \ \ \mathbb{E}_{PCE(SC)}[T]\Big|; \tag{4.34}$$

$$\varepsilon_{s,PCE(SC)} = \Big|\sqrt{\mathbb{V}_{SC}[T]} - \sqrt{\mathbb{V}_{PCE(SC)}[T]}\Big|. \tag{4.35}$$

In Figures 4.9, 4.10, and 4.11 we solve $\varepsilon_{s,PCE(SC,\boldsymbol{Q})}$ at $\boldsymbol{Q} = \{2,4\}$, $\boldsymbol{Q} = \{5,9\}$, and $\boldsymbol{Q} = \{7,7\}$ for increasing orders of the initial iPCE truncation $I$. We have chosen these three cases of PCE convergence to represent three different types of behavior, though in all cases we come to the same conclusion.
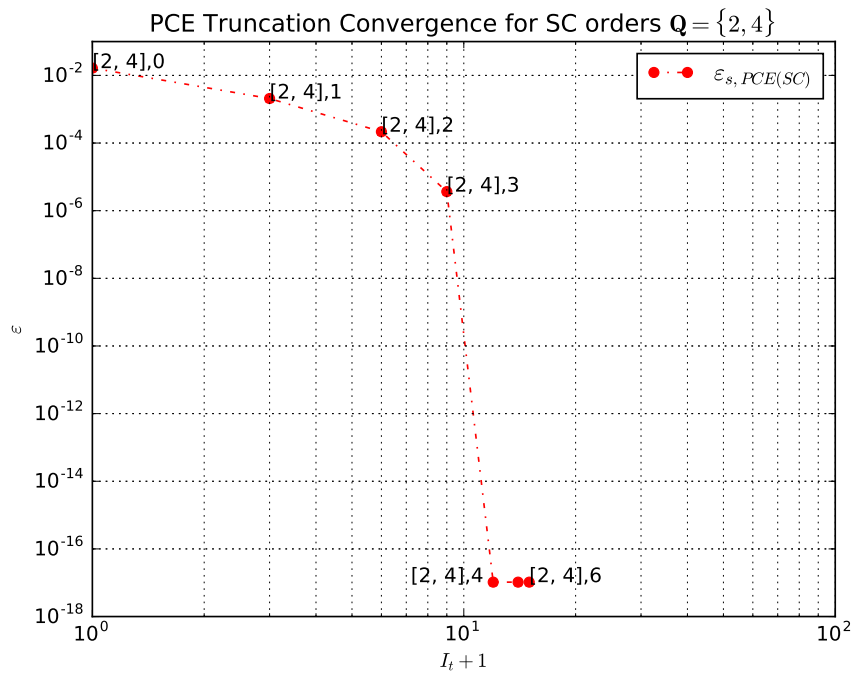


FIGURE 4.9: Convergence of aPCE Model at $\boldsymbol{Q} = \{2,4\}$
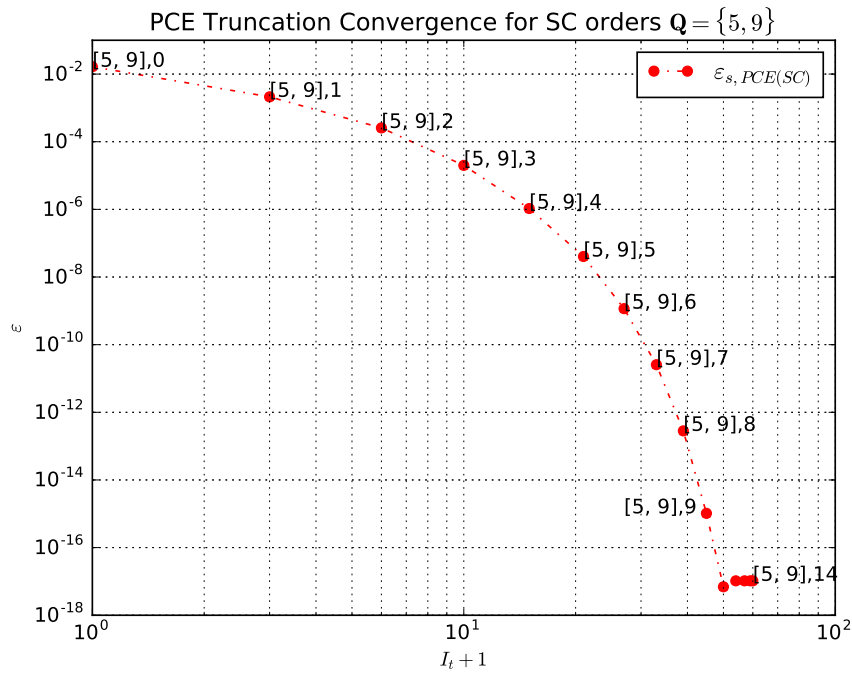
FIGURE 4.10: Convergence of aPCE Model at $\boldsymbol{Q} = \{5, 9\}$
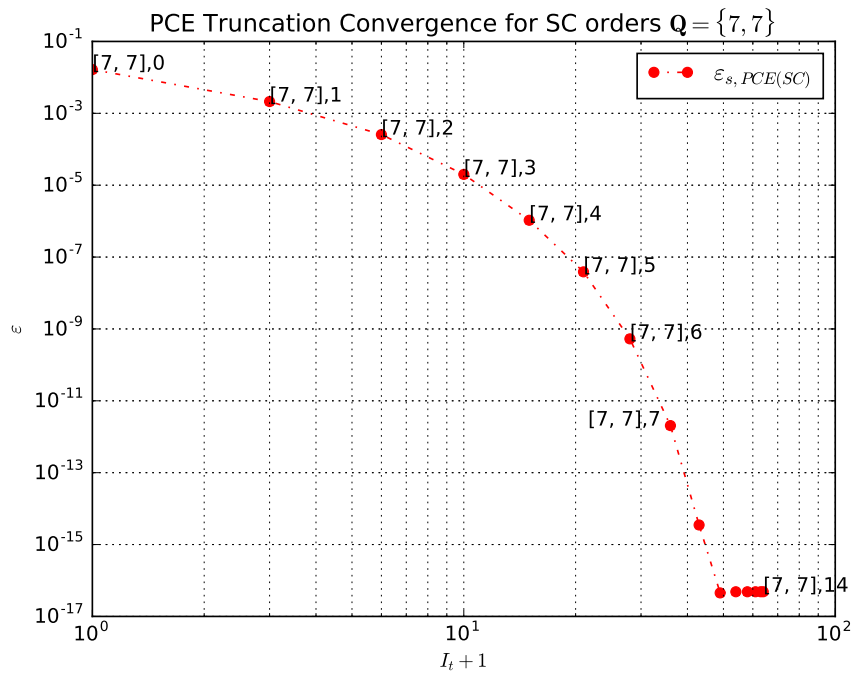


FIGURE 4.11: Convergence of aPCE Model at $\boldsymbol{Q} = \{7, 7\}$

In Figure 4.9 we solve $\varepsilon_{s,PCE(SC,\boldsymbol{Q}=\{2,4\})}$ for increasing orders of $I$. We note that for this problem, according to Figure 4.6, the stochastic collocation error was about $10^{-4}$. The PCE error for $I = 4$ and $I = 6$ were about the same, and much smaller than $10^{-4}$. We observe for this and other lower-order cases that the PCE error tends to be very

small compared to the SC error, suggesting convergence of the SC-PCE error with an appropriate PCE scheme will be dominated by the SC convergence.

In Figure 4.10 we solve $\varepsilon_{s,PCE(SC,\boldsymbol{Q}=\{5,9\})}$ for increasing orders of $I$. When error of less than about $10^{-10}$ was desired, this cubature was the best bargain (Figure 4.6) and had a SC error of about $10^{-12}$. While the PCE error for $I = 14$ was smaller than that for $I = 9$, both schemes produced PCE truncation errors of less than $10^{-14}$. For this and similar higher-order anisotropic cubature order sets the PCE truncation error for a reasonable PCE scheme was at least two orders of magnitude less than the SC error, justifying use of the joint SC-PCE method for converging the joint errors.

In Figure 4.11 we solve $\varepsilon_{s,PCE(SC,\boldsymbol{Q}=\{7,7\})}$ for increasing orders of $I$. For this collocation point, according to Figure 4.6, the error was a little more than $10^{-9}$. Again, the higher PCE truncation order $I = 14$ resolved PCE error more than the lower PCE truncation order $I = 7$, but both produced PCE truncation errors at least two orders of magnitude less than the SC error.

In each case–a lower-order aSC case, a higher-order aSC case, and an iSC case–the PCE truncation error was considerably less than the SC error. In the rest of this work, when we use the PCE, we choose to converge the SC and PCE errors as one error, and denote the combined SC and PCE method as SC-PCE.

We show for a problem that the convergence of the aPCE model for a QoI is limited by the error of the SC solve; PCE polynomial orders which are higher than the SC quadrature orders should not be used. The computational overhead of operations on the PCE model is assumed to be small compared to the cost of additional solves of the physical problem; PCE polynomial orders should be at least as high as the corresponding SC quadrature orders. Because of these two constraints, the allowed and optimal use of a PCE truncation scheme is significantly limited by the choice of parameters in the SC solve, with freedom being only in which allowed higher-order cross moments the user wants to truncate from the PCE. A reasonable PCE model built using SC cubature has little freedom in truncation. We therefore propose converging the combined SC-PCE method as one error source.

### 4.3.6 Comparison of RS and SC-PCE Convergence Rates

Here we compare the convergence of random sampling (RS) and stochastic collocation (SC) for our problem. We compare convergence of transmittance mean and standard deviation using the random sampling approach from Section 4.3.2 and the convergence of the isotropic polynomial chaos model built from stochastic collocation solves from Section 4.3.3 in Figures 4.12 and 4.13. We do not show anisotropic points for the SC-PCE solve, rather we emphasize for this problem the general convergence trends. In the case of the mean convergence we plot the standard error of the mean, $s_{\langle T \rangle}$, for the two random sampling convergence data sets generated in Section 4.3.2, and in the case of the standard deviation we plot both data sets along with an $R^{-\frac{1}{2}}$ line to demonstrate the convergence rate of random sampling. SC-PCE converges to any tolerance with many less solves than RS for the QoIs for this problem, especially when using an appropriate aSC grid. This stochastically smooth, two-dimensional problem presents a case in which SC-PCE outperforms RS.
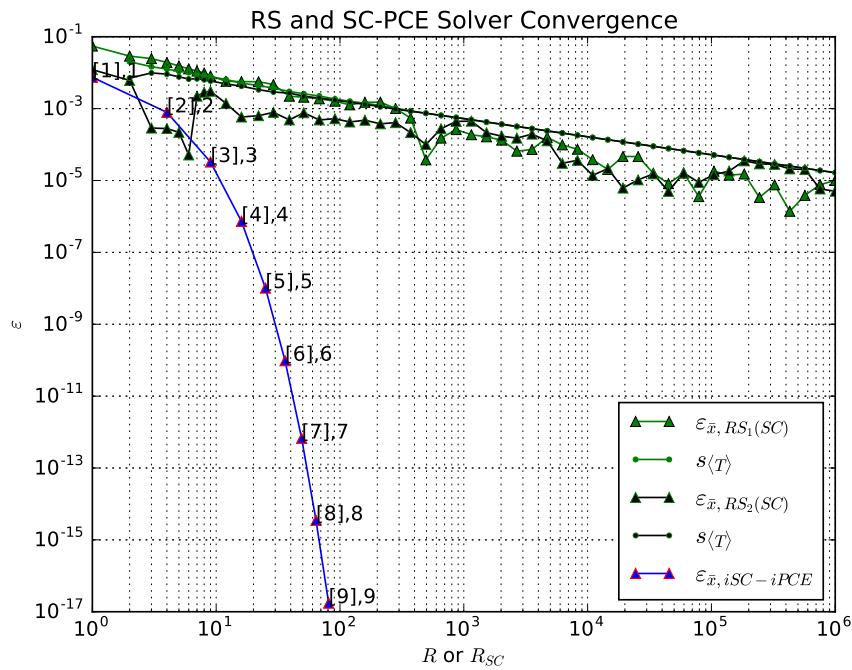


FIGURE 4.12: Convergence of RS and SC-PCE Solvers for QoI Mean
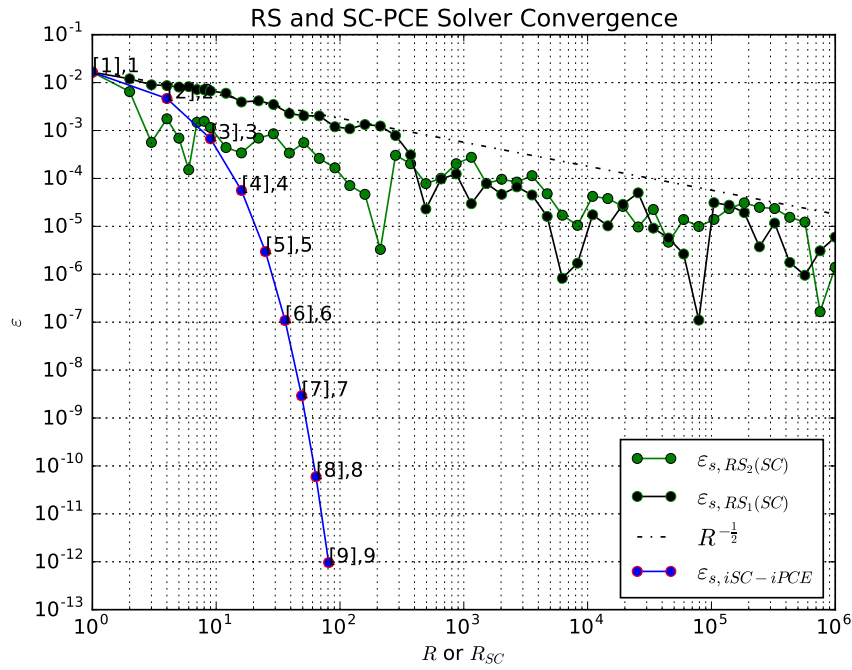
FIGURE 4.13: Convergence of RS and SC-PCE for QoI Standard Deviation

We next demonstrate the curse of dimensionality that SC and therefore SC-PCE suffers from. As the dimensionality of a problem increases or the complexity of the response over the stochastic domain increases, the convergence rate for SC-PCE suffers, whereas the convergence rate for RS does not. In these cases RS may be the more reasonable choice of a stochastic solver based on convergence.

We demonstrate by creating a 10-dimensional problem similar to our 2-dimensional problem. We use the same slab length as before, $L = 5$ cm, but define eight new materials, each with $\langle \Sigma_t \rangle = 1$ cm and either $\widehat{\Sigma_t} = 0.1$ cm or $\widehat{\Sigma_t} = 0.9$ cm. We allot equal slab length for each material and place them sequentially in the slab as in Table 4.2.

TABLE 4.2: 10-dimensional Problem Parameters

| n | 1 | 2 | 3 | 4 | 5 | 6 | 7 | 8 | 9 | 10 |
|---|---|---|---|---|---|---|---|---|---|----|
| $\langle \Sigma_{t,n} \rangle$ [cm$^{-1}$] | 1 | 1 | 1 | 1 | 1 | 1 | 1 | 1 | 1 | 1 |
| $\widehat{\Sigma_{t,n}}$ [cm$^{-1}$] | 0.1 | 0.9 | 0.1 | 0.9 | 0.1 | 0.9 | 0.1 | 0.9 | 0.1 | 0.9 |
| $x_{n-1}$ [cm] | 0.0 | 0.5 | 1.0 | 1.5 | 2.0 | 2.5 | 3.0 | 3.5 | 4.0 | 4.5 |
| $x_n$ [cm] | 0.5 | 1.0 | 1.5 | 2.0 | 2.5 | 3.0 | 3.5 | 4.0 | 4.5 | 5.0 |
| $L$ [cm] | | | | | | | | | | 5 |
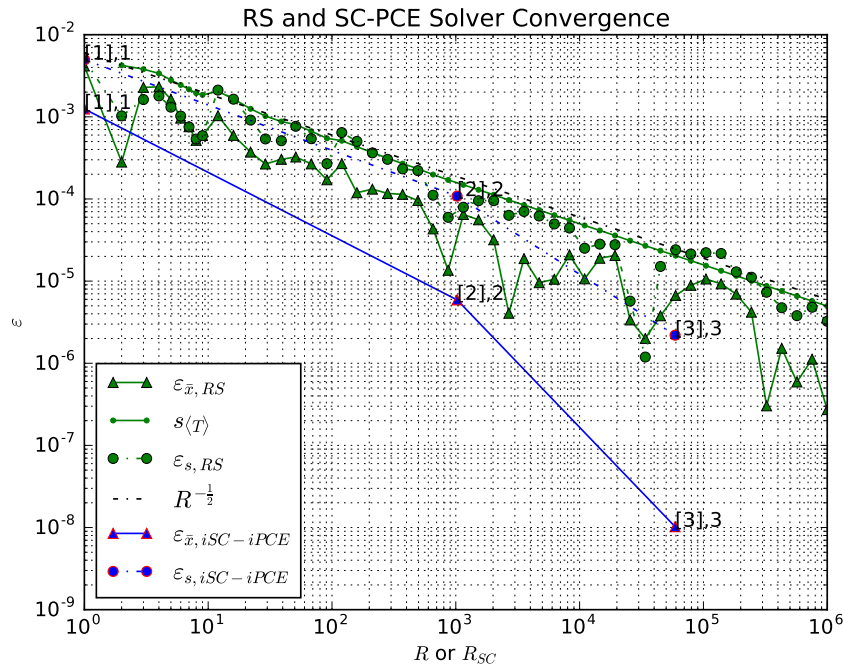
FIGURE 4.14: Convergence of RS and SC-PCE Solvers for 10-dimensional Problem

We observe in Figure 4.14 that the convergence of either QoI for SC-PCE is still exponential, but considerably slower. We also observe that the RS convergence is not affected by the number of stochastic dimensions in the problem. This demonstrates the need to apply SC and SC-PCE in problems with a fairly low stochastic dimensionality. If there are many stochastic dimensions, one should either reduce the number of stochastic dimensions by doing some sort of sensitivity analysis or simply use a method like random sampling.

## 4.4 Demonstration of Multi-Method Convergence of Error to Tolerance

In this section we demonstrate an approach to the set of solver parameters which solves a quantity of interest to within a tolerance most efficiently for a chosen set of convergence parameters $TOL$ and $\theta$. We solve in the physical domain with Monte Carlo particle simulation, and in the stochastic domain first through random sampling and second by building a polynomial chaos expansion model from a stochastic collocation solve. We demonstrate that for this problem SC-PCE solves moments of the response much more efficiently than RS. Additionally, SC-PCE can generate a PDF of the QoI, something

SC alone cannot do. The solution attained from RS serves both as a benchmark of the accuracy of our methods and their implementations and establishes a solution efficiency against which to compare the efficiency of SC-PCE.

We choose $TOL = 10^{-3}$ and split the error allowed in the physical and stochastic domains to be the same:

$$TOL = TOL_1 + TOL_2;$$
$$TOL_1 = TOL\theta, \quad TOL_2 = TOL(1 - \theta), \quad (4.36)$$
$$\theta = 0.5.$$

When solving with RS in the stochastic domain our error terms are defined as

$$\varepsilon = \varepsilon_{s,RS} + \varepsilon_{s,MC(RS)};$$
$$\varepsilon_{s,RS} \qquad = \left| \sqrt{\mathbb{V}[T]} - \sqrt{\mathbb{V}_{RS}[T]} \right|, \quad (4.37)$$
$$\varepsilon_{s,MC(RS)} = \left| \sqrt{\mathbb{V}_{RS}[T]} - \sqrt{\mathbb{V}_{RS}[T_{MC}]} \right|.$$

When solving with SC-PCE in the stochastic domain our error terms are defined as

$$\varepsilon = \varepsilon_{s,SC-PCE} + \varepsilon_{s,MC(SC-PCE)};$$
$$\varepsilon_{s,SC-PCE} \qquad = \left| \sqrt{\mathbb{V}[T]} - \sqrt{\mathbb{V}_{SC-PCE}[T]} \right|, \quad (4.38)$$
$$\varepsilon_{s,MC(SC-PCE)} = \left| \sqrt{\mathbb{V}_{SC-PCE}[T]} - \sqrt{\mathbb{V}_{SC-PCE}[T_{MC}]} \right|.$$

In both cases we require convergence of each error below the respective tolerance: for RS $\varepsilon_{s,RS} \leq TOL_1$ and $\varepsilon_{s,MC(RS)} \leq TOL_2$ and for SC-PCE $\varepsilon_{s,SC-PCE} \leq TOL_1$ and $\varepsilon_{s,MC(SC-PCE)} \leq TOL_2$.

### 4.4.1 Convergence in the Stochastic Domain

We solve $\varepsilon_{s,RS}$ with a successively increased number of samples with two different random number seeds in Figure 4.15 and plot the random sampling convergence along with an $R^{-\frac{1}{2}}$ line, the tolerance $TOL_1$, and the number of samples we choose. The RS error appears to be converged to the tolerance at about 800 samples; we therefore use 800 samples in our further analysis.
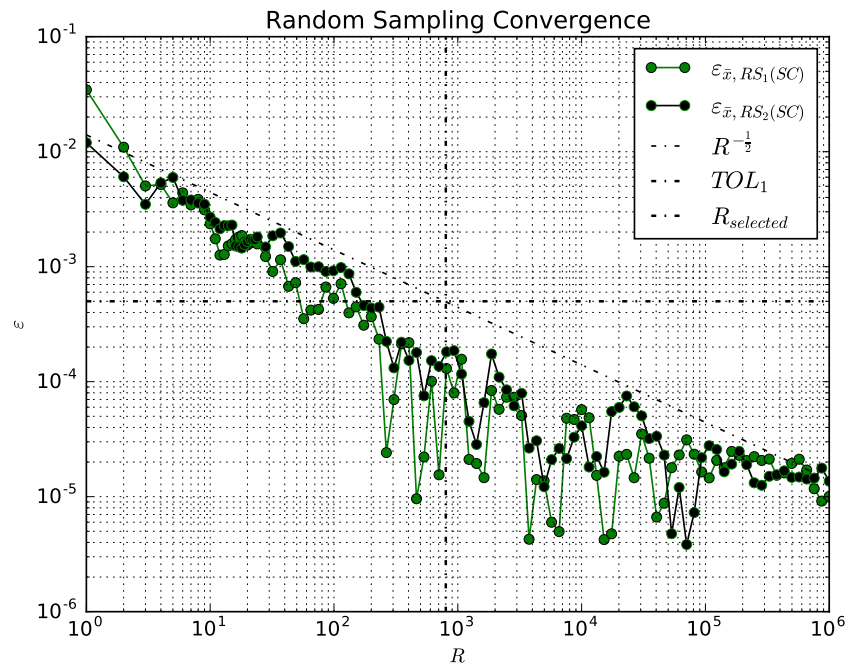
FIGURE 4.15: Convergence of RS Solver for Standard Deviation Below Tolerance

We solve $\varepsilon_{s,iSC-iPCE}$ with a successively increased set of quadrature orders and PCE truncation orders in Figure 4.16. We also solve at a collection of parameter sets for $\varepsilon_{s,aSC-aPCE}$ and plot the error for the set which required the least number of solves but was below the required tolerance. We plot the tolerance below which the method is to converge. We use $\boldsymbol{Q} = \{1, 5\}$ with an anisotropic PCE order of $I = 5$ in our further analysis.
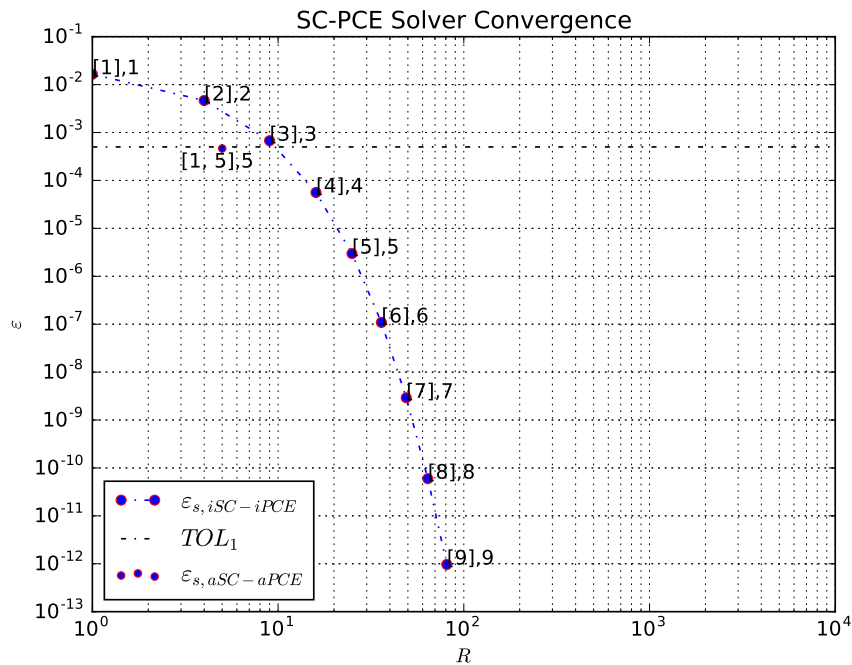
FIGURE 4.16: Convergence of SC-PCE Solver for Standard Deviation Below Tolerance

Note that the same error was achieved with 800 solves of our physical problem using RS and only 5 solves using aSC-aPCE.

### 4.4.2 Convergence in the Physical Domain

We generate convergence plots of the Monte Carlo solver in the physical domain for $R = 800$ random samples in Figure 4.17 using two different random number seeds. Plots are generated by comparing a Monte Carlo physical solve against an analytic physical solve for the same 800 realizations. Similarly, we provide convergence plots of the MC solver for $Q = \{1, 5\}$, $I = 5$ using aSC-aPCE in Figure 4.18 using two different random number seeds.
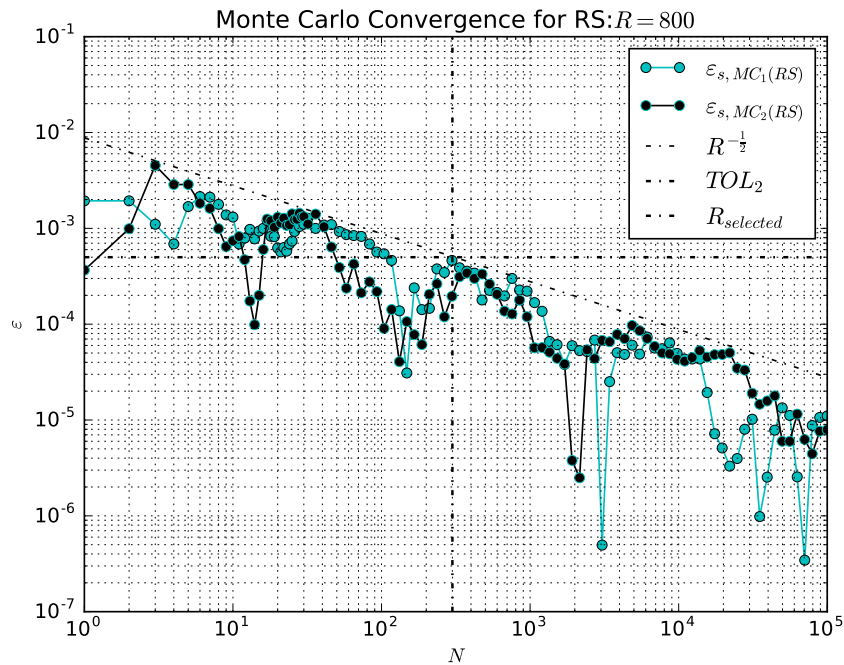
FIGURE 4.17: Convergence of MC for RS Solve for Standard Deviation Below Tolerance
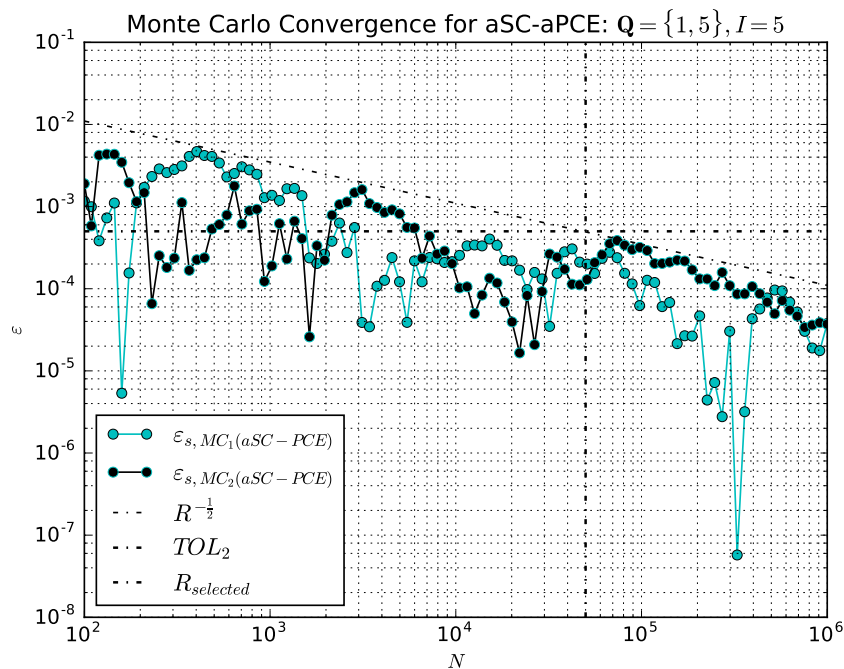


FIGURE 4.18: Convergence of MC for aSC-aPCE Solve for Standard Deviation Below Tolerance

The Monte Carlo error $\varepsilon_{s,MC(RS)}$ appears to converge below $TOL_2$ at about 400 particle histories on each of 800 samples. The total number of particle histories required for this

set of solution methods with our chosen tolerance parameters is therefore about 320,000 particle histories.

The Monte Carlo error $\varepsilon_{s,MC(SC-PCE)}$ appears to converge below $TOL_2$ at about 5,000 particle histories on each of 5 nodes. The total number of particle histories required for this set of solution methods with our chosen tolerance parameters is therefore about 25,000 particle histories.

Though the aSC-aPCE solution method required more particle histories on each node than the RS method, SC-PCE required about 13 times fewer particle histories. It is likely that the efficiency of the aSC-aPCE method could be improved with a smart choice of $\theta$ by choosing a larger value for $\theta$, placing a tighter tolerance on the exponentially converging stochastic solver. Additionally, should a smaller tolerance be desired, aSC-aPCE is expected to show even better solve efficiency compared to RS by taking advantage of the exponential convergence of the aSC-aPCE solver as compared to the linear convergence of the RS solver.

### 4.4.3 Comparison of RS and SC-PCE Probability Density Functions

We have chosen parameters for a random sampling and a stochastic collocation polynomial chaos expansion approach which resolve the transmittance standard deviation within our chosen tolerance of $TOL = 1 \times 10^{-3}$ using splitting parameter $\theta = 0.5$. Here we generate probability density functions (PDFs) of the transmittance using each method with the chosen parameters. Whereas the number of samples in a PDF constructed using RS is equal to the number of physical solves performed, once the PCE model is constructed using SC, the SC-PCE method allows many samples to be taken from the PCE model cheaply.

In Figure 4.19 we plot PDFs yielded with the chosen parameters: $R = 800$ and $N = 400$ in the RS case, for a total cost of 320,000 particle histories, and $\mathbf{Q} = \{1, 5\}$ and $N = 5000$ in the SC-PCE case, for a total cost of 25,000 particle histories. We sample from the PCE model 100,000 times. The PDFs in general appear to be in agreement, though the PDF generated using the SC-PCE method was cheaper to generate and is more well-resolved.
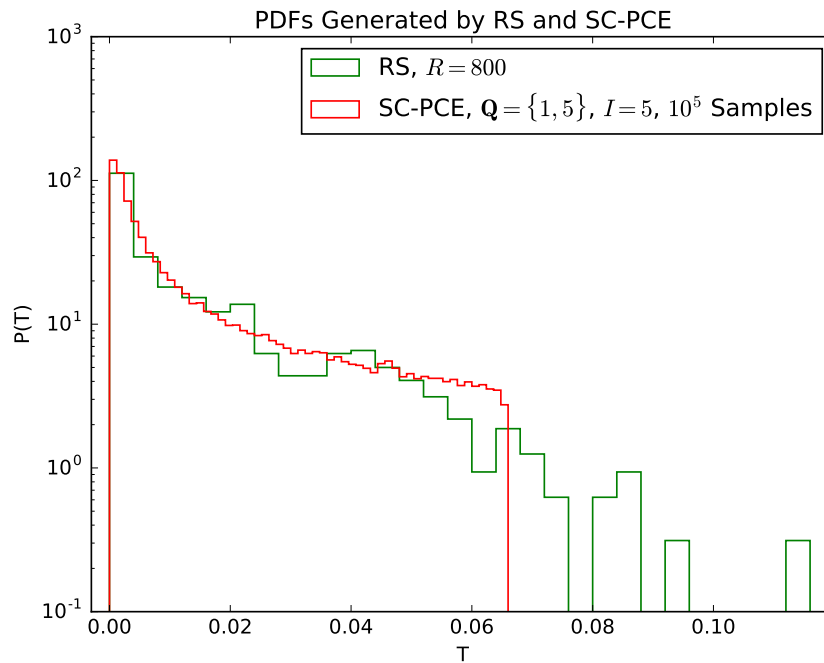
FIGURE 4.19: PDFs Generated by RS and SC-PCE, $\varepsilon_s \approx 1 \times 10^{-3}$

In Figure 4.20 we demonstrate that with increased resolution PDFs generated by the two methods are converging towards the same distribution, and further demonstrate the efficiency of the SC-PCE approach. For the random sampling case, we choose 10,000 particle histories to be solved on each of 10,000 realizations, and according to Figures 4.15 and 4.17 estimate the bound on the error of the transmittance standard deviation to be about $2.3 \times 10^{-4}$. In the SC-PCE case, we choose $\mathbf{Q} = \{4, 9\}$ and estimate the error in the transmittance standard deviation from the SC-PCE representation to be less than $1 \times 10^{-10}$ based on Figure 4.6. We choose 20,000 histories per realization based on Figure 4.18 and estimate the bound on the transmittance standard deviation due to the MC physical solver to be about $2.3 \times 10^{-4}$, such that the total error using either method is about the same. Whereas the random sampling method required a total of $1 \times 10^8$ particle histories, the SC-PCE method required a total of about $7.2 \times 10^5$ particle histories, such that the SC-PCE method was about 139 times cheaper. The methods produced similar PDFs, though the PDF produced using SC-PCE was more cheaply generated and well-resolved (100,000 plotted point instead of 10,000).
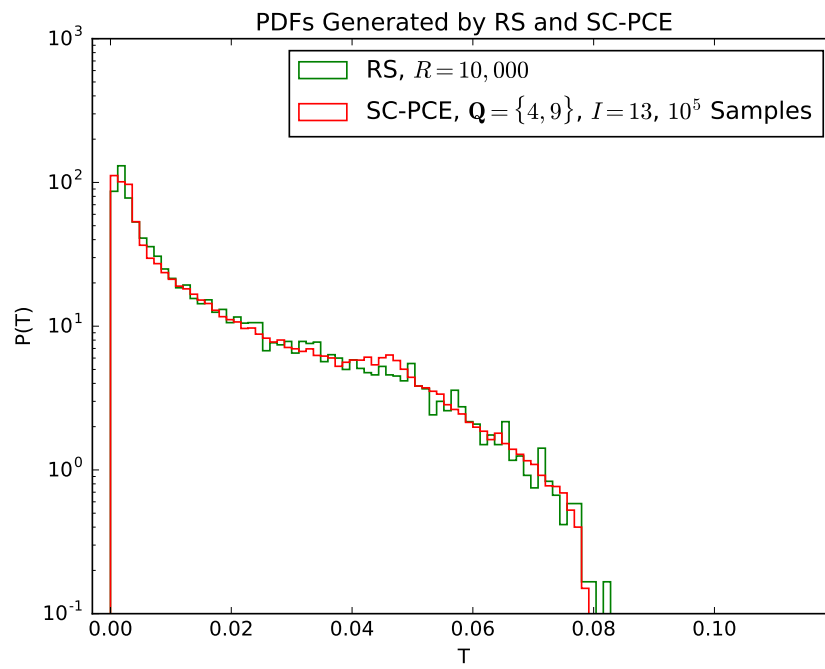
FIGURE 4.20: PDFs Generated by RS and SC-PCE, $\varepsilon_s \approx 2.3 \times 10^{-4}$

# Chapter 5

# Transport in Spatially Random, Continuous Cross Sections

In this chapter we solve the stochastic transport equation for which nuclear cross sections are modeled as lognormal random processes. We model material density as a continuously varying property such that macroscopic cross sections vary proportionately. Direct application of this approach is radiation transport calculations through a fluid of non-constant density, e.g., radiation transport in the upper-atmosphere. Such fields can be used to approximate spatially discontinuous quantities such as heterogeneous mixing in radiation shields or porosity of subterranean structures. The domain of problems this method can be applied to expands when modeling a quantity other than the atomic density, for example, modeling the temperature gradient in nuclear reactor moderator or modeling burnup fractions in aging nuclear reactor cores. In this work we only model the density of a material using a lognormal field.

We create a Gaussian random field described by independent Gaussian random variables using the Karhunen-Loève (KL) expansion. While a Gaussian field can represent the mean and variance of a subject field, it also allows for negative values of the field. We therefore use a lognormal transformation of the field, and create inputs for the Gaussian distributed KL field, by mapping values of the material density through the lognormal transformation.

Recent work in the literature includes using a lognormal transformation of the KL expansion to model material density for radiation transport applications [10, 44], though

78

this work extends investigation of this idea by accurately and numerically solving KL eigenvalues and eigenvectors, solving the physical problem using Woodcock Monte Carlo instead of deterministic methods, performing error analysis, and using a different approach to stochastic collocation (SC) and the response modeling with the polynomial chaos expansion (PCE).

In this chapter we state our problem and solution methods, present the lognormal transformation of a Gaussian field, and perform an error convergence study on three stochastic transport problems.

## 5.1   Problem Statement

In this chapter we solve the one-dimensional, mono-energetic, neutral-particle, steady-state, and isotropically scattering transport equation with a normally incident beam boundary source:

$$\mu\frac{\partial\psi(x,\mu,\omega)}{\partial x} + \Sigma_t(x,\omega)\psi(x,\mu,\omega) = \frac{\Sigma_s(x,\omega)}{2}\int_{-1}^{1}d\mu'\psi(x,\mu',\omega),$$

$$0 \le x \le L; \qquad -1 \le \mu \le 1 \tag{5.1}$$

$$\psi(0,\mu) = \delta(1-\mu), \quad \mu > 0; \qquad \psi(L,\mu) = 0, \quad \mu < 0.$$

We represent random macroscopic cross section $r$ as

$$\Sigma_r(x,\omega) = N_{at}(x,\omega)\sigma_r, \tag{5.2}$$

where $N_{at}(x,\omega)$ is the material atom density and $\sigma_r$ is the material microscopic cross section. Modeling the atom density allows modeling of all material properties derived from the atom density including various macroscopic cross sections.

Equation 5.1 is solved in this chapter using the solution methods discussed in Chapters 2 and 3–Woodcock Monte Carlo (WMC), the Karhunen-Loève (KL) expansion, random sampling (RS), stochastic collocation (SC), and the polynomial chaos expansion (PCE)– and the approach to error analysis presented in Chapter 4. Material atom density is modeled with a lognormal transformation of the Karhunen-Loève expansion and KL eigenvalues and eigenvectors are solved numerically using the Nyström method. Since

the KL random variables have a standard normal distribution, the probablists' Gauss-Hermite (GH) quadrature rule is used when solving with SC and Hermite polynomials are used when modeling with the PCE.

## 5.2   The Karhunen-Loève Representation of Continuous, Random Cross Sections

To ensure independence of the KL random variables, we choose them as Gaussian-distributed [9]. Subsequently, the joint probability density can be factored into the product of univariate probability densities as in Eq. (3.34). This separation simplifies sampling from the probability distribution, analysis of analytic solutions such as those presented in Chapter 4 (Eq. (4.19) and Eq. (4.26)), and enables factoring of multivariate Askey polynomials into the product of univariate polynomials when using the PCE.

Though Gaussian random variables provide these advantages over other distributions, they also produce a random process which can be negative, an undesirable and un-physical trait when modeling atom density. We therefore model the random process as lognormal through a transformation of the Gaussian KL process, preserving second-order statistics through the transformation.

The Gaussian and lognormal distributions are described by

$$p(\xi) = \frac{1}{\sqrt{v_g 2\pi}} \exp\left[ -\frac{(\xi - \langle g \rangle)^2}{2v_g} \right], \text{and} \tag{5.3a}$$

$$p(\xi) = \exp\left( \frac{1}{\sqrt{v_g 2\pi}} \exp\left[ -\frac{(\xi - \langle g \rangle)^2}{2v_g} \right] \right), \tag{5.3b}$$

respectively, where $\langle g \rangle$ is the mean and $v_g$ is the variance of variable $g$. It is readily observed that values of $p(\xi)$ always exist for which $\xi$ is negative in the Gaussian case, and that values of $p(\xi)$ never exist for which $\xi$ is negative in the lognormal case. We demonstrate the positive-preserving property of the lognormal distribution in Figure 5.1 by plotting six Gaussian distributions in the left plot and six lognormal distributions with the same average and variance in the right plot.
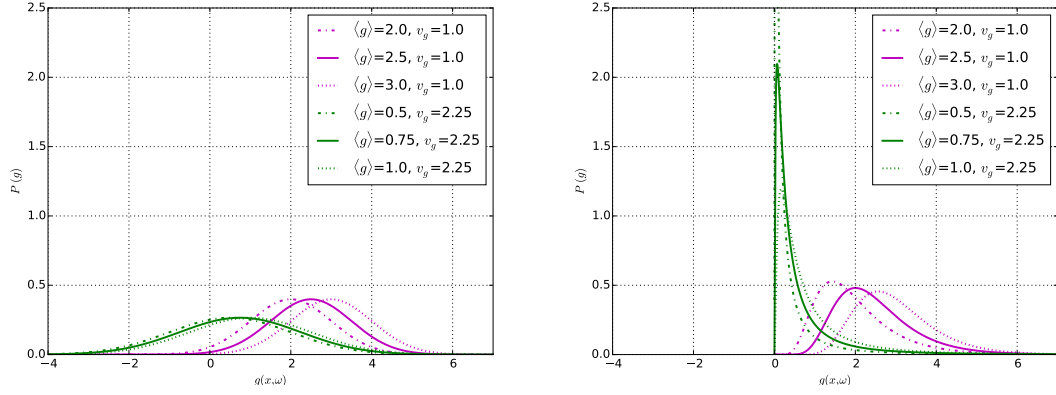
FIGURE 5.1: Example Gaussian and Lognormal Probability Distributions

The lognormal distribution is peaked towards smaller values, especially as the distribution average to variance ratio is small. As the distribution average to variance ratio becomes large the lognormal distribution looks more like the Gaussian distribution with the same parameters, but in all parameter cases enforces distribution positivity.

### 5.2.1 The Lognormal Transformation

The lognormal random atom density $N_{at}(x,\omega)$ is related to the Gaussian random process $g(x,\omega)$ by

$$N_{at}(x,\omega) = \exp\big[g(x,\omega)\big]. \tag{5.4}$$

The Gaussian process mean $\langle g \rangle$, variance $v_g$, and covariance $c_g(x,x')$ are solved as a function of the corresponding lognormal atom density statistics as [10]

$$\langle g \rangle = \ln\left(\frac{\langle N_{at} \rangle^2}{\sqrt{v_{N_{at}} + \langle N_{at} \rangle^2}}\right), \tag{5.5a}$$

$$v_g = \ln\left(\frac{v_{N_{at}}}{\langle N_{at} \rangle^2} + 1\right), \text{and} \tag{5.5b}$$

$$c_g(x,x') = \frac{\ln\left(c_{N_{at}}(x,x')\frac{v_{N_{at}}}{\langle N_{at} \rangle} + 1\right)}{\ln\left(\frac{v_{N_{at}}}{\langle N_{at} \rangle^2} + 1\right)}, \tag{5.5c}$$

where $c_{N_{at}}(x,x') = C_{N_{at}}(x,x')/v_{N_{at}}$ and $c_g(x,x') = C_g(x,x')/v_g$.

The atom density is represented as a function of the Gaussian-random KL expansion:

$$N_{at}(x, \omega) = \exp\left[\langle g \rangle + \sum_{k=1}^{\infty} \sqrt{\gamma_k} u_k(x)\xi_k(\omega)\right], \qquad (5.6)$$

where $\langle g \rangle$ is the Gaussian process mean and $\gamma_k$, $u_k$, and $\xi_k$ are the eigenvalue, eigenvector, and Gaussian-random variables for each KL term $k$. The eigenvalues and eigenvectors are solved using Eq 3.4 as a function of the Gaussian variance and relative covariance:

$$\int_0^L v_g c_g(x, x')u(x')dx' = \gamma u(x). \qquad (5.7)$$

Macroscopic cross section profiles are yielded by truncating the KL expansion at order $K$ and multiplying the lognormal random atom density by the correct microscopic cross section:

$$\Sigma_r(x, \omega) = \sigma_r \exp\left[\langle g \rangle + \sum_{k=1}^{K} \sqrt{\gamma_k} u_k(x)\xi_k(\omega)\right]. \qquad (5.8)$$

Through Eq. (5.8) realizations of various macroscopic cross sections can be constructed using only $K$ independent and Gaussian random variables.

We demonstrate realizations of Gaussian and lognormal processes with the same second-order statistics in Figure 5.2 and, for reference, plot one and two standard deviation marks from the process mean. It is observed that some Gaussian realizations contain negative values, whereas lognormal realizations do not. The lognormal realizations contain more values close to zero and have higher peaks.
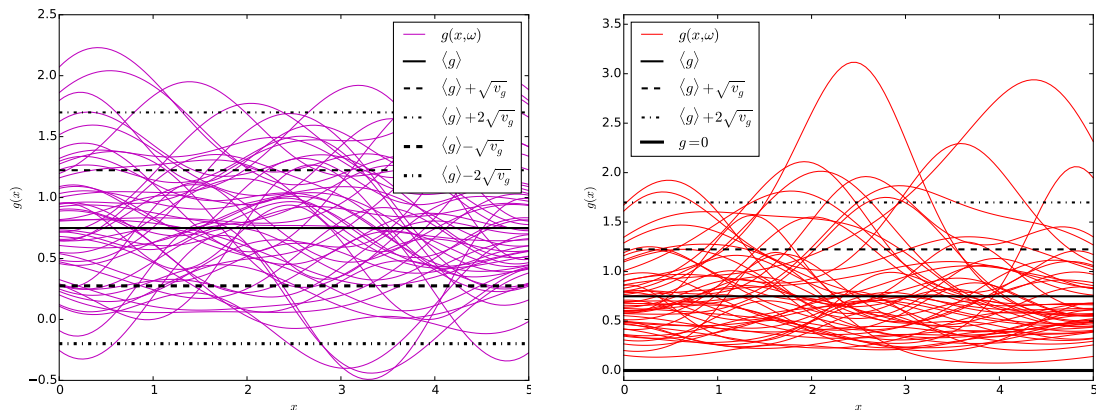


FIGURE 5.2: Fifty Gaussian and Lognormal Realizations ($\langle g \rangle = 0.75$, $v_g = 0.225$)

We test our lognormal KL implementation by constructing many realizations and computing an observed mean and standard deviation across an ensemble of realizations. Observed moment values for an ensemble of 50,000 random process realizations are plotted at 20 locations throughout the slab in Figure 5.3 using 3, 7, or 15 KL eigenmodes along with the true process mean and standard deviation for reference.
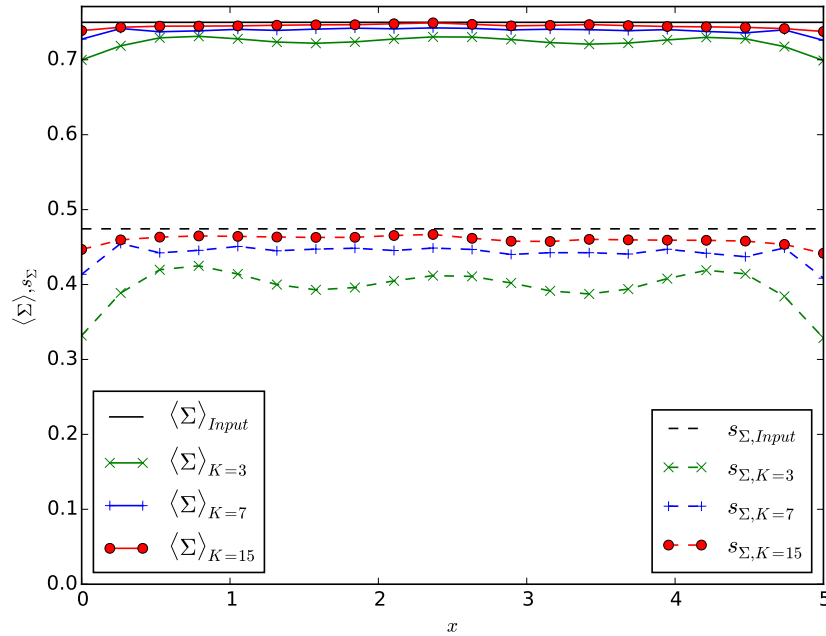


FIGURE 5.3: Observed Mean and Standard Deviation in Lognormal Random Process Ensemble ($\langle \Sigma \rangle = 0.75$, $\sqrt{v_\Sigma} = \sqrt{0.225} \approx 0.474$)

Observed moment values converge towards input moment values with higher KL truncation orders. The process standard deviation contains a larger error than the process mean for the same number of KL terms. Any truncation of a Gaussian KL process would fully preserve the process mean; introduction of the lognormal transformation, however, favors values below the mean. Transport results performed over lognormally modeled cross sections will therefore tend to overestimate transmittance and underestimate reflectance.

The oscillatory behavior in the physical domain for the observed ensemble mean and standard deviation is an artifact of the oscillatory shape of the KL eigenfunctions which provide variation in the physical domain. Though the KL eigenfunctions used to model a lognormal process are not strictly sines and cosines as they are for modeling a Gaussian process (Section 3.1.3.1), the shapes are similar, and provide the oscillating shape.

## 5.3   Semi-infinite Slab Reflection Problem

It has been shown that an analytic solution exists for the angular reflective flux profile when a beam particle source is incident on a semi-infinite slab comprised of material with a constant scattering ratio regardless of the mixing statistics of the slab material. We solve this problem for reflectance using a simple Monte Carlo particle simulation implementation and benchmark our transport-with-scattering implementation against the more simply generated solution. We demonstrate numerically the preservation of the reflectance with different mixing statistics by showing a convergence of the solution generated in multiple ways towards the same value.

### 5.3.1   Problem Statement and Solution Methods

This problem is described through modification of the stochastic transport equation stated at the beginning of this chapter (Eq. (5.1)) by assigning the slab's length $L$ to be infinitely long and enforcing a constant scattering ratio $c$:

$$\mu \frac{\partial \psi(x,\mu,\omega)}{\partial x} + \Sigma_t(x,\omega)\psi(x,\mu,\omega) = \frac{\Sigma_s(x,\omega)}{2} \int_{-1}^{1} d\mu' \psi(x,\mu',\omega),$$

$$0 \leq x < \infty; \qquad -1 \leq \mu \leq 1; \qquad c = \frac{\Sigma_s(x,\omega)}{\Sigma_t(x,\omega)} \tag{5.9}$$

$$\psi(0,\mu) = \delta(1-\mu), \quad \mu > 0.$$

Dividing by the total cross section removes $x$ dependence from all terms but the first:

$$\mu \frac{\partial \psi(x,\mu,\omega)}{\Sigma_t(x,\omega)\partial x} + \psi(x,\mu,\omega) = \frac{c}{2} \int_{-1}^{1} d\mu' \psi(x,\mu',\omega),$$

$$0 \leq x < \infty; \qquad -1 \leq \mu \leq 1 \tag{5.10}$$

$$\psi(0,\mu) = \delta(1-\mu), \quad \mu > 0.$$

Integrating the total cross section over $x$ yields the optical thickness $\tau$:

$$\tau(x,\omega) = \int_0^x \Sigma_t(x',\omega)dx'. \tag{5.11}$$

Inserting Eq. (5.11) into Eq. (5.10) along with the boundary conditions

$$\tau(x = 0) = 0, \text{and} \tag{5.12a}$$

$$\tau(x = a) = \int_0^a \Sigma_t(x', \omega) dx', \quad \text{as } a \to \infty, \tau \to \infty. \tag{5.12b}$$

removes $x$ dependence, and thus stochastic dependence, from the equation:

$$\mu \frac{\partial \psi(\tau, \mu)}{\partial \tau} + \psi(\tau, \mu) = \frac{c}{2} \int_{-1}^{1} d\mu' \psi(\tau, \mu'),$$

$$0 \leq \tau < \infty; \qquad -1 \leq \mu \leq 1 \tag{5.13}$$

$$\psi(0, \mu) = \delta(1 - \mu), \quad \mu > 0.$$

It is seen that the angular flux is a function of optical thickness $\tau$ and direction of particle travel $\mu$, but not position in the slab $x$ or sample from the stochastic domain $\omega$. This relationship is possibly the most useful on the reflective boundary, at which both the optical thickness and position in slab are equal to zero for all realizations. Though the entire angular flux distribution at the reflective boundary is therefore analytic for a value of $c$, we choose to benchmark our transport-with-scattering implementation using mean reflectance.

We first solve a benchmark value for mean reflectance using a simple Monte Carlo transport implementation to effect transport through and tally reflectance on a semi-infinite slab with a constant scattering ratio and approximate the exact reflectance using $10^{10}$ particle histories:

$$\mathbb{E}[R] \approx \mathbb{E}[R_{Bench-MC,N=10^{10}}]. \tag{5.14}$$

To demonstrate the simplicity of this optical-thickness-based Monte Carlo transport calculation, we provide a minimalist Python script for performing the MC computation in Appendix D.

We also calculate the reflectance for a problem using random sampling and stochastic collocation in our transport-with-scattering code. Karhunen-Loève truncation $K$ and Nyström discretization order $N_{Ny}$ are arbitrarily chosen along with the number of random samples $R$ when solving using random sampling and a set of collocation orders $\mathbf{Q}$ when solving using stochastic collocation since any combination of these parameters

should converge towards the same value for the reflectance mean with an increased number of Monte Carlo particle histories $N$. Both cases are solved with a slab thickness $L$ of 1000 cm, for which no transmittance tallies were recorded in our simulations. The atom density average and variance are set to $N_{at} = 1$ cm$^{-3}$ and $v_{N_{at}} = 0.3$ cm$^{-3}$, and the microscopic absorption and scattering cross sections $\sigma_a$ and $\sigma_s$ are equal to 1 cm$^2$, producing a scattering ratio of $c = 0.5$. A correlation length of $\lambda_c = 1.5$ cm and a KL truncation order of $K = 5$ are selected. Reflectance is solved for these parameters using RS with $R = 100$ realizations and SC with orders $\mathbf{Q} = \{4, 3, 3, 2, 2\}$ for a total of $R_{SC} = 144$ realizations. In each case the solution is generated with up to $N = 10^7$ particles on each realization.

When performing a convergence study on the reflectance values as the number of particle histories $N$ is increased, error terms are defined as

$$\varepsilon_{Bench-MC} = \left| \mathbb{E}[R_{Bench-MC,N=10^{10}}] - \mathbb{E}[R_{Bench-MC,N<10^{10}}] \right|, \tag{5.15a}$$

$$\varepsilon_{MC(RS)} = \left| \mathbb{E}[R_{Bench-MC,N=10^{10}}] - \mathbb{E}_{RS}[R_{MC,N\leq10^7}] \right|, \tag{5.15b}$$

$$\varepsilon_{MC(SC)} = \left| \mathbb{E}[R_{Bench-MC,N=10^{10}}] - \mathbb{E}_{SC}[R_{MC,N\leq10^7}] \right|. \tag{5.15c}$$

## 5.3.2 Monte Carlo Convergence of Benchmark and Scattering Implementation

The most converged reflectance values for each method are provided in Table 5.1 with enough digits to gain an intuitive feel for the convergence of the reflectance values. Based on the data in this table, we expect the error produced using the RS and SC solves to be about $10^{-5}$ or $10^{-6}$.

TABLE 5.1: Semi-Infinite Slab Reflectance Values for Lognormal KL Implementation

| Solution Method | Num. Histories $N$ | $\langle R \rangle$ |
|---|---|---|
| Benchmark-MC | $1.0 \times 10^{10}$ | 0.11522526 |
| MC(RS) | $1.0 \times 10^9$ | 0.11522577 |
| MC(SC) | $1.44 \times 10^9$ | 0.11522148 |

Error convergence plots for the error terms defined in Eq. (5.15) are given in Figure 5.4. A line of the expected Monte Carlo convergence rate is plotted for reference.
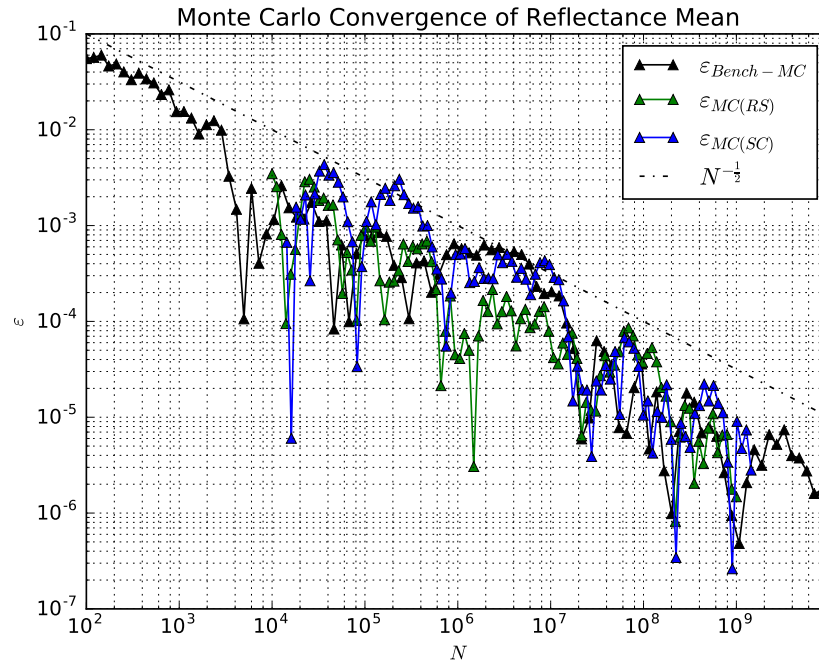


FIGURE 5.4: Semi-Infinite Slab Reflectance Mean MC Convergence for Lognormal KL Implementation

The solutions calculated using RS and SC by our transport-with-scattering implementation converge as a function of the number of total Monte Carlo particle histories towards the benchmark solution. The error in the most converged solutions is about $10^{-5}$ or $10^{-6}$ as expected based on the most converged reflectance values. While the most converged value yielded by the RS method appears to have an error of about $10^{-6}$, a quick investigation of Figure 5.4 informs that the error is only this small due to serendipitous statistical variation. Were this simulation run with different random number seeds, we would expect the error to be about $10^{-5}$ or less in serendipitous cases like this.

## 5.4   Uncollided Flux Transmission Problem

Another problem for which solution method error may be carefully studied and our transport-with-scattering implementation may be benchmarked against a simpler implementation is in the case of an uncollided flux, or absorption-only, calculation. In such a problem, particles are introduced to the left side of an absorption-only slab and

the transmittance of a realization can be solved purely as a function of the optical thickness of the realization. Unfortunately, the lognormal processes of our implementation do not provide an analytic integration of the total macroscopic cross section, and integration must be carried out numerically, yielding a "semi-analytic" solution. We study the sources of error due to modeling the lognormal macroscopic cross sections for chosen parameters in the resulting stochastic solve using such semi-analytic solutions and then observe Monte Carlo convergence towards the semi-analytic values using our transport-with-scattering implementation by setting the scattering cross section equal to zero.

### 5.4.1   Problem Statement and Solution Methods

This problem is described as a modification of the stochastic transport equation stated at the beginning of this chapter (Eq. (5.1)) for which the scattering cross section $\Sigma_s(x,\omega)$ is set to zero. By imposing a beam source and removing the possibility of scatter, the direction of particle travel is restricted to one value and can be removed from the equation altogether yielding

$$\mu\frac{\partial\psi(x,\omega)}{\partial x} + \Sigma_t(x,\omega)\psi(x,\omega) = 0,$$
$$0 \leq x \leq L \tag{5.16}$$
$$J^+(0) = 1, \qquad J^-(L) = 0.$$

The stochastically-dependent transmittance is solved as in Eq. (4.15) as a function of the stochastically-dependent slab optical thickness $\tau$:

$$T(\boldsymbol{\xi}) = \frac{J^+(L,\boldsymbol{\xi})}{J^+(0)} = \exp\big[-\tau(\boldsymbol{\xi})\big]. \tag{5.17}$$

The expectation of transmittance moments $\mathbb{E}[T^m]$ is solved by integrating over the stochastic domain

$$\mathbb{E}[T^m] = \int_{\boldsymbol{\xi}} \exp\big[-\tau(\boldsymbol{\xi})\big]p(\boldsymbol{\xi})d\boldsymbol{\xi} \tag{5.18}$$

using a method such as random sampling or stochastic collocation. For lack of an analytic expression to integrate $\Sigma_t(x,\omega)$ ($\Sigma_t(x,\omega) = \Sigma_a(x,\omega) \,\forall\, \Sigma_s = 0$) over $x$ yielding

$\tau(\omega)$,

$$
\begin{aligned}
\tau(\boldsymbol{\xi}) &= \int_0^L \Sigma_t(x, \boldsymbol{\xi}) dx \\
&= \int_0^L \sigma_t \exp\left[\langle g \rangle + \sum_{k=1}^K \sqrt{\gamma_k} u_k(x) \xi_k(\boldsymbol{\xi})\right] dx,
\end{aligned}
\tag{5.19}
$$

we perform this integral numerically:

$$
\tau(\boldsymbol{\xi}) \approx \sigma_t \exp\left[\langle g \rangle\right] \sum_{q=1}^{Q_x} w^{(q)} \exp\left[\sum_{k=1}^K \sqrt{\gamma_k} u_k\left(x^{(q)}\right) \xi_k(\boldsymbol{\xi})\right],
\tag{5.20}
$$

where $Q_x$ is spatial integration quadrature order, $w^{(q)}$ is the weight of quadrature term $q$, and $x^{(q)}$ is the $x$ value of quadrature node $q$. As discussed in Section 3.1.3.2, $u_k(x)$ is not a smooth eigenfunction, but the eigenfunction yielded by one of three interpolation schemes applied to eigenvector $\mathbf{u}_k$. The first "discrete" interpolation function produces a spatially discontinuous eigenfunction according to the discretization order of the Nyström solve $N_{Ny}$. The second "linear" interpolation function linearly interpolates between the discrete values and is continuous but not differentiable. The "linear" interpolation scheme defaults to the interpolation given in the Nyström theory near the edges of the slab. Finally, the "Nyström" interpolation scheme comes from the Nyström theory, and is the most accurate, but also computationally expensive. We compare the integration of Eq. (5.20) for a problem with each combination of "discrete" and "linear" interpolation schemes and Gauss-Legendre (GL) and midpoint rule (MP) numerical integration. No investigation is made of the "Nyström" interpolation scheme as it becomes computationally prohibitive with even modest values of $N_{Ny}$.

The investigation of this problem is performed by setting the correlation length and slab thickness as $\lambda_c = 1.5$ cm and $L = 5$ cm, the microscopic total cross section as $\sigma_t = \sigma_a = 2$ cm$^2$, the average atom density equal to one, $\langle N_{at} \rangle = 1$ cm$^{-3}$, and choosing the atom density variance as $v_{N_{at}} = 0.225$ cm$^{-3}$. The KL truncation order is chosen as $K = 5$ and stochastic collocation quadrature orders are set to $\mathbf{Q} = \{3, 3, 3, 3, 3\}$. The error convergence in transmittance values is first observed through semi-analytic solution of transmittance on individual realizations for the choice of Nyström discretization scheme ("discrete" or "linear"), Nyström discretization order $N_{Ny}$, numerical spatial integration scheme (GL or MP), and numerical spatial integration order $Q_x$. Next, transmittance values are solved using our transport-with-scattering implementation, and Monte Carlo

convergence is observed towards solutions generated using the semi-analytic solutions using one set of isotropic, and one set of anisotropic, stochastic collocation orders.

## 5.4.2   Numerical Spatial Integration Convergence

We solve transmittance values and plot error convergence for Gauss-Legendre (GL) and midpoint rule (MP) integration of the lognormal macroscopic cross section realizations which are used to analytically calculate transmittance for both the "discrete" and "linear" Nyström interpolating schemes. Arbitrary values are chosen for the Nyström discretization order ($N_{Ny} = 100$), the KL truncation order ($K = 5$), and the SC quadrature orders ($\mathbf{Q} = \{3, 3, 3, 3, 3\}$).

Documentation of the NymPy Python package used to generate Gauss-Legendre quadrature nodes and weights, [numpy.polynomial.legendre.leggauss()](), claims to be tested up to $Q_x = 100$; we therefore limit use of GL to a quadrature order of no greater than $Q_x = 100$. Since the functions we integrate are either discontinuous or continuous but not differentiable, approximations of the exact solutions are generated using the MP rule with $Q_x = 10,000$ for each Nyström interpolation scheme.

When using the "discrete" eigenfunction interpolation scheme exact solutions are approximated as

$$\mathbb{E}[T_{N_{NM-discrete}}] \approx \mathbb{E}_{SC,KL}[T_{N_{NM-discrete}=100,MP,Q_x=10,000}], \text{ and} \tag{5.21a}$$

$$\sqrt{\mathbb{V}[T_{N_{NM-discrete}}]} \approx \sqrt{\mathbb{V}_{SC,KL}[T_{N_{NM-discrete}=100,MP,Q_x=10,000}]}. \tag{5.21b}$$

Similarly, when using the "linear" eigenfunction interpolation scheme exact solutions are approximated as

$$\mathbb{E}[T_{N_{NM-linear}}] \approx \mathbb{E}_{SC,KL}[T_{N_{NM-linear}=100,MP,Q_x=10,000}], \text{ and} \tag{5.22a}$$

$$\sqrt{\mathbb{V}[T_{N_{NM-linear}}]} \approx \sqrt{\mathbb{V}_{SC,KL}[T_{N_{NM-linear}=100,MP,Q_x=10,000}]}. \tag{5.22b}$$

Error terms are subsequently defined:

$$\varepsilon_{\bar{x},MP(N_{NM-linear})} = \Big| \ \mathbb{E}[T_{N_{NM-linear}}] \ - \ \mathbb{E}_{SC,KL}[T_{N_{NM-linear}=100,MP}] \ \Big|, \quad (5.23\text{a})$$

$$\varepsilon_{s,MP(N_{NM-linear})} = \Big| \sqrt{\mathbb{V}[T_{N_{NM-linear}}]} - \sqrt{\mathbb{V}_{SC,KL}[T_{N_{NM-linear}=100,MP}]} \ \Big|, \quad (5.23\text{b})$$

$$\varepsilon_{\bar{x},MP(N_{NM-discrete})} = \Big| \ \mathbb{E}[T_{N_{NM-discrete}}] - \ \mathbb{E}_{SC,KL}[T_{N_{NM-discrete}=100,MP}] \Big|, \quad (5.23\text{c})$$

$$\varepsilon_{s,MP(N_{NM-discrete})} = \Big| \sqrt{\mathbb{V}[T_{N_{NM-discrete}}]} - \sqrt{\mathbb{V}_{SC,KL}[T_{N_{NM-discrete}=100,MP}]} \Big|. \quad (5.23\text{d})$$

The most converged result calculated using each method is provided in Table 5.2.

TABLE 5.2: Uncollided Flux Transmittance Values for Lognormal KL Implementation - Converged Optical Thickness Quadrature Solutions

| Solution Method | Quad. Ord. $Q_x$ | $\langle T \rangle$ | $\sqrt{v_T}$ |
|---|---|---|---|
| MP($N_{\text{NM-Linear}}$) | 10,000 | 0.000673827496 | 0.0014071572552 |
| GL($N_{\text{NM-Linear}}$) | 100 | 0.0006738267 | 0.0014071542 |
| MP($N_{\text{NM-Discrete}}$) | 10,000 | 0.000673799 | 0.001407192 |
| GL($N_{\text{NM-Discrete}}$) | 100 | 0.0006744 | 0.0014084 |

Transmittance errors due to numerical integration as defined in Eq. (5.23) are plotted in Figures 5.5 and 5.6.
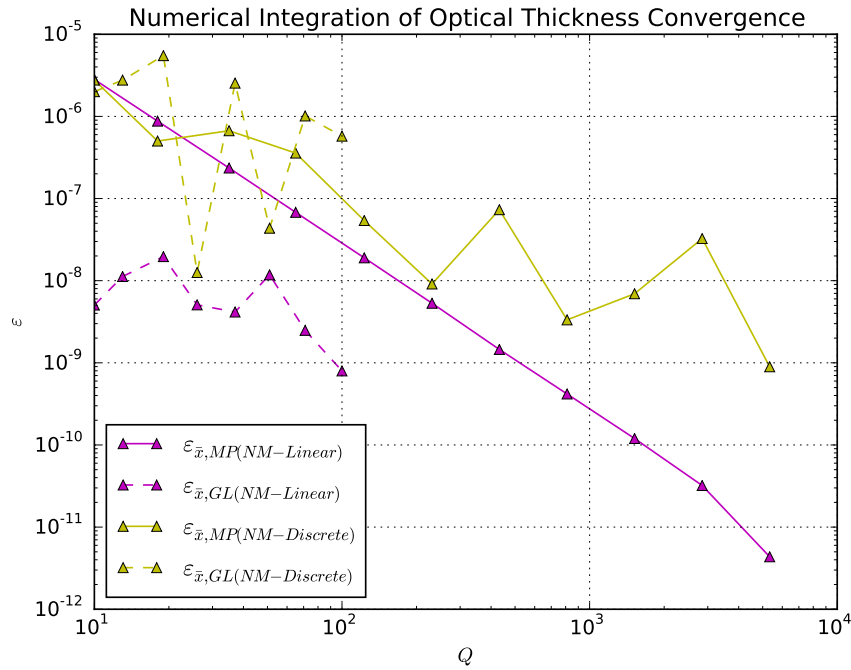
FIGURE 5.5: Uncollided Flux Mean Transmittance MC Convergence for Numerical Optical Thickness Integration Schemes using Nyström Method of Order $N_{Ny} = 100$ for Lognormal KL Implementation
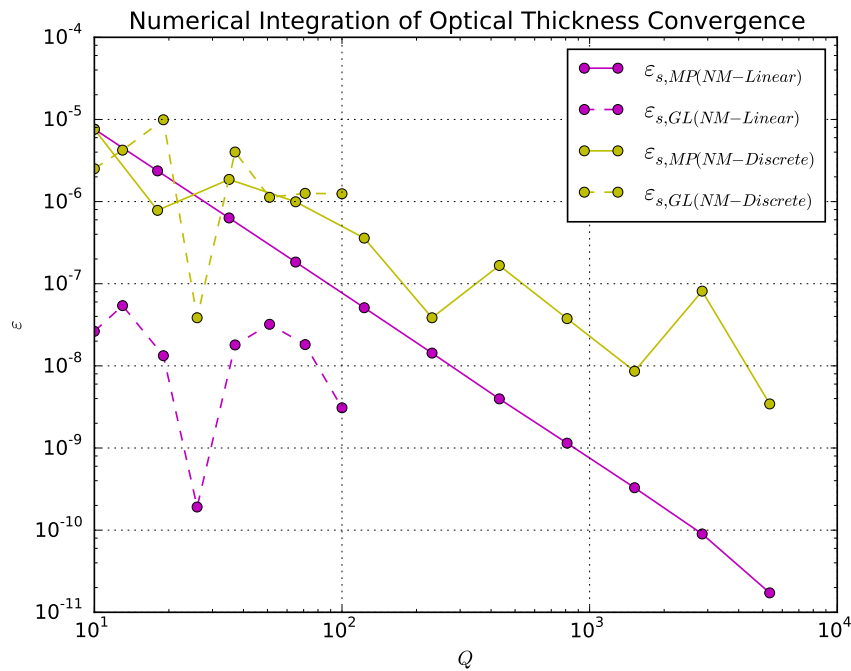


FIGURE 5.6: Uncollided Flux Standard Deviation Transmittance Convergence for Numerical Optical Thickness Integration Schemes using Nyström Method of Order $N_{Ny} = 100$ for Lognormal KL Implementation

Neither the transmittance mean nor standard deviation converges monotonically for either Nyström interpolation scheme when using Gauss-Legendre quadrature. This is not

a surprise since the integrands are either discontinuous or $C^0$ continuous. Errors produced using the GL scheme range from about $10^{-5}$ to $10^{-10}$ and therefore may or may not be sufficiently small for a specific application. Gauss-Legendre quadrature performs better when integrating over the "linear" Nyström interpolation function, which has $C^0$ continuity, than over the "discrete" Nyström interpolation function, which is discontinuous. Additionally, GL quadrature produced a smaller error in the solution for any quadrature order than MP quadrature over the $C^0$ surface. If the Nyström order $N_{Ny}$ were larger, the function would more closely approximate a smooth function, and we would expect GL quadrature to produce smaller errors than for the chosen value of $N_{Ny}$. We choose not to use the GL integration scheme for integrating the discrete lognormal macroscopic cross sections after this section, however, since the MP integration scheme integrates more reliably.

Both the transmittance mean and standard deviation converge monotonically for the "linear" Nyström interpolation scheme, though not for the "discrete" Nyström interpolation scheme, when using midpoint rule quadrature. For the "linear" interpolation scheme, the error at 5,000 samples appears to deviate from an otherwise linear convergence. This behavior is expected since the error is underestimated by the error in the approximated-as-exact solution. Though the "discrete" interpolation scheme does not show monotonic convergence, it does appear to be converging at a slower rate than when using the "linear" interpolation scheme. The "linear" Nyström interpolation scheme shows a preferable convergence behavior to the "discrete" interpolation scheme, but is about three times as expensive, such that either may be preferred for a specific problem.

### 5.4.3   Nyström Discretization Convergence

We solve transmittance values and plot error convergence for Nyström discretization order using the "linear" and "discrete" Nyström interpolation schemes. As in Section 5.4.2, the KL truncation order ($K = 5$) and SC quadrature orders ($\mathbf{Q} = \{3, 3, 3, 3, 3\}$) are chosen arbitrarily, and a midpoint rule quadrature of order $Q_x = 1000$ is chosen.

The exact solution is approximated using a Nyström discretization order of $N_{Ny} = 1000$ and approximated-as-exact transmittance moments are represented as

$$\mathbb{E}[T_{N_{NM-discrete}}] \approx \mathbb{E}_{SC,KL}[T_{N_{NM-discrete}=1000,MP,Q_x=1000}], \tag{5.24a}$$

$$\sqrt{\mathbb{V}[T_{N_{NM-discrete}}]} \approx \sqrt{\mathbb{V}_{SC,KL}[T_{N_{NM-discrete}=1000,MP,Q_x=1000}]}, \tag{5.24b}$$

$$\mathbb{E}[T_{N_{NM-linear}}] \approx \mathbb{E}_{SC,KL}[T_{N_{NM-linear}=1000,MP,Q_x=1000}], \text{ and} \tag{5.24c}$$

$$\sqrt{\mathbb{V}[T_{N_{NM-linear}}]} \approx \sqrt{\mathbb{V}_{SC,KL}[T_{N_{NM-linear}=1000,MP,Q_x=1000}]}. \tag{5.24d}$$

Error terms are subsequently defined:

$$\varepsilon_{\bar{x},N_{NM-linear}}(MP) = \left| \mathbb{E}[T_{N_{NM-linear}}] - \mathbb{E}_{SC,KL}[T_{N_{NM-linear},MP,Q_x=1000}] \right|, \tag{5.25a}$$

$$\varepsilon_{s,N_{NM-linear}}(MP)) = \left| \sqrt{\mathbb{V}[T_{N_{NM-linear}}]} - \sqrt{\mathbb{V}_{SC,KL}[T_{N_{NM-linear},MP,Q_x=1000}]} \right|, \tag{5.25b}$$

$$\varepsilon_{\bar{x},N_{NM-discrete}}(MP) = \left| \mathbb{E}[T_{N_{NM-discrete}}] - \mathbb{E}_{SC,KL}[T_{N_{NM-discrete},MP,Q_x=1000}] \right|, \tag{5.25c}$$

$$\varepsilon_{s,N_{NM-discrete}}(MP) = \left| \sqrt{\mathbb{V}[T_{N_{NM-discrete}}]} - \sqrt{\mathbb{V}_{SC,KL}[T_{N_{NM-discrete},MP,Q_x=1000}]} \right|. \tag{5.25d}$$

The most converged transmittance values calculated using each method are provided in Table 5.3.

TABLE 5.3: Uncollided Flux Transmittance Values for Lognormal KL Implementation - Converged NM Discretization Solutions

| Solution Method | Nyst. Ord. $N_{Ny}$ | $\langle T \rangle$ | $\sqrt{v_T}$ |
|---|---|---|---|
| "Linear" Interpolater | 1000 | 0.0006737411 | 0.0014070044 |
| "Discrete" Interpolater | 1000 | 0.0006737411 | 0.0014070044 |

Since the most converged results were calculated using a Nyström discretization and numerical quadrature of the same order, $N_{Ny} = Q_x = 1000$, the most converged solution of each is identical. The two interpolation schemes only produce the exact same solution when $N_{Ny} = Q_x$.

Transmittance errors due to Nyström discretization as defined in Eq. (5.25) are plotted in Figures 5.7 and 5.8.
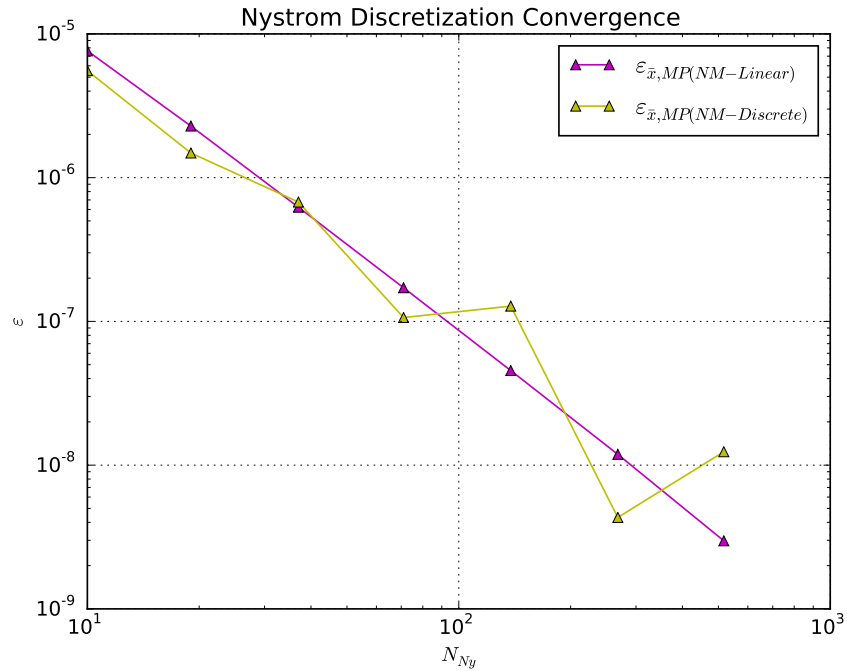


FIGURE 5.7: Uncollided Flux Mean Transmittance Convergence for Nyström Discretization Schemes for Lognormal KL Implementation
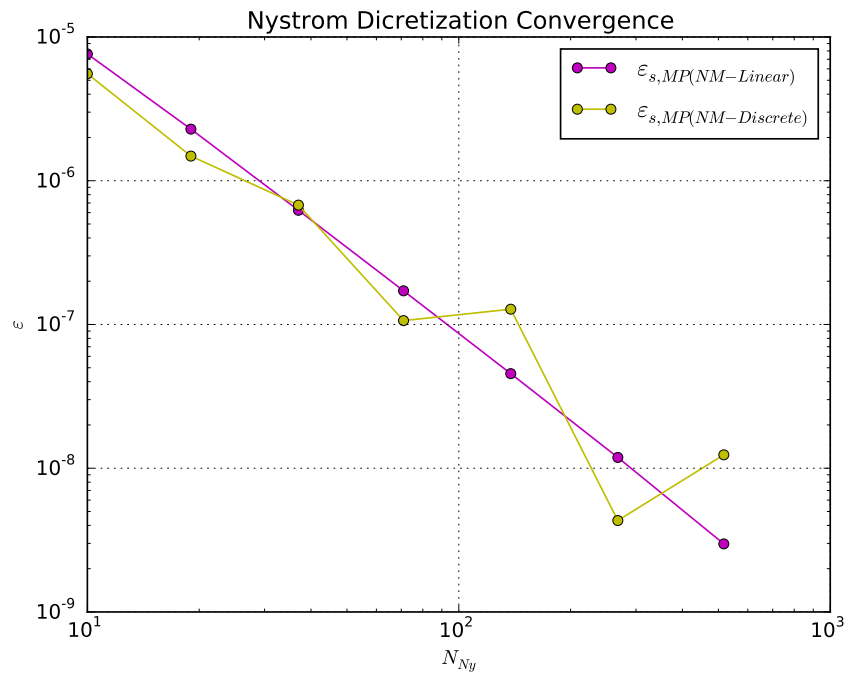


FIGURE 5.8: Uncollided Flux Standard Deviation Transmittance Convergence for Nyström Discretization Schemes for Lognormal KL Implementation

The transmittance mean and standard deviation appear to converge linearly when using the "linear" Nyström interpolation scheme, and with the same general convergence rate but not monotonically when using the "discrete" Nyström interpolation scheme. Such behavior is not surprising when performing numerical integration on a discontinuous function. As concluded in Section 5.4.2, the best choice of Nyström interpolation scheme is likely problem dependent since the "linear" interpolation scheme has preferable convergence behavior but is roughly three times more expensive.

### 5.4.4   Monte Carlo Convergence of Scattering Implementation Towards Uncollided Flux Solution

Having characterized the convergence behavior of transmittance values for an uncollided flux problem using different Nyström discretization orders and interpolation schemes and quadrature orders and rules, we now seek to use the semi-analytic uncollided flux solutions to benchmark our transport-with-scattering Monte Carlo solver.

The "linear" Nyström discretization scheme is selected with a discretization order of $N_{Ny} = 100$ and the KL truncation order is chosen as $K = 5$. Benchmark solutions, used to approximate the exact solutions, are provided using the semi-analytic solve with a midpoint rule quadrature of order $Q_x = 1000$. Based on the analysis in the previous sections, the error of these benchmark solutions for the transmittance mean and standard deviation is roughly $10^{-7}$. Error convergence is observed against these solutions for an isotropic problem with isotropic stochastic collocation (iSC) orders $\mathbf{Q} = \{3, 3, 3, 3, 3\}$ and an anisotropic problem with anisotropic stochastic collocation (aSC) orders $\mathbf{Q} = \{5, 4, 3, 2, 2\}$. A lower- and higher-order polynomial chaos expansion (PCE) order is chosen, as per the discussion in Section 3.2.3.2; the PCE orders are set to $I = 3$ and $I = 15$ respectively in the isotropic case and $I = 5$ and $I = 16$ respectively in the anisotropic case. Polynomial chaos expansion models are built using the stochastic collocation solves, such that the difference between the SC-PCE and SC solutions is due to PCE truncation error.

Exact transmittance expectation values are approximated as

$$\mathbb{E}_{iSC,KL}[T] \approx \mathbb{E}_{iSC,KL}[T_{N_{NM-linear}=100,MP,Q_x=1000}], \tag{5.26a}$$

$$\sqrt{\mathbb{V}_{iSC,KL}[T]} \approx \sqrt{\mathbb{V}_{iSC,KL}[T_{N_{NM-linear}=100,MP,Q_x=1000}]}, \tag{5.26b}$$

$$\mathbb{E}_{aSC,KL}[T] \approx \mathbb{E}_{aSC,KL}[T_{N_{NM-linear}=100,MP,Q_x=1000}], \text{ and} \tag{5.26c}$$

$$\sqrt{\mathbb{V}_{aSC,KL}[T]} \approx \sqrt{\mathbb{V}_{aSC,KL}[T_{N_{NM-linear}=100,MP,Q_x=1000}]}. \tag{5.26d}$$

Error terms are subsequently defined as

$$\varepsilon_{\bar{x},MC} = \left| \mathbb{E}_{SC,KL}[T] - \mathbb{E}_{SC,KL}[T_{MC}] \right|, \tag{5.27a}$$

$$\varepsilon_{s,MC} = \left| \sqrt{\mathbb{V}_{SC,KL}[T]} - \sqrt{\mathbb{V}_{SC,KL}[T_{MC}]} \right|, \tag{5.27b}$$

when using SC to generate solutions and similarly

$$\varepsilon_{\bar{x},MC} = \left| \mathbb{E}_{SC,KL}[T] - \mathbb{E}_{SC-PCE,KL}[T_{MC}] \right|, \tag{5.28a}$$

$$\varepsilon_{s,MC} = \left| \sqrt{\mathbb{V}_{SC,KL}[T]} - \sqrt{\mathbb{V}_{SC-PCE,KL}[T_{MC}]} \right|, \tag{5.28b}$$

when solving transmittance values from the joint SC-PCE method discussed in Section 4.3.5.

The most converged transmittance values calculated using each method are provided in Table 5.4.

TABLE 5.4: Uncollided Flux Transmittance Values for Lognormal KL Implementation - Benchmark and Full Implementation Values

| Solution Method | $N$ | $R_{SC}$ | $\langle T \rangle$ | $\sqrt{v_T}$ |
|---|---|---|---|---|
| MC(Quad($\Sigma_a(x)$),iSC) | N/A | 243 | 0.000673829 | 0.001407160 |
| MC(iSC) | $10^{10}$ | 243 | 0.0006746 | 0.00140738 |
| MC(iSC-PCE,I=3) | $10^{10}$ | 243 | 0.0006746 | 0.001407136 |
| MC(iSC-PCE,I=15) | $10^{10}$ | 243 | 0.0006746 | 0.00140738 |
| MC(Quad($\Sigma_a(x)$),iSC) | N/A | 240 | 0.000669984 | 0.002023566 |
| MC(aSC) | $10^{10}$ | 240 | 0.00067039 | 0.002023612 |
| MC(aSC-PCE,I=5) | $10^{10}$ | 240 | 0.00067039 | 0.00202318 |
| MC(aSC-PCE,I=16) | $10^{10}$ | 240 | 0.00067039 | 0.002023612 |

Transmittance errors due to MC convergence as defined in Eqs. (5.27) and (5.28) are plotted in Figures 5.9 and 5.10 for the isotropic solves and in Figures 5.11 and 5.12 for the anisotropic solves.
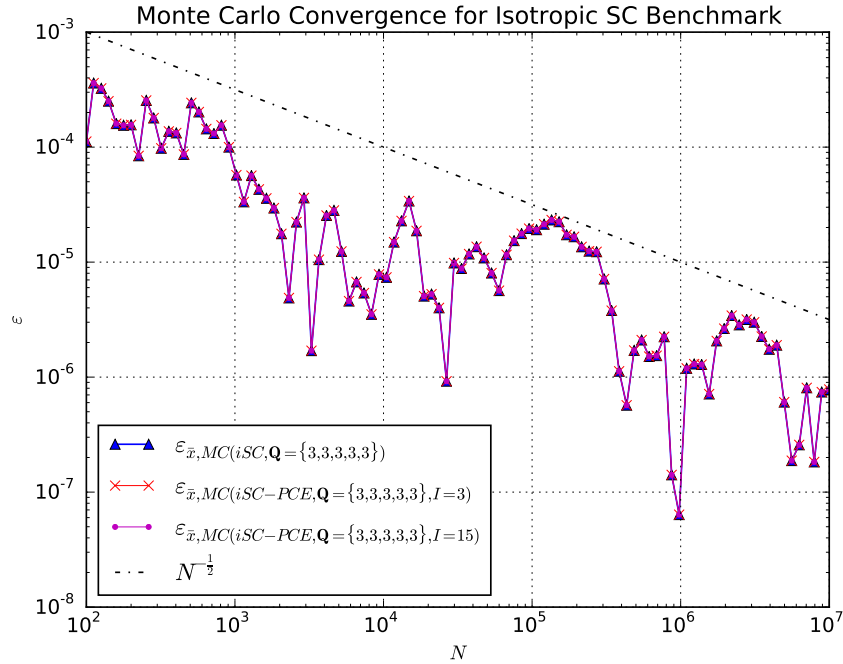


FIGURE 5.9: Uncollided Flux Transmittance Mean MC Convergence for iSC and iSC-PCE for Lognormal KL Implementation
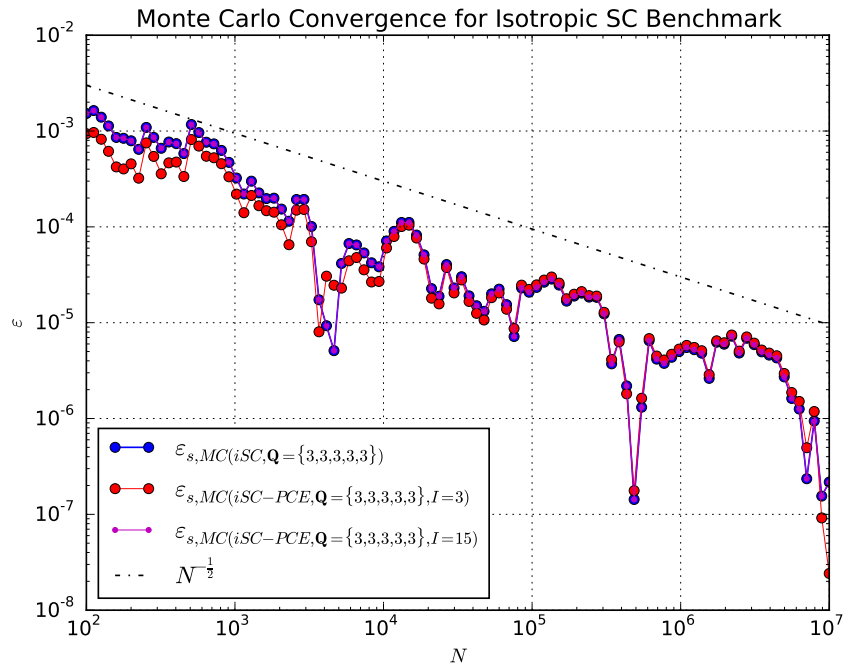


FIGURE 5.10: Uncollided Flux Transmittance Standard Deviation MC Convergence for iSC and iSC-PCE for Lognormal KL Implementation
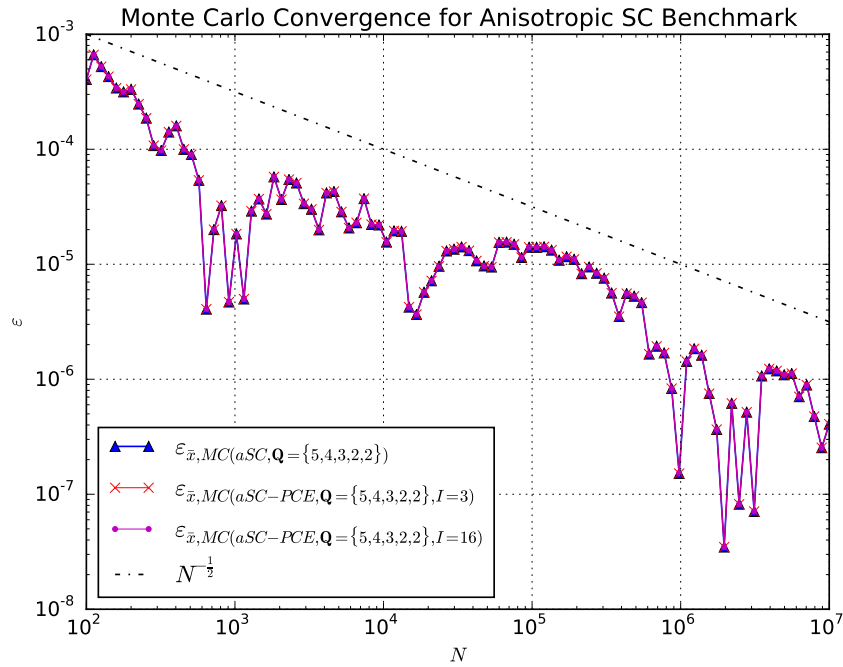
FIGURE 5.11: Uncollided Flux Transmittance Mean MC Convergence for aSC and aSC-PCE for Lognormal KL Implementation
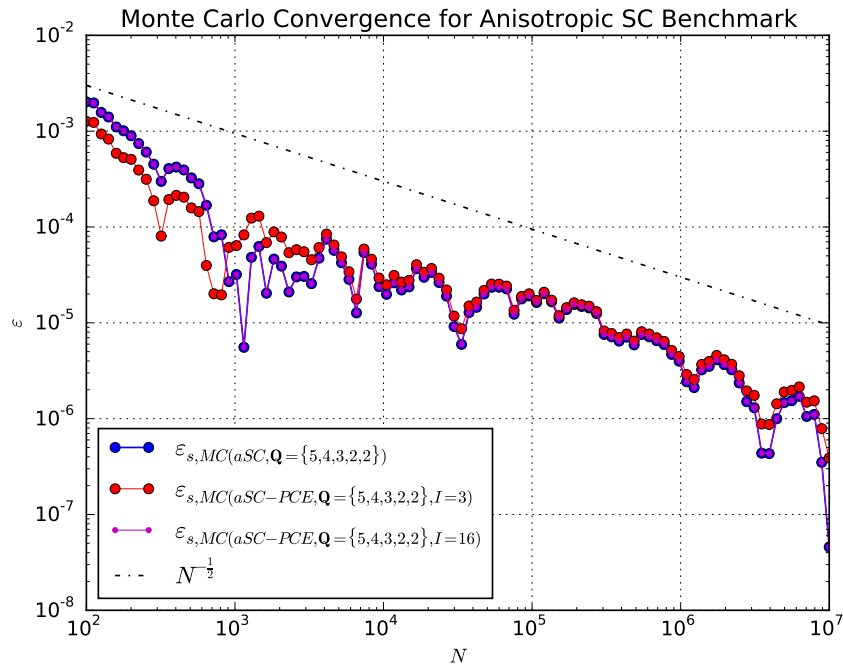


FIGURE 5.12: Uncollided Flux Transmittance Standard Deviation MC Convergence for aSC and aSC-PCE for Lognormal KL Implementation

The expected $N^{-\frac{1}{2}}$ linear convergence of the MC solver towards the semi-anaytic solution, which contains error of about an order of magnitude or less than the smallest MC error solved for, is observed in each case. Consequently, we gain confidence

in our transport-with-scattering implementation. The behavior for the isotropic and anisotropic cases is similar and is discussed here simultaneously. When solving the transmittance mean, the lower and higher order PCE models converge in exactly the same way as one another and the SC solve without building a PCE model. This is expected since the mean is represented by only the lowest order PCE term such that the mean should be the same with any truncation of the PCE. The lower and higher order PCE models do not produce the exact same solutions for the standard deviation, however. This too is expected, since all PCE terms contribute to the standard deviation, and the higher-order PCE model contains more terms. As confirmed by an examination of the numerical data, the higher-order PCE model produces exactly the same solutions as the SC solve within machine precision. The higher-order PCE model clearly captures more information from the SC solve, but also contains more PCE terms. The computational overhead of PCE operations is generally considered to be negligible compared to the cost of evaluating the physical model, suggesting that the higher-order PCE truncation should be chosen, but if the cost of operations involving the PCE is not negligible, which may be the case in problems with many stochastic dimensions $D$, the lower-order PCE may be preferred.

## 5.5 Transport with Scattering Problem

Here we demonstrate on another problem which includes particle scattering. The transmittance standard deviation is converged for each contributing error such that the overall error is converged below a chosen tolerance. Once the solver parameters have been chosen, a suite of transport results are generated including leakage values, internal flux profiles, and probability density functions (PDFs) of leakage values and selected internal flux values. All results in this section are computed using our transport-with-scattering code that has been benchmarked in Section 5.3 using the semi-infinite slab with constant scattering ratio reflectance problem and in Section 5.4 using the uncollided flux transmittance with a semi-analytic solution problem.

### 5.5.1 Problem Statement and Solution Methods

The stochastic transport problem solved here is equivalent to that stated at the beginning of this chapter (Eq. (5.1)):

$$\mu\frac{\partial\psi(x,\mu,\omega)}{\partial x} + \Sigma_t(x,\omega)\psi(x,\mu,\omega) = \frac{\Sigma_s(x,\omega)}{2}\int_{-1}^{1}d\mu'\psi(x,\mu',\omega),$$

$$0 \leq x \leq L; \qquad -1 \leq \mu \leq 1 \tag{5.29}$$

$$\psi(0,\mu) = \delta(1-\mu), \quad \mu > 0; \qquad \psi(L,\mu) = 0, \quad \mu < 0.$$

We choose a problem with a correlation length $\lambda_c = 1.5$ cm, slab thickness $L = 5$ cm, and microscopic absorption cross sections $\sigma_a = \sigma_s = 2$ cm$^2$, and choose the atom density average and variance equal to one: $\langle N_{at}\rangle = 1$ cm$^{-3}$ and $v_{N_{at}} = 1$ cm$^{-3}$. Random sampling (RS), stochastic collocation (SC), and the joint stochastic collocation polynomial chaos expansion (SC-PCE) method are used on the random variables of the Karhunen-Loéve (KL) expansion in the stochastic domain and the Monte Carlo (MC) method with Woodcock sampling is used to solve in the physical domain. Solver parameters are chosen based on a convergence study of the transmittance standard deviation, $\sqrt{\mathbb{V}[T]}$, for which a 3% relative error is chosen as the tolerance. This relative error is defined as

$$\varepsilon_{s_{rel},NM-Discrete,KL,MC,SC} = \frac{\sqrt{\mathbb{V}[T]} - \sqrt{\mathbb{V}_{SC,KL,NM-Discrete}[T_{MC}]}}{\sqrt{\mathbb{V}[T]}}, \tag{5.30}$$

where SC may also be the joint SC and PCE solver SC-PCE. The "discrete" Nyström interpolation scheme is selected since the error produced for either Nyström scheme is expected to be negligible compared to the other errors for the tolerance chosen and the "discrete" Nyström interpolation scheme is the least expensive interpolation scheme.

The number of Monte Carlo particle histories $N$ required to converge within the chosen tolerance is first estimated by performing a MC convergence study with moderate parameters chosen for the other solution methods. The number of random samples $R$ is then similarly estimated, using a number of MC histories $N$ such that the MC error is smaller than the RS error. The Karhunen-Loève truncation order $K$ and Nyström discretization order $N_{Ny}$ required are then examined in a similar fashion. Subsequently, error convergence of isotropic stochastic collocation and a PCE model built from that iSC solve is observed, along with the error of three selected anisotropic solves. Once

parameters have been chosen, a suite of transport results are generated comparing the solutions yielded by the various solution methods.

### 5.5.2 Monte Carlo Convergence

Monte Carlo error convergence of transmittance standard deviation is studied using a KL truncation order $K = 5$, a Nyström discretization order of $N_{Ny} = 100$, and 100 random samples ($R = 100$). The problem is solved twice with different random number seeds and the most converged solution from each instance is used as the approximation for the exact solution for the other instance.

The exact solution is approximated using two different Monte Carlo solution instances ($MC_1$ and $MC_2$):

$$\sqrt{\mathbb{V}_{RS,KL,NM}[T_{MC_1}]} \approx \sqrt{\mathbb{V}_{RS,KL,NM}[T_{MC_1,N=10^7}]}, \quad (5.31a)$$

$$\sqrt{\mathbb{V}_{RS,KL,NM}[T_{MC_2}]} \approx \sqrt{\mathbb{V}_{RS,KL,NM}[T_{MC_2,N=10^7}]}. \quad (5.31b)$$

Relative errors are defined by comparing solutions using one MC instance against the most converged value of the other instance:

$$\varepsilon_{s_{rel},MC_1(RS,KL,NM)} = \frac{\left| \sqrt{\mathbb{V}_{RS,KL,NM}[T_{MC_2}]} - \sqrt{\mathbb{V}_{RS,KL,NM}[T_{MC_1,N<10^7}]} \right|}{\sqrt{\mathbb{V}_{RS,KL,NM}[T_{MC_2}]}}, \quad (5.32a)$$

$$\varepsilon_{s_{rel},MC_2(RS,KL,NM)} = \frac{\left| \sqrt{\mathbb{V}_{RS,KL,NM}[T_{MC_1}]} - \sqrt{\mathbb{V}_{RS,KL,NM}[T_{MC_2,N<10^7}]} \right|}{\sqrt{\mathbb{V}_{RS,KL,NM}[T_{MC_1}]}}. \quad (5.32b)$$

The most converged transmittance standard deviations are provided in Table 5.5.

TABLE 5.5: Transport with Scattering Transmittance Standard Deviation for Lognormal KL Implementation - Converged MC Solutions

| Solution Method | Num. Part. $N$ | $\sqrt{v_T}$ |
|---|---|---|
| $MC_1(RS,KL,NM)$ | $10^7$ | 0.0312574 |
| $MC_2(RS,KL,NM)$ | $10^7$ | 0.0312335 |

Transmittance standard deviation error due to MC convergence as defined in Eq. (5.32) are plotted in Figure 5.13 along with an $N^{-\frac{1}{2}}$ line based on the expected MC convergence rate which has been positioned to function as an estimate of the expected MC convergence for this problem.
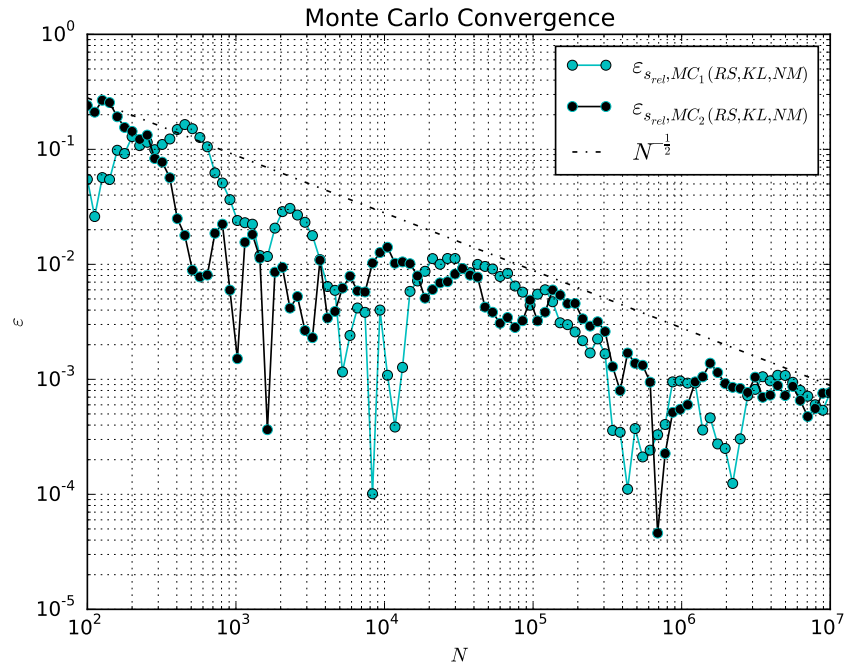


FIGURE 5.13: Transport with Scattering MC Convergence for Lognormal KL Implementation

Though the error for any number of particle histories may be larger or smaller than the expected error for that number due to statistical variation, the expected $N^{-\frac{1}{2}}$ Monte Carlo convergence rate for each error is observed. Using the plotted approximate convergence line, we choose $N = 1.6 \times 10^5$ histories, yielding a relative error of approximately $7 \times 10^{-3}$, for further use in error analysis.

### 5.5.3  Random Sampling Convergence

Random sampling error convergence of transmittance standard deviation is studied using a KL truncation order $K = 5$, a Nyström discretization order of $N_{Ny} = 100$, and the number of Monte Carlo particle histories chosen in the previous section, $N = 1.6 \times 10^5$. The problem is solved twice with different random sampling random number seeds and the most converged solution from each instance is used as the approximation for the exact solution for the other instance.

The exact solution is approximated using two different random sampling solution instances ($RS_1$ and $RS_2$):

$$\sqrt{\mathbb{V}_{RS_1(KL,NM)}[T_{MC}]} \approx \sqrt{\mathbb{V}_{RS_1(KL,NM),R=5\times10^5}[T_{MC}]}, \tag{5.33a}$$

$$\sqrt{\mathbb{V}_{RS_2(KL,NM)}[T_{MC}]} \approx \sqrt{\mathbb{V}_{RS_2(KL,NM),R=5\times10^5}[T_{MC}]}. \tag{5.33b}$$

Relative errors are defined by comparing solutions using one RS instance against the most converged value of the other instance:

$$\varepsilon_{s_{rel},RS_1(MC,KL,NM)} = \frac{\left|\sqrt{\mathbb{V}_{RS_2(KL,NM)}[T_{MC}]} - \sqrt{\mathbb{V}_{RS_1(KL,NM),R<5\times10^5}[T_{MC}]}\right|}{\sqrt{\mathbb{V}_{RS_2(KL,NM)}[T_{MC}]}},$$

$$\tag{5.34a}$$

$$\varepsilon_{s_{rel},RS_2(MC,KL,NM)} = \frac{\left|\sqrt{\mathbb{V}_{RS_1(KL,NM)}[T_{MC}]} - \sqrt{\mathbb{V}_{RS_2(KL,NM),R<5\times10^5}[T_{MC}]}\right|}{\sqrt{\mathbb{V}_{RS_1(KL,NM)}[T_{MC}]}}.$$

$$\tag{5.34b}$$

The most converged transmittance standard deviations are provided in Table 5.6.

TABLE 5.6: Transport with Scattering Transmittance Standard Deviation for Lognormal KL Implementation - Converged RS Solutions

| Solution Method | Num. Samp. $R$ | $\sqrt{v_T}$ |
|---|---|---|
| $RS_1$(MC,KL,NM) | $10^6$ | 0.03449 |
| $RS_2$(MC,KL,NM) | $10^6$ | 0.03429 |

Transmittance standard deviation error due to RS convergence as defined in Eq. (5.34) is plotted in Figure 5.14 along with an $R^{-\frac{1}{2}}$ line based on the expected RS convergence rate which has been positioned to function as an estimate of the expected RS error for this problem.
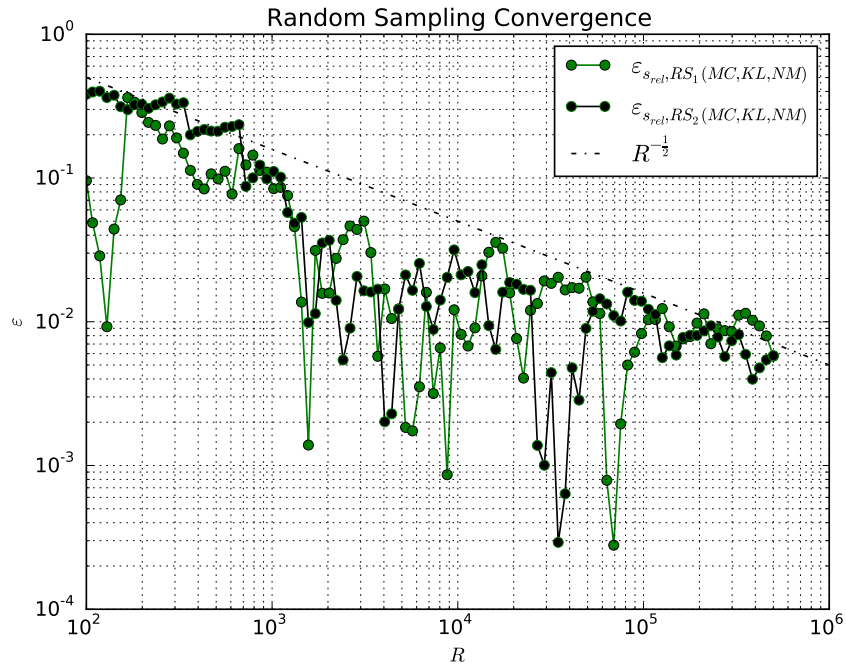
FIGURE 5.14: Transport with Scattering RS Convergence for Lognormal KL Implementation

Though the error for any number of random samples may be smaller than the expected error for that number due to statistical variation, the expected $R^{-\frac{1}{2}}$ random sampling convergence rate for each error is observed. Using the plotted approximate convergence line, we choose $R = 2 \times 10^5$ histories, yielding a relative error of approximately $1 \times 10^{-2}$, for use in further error analysis.

### 5.5.4   Karhunen-Loève Truncation Convergence

Karhunen-Loève error convergence of transmittance standard deviation is studied using a Nyström discretization order of $N_{Ny} = 100$ and the number of Monte Carlo particle histories and random samples chosen in the previous sections:  $N = 1.6 \times 10^5$ and $R = 2 \times 10^5$.

The exact solution is approximated using $K = 10$:

$$\sqrt{\mathbb{V}_{KL(RS,NM)}[T_{MC}]} \approx \sqrt{\mathbb{V}_{KL(RS,NM),K=10}[T_{MC}]}. \tag{5.35}$$

The relative error is subsequently defined:

$$\varepsilon_{s_{rel},KL(RS,MC,NM)} = \frac{\left|\sqrt{\mathbb{V}_{KL(RS,NM)}[T_{MC}]} - \sqrt{\mathbb{V}_{KL(RS,NM),K<10}[T_{MC}]}\right|}{\sqrt{\mathbb{V}_{KL(RS,NM)}[T_{MC}]}}. \quad (5.36)$$

The most converged transmittance standard deviation value is provided in Table 5.7.

TABLE 5.7: Transport with Scattering Transmittance Standard Deviation for Lognormal KL Implementation - Converged KL Solution

| Solution Method | KL Trun. Ord. $K$ | $\sqrt{v_T}$ |
|---|---|---|
| KL(RS,MC,NM) | 10 | 0.03322 |

Transmittance standard deviation error due to KL truncation convergence as defined in Eq. (5.36) is plotted in Figure 5.15.
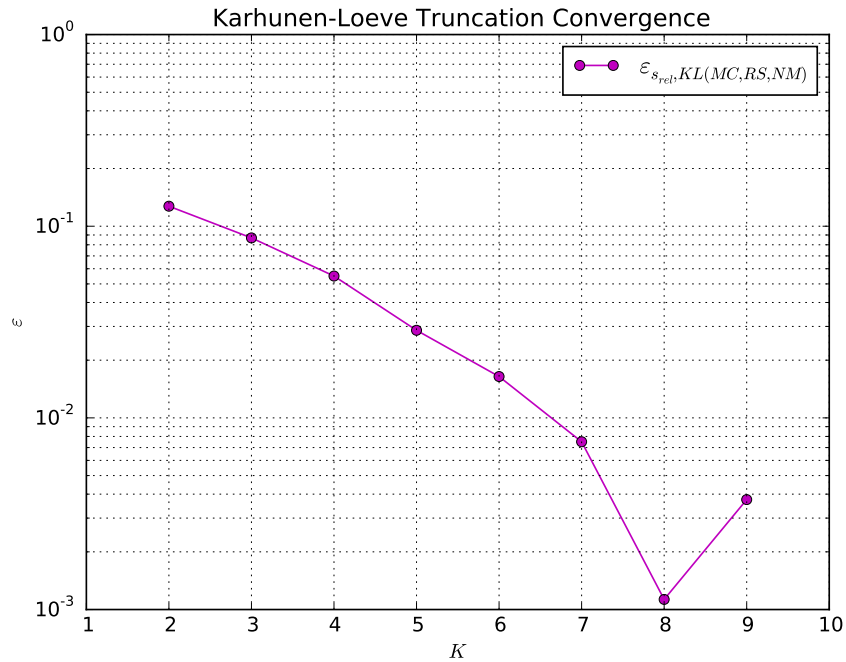


FIGURE 5.15: Transport with Scattering KL Truncation Convergence for Lognormal KL Implementation

Until MC and RS error begin to dominate ($< 1.5 \times 10^{-2}$), monotonic and possibly linear convergence is observed. We choose a KL truncation order of $K = 7$ and estimate that the error at this KL truncation order is about $8 \times 10^{-3}$. Though the error here is dominated by MC and RS error, we consider $8 \times 10^{-3}$ to be a decent estimation of

the error for $K = 7$ based on the observed convergence trend for the lower-order KL truncation orders.

### 5.5.5 Nyström Discretization Convergence

Nyström discretization error convergence of transmittance standard deviation using the "discrete" Nyström interpolation scheme is studied using the chosen number of particle histories, random samples, and KL truncation order: $N = 1.6 \times 10^5$, $R = 2 \times 10^5$, and $K = 7$.

The exact solution is approximated using $N_{Ny} = 300$:

$$\sqrt{\mathbb{V}_{NM(RS,KL)}[T_{MC}]} \approx \sqrt{\mathbb{V}_{NM(RS,KL),N_{Ny}=300}[T_{MC}]}. \tag{5.37}$$

The relative error is subsequently defined:

$$\varepsilon_{s_{rel},NM(RS,MC,KL)} = \frac{\left| \sqrt{\mathbb{V}_{NM(RS,KL)}[T_{MC}]} - \sqrt{\mathbb{V}_{NM(RS,KL),N_{Ny}<300}[T_{MC}]} \right|}{\sqrt{\mathbb{V}_{NM(RS,KL)}[T_{MC}]}}. \tag{5.38}$$

The most converged transmittance standard deviation value is provided in Table 5.8

TABLE 5.8: Transport with Scattering Transmittance Standard Deviation for Lognormal KL Implementation - Converged NM Solution

| Solution Method | Ny Disc. Ord. $N_{Ny}$ | $\sqrt{v_T}$ |
|---|---|---|
| NM(RS,MC,KL) | 300 | 0.03347 |

Transmittance standard deviation error due to Nyström discretization order as defined in Eq. (5.38) is plotted in Figure 5.16.
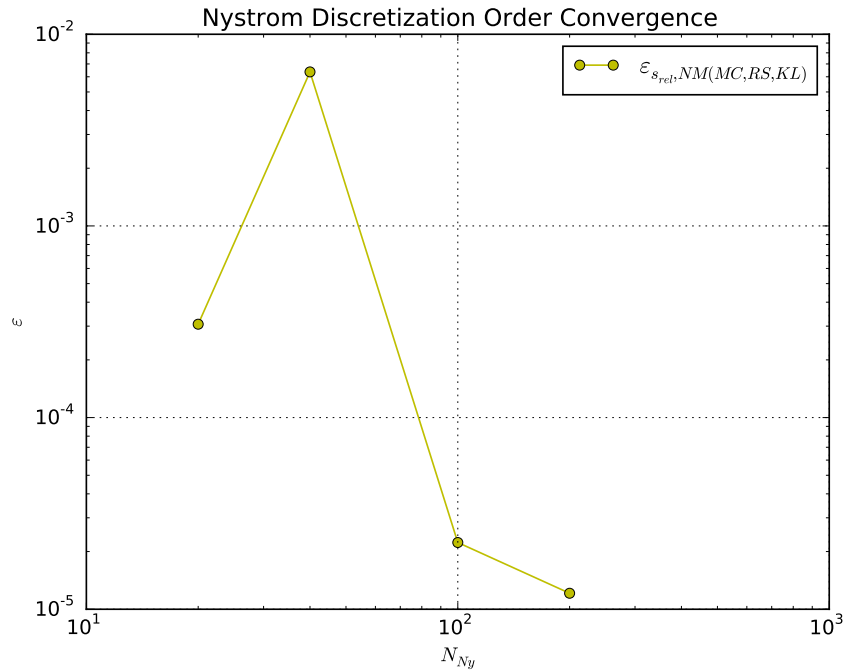
FIGURE 5.16: Transport with Scattering NM Discretization Convergence for Lognormal KL Implementation

For all relative error data points computed, relative errors are observed that are smaller than the cumulative error estimate of the other methods ( $2.5 \times 10^{-2}$). Expecting the convergence behavior of the Nyström discretization to be similar to that shown in Figure 5.8 and assuming that the Nyström error at $N_{Ny} = 20$ is in fact equal to error of the other solution methods involved in this solve $(2.5 \times 10^{-2})$, we conservatively estimate the Nyström error to be equal to or less than $2 \times 10^{-3}$.

### 5.5.6 SC and SC-PCE Convergence

Stochastic collocation and the joint stochastic collocation and polynomial choas expansion error convergence of transmittance standard deviation is studied using the chosen number of particle histories, KL truncation order, and Nyström discretization order: $N = 1.6 \times 10^5$, $K = 7$, and $N_{Ny} = 100$. Error convergence is observed by increasing the SC quadrature order in each dimension using isotropic SC (iSC) and SC-PCE (iSC-PCE). The relative error is then plotted for three selected anisotropic SC sets of quadrature orders.

The exact solution is approximated using iSC with $\mathbf{Q} = \{7, 7, 7, 7, 7, 7, 7\}$:

$$\sqrt{\mathbb{V}_{SC(KL,NM)}[T_{MC}]} \approx \sqrt{\mathbb{V}_{SC(KL,NM),\mathbf{Q}=\{7,7,7,7,7,7,7\}}[T_{MC}]}. \tag{5.39}$$

Relative errors are subsequently defined:

$$\varepsilon_{s_{rel},SC(MC,KL,NM)} = \frac{\left|\sqrt{\mathbb{V}_{SC(KL,NM)}[T_{MC}]} - \sqrt{\mathbb{V}_{SC(KL,NM),\mathbf{Q}}[T_{MC}]}\right|}{\sqrt{\mathbb{V}_{SC(KL,NM)}[T_{MC}]}}, \tag{5.40a}$$

$$\varepsilon_{s_{rel},SC-PCE(MC,KL,NM)} = \frac{\left|\sqrt{\mathbb{V}_{SC(KL,NM)}[T_{MC}]} - \sqrt{\mathbb{V}_{SC-PCE(KL,NM),\mathbf{Q},I}[T_{MC}]}\right|}{\sqrt{\mathbb{V}_{SC(KL,NM)}[T_{MC}]}}. $$
$$\tag{5.40b}$$

The most converged iSC and iSC-PCE transmittance standard deviation values are provided in Table 5.9.

TABLE 5.9: Transport with Scattering Transmittance Standard Deviation for Lognormal KL Implementation - Converged iSC and iSC-PCE Solutions

| Solution Method | iSC Ord. $Q$ | PCE Trunc. Ord. $I$ | $\sqrt{v_T}$ |
|---|---|---|---|
| iSC(MC,KL,NM) | 6 | N/A | 0.033824 |
| iSC-PCE(MC,KL,NM) | 6 | 6 | 0.033820 |

Isotropic SC and SC-PCE solutions were generated from the same SC solutions such that the difference in the values is due to PCE truncation error. The solution generated using iSC is used as the approximated-as-exact solution in each case when calculating relative error for SC and SC-PCE solutions.

Transmittance standard deviation error due to SC and SC-PCE quadrature and truncation orders as defined in Eq. (5.40) are plotted in Figure 5.17.
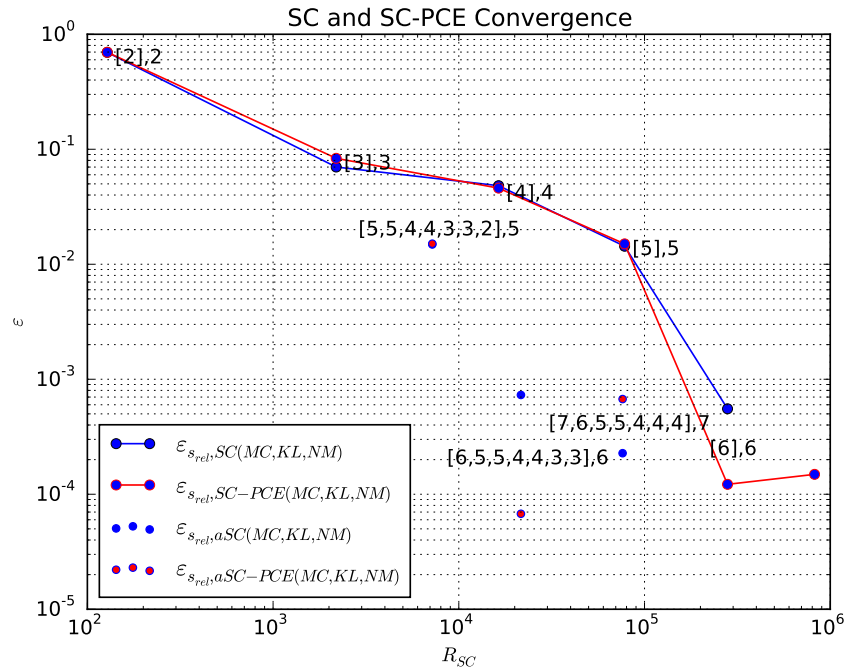
FIGURE 5.17: Transport with Scattering SC and SC-PCE Convergence for Lognormal KL Implementation

Until the error of other system parameters begin to dominate ( $1.7 \times 10^{-2}$) a monotonic convergence is observed for which the SC-PCE solutions are only minimally different than the SC solutions. Other than the very crude solution at $\mathbf{Q} = \{2, 2, 2, 2, 2, 2, 2\}$ and before the error of other system parameters begin to dominate the convergence rate appears to be exponential, as expected for SC. No relative error estimate is provided for iSC with $\mathbf{Q} = \{7, 7, 7, 7, 7, 7, 7\}$ since that solve is used to approximate the exact solution; the error reported for iSC-PCE using this collocation grid provides an estimate of the PCE truncation error.

The quadrature orders chosen for the three anisotropic solves were chosen arbitrarily based on some intuition of what orders might provide an efficient solve. In isotropic and anisotropic cases where the MC, KL, and NM errors dominate the corresponding SC and SC-PCE values show less agreement. We hypothesize that the PCE model is therefore rather sensitive to the solutions at the collocation points, and expect the PCE error to increase as soon as the error from the other system solution methods is greater than the SC error.

The error for the isotropic case at $\mathbf{Q} = \{5, 5, 5, 5, 5, 5, 5\}$ is about $1.4 \times 10^{-2}$. We expect the error at $\mathbf{Q} = \{6, 5, 5, 4, 4, 3, 3\}$ to be less than the error of the other solution methods,

and estimate the relative error at a conservative value of $7 \times 10^{-3}$.

### 5.5.7 Summary of Convergence Relative Errors

Error due to the number of Monte Carlo (MC) particle histories in the physical solve; the Karhunen-Loève (KL) truncation and Nyström method (NM) discretization in modeling of random processes; and the number of samples, quadrature orders, and polynomial chaos truncation (PCE) order in the random sampling (RS), stochastic collocation (SC), and joint SC-PCE solves in the stochastic domain is summarized in Table 5.10. Columns represent five distinct combinations of solution methods for the problem by specifying what is different, the solver in the stochastic domain, whereas rows display the estimated error for each solver involved in that combination of solver methods.

TABLE 5.10: Transport with Scattering Summary of Estimated Transmittance Standard Deviation Relative Errors for Lognormal KL Implementation

|  | RS | iSC | iSC-PCE | aSC | aSC-PCE |
|---|---|---|---|---|---|
| MC | $7 \times 10^{-3}$ | $7 \times 10^{-3}$ | $7 \times 10^{-3}$ | $7 \times 10^{-3}$ | $7 \times 10^{-3}$ |
| KL | $8 \times 10^{-3}$ | $8 \times 10^{-3}$ | $8 \times 10^{-3}$ | $8 \times 10^{-3}$ | $8 \times 10^{-3}$ |
| NM | $2 \times 10^{-3}$ | $2 \times 10^{-3}$ | $2 \times 10^{-3}$ | $2 \times 10^{-3}$ | $2 \times 10^{-3}$ |
| RS | $1 \times 10^{-2}$ | N/A | N/A | N/A | N/A |
| SC | N/A | $1.4 \times 10^{-3}$ | N/A | $7 \times 10^{-3}$ | N/A |
| SC-PCE | N/A | N/A | $1.4 \times 10^{-2}$ | N/A | $7 \times 10^{-3}$ |
| Total | $2.7 \times 10^{-2}$ | $3.1 \times 10^{-2}$ | $3.1 \times 10^{-2}$ | $2.4 \times 10^{-2}$ | $2.4 \times 10^{-2}$ |

The transmittance standard deviation relative error for each of the sets of solution methods with the chosen parameters is about 3%. Since the cost of the physical solver is generally considered to be the most expensive part of solving a stochastic differential equation, the number of realizations required to produce the estimated errors in Table 5.10 is given in Table 5.11.

TABLE 5.11: Transport with Scattering Number of Realizations to Converge Transmittance Standard Deviation to Three Percent for Lognormal KL Implementation

|  | RS | iSC | iSC-PCE | aSC | aSC-PCE |
|---|---|---|---|---|---|
| $R$ | 200,000 | 78,125 | 78,125 | 21,600 | 21,600 |

For this problem, quantity of interest, and error tolerance, the anisotropic stochastic collocation solution method converged the QoI the most efficiently, about three times more efficiently than the isotropic stochastic collocation solution method and about ten times more efficiently than the random sampling solution method. If the error tolerance was smaller, the stochastic collocation methods are expected be even more efficient than the random sampling method, as they converge exponentially in log space whereas random sampling converges linearly. If the problem required more KL terms, however, or higher-order quadrature over each KL random variable, random sampling may be the most efficient since stochastic collocation suffers from the curse of dimensionality and thus requires additional solves with an additional number of stochastic dimensions. Because of the monotonic decrease in the contribution of KL terms, a well-chosen set of aSC quadrature orders is expected to always be more efficient than iSC quadrature order sets. It is, however, easier to study the convergence of iSC, and for this reason it may be preferred over aSC.

We have solved solution method parameters which converge the transmittance standard deviation to roughly 3%. In the following section, we solve additional transport results for this problem using the method parameters chosen here for each combination of solution methods.

### 5.5.8   Transport Results for Converged Problem

Leakage values, vis., transmittance and reflectance mean and standard deviation, are provided in Table 5.12 for each of five combinations of solution methods with parameters chosen in the previous sections.

TABLE 5.12: Transport with Scattering Leakage Values for Lognormal KL Implementation

| Solution Method | $\langle R \rangle$ | $\sqrt{v_R}$ | $\langle T \rangle$ | $\sqrt{v_T}$ |
|:---:|:---:|:---:|:---:|:---:|
| RS | 0.115139 | 0.00098 | 0.01280 | 0.03347 |
| iSC | 0.115122 | 0.00098 | 0.01291 | 0.03334 |
| iSC-PCE | 0.115122 | 0.00064 | 0.01291 | 0.03332 |
| aSC | 0.115192 | 0.00100 | 0.01284 | 0.03385 |
| aSC-PCE | 0.115192 | 0.00074 | 0.01284 | 0.03383 |

Transmittance standard deviation values agree within about 1.5%, less than our estimated error of 3%. Transmittance and reflectance mean vary across solution method combinations even less: 0.9% and 0.06%. While the absolute difference in reflectance standard deviation among our solution methods is similar in scale to the absolute difference for other leakage values, the reflectance standard deviation varies by about 56% among our solution methods. If the reflectance standard deviation is desired to be known more precisely, system paramers such as the number of particle histories $N$ could be changed. The fact that the quantity of interest we chose, transmittance standard deviation, converged within our chosen relative error tolerance while other quantities of interest did not highlights the importance of assuring convergence for all quantities truly of interest.

Mean flux values solved using tallies in each of 100 flux tally cells on each realization using random sampling and stochastic collocation solution methods are plotted for flux mean in 5.18. No values are plotted from polynomial chaos expansion models since the PCE models are generated using the SC data already plotted.
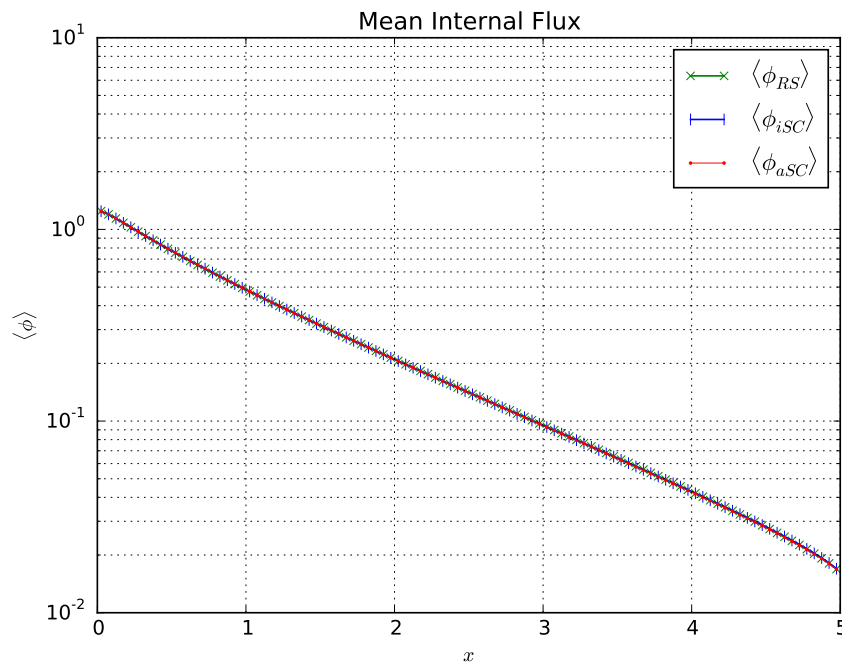


FIGURE 5.18: Transport with Scattering Mean Internal Flux Profiles for Lognormal KL Implementation

Similarly, relative standard deviation, calculated as standard deviation divided by mean, of flux solved in 100 cells using random sampling and stochastic collocation are plotted

in Figure 5.19.
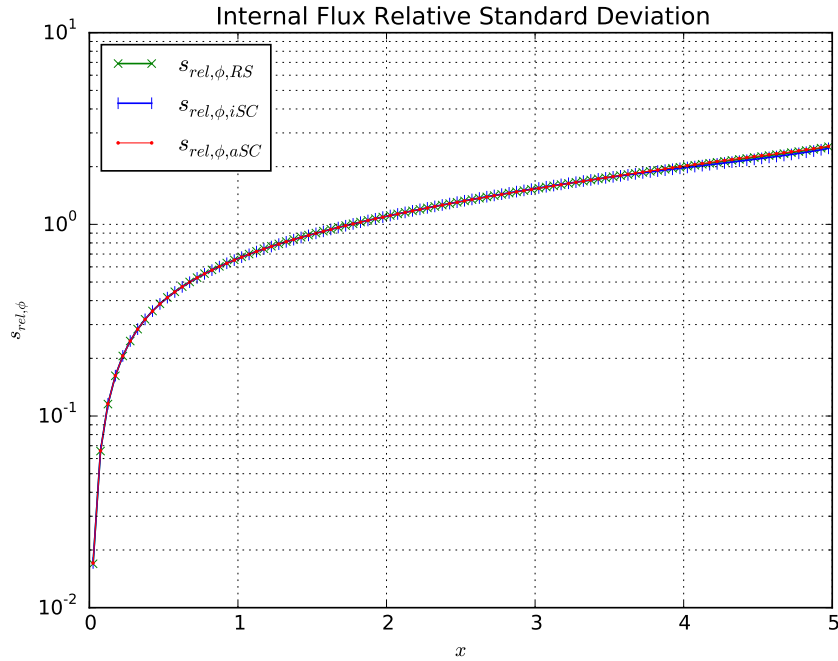


FIGURE 5.19: Transport with Scattering Internal Flux Standard Deviation Profiles for Lognormal KL Implementation

The solution methods provide very similar flux profiles for which the average flux drops off nearly linearly in log space and the relative standard deviation grows rapidly at first as particles become less forward-peaked due to scattering, then grows more slowly as flux mean decreases. The flux mean drops off nearly two orders of magnitude and the flux relative standard deviation increases from about 2% to almost 200%. While the flux profiles are very similar, the largest discrepancy in either plot exists in the relative standard deviation plot near the transmissive boundary at which the isotropic solution, which contained the largest error in the transmittance standard deviation, deviates slightly from the other solutions.

When only desiring the mean or standard deviation of a quantity of interest, there is no need to build a polynomial chaos expansion (PCE) model, since moment information is provided from a stochastic collocation (SC) solve and building a PCE model introduces PCE truncation error. Building a PCE model does, however, provide the benefits of a surrogate model, such as the ability to sample from the model cheaply to construct probability density functions (PDFs). Probability density functions generated using random sampling (RS) are expensive to construct, requiring a physical solve on an

additional realization for each additional PDF value, whereas once a PCE model is built, it can be sampled against comparatively cheaply. Here we create PDFs of leakage values and selected internal cell flux values using the random sampling method, the joint isotropic SC-PCE method, and the joint anisotropic SC-PCE method.

Probability density functions of transmittance and reflectance, generated using the parameters which converged the transmittance standard deviation to roughly 3% and sampling from PCE models $10^6$ times (compared to $2 \times 10^5$ leakage values generated by RS), are plotted in Figures 5.20 and 5.21.



FIGURE 5.20: Transport with Scattering Reflectance Probability Density Functions for Lognormal KL Implementation
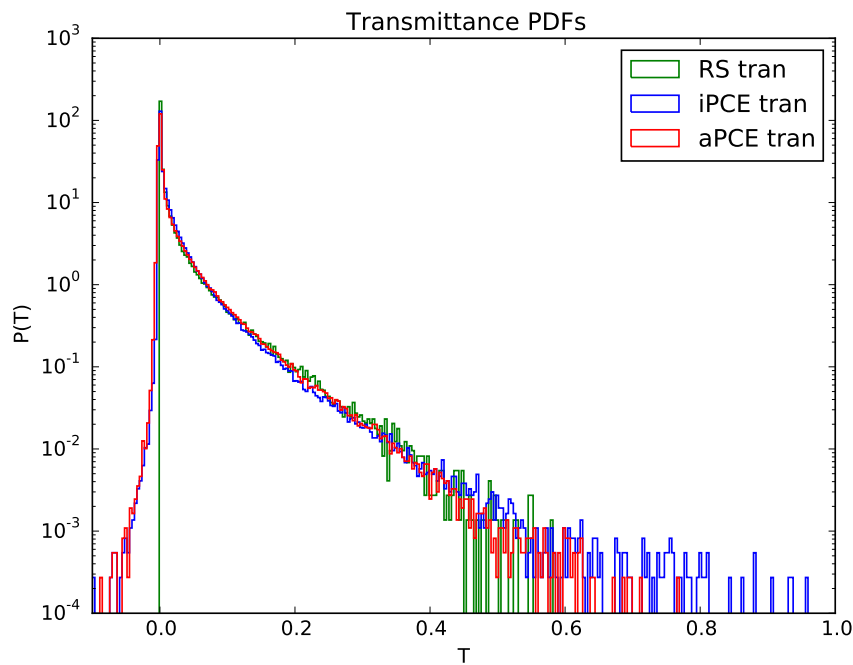
FIGURE 5.21:  Transport with Scattering Transmittance Probability Density Functions
for Lognormal KL Implementation

The isotropic and anisotropic solves generated one and three transmittance values lower
than the lowest shown and the anisotropic solve generated two transmittance values
higher than the highest shown in Figure 5.21.  The isotropic solve generated two re-
flectance values higher than the highest shown and the anisotropic solve generated one
reflectance value lower than the lowest shown in Figure 5.20.

Probability density functions generated using the different methods provide similar
shapes, though the PCE models produce negative transmittance values and the shape
of the reflectance peak generated by the PCE models is taller and less wide than the
one generated by RS.

Since these PCE models are being built to represent surfaces which are not polynomial
and are built on probability density functions with infinitely large domains, some samples
will always be misrepresentative of the true response if enough samples are taken. We
expect that the nine apparent outliers (from four million samples) described in the
paragraph preceding this one as well as some of the points that are shown but outside
of the expected bounds, are thus located due to this phenomenon. Perhaps a screening
method may be developed for rejecting samples taken in portions of the stochastic

domain of sufficiently low probability to remove samples taken from low-probability portions of the domain where the polynomial fit is very poor.

While some of the data points sampled from the PCE models are expected to be sampled from low-probability, poorly fit sections of the stochastic domain, these outliers do not account for the number of transmissive samples which were sampled as negative. It is expected that this lack of a sharp drop-off at transmittance values near zero would be improved with more converged system parameters or use of a higher PCE truncation order such that more of the SC information would be captured in the construction of the PCE model by keeping more expansion terms.

The PDFs of the reflectance generated by the PCE models do not provide flagrantly non-physical values as for the transmittance, but the shape of the peak provides less agreement with the peak generated using RS than the transmittance PDF peak. This is not altogether an unexpected result since the relative disagreement between the reflectance standard deviation produced with different methods was about 56%. The discrepancy is likely a lack of convergence of the moments of the reflectance, and solver parameters which converge the problem more would be expected to capture more of this shape. As in the case of the transmittance, a higher-order PCE truncation would likely improve the shape as well.

Probability density functions of flux in Cells 1, 50, and 100 out of 100 total cells generated using the parameters which converged the transmittance standard deviation to roughly 3% sampling from PCE models $10^6$ times (compared to $2 \times 10^5$ flux valued generated by RS), are plotted in Figures 5.22, 5.23, and 5.24.
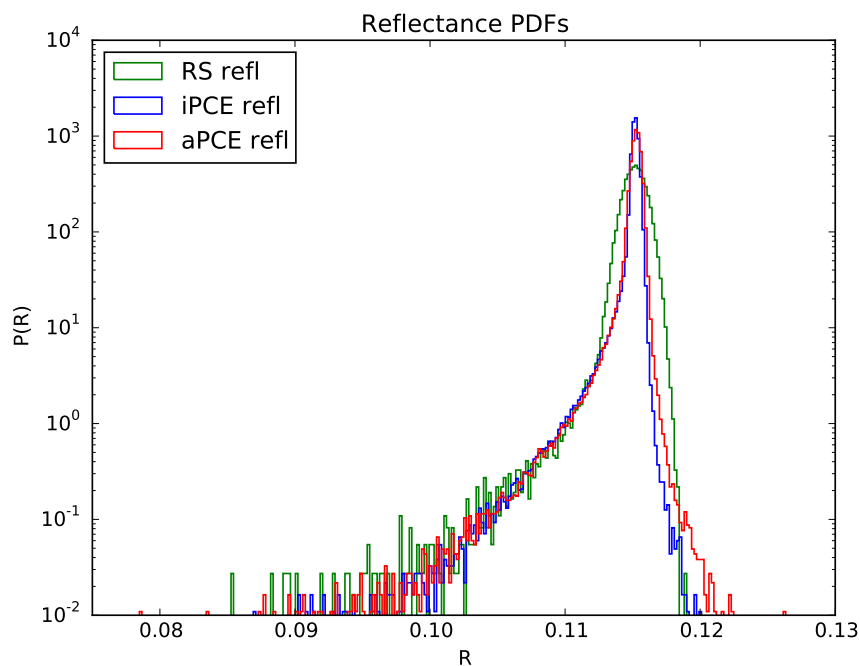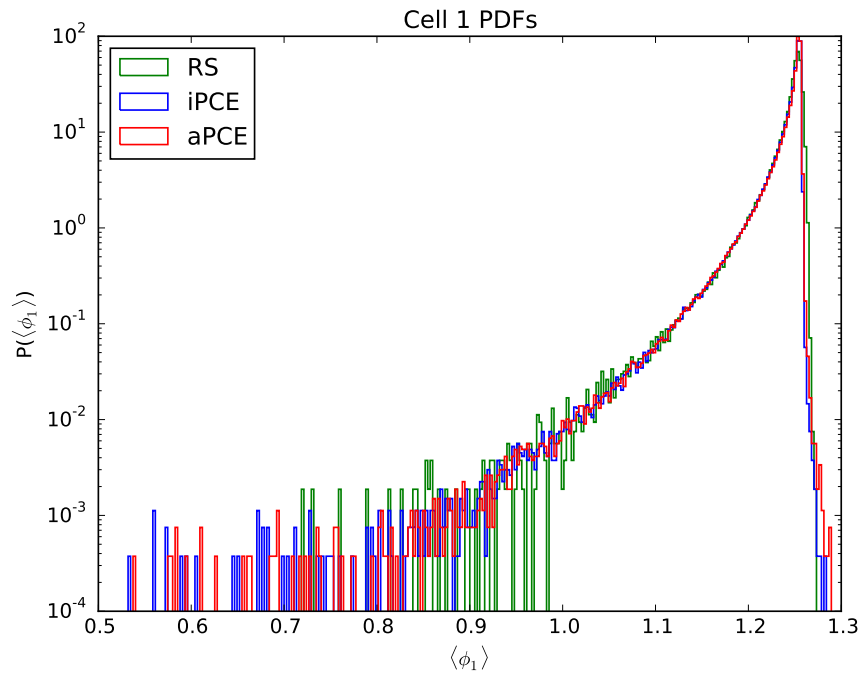
FIGURE 5.22: Transport with Scattering Internal Flux Cell 1 Probability Density Functions for Lognormal KL Implementation
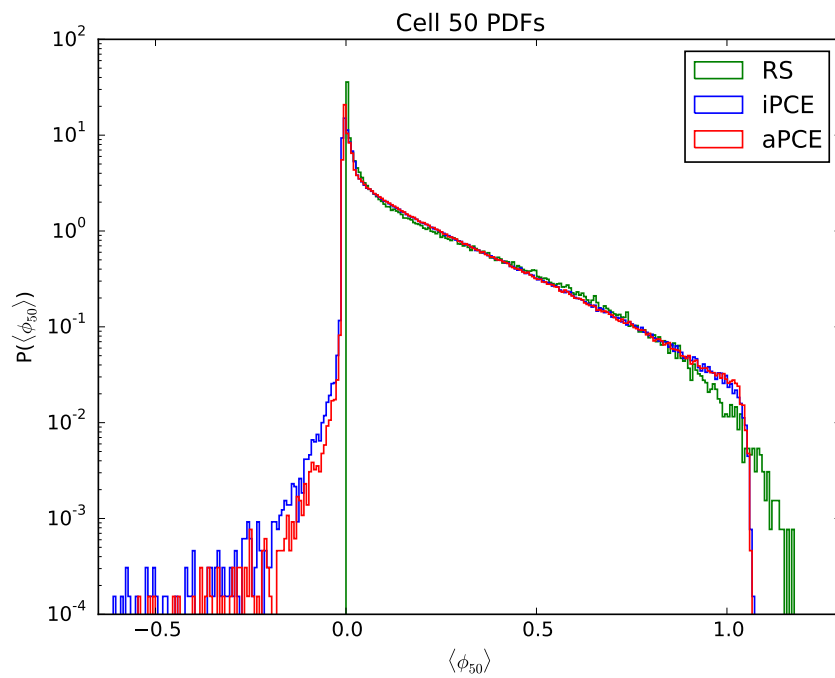


FIGURE 5.23: Transport with Scattering Internal Flux Cell 50 Probability Density Functions for Lognormal KL Implementation
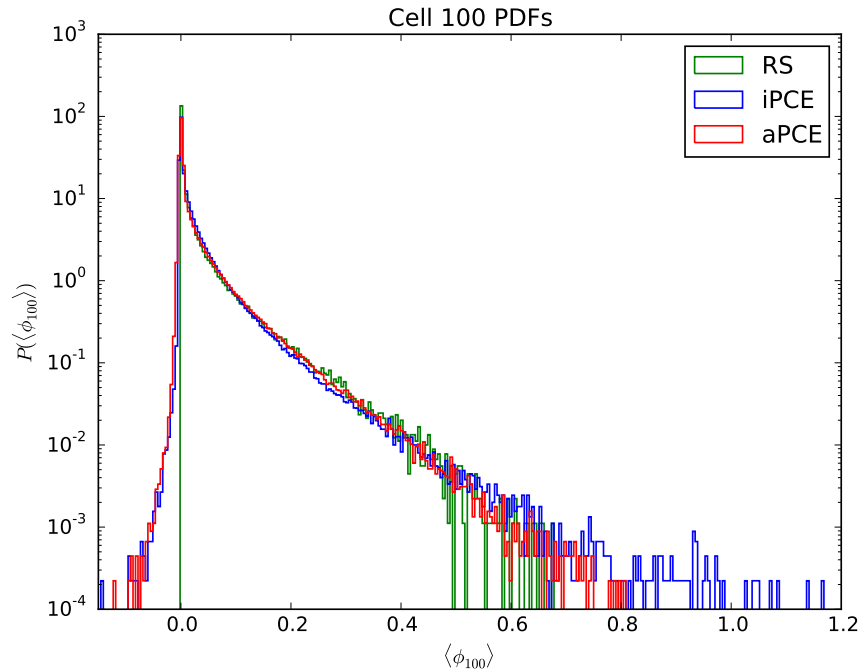
FIGURE 5.24: Transport with Scattering Internal Flux Cell 100 Probability Density Functions for Lognormal KL Implementation

A total of ten values sampled from PCEs (of six million samples) are not included in these plots as they exist beyond the bounds chosen for the PDF plots.

The PDFs of flux values in Cell 1 and Cell 100 are similar to the PDFs of reflectance and transmittance values respectively. This behavior is expected since the flux near the boundaries is related to the current at the boundaries. The flux in Cell 50 probably resembles the transmittance flux distribution more than the reflectance distribution, but is not as similar to the transmittance PDF as the PDF of flux in cell 100. As with the leakage PDFs, some PCE samples still exist which do not fit cleanly into the PDFs, some flux values are still sampled as being negative, and the shape of the RS PDF does not seem to match up exactly with the shape of the PDFs sampled from the PCE models. Screening of samples from low probability locations in the stochastic domain, solver parameters which converge errors more, and a higher PCE truncation order would likely mitigate these PDF discrepancies.

As the Karhunen-Loève expansion was transformed lognormally to remove the possibility of negative values, a lognormal transformation of the PCE may be equally as useful to remove the possibility of sampling negative leakage and flux values. Such a transformation would require less effort, since the PCE does not require transformation of

a covariance function. Such a PCE transformation would in fact only require trivial modification of coefficient generation (Eq. (3.48)) and PCE evaluation (Eq. (3.42)), and is likely to be a topic of future work.

In this chapter we demonstrate the use of a lognormal transformation of the Karhunen-Loève expansion for representation of continuously varying material properties in solving the stochastic transport equation. Stochastic collocation is used to increase solution efficiency and the polynomial chaos expansion is used to produce a surrogate model of the stochastic response which can be sampled from cheaply. Two problems with simplified physics are presented so that analysis can be performed cheaply and a full implementation of these methods can be benchmarked. A careful error convergence study is demonstrated for the transmittance standard deviation, and additional transport results are shown for the solution methods and parameters which converged the transmittance standard deviation to a chosen tolerance.

Use of the lognormal KL expansion is shown to be an effective way to represent continuously varying media while creating only purely-positive realizations. Stochastic collocation can improve the efficiency of the solve over random sampling for problems with a relatively smooth response and low stochastic dimensionality. The polynomial chaos expansion can be used to create a surrogate model of the response which can be sampled against to create PDFs of the response.

## Chapter 6

# Transport in Spatially Random, Discontinuous Cross Sections

In this chapter we solve the stochastic transport equation in slabs comprised of two heterogeneously mixed materials. Material index is modeled as a discontinuous random field and all other material properties defined as a function of the material index for each location in the slab. Such mixing arises in plasma and gas mixing in inertial confinement fusion experiments, and resolving the effects of these randomly mixed materials has significant ramifications on the attenuation of the photon beams driving the implosion and thus the yield of the reaction. This type of mixing also affects photon transport through clouds and subsequently the accuracy of weather modeling, neutron transport in liquid and gas moderator mixtures in boiling water reactors in turn affecting the neutron count of the reactor, and in other applications.

As in Chapter 5 we begin by using the Karhunen-Loève (KL) expansion to model a Gaussian random field, ensuring independence of KL random variables, and transform to model the process of interest. In this case the process of interest, material index, is spatially discontinuous consists of one of two values at each point in the slab. The mapping between the Gaussian process and the process of interest is performed using the Nataf transformation, preserving second-order statistics.

In this chapter we begin by describing the problem type to be solved, discuss several approaches to solving transport through spatially random and discontinuous materials,

121

describe modeling using the Nataf transformation with the Karhunen-Loève expansion, and examine three problems.

## 6.1   Problem Statement

In this chapter we solve the one-dimensional, mono-energetic, neutral-particle, steady-state, and isotropically scattering transport equation with either a normally incident beam boundary source or an isotropic boundary source:

$$\mu\frac{\partial\psi(x,\mu,\omega)}{\partial x} + \Sigma_t(x,\omega)\psi(x,\mu,\omega) = \frac{\Sigma_s(x,\omega)}{2}\int_{-1}^{1}d\mu'\psi(x,\mu',\omega), \tag{6.1a}$$

$$0 \leq x \leq L; \qquad -1 \leq \mu \leq 1 \tag{6.1b}$$

$$\psi(0,\mu) = \delta(1-\mu), \quad \mu > 0; \qquad \psi(L,\mu) = 0, \quad \mu < 0 \text{ or} \tag{6.1c}$$

$$\psi(0,\mu) = 2, \quad \mu > 0; \qquad \psi(L,\mu) = 0, \quad \mu < 0. \tag{6.1d}$$

We represent random macroscopic cross section $r$ as

$$\Sigma_r(x,\omega) = \Sigma_{r,z}, z(x,\omega) \in \{0,1\}, \tag{6.2}$$

where $z$ is a discrete-valued random process and denotes either Material 0 or Material 1. Materials are mixed according to Markovian statistics in this work, though mixing according to other statistical models is a topic of interest for future work.

Equation 6.1 is solved using the solution methods discussed in Chapters 2 and 3– Woodcock Monte Carlo (WMC), the Karhunen-Loève (KL) expansion, random sampling (RS), stochastic collocation (SC), and the polynomial chaos expansion (PCE)– and the approach to error analysis presented in Chapter 4. Material index is modeled with a Nataf transformation of the Karhunen-Loève expansion and KL eigenvalues and eigenvectors are solved numerically using the Nyström method. Since the KL random variables have a standard normal distribution, the probablists' Gauss-Hermite (GH) quadrature rule is used when solving with SC and probablists' Hermite polynomials are used when modeling with the PCE.

## 6.2   Binary, Markovian-mixed Materials

Materials are mixed according to Markovian statistics such that the chord lengths $\Lambda_0$ and $\Lambda_1$ over an ensemble are distributed exponentially. The probability of material $z$ for a randomly chosen position $x$ in realization $\omega$ of such materials $p_z$ is

$$p_z = \frac{\Lambda_z}{\Lambda_0 + \Lambda_1}. \tag{6.3}$$

The correlation length of the binary mixture $\lambda_c$ is solved as

$$\lambda_c = \frac{\Lambda_0 \Lambda_1}{\Lambda_0 + \Lambda_1}. \tag{6.4}$$

Transport through this problem type has been approached in a variety of ways, some of which are summarized in Ref. [66], but there is still room for more efficient solutions to a variety of problem cases. In this section we discuss several of the approaches to effecting transport through these types of material systems including a brute force method, an approximation, a closure, and another attempt at using the Karhunen-Loève expansion [39].

### 6.2.1   Chord Length Sampling for Construction of Binary, Markovian-mixed Media

The most straightforward approach to solving transport through binary, Markovian-mixed media in 1D is by randomly sampling from the stochastic domain by constructing realizations of such media and solving transport results on a large ensemble of realizations. This approach is reliable and converges towards the correct solution for a quantity of interest, but the random sampling convergence rate, $R^{-\frac{1}{2}}$, is not particularly fast, especially when requiring error convergence within a small tolerance. Additionally, while creating realizations of Markovian-mixed media is straightforward in 1D, the process is less simple in 2D [67] and even more so in 3D. In spite of the slow convergence rate and difficulty in multi-D of random sampling through construction of realizations in the stochastic domain, this approach has remained the most accurate solution method for problems involving one or two physical dimensions.

Chord lengths of material $z$, $\lambda_z$, obey Markovian mixing statistics about average chord length $\Lambda_z$:

$$p(\lambda_z)d\lambda_z = \frac{1}{\Lambda_z} \exp\left[-\frac{\lambda_z}{\Lambda_z}\right] d\lambda_z. \tag{6.5}$$

A chord length $\lambda_z$ of material $z$ can be sampled by transforming the probability density function in Eq. (6.5) into a cumulative density function by integrating from zero to $\lambda_z$ and sampling using a pseudo-random number $\eta \in \mathcal{U}(0, 1)$:

$$\lambda_z = \Lambda_z \ln\left(\frac{1}{\eta}\right), \quad z \in \{0, 1\}. \tag{6.6}$$

Realizations of binary, Markovian-mixed media are created in 1D by first sampling which material exists at a slab boundary by comparing a pseudo-random number to the probability of material, $p_z$, as defined in Eq. (6.3). Material chord lengths are then sampled according to Eq. (6.6) beginning at the left boundary with the material chosen to exist there and alternating materials until a material has been designated for every location in the slab. The last material segment in the slab is truncated at the slab boundary. Many realizations are created in this manner when solving transport over binary, Markovian-mixed media using random sampling in the stochastic domain and transport is solved over each realization. Four such realizations, sampled at instances of $\omega$ and for $L = 5$ cm, $\Sigma_0 = 0.5$ cm$^{-1}$, $\Sigma_1 = 1.5$ cm$^{-1}$, $p_0 = 0.5$, and $\lambda_c = 0.375$ cm, are shown in Figure 6.1.
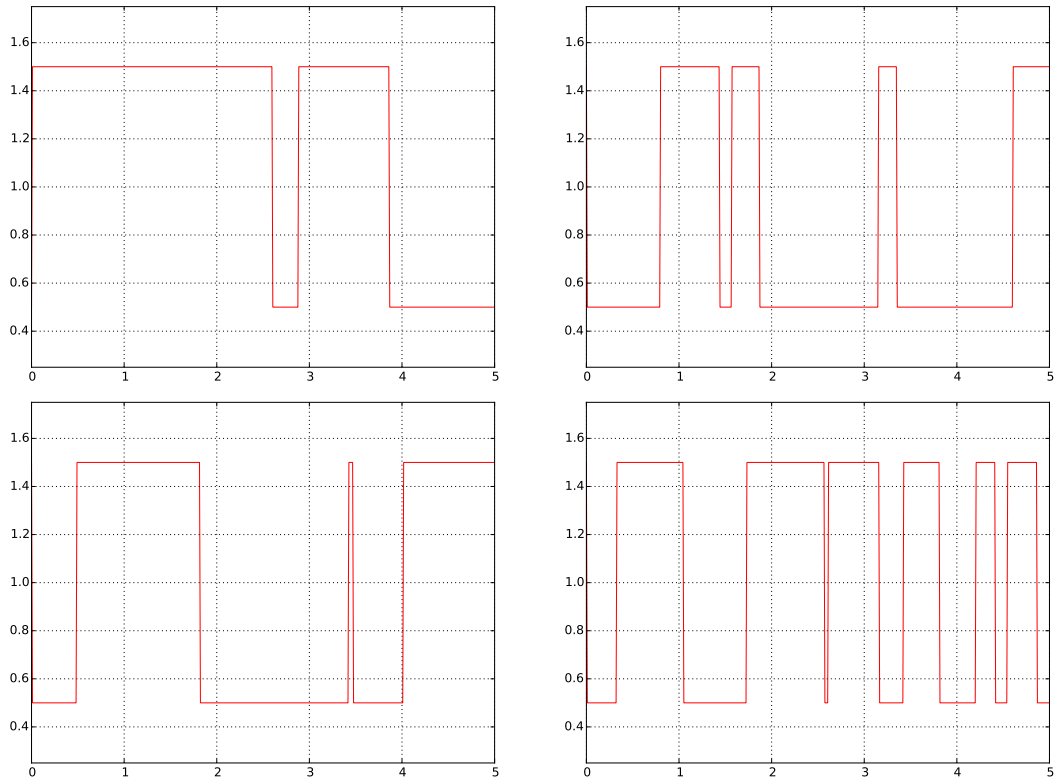
FIGURE 6.1: Four Binary, Markovian-mixed Realizations Generated Using the Chord Length Sampling Method

### 6.2.2 The Atomic Mix Approximation

While constructing realizations of binary, Markovian-mixed media is the most straight-forward way to approach solving transport over such materials, the simplest is to assume that the materials are mixed homogeneously at the atomic level. An atomic mix (AM) approximation creates one such homogeneously mixed realization with binary media averaged material properties:

$$\Sigma_r = p_0 \Sigma_{r,0} + p_1 \Sigma_{r,1}. \tag{6.7}$$

The AM approximation is cheap, requiring a transport solve on only one realization, and for this reason it is often performed when the transport solver is expensive, especially when little is known about the mixing statistics or time has not been invested to otherwise model the random media. Since only one realization is created, the AM approximation provides an estimate of response mean values, but no higher moments

or uncertainty estimates. The AM approximation does best in highly scattering media when the transport behavior approaches the diffusion limit.

### 6.2.3   The Levermore-Pomraning Closure

The Levermore-Pomraning (LP) closure, developed in the 1980s [3, 4], creates a system of two transport equations which approximate the behavior of transport through 1D binary materials with Markovian mixing. It is exact for purely absorbing materials, but the accuracy of the closure diminishes as materials become more scattering. The LP closure can be generalized to yield higher-moment response data, though the implementation is not trivial for purely absorbing materials [5], and requires an additional closure and source of error when scattering is present [6]. As a result of this, the LP closure is usually used to provide an estimate of response mean values and not to provide higher-moments of the response or uncertainty estimations. It generally produces more accurate results than the AM approximation, as long as the media are not scattering-dominant.

Shortly after the introduction of the LP closure, a Monte Carlo algorithm was developed which solves the spatially memory-less equations along with others that are slightly more accurate by retaining some memory of encountered material interfaces [68]. The LP Monte Carlo algorithm adds a third distance term to the MC streaming operation–a sampled distance to material interface. The distance to interface competes with the distance to slab boundary and distance to collision values to determine what occurs next; if the distance to interface is the shortest of these values the material simulated as present is switched and the particle continues streaming with its previous streaming parameters. Modifications to this algorithm increase accuracy by remembering some of the otherwise on-the-fly-generated material interface information.

A suite of benchmark results for the chord length sampling method of random sampling in the stochastic domain, the atomic mix approximation, and the Levermore-Pomraning closure was published in 1989 [1]. The suite was expanded to include additional response values and internal particle sources and was solved using the Monte Carlo algorithm in 2011 [2]. At least three researchers are continuing efforts to improve the Levermore-Pomraning closure in various ways, reporting the most recent advancements for each of these efforts at a recent conference [69–71].

### 6.2.4 Numerical Construction of Karhunen-Loève Random Variable PDFs

Before the efforts chronicled in the rest of this chapter to model Markovian-mixed media using the Karhunen-Loève (KL) expansion, we examined use of Eq. (3.5) to populate KL random variable PDFs using realizations created with the chord length sampling (CLS) method from which we created realizations of the random media over which to compute transport results [39]. The hope was that solving the random variable PDFs numerically based on an ensemble of the realizations faithful to the binary media statistics would allow for the creation of statistically faithful realizations using the KL expansion. If few enough KL terms were required to generate sufficiently accurate transport results, further reduced order techniques could then be applied through use of stochastic collocation and possibly the polynomial chaos expansion over the KL random variables. The method would be most useful if after examining a large number of numerically constructed KL random variable PDFs, PDFs would then be able to be constructed a priori without such computation based on input parameters. This approach to transport in binary, Markovian-mixed media showed some promise of being more accurate than the AM approximation and LP closure while having the potential to become less expensive than random sampling using the CLS method through use of stochastic collocation, but had challenges of its own.

The largest challenge to use of the KL expansion for modeling binary, Markovian-mixed media through construction of KL random variable PDFs was that realizations at times contained negative values, a quality unphysical for a nuclear cross section and unbecoming for application of Monte Carlo transport. The KL expansion preserves ensemble second-order statistics, but does not guarantee positivity of realizations–this was the motivation for the lognormal transformation in Chapter 5. Several approaches were used to attempt to solve transport results over such realizations including rejection of realizations containing any negative value, assumption of any negative cross section as being equal to zero, and a modification of the Woodcock Monte Carlo algorithm based loosely on the correlated sampling work of Rief [72, 73] in which we performed transport on the negative cross sections through use of particle weights that were allowed to be negative. The method of assuming negative cross sections as equal to zero showed promise, especially when modifying cross section mean values such that the ensemble mean for

each cross section over the ensemble was preserved to the input value. Transport results generated in this manner were more accurate than those for which the ensemble mean was not preserved, but not fully accurate. We hypothesize that preserving the ensemble variance in a similar way may further improve transport results, but chose not to pursue this avenue any further. The Monte Carlo algorithm that used particle weights to perform transport over negative cross sections produced accurate transport results when stable, but was prone to becoming unstable due to inordinately large particle weight magnitudes with even modest amounts of ensemble cross section negativity.

An additional challenge to this method was that, though KL random variables were uncorrelated, we did not yet know if they were independent, a property only guaranteed when the KL random variables are Gaussian. A further challenge was that non-Gaussian KL random variable distributions do not lend for efficient numerical integration using Gauss-Hermite quadrature; a custom quadrature should be used based on the shape of the PDF.

We had characterized the shapes of the PDFs enough to propose an a priori expectation of the shape of the PDFs consisting of a Gaussian distribution and two delta functions for which each delta function corresponds to the case of a realization containing only one material or the other and the Gaussian distribution approximates the shape of the PDF when both materials are present. The height of each delta function in the constructed PDF is solved by attaining the probability that the first chord length of either material is at least as long as the slab using Eq. (6.5) and the value at which the delta function is located is solved by sampling the value on that trivial realization using Eq. (3.5). The mean and variance of the Gaussian is then solved by integrating over the PDF and enforcing that the PDF is zero-mean and unit-variance. This approximation is not exact, but may be sufficient to create an a priori approximation of the KL random variable PDFs for producing small errors in transport results. This method of modeling random variable PDFs would enable a custom stochastic collocation quadrature consisting of Gauss Hermite quadrature over the Gaussian portion of the PDF plus two additional nodes, one at each delta function. Whether this method of modeling random variable PDFs a priori is moot, however, unless the cross section negativity issue is addressed.

## 6.3 Karhunen-Loève Representation of Discontinuous, Random Cross Sections

While methods exist for effecting transport through binary statistical materials with Markovian mixing, there is still a need for a general, accurate, and efficient method for many applications. We examine use of a discontinuous implementation of the Karhunen-Loève (KL) expansion using the Nataf transformation as a possible solution.

Interest in modeling of discontinuous random fields using the transformation of a spectral field has grown in recent years [11–13]. In this work we present modeling binary, Markovian-mixed materials for radiation transport applications by modeling material index as a discrete-valued random process

$$z(x,\omega) = \begin{cases} 0 & \text{if in Material 0} \\ 1 & \text{if in Material 1,} \end{cases} \tag{6.8}$$

based on a Karhunen-Loève expansion with Gaussian random variables. Macroscopic cross sections are modeled as a function of material index $z$ as

$$\Sigma_r(x,\omega) = \Sigma_{r,z} = \begin{cases} \Sigma_{r,0} & \text{if in Material 0} \\ \Sigma_{r,1} & \text{if in Material 1.} \end{cases} \tag{6.9}$$

The material index random process $z$ is normalized to zero mean and unit variance $Z$:

$$Z(x,\omega) = \begin{cases} \frac{p_0 - 1}{\sqrt{p_0(1-p_0)}} & \text{if in Material 0} \\ \frac{p_0}{\sqrt{p_0(1-p_0)}} & \text{if in Material 1,} \end{cases} \tag{6.10}$$

where $p_0$ is the probability that Material 0 exists at randomly chosen values of $x$ and $\omega$. The normalized and discrete-valued random process has a covariance of

$$C_Z(x,x') = c_Z(x,x') = \mathbb{E}[Z(x)Z(x')]. \tag{6.11}$$

The Karhunen-Loève expansion is used to create random field $g(x,\omega)$, which through Nataf's transformation is mapped to the discrete random field $Z(x,\omega)$ and subsequently

$z(x, \omega)$ and finally $\Sigma_{r,z}$.

### 6.3.1  The Nataf Transformation

Nataf's transformation maps values from one field to another such that the cumulative probability distributions are equal. Using Nataf's transformation the Gaussian random field described using the KL expansion

$$g(z, \omega) = \sum_{k=0}^{\infty} \sqrt{\gamma_k} u_k(x) \xi_k(\omega) \tag{6.12}$$

maps to $Z(x, \omega)$ by equating the cumulative probability density functions of the two distributions,

$$\int_{-\infty}^{g^*} \frac{1}{\sqrt{2\pi}} \exp\left[ -\frac{\xi^2}{2} \right] d\xi = p_0, \tag{6.13}$$

where $g^*$ is solved in terms of the inverse of the "error" function [74]:

$$g^* = \sqrt{2} \operatorname{erf}^{-1}(2p_0 - 1). \tag{6.14}$$

The definition of fields $z$ and $Z$ are then updated, the latter in terms of new function $h(g)$, as

$$z(x, \omega) = \begin{cases} 0 & \text{if } g(x, \omega) < g^* \\ 1 & \text{if } g(x, \omega) > g^*, \end{cases} \tag{6.15}$$

and

$$Z(x, \omega) = h(g(x, \omega)) = \begin{cases} \frac{p_0 - 1}{\sqrt{p_0(1 - p_0)}} & \text{if } g(x, \omega) < g^* \\ \frac{p_0}{\sqrt{p_0(1 - p_0)}} & \text{if } g(x, \omega) > g^*, \end{cases} \tag{6.16}$$

The eigenvalues and eigenfunctions $\gamma_k$ and $u_k(x)$ of the KL expansion in Eq. (6.12) must be solved from the Fredholm equation

$$\int_D c_g(x, x') u(x') dx' = \gamma u(x), \tag{6.17}$$

in which values of the covariance of the Gaussian field, $c_g(x, x')$, must first be solved as a function of values of the normalized material index covariance $c_Z(x, x')$ (Eq. (6.11)).

The normalized material index covariance $c_Z(x, x')$ is solved as the expectation of the product of values in the physical domain:

$$c_Z(x, x') = \mathbb{E}[Z(x)Z(x')] = \int_{-\infty}^{\infty} \int_{-\infty}^{\infty} h(g_1)h(g_2)p_g(g_1, g_2)dg_1 dg_2, \qquad (6.18)$$

where $g_1$ and $g_2$ are values of $g(x, \omega)$ at different values of $x$, vis., $x$ and $x'$, and $p_g$ is the bivariate Gaussian distribution. Equation 6.18 is written with the bivariate Gaussian distribution more explicitly as

$$c_Z(x, x')$$
$$= \int_{-\infty}^{\infty} \int_{-\infty}^{\infty} h(g_1)h(g_2) \frac{\exp[-((g_1^2 - 2c_g(x, x')g_1 g_2 + g_2^2)/(2(1 - c_g^2(x, x'))))]}{2\pi\sqrt{1 - c_g^2(x, x')}} dg_1 dg_2,$$
$$(6.19)$$

relating the two covariance functions $c_Z(x, x')$ and $c_g(x, x')$.

The bivariate Gaussian distribution modeled with probabalists' Hermite polynomials $H$ is

$$p_g(x, x') = \sum_{i_1=0}^{\infty} \sum_{i_2=0}^{\infty} \widehat{u}_{i_1 i_2} H_{i_1}(g_1) H_{i_2}(g_2) p(g_1) p(g_2), \qquad (6.20)$$

where $p(g_1)$ and $p(g_2)$ are the standard Gaussian probability distributions corresponding to dimensions 1 and 2. Taking advantage of Hermite polynomial orthogonality, discussed in Appendix C and stated in Eq. (C.5), Eq. (6.20) becomes

$$\widehat{u}_{i_1 i_2} = \frac{1}{i_1! i_2!} \int_{-\infty}^{\infty} \int_{-\infty}^{\infty} \frac{\exp[-((g_1^2 - 2c_g g_1 g_2 + g_2^2)/(2(1 - c_g^2)))]}{2\pi\sqrt{1 - c_g^2}} H_{i_1}(g_1) H_{i_2}(g_2) dg_1 dg_2,$$
$$(6.21)$$

in which covariance spatial dependence, $(x, x')$, for simplicity, is not stated explicitly. Integrating through the use of

$$\int_{-\infty}^{\infty} e^{(x-y)^2} H_m(ax)dx = \sqrt{\pi}\left(1 - \frac{a^2}{2}\right)^{\frac{n}{2}} H_m\left(\frac{ay}{\left(1 - \frac{a^2}{2}\right)^{\frac{1}{2}}}\right) \qquad (6.22)$$

from [75] as in [11], expansion coefficients are solved:

$$\widehat{u}_{i_1 i_2} = \frac{1}{i_1!} c_g^{i_1} \delta_{i_1 i_2}. \qquad (6.23)$$

The bivariate Gaussian is thus represented as

$$p_g(g_1, g_2) = \sum_{i_1=0}^{\infty} \frac{c_g^{i_1}}{i_1!} H_{i_1}(g_1) H_{i_1}(g_2) p(g_1) p(g_2).$$ (6.24)

Insertion of the Hermite polynomial expansion of the bivariate Gaussian (Eq. (6.24)) into Eq. (6.20), and noting the independence of the Gaussian fields, yields

$$c_Z = \sum_{i_1=0}^{\infty} \frac{c_g^{i_1}}{i_1!} \int_{-\infty}^{\infty} h(g_1) H_{i_1}(g_1) p(g_1) dg_1 \int_{-\infty}^{\infty} h(g_2) H_{i_1}(g_2) p(g_2) dg_1,$$ (6.25)

which further reduces by recognizing that the integrals are equivalent:

$$c_Z = \sum_{i_1=0}^{\infty} \frac{c_g^{i_1}}{i_1!} \left( \int_{-\infty}^{\infty} h(g) H_{i_1}(g) p(g) dg \right)^2.$$ (6.26)

### 6.3.2 Numerical Evaluation of Discontinuous, Random Cross Sections

Being applied to an isotropic field, the Gaussian process covariance $c_g(x, x')$ reduces to $c_g(r)$, where $r = |x - x'|$. To use the Nataf transformation, the Gaussian process covariance $c_g(r)$ used by the Karhunen-Loève (KL) expansion must first be solved numerically according to Eq. (6.26) for values of $r$. Since we already evaluate the KL Fredholm solve Eq. (6.17) using the Nyström method (as discussed in Section 3.1.3.2) with a uniform discretization in physical space, we choose to solve $c_g(r)$ at the same $N_{Ny}$ locations as in the Nyström solve.

The Gaussian process covariance, $c_g(r)$, is solved at $N_{Ny}$ values of $r$ through evaluation of Eq. (6.26). For each value of $r$ we solve the integral of Eq. (6.26) by splitting it into two integrals at $g^*$ so that we are integrating over continuous functions

$$\int_{-\infty}^{\infty} h(g) H_{i_1}(g) p(g) dg = \int_{-\infty}^{g^*} h(g) H_{i_1}(g) p(g) dg + \int_{g^*}^{\infty} h(g) H_{i_1}(g) p(g) dg,$$ (6.27)

and solve each integral numerically using scipy.integrate.quad(). Based on the investigation of Ilango et al. [11], we truncate the summation at 32 terms. Ilango et al. noted that there were "numerical problems when $[c_Z] \approx 1$ and the values of $[c_g]$ were interpolated linearly in those situations". We observe that when $c_Z$ is near a value of 1, many expansion terms are required in Eq. (6.26) to converge the resulting value of $c_g$. When

not enough terms are kept to converge the value of $c_g$, it has values of greater than 1, an unusable result for a covariance function. As more terms are kept in the expansion in Eq. (6.26) with $c_Z$ values near one, the error in the numerical integration of the integral grows such that numerical evaluation of terms is not reliable. We mitigate this numerical limitations of evaluating Eq. (6.26) for values near 1 by requiring that $c_g$ be below 1 and that the magnitude of the difference in its value evaluated with 31 and with 32 terms must be less than a tolerance arbitrarily chosen as $10^{-9}$. If these criteria are not met we reject the value of $c_g$ yielded and resort to interpolation to approximate these values.

To approximate the values of the Gaussian process covariance function $c_g(x, x')$ not solved with accuracy dictated by the screening method described in the previous paragraph, we use NumPy package scipy.optimize.curve_fit() to create a polynomial fit of $c_g(x, x')$ using the values of the Gaussian process covariance not rejected and the boundary value of $c_g(r = 0) = 1$. Polynomial fits of increasing order are used to approximate the values of $c_g(x, x')$ which were not solved from evaluation of Eq. (6.27). The fit which minimizes the Frobenius vector norm of the difference between the original process covariance $c_Z(x, x')$ and the process covariance reconstructed through Eq. (6.27) at $N_{Ny}$ discrete values $c_Z^*(x, x')$,

$$||c_Z(r) - c_Z^*(r)||_F \equiv \sqrt{\sum_{j=0}^{N_{Ny}} (c_Z(r_j) - c_Z^*(r_j))^2}, \qquad (6.28)$$

evaluated using numpy.linalg.norm() is selected. The Frobenius norm for various polynomial fit orders for a problem defined by $L = 5$ cm, $\Sigma_0 = 0.5$ cm$^{-1}$, $\Sigma_1 = 1.5$ cm$^{-1}$, $p_0 = 0.5$, $\lambda_c = 2.0$ cm, $N_{Ny} = 100$, and $K = 20$ is shown in Figure 6.2 in which the norm plotted at a polynomial order of 0 is the norm of the linear fit between (0,1) and the last value not rejected by our convergence screening method described in the preceding paragraph.
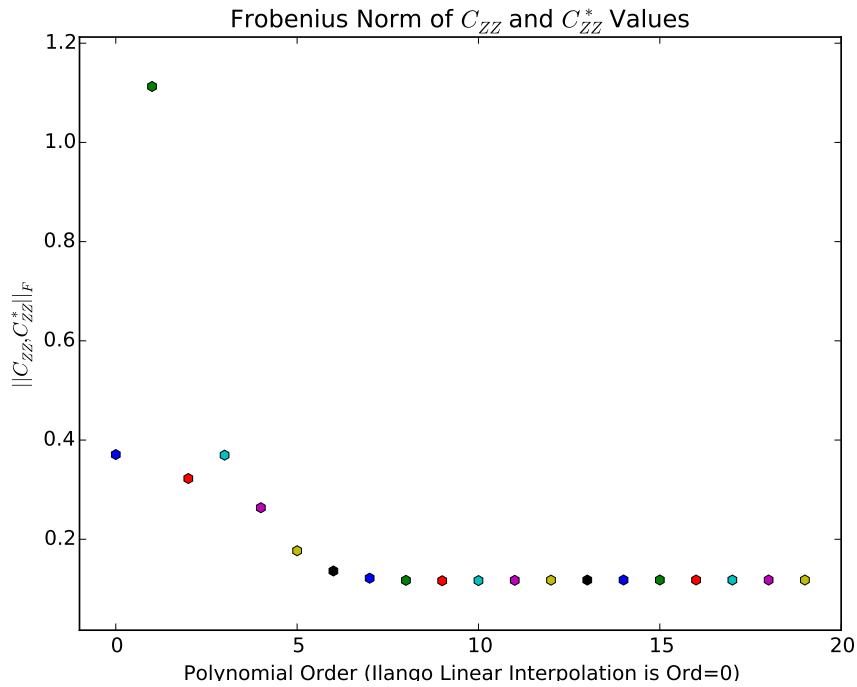
FIGURE 6.2: Frobenius Norm of Curve Fits for Covariance Values Near One

For this problem the polynomial fit of order nine minimized the Frobenius norm of the original and reconstructed process covariance vectors. A second-order polynomial and any polynomial over the order of three produce a smaller value for the Frobenius norm than the linear interpolation between the covariance boundary and the last trusted covariance value.

Figure 6.3 plots the original process covariance $c_Z(r)$, the Gaussian process covariance $c_g(r)$ including values solved by interpolation, the process covariance solved by reconstruction through evaluation of Eq. (6.27) $c_Z^*(r)$, and selected values of the covariance reconstructed over a large ensemble of realizations, the observed $c_Z(r)$ for the same problem used in the last paragraph. The plot on the left is generated using linear interpolation between the boundary covariance value and the last trusted value and the plot on the right is generated using the polynomial fit which minimizes the Frobenius norm of the difference between the true material index covariance and the material index covariance solved using polynomial interpolation.
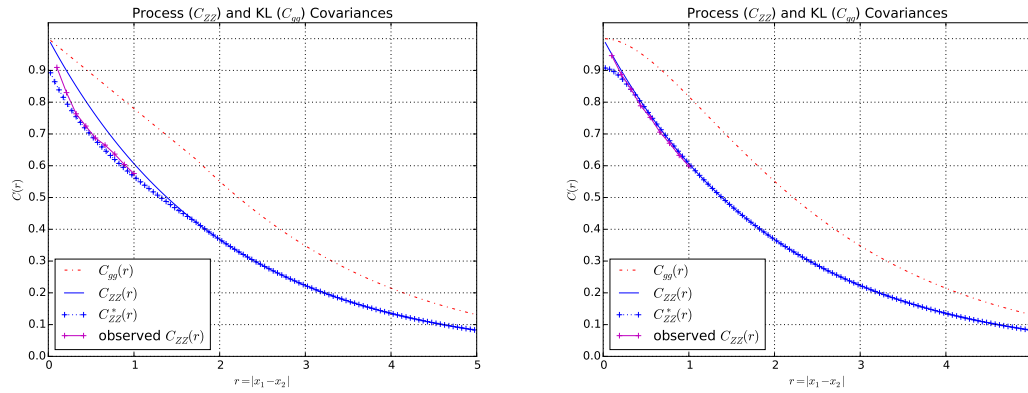
FIGURE 6.3: Process and Gaussian process covariance Functions, Using Linear Interpolation (left) and the Best Polynomial Fit (right)

The covariance generated using the best polynomial fit reconstructs a covariance closer to the original material index covariance than the covariance generated using the simple linear interpolation method. It can be seen that the Gaussian process covariance $c_g(r)$ has a more rounded, concave-down shape using the polynomial fit than when using the linear interpolation method that appears to be more faithful to the actual Gaussian process covariance. The covariance yielded by reconstruction over an ensemble of results is more accurate than through evaluation of Eq. (6.26); we hypothesize this is due to the same type of numerical issues which necessitate some form of interpolation in the first place.

While use of the best polynomial fit for interpolation appears to be an improvement over the linear interpolation of the covariance boundary and last trusted value method for covariance functions which contain values near 1, ideally an approach should be developed which is numerically robust for values of $c_Z(r)$ much closer to 1 such that the need for interpolation is minimized or removed altogether. Use of higher-precision variables may help bridge this gap. An integration scheme better suited for evaluating the integral in Eq. (6.26) may help, such as a different numerical quadrature or use of a package which integrates polynomials analytically over a portion of a Gaussian distribution. A method similar to Richardson's extrapolation which estimates the final value of the summation based on a reduction of the contribution of successive terms may be developed, and a more careful examination of the truncation order or the rejection tolerance chosen for the summation in Eq. (6.26) may improve the accuracy of numerical evaluation of $c_g(r)$. We hope to further examine this issue in future work.

Realizations of the discontinuous Karhunen-Loève (KL) expansion are generated through an updated form of Eq. (6.9):

$$\Sigma(x,\omega) = \Sigma_{r,z} = \begin{cases} \Sigma_{r,0} & \text{if } g(x,\omega) < g^* \\ \Sigma_{r,1} & \text{if } g(x,\omega) > g^*, \end{cases} \tag{6.29}$$

for which the process $g(x,\omega)$ is the zero-mean KL expansion

$$g(z,\omega) = \sum_{k}^{\infty} \sqrt{\gamma_k} u_k(x) \xi_k(\omega) \tag{6.30}$$

with eigenvalues and eigenvectors $\gamma_k$ and $u_k$ generated using the Gaussian process co-variance $c_g(r)$ and $g^*$ has been solved as the location in the cumulative distribution function of the Gaussian distribution equal to $p_0$:

$$g^* = \sqrt{2}\,\text{erf}^{-1}(2p_0 - 1). \tag{6.31}$$

Two Gaussian realizations $g(x,\omega)$, using the "discrete" Nyström interpolation scheme, and subsequent cross section realizations for $L = 5$ cm, $\Sigma_0 = 0.5$ cm$^{-1}$, $\Sigma_1 = 1.5$ cm$^{-1}$, $p_0 = 0.5$, $\lambda_c = 2.0$ cm, $N_{Ny} = 100$, and $K = 20$ are plotted in Figure 6.4 along with the CDF cutoff value $g^*$ and process average and one and two standard deviation values.
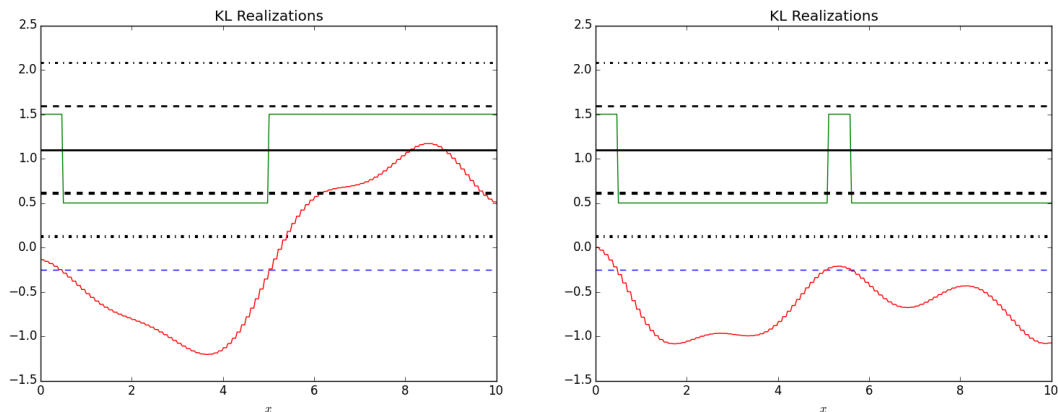


FIGURE 6.4: Mapping of Gaussian-based Karhunen-Loève Realizations to Discontinuous Realizations

Anywhere the value of $g(x,\omega)$ is less than $g^*$, Material 0 is chosen and $\Sigma_{t,0}$ is plotted, conversely where $g(x,\omega)$ is greater than $g^*$, Material 1 is chosen and $\Sigma_{t,1}$ is plotted.

Four such realizations are plotted in Figure 6.5 using $K = 15$ with the same problem parameters used to generate Figure 6.1 ($L = 5$ cm, $\Sigma_0 = 0.5$ cm$^{-1}$, $\Sigma_1 = 1.5$ cm$^{-1}$, $p_0 = 0.5$, and $\lambda_c = 0.375$ cm) such that realizations created using the two different methods can be compared visually.
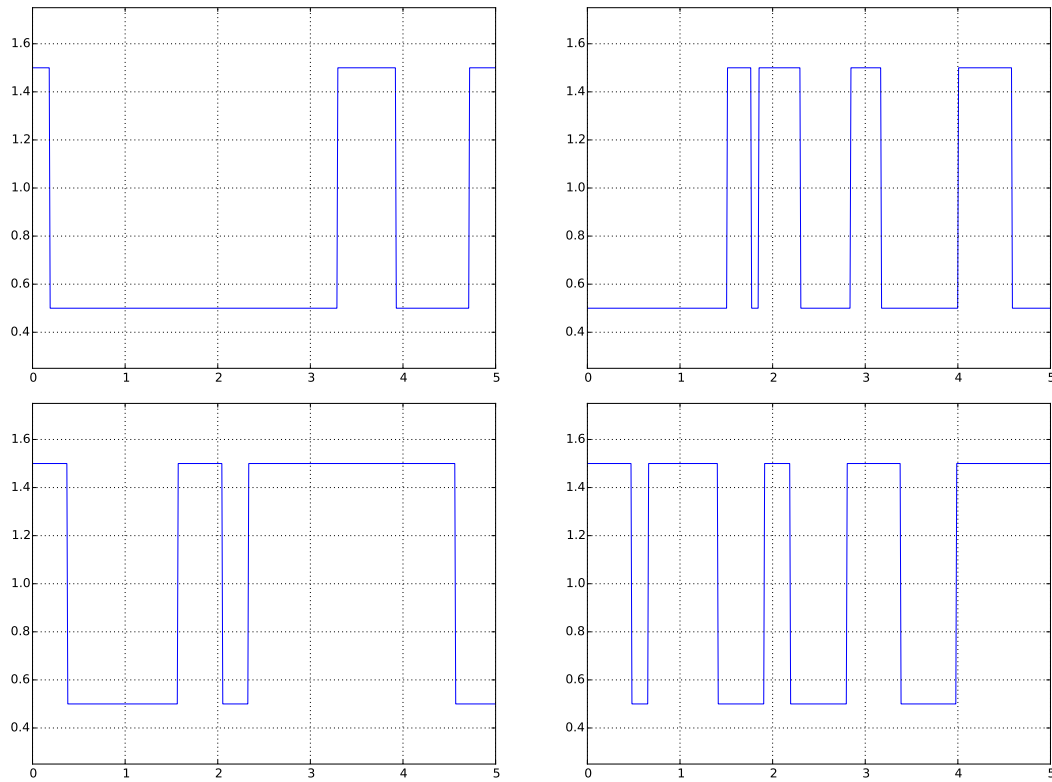


FIGURE 6.5: Four Binary, Markovian-mixed Realizations Generated Using the Discontinuous KL Method

In Figure 6.6, the mean and standard deviation of the random process generated using the discontinuous KL method is sampled from an ensemble of realizations at 25 locations throughout the slab along with the true process mean and variance for reference.
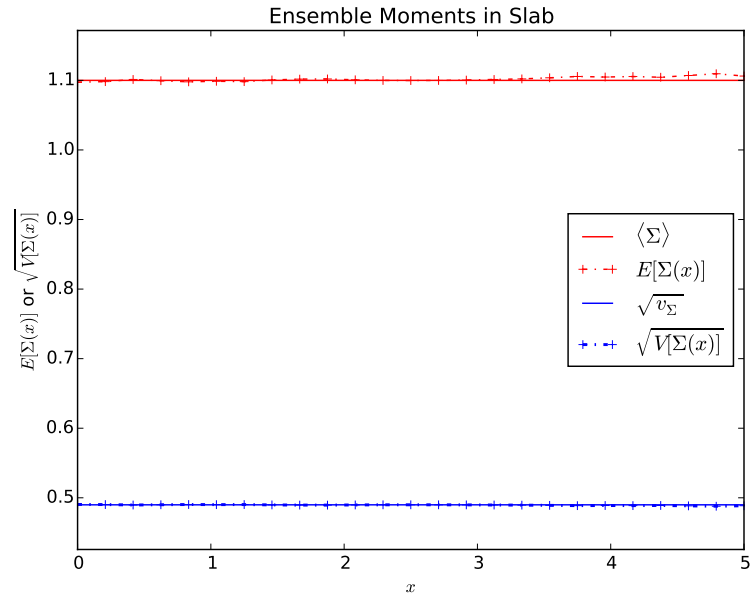
FIGURE 6.6: Observed Cross Section Moments

The moments are converging towards the input values with a large ensemble of sampled realizations.

A final plot is provided which shows the material index covariance $c_Z(r)$, the Gaussian process covariance $c_g(r)$, and the material index covariance observed by taking samples over an ensemble of 10,000 realizations $c_Z^*(r)$ for $L = 10$ cm, $\Sigma_0 = 0.5$ cm$^{-1}$, $\Sigma_1 = 1.5$ cm$^{-1}$, $p_0 = 0.25$, $\lambda_c = 2.0$ cm, and $K = 20$.
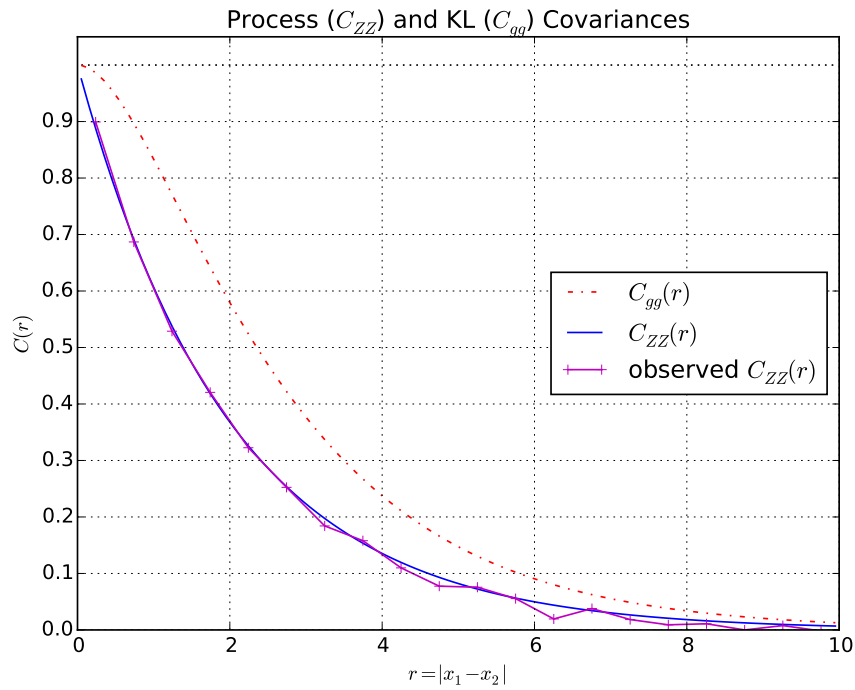
FIGURE 6.7: Process, Gaussian, and Sampled Covariances

## 6.4    Semi-infinite Slab Reflection Problem

A semi-infinite slab constructed of material with a constant scattering ratio and a source incident on the boundary will produce the same reflection distribution regardless of the mixing statistics of the slab. We numerically solve a semi-infinite slab problem as a benchmark of our discontinuous Karhunen-Loève (KL) method and implementation in a similar manner as in Section 5.3 for the lognormal transformation of the KL expansion. In this section, as there, Monte Carlo convergence with an increased number of particle histories is observed for an arbitrary choice of mixing statistics.

### 6.4.1    Problem Statement and Solution Methods

As shown in Section 5.3, the stochastic transport equation,

$$\mu \frac{\partial \psi(x,\mu,\omega)}{\partial x} + \Sigma_t(x,\omega)\psi(x,\mu,\omega) = \frac{\Sigma_s(x,\omega)}{2} \int_{-1}^{1} d\mu' \psi(x,\mu',\omega),$$

$$0 \leq x < \infty; \qquad -1 \leq \mu \leq 1; \qquad c = \frac{\Sigma_s(x,\omega)}{\Sigma_t(x,\omega)} \qquad (6.32)$$

$$\psi(0,\mu) = \delta(1-\mu), \quad \mu > 0,$$

in which the scattering ratio $c$ is constant throughout the physical, $x$, and stochastic, $\omega$, domains, the slab continues infinitely in one direction, and a particle source is incident on the boundary of the slab reduces to

$$\mu\frac{\partial\psi(\tau,\mu)}{\partial\tau} + \psi(\tau,\mu) = \frac{c}{2}\int_{-1}^{1}d\mu'\psi(\tau,\mu'),$$

$$0 \leq \tau < \infty; \qquad -1 \leq \mu \leq 1 \tag{6.33}$$

$$\psi(0,\mu) = \delta(1-\mu), \quad \mu > 0.$$

As can be seen from Eq. (6.33), all dependence on $x$ and $\omega$ has been exchanged for dependence on the optical thickness from the boundary $\tau$. Since the distance in the slab and optical thickness are equal at $x = \tau = 0$, the flux at the boundary is deterministic for any realization $\omega$.

We solve a benchmark value for mean reflectance using a Monte Carlo transport implementation to effect transport through and tally reflectance on such a semi-infinite slab with a constant scattering ratio and approximate the exact reflectance using $10^{10}$ particle histories:

$$\mathbb{E}[R] \approx \mathbb{E}[R_{Bench-MC,N=10^{10}}]. \tag{6.34}$$

This is the same benchmark Monte Carlo computation as in Section 5.3.

We also calculate the reflectance for a problem using random sampling and stochastic collocation in our transport-with-scattering code. Karhunen-Loève truncation $K$ and Nataf/Nyström discretization $N_{Ny}$ are arbitrarily chosen along with the number of random samples $R$ when solving using random sampling and a set of collocation orders $\mathbf{Q}$ when solving using stochastic collocation since any combination of these parameters should converge towards the same value for the reflectance mean with an increased number of Monte Carlo particle histories $N$. Both cases are solved with a slab thickness $L$ of 1,000 cm, for which no transmittance tallies were recorded in our simulations. Macroscopic total cross sections for the two materials are set to $\Sigma_{t,0} = 0.1$ cm$^{-1}$ and $\Sigma_{t,1} = 1.5$ cm$^{-1}$, each with scattering ratios of $c = 0.5$. The probability of Material 0, the correlation length, and the KL truncation order are set to $p_0 = 0.6$, $\lambda_c = 1.5$ cm, and $K = 5$, respectively. Reflectance is solved for these parameters using RS with $R = 100$ realizations and SC with orders $\mathbf{Q} = \{4, 3, 3, 2, 2\}$ for a total of $R_{SC} = 144$ realizations.

In each case the solution is generated with up to $N = 10^7$ particles histories on each realization.

When performing a convergence study on the reflectance values as the number of particle histories $N$ is increased, error terms are defined as

$$\varepsilon_{Bench-MC} = \left| \mathbb{E}[R_{Bench-MC,N=10^{10}}] - \mathbb{E}[R_{Bench-MC,N<10^{10}}] \right|, \quad (6.35a)$$

$$\varepsilon_{MC(RS)} = \left| \mathbb{E}[R_{Bench-MC,N=10^{10}}] - \mathbb{E}_{RS}[R_{MC,N\leq10^7}] \quad \right|, \quad (6.35b)$$

$$\varepsilon_{MC(SC)} = \left| \mathbb{E}[R_{Bench-MC,N=10^{10}}] - \mathbb{E}_{SC}[R_{MC,N\leq10^7}] \quad \right|. \quad (6.35c)$$

### 6.4.2 Monte Carlo Convergence of Benchmark and Scattering Implementations

The most converged reflectance values for each method are provided in Table 6.1. Based on the data in this table, we expect the error produced using the RS and SC solves to be about $10^{-5}$.

TABLE 6.1: Semi-Infinite Slab Reflectance Values for Discontinuous KL Implementation

| Solution Method | Num. Histories $N$ | $\langle R \rangle$ |
|---|---|---|
| Benchmark-MC | $1.0 \times 10^{10}$ | 0.11522526 |
| MC(RS) | $1.0 \times 10^{9}$ | 0.11521708 |
| MC(SC) | $1.44 \times 10^{9}$ | 0.11521387 |

Error convergence plots for the error terms defined in Eq. (6.35) are given in Figure 6.8 along with a plot of the expected Monte Carlo convergence rate $N^{-\frac{1}{2}}$.
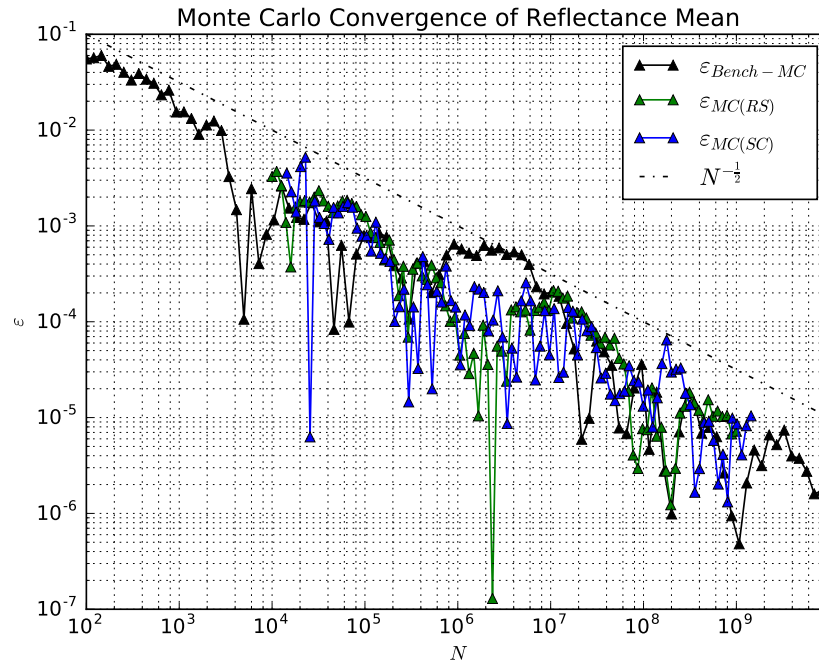
FIGURE 6.8: Discontinuous KL Reflection Benchmark - MC Convergence

The solutions calculated using RS and SC by our transport-with-scattering implementation converge as a function of the number of total Monte Carlo particle histories towards the benchmark solution. The error in the most converged solutions is about $10^{-5}$ as expected based on the most converged reflectance mean values.

## 6.5   Uncollided Flux Transmission Problem

The computation of the uncollided flux through a slab, equivalent to transport in purely absorbing media, serves as a simplified transport problem for observing error convergence behavior and benchmarking our transport-with-scattering implementation. Transmittance can be computed analytically for a realization generated using Chord Length Sampling (CLS) or the discontinuous Karhunen-Loève (KL) method as a function of the optical thickness. The CLS method is used to establish the correct solution for a problem by analytically computing the transmittance over realizations of absorption-only, binary, and Markovian-mixed media. Implementation of the discontinuous KL method with the analytical physical solver is benchmarked against the CLS solutions and a careful study of the errors inherent in the solution method is performed. This error study is simplified through use of the analytical physical solver that the uncollided flux problem enables.

Lastly, we benchmark our transport-with-scattering implementation by observing Monte Carlo convergence towards the solutions established by the CLS method.

### 6.5.1 Problem Statement and Solution Methods

This problem is described as a modification of the stochastic transport equation stated at the beginning of this chapter (Eq. (6.1)) for which the scattering cross sections $\Sigma_{s,z}$ are set to zero. By imposing a beam source and removing the possibility of scatter, the direction of particle travel is restricted to one value and can be removed from the equation altogether yielding

$$\mu\frac{\partial\psi(x,\omega)}{\partial x} + \Sigma_t(x,\omega)\psi(x,\omega) = 0,$$
$$0 \leq x \leq L \tag{6.36}$$
$$J^+(0) = 1, \qquad J^-(L) = 0.$$

The stochastically dependent transmittance is solved as in Eq. (4.15) as a function of the stochastically dependent slab optical thickness $\tau$:

$$T(\boldsymbol{\xi}) = \frac{J^+(L,\boldsymbol{\xi})}{J^+(0)} = \exp\big[-\tau(\boldsymbol{\xi})\big]. \tag{6.37}$$

The expectation of transmittance moments $\mathbb{E}[T^m]$ is solved by integrating over the stochastic domain

$$\mathbb{E}[T^m] = \int_{\boldsymbol{\xi}} \exp\big[-\tau(\boldsymbol{\xi})\big]p(\boldsymbol{\xi})d\boldsymbol{\xi} \tag{6.38}$$

using a method such as random sampling or stochastic collocation. The optical thickness $\tau(\boldsymbol{\xi})$ is solved for each realization, corresponding to a set of values for $\boldsymbol{\xi}$, by integrating the macroscopic total cross section over the physical domain:

$$\tau(\boldsymbol{\xi}) = \int_0^L \Sigma_t(x,\boldsymbol{\xi})dx, \quad \Sigma_t(x,\omega) = \Sigma_a(x,\omega) \,\forall\Sigma_s = 0. \tag{6.39}$$

We perform this integral for each realization by solving the locations $x_j$ in the slab at which the material types $z$ change and summing the product of material chord lengths

$\Delta x_j$ and absorption cross sections $\Sigma_{t,z}$:

$$\tau(\boldsymbol{\xi}) = \sum_j \Delta x_j \Sigma_{t,z(j)} \qquad (6.40)$$

This problem is solved by setting the correlation length and slab thickness as $\lambda_c = 1$ cm and $L = 5$ cm. The total cross sections for Material 0 and 1 are set to $\Sigma_{t,0} = \Sigma_{a,0} = 0.1$ cm$^{-1}$ and $\Sigma_{t,1} = \Sigma_{a,1} = 1.0$ cm$^{-1}$ and the probability of Material 0 is set to $p_0 = 0.5$. Transmittance mean and standard deviation are established using the Chord Length Sampling method and the error in this solution is quantified. A study is made of the error contributed by random sampling (RS), KL truncation, and Nataf and Nyström discretization order. Finally Monte Carlo (MC) convergence towards CLS solution is observed using the transport-with-scattering implementation.

### 6.5.2 Random Sampling Convergence of Chord Length Sampling Method

The transmittance mean and standard deviation are established using an ensemble of realizations generated with the Chord Length Sampling method. Transmittance is solved over ensembles of $10^9$ randomly generated realizations using the CLS method. Transmittance mean and standard deviation solved using each ensemble is given in Table 6.2.

TABLE 6.2: Uncollided Flux Transmittance Values for Discontinuous KL Implementation - Chord Length Sampling Solutions

|  | Num. Real. $R$ | $\langle T \rangle$ | $\sqrt{v_T}$ |
| --- | --- | --- | --- |
| Ensemble 1 | $10^9$ | 0.13215543 | 0.159402567 |
| Ensemble 2 | $10^9$ | 0.13215461 | 0.159402434 |

Random sampling (RS) convergence of the transmittance mean and standard deviation generated by each ensemble with an increased number of realizations against the solution provided by the other ensemble are plotted in Figures 6.9 and 6.10.
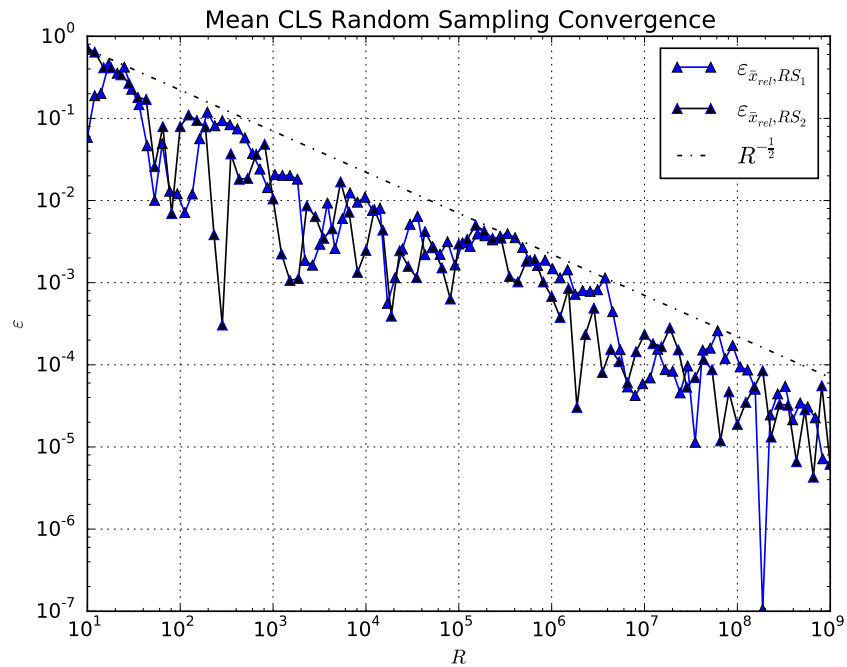
FIGURE 6.9: Mean Transmission Convergence for Random Sampling of Realizations of Binary Media with Markovian Statistics
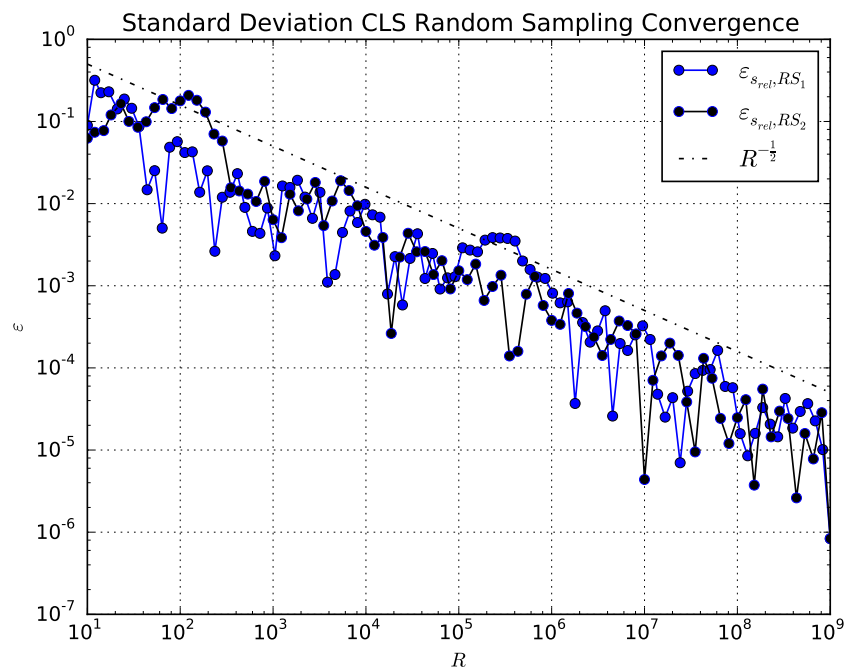


FIGURE 6.10: Standard Deviation Transmission Convergence for Random Sampling of Realizations of Binary Media with Markovian Statistics

Each ensemble of $10^9$ realizations produces transmittance mean and standard deviation values with a relative error of about $10^{-4}$. These transmittance values are used as the

correct solution in the following sections, and relative error is not studied for values lower than $10^{-4}$.

### 6.5.3 Random Sampling Convergence of Discontinuous KL Method

The error convergence of random sampling in the stochastic domain is observed for the transmittance mean and standard deviation by modeling stochastic media using a KL truncation order of $K = 5$, the "linear" Nyström interpolating function, and a Nataf and Nyström discretization order of $N_{Ny} = 100$ and evaluating the transmittance for a realization analytically according to Eq. (6.38). Exact mean and standard deviation values are solved for these system parameters over $10^7$ realizations, and relative error against these approximated-as-exact solutions is computed using an independent set of $3 \times 10^6$ realizations. The approximated-as-exact solutions and the most converged solutions using the ensemble relative error are provided in Table 6.3.

TABLE 6.3: Uncollided Flux Transmittance Values for Discontinuous KL Implementation - Random Sampling Solutions

| Solution Method | Num. Real. $R$ | $\langle T \rangle$ | $\sqrt{v_T}$ |
|:---:|:---:|:---|:---|
| RS(KL,NM) | $1 \times 10^7$ | 0.136349 | 0.168133 |
| RS(KL,NM) | $3 \times 10^6$ | 0.136307 | 0.168046 |

Convergence of the transmittance values of the second ensemble computed against the most converged solutions of the first and larger ensemble are plotted in Figures 6.11 and 6.12.
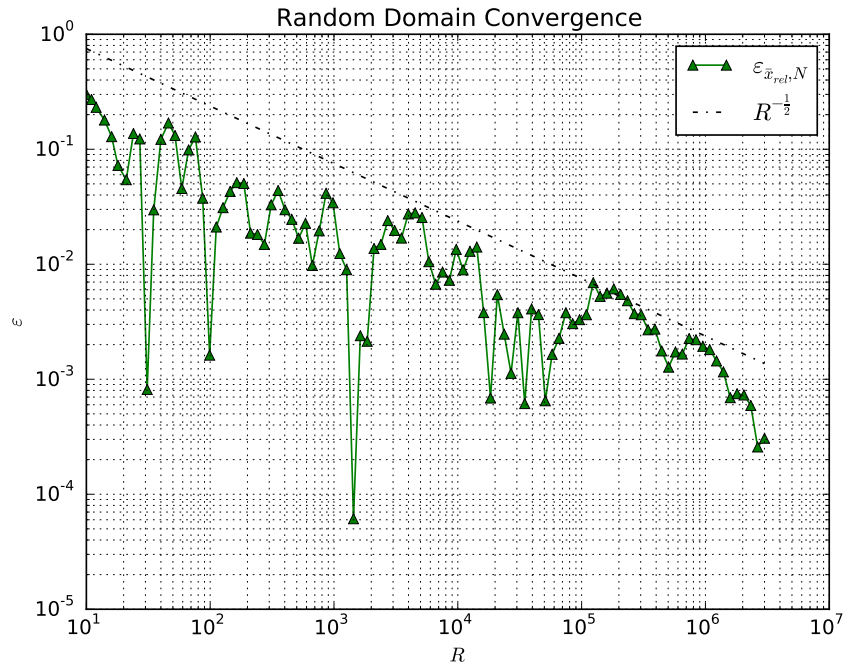
FIGURE 6.11: Uncollided Flux Mean Transmittance Convergence for Random Sampling for Discontinuous KL Implementation



FIGURE 6.12: Uncollided Flux Standard Deviation Transmittance Convergence for Random Sampling for Discontinuous KL Implementation

The relative error of each value converges as $R^{-\frac{1}{2}}$ as we expect from a random sampling method. We estimate the relative error due to the random sampling solve of the transmittance mean and transmittance standard deviation to be about $1.4 \times 10^{-3}$ for

$R = 3 \times 10^6$ realizations using the chosen values of $K$ and $N_{Ny}$. This number of samples is used in the following analysis and relative error is estimated as $1.4 \times 10^{-3}$.

### 6.5.4   Karhunen-Loève Truncation Convergence

The Karhunen-Loève truncation order convergence is observed in this section using the chosen $R = 3 \times 10^6$ samples, the "linear" Nyström interpolation scheme, and Nataf and Nyström discretization order $N_{Ny} = 100$. Transmittance values generated using the first Chord Length Sampling ensemble are used to approximate the exact solution. The CLS values and most converged discontinuous KL values are provided in Table 6.2.

TABLE 6.4: Uncollided Flux Transmittance Values for Discontinuous KL Implementation - Karhunen-Loève Truncation Solutions

| Solution Method | Num. Real. $R$ | KL Trunc. $K$ | $\langle T \rangle$ | $\sqrt{v_T}$ |
|:---:|:---:|:---:|:---:|:---:|
| CLS | $10^9$ | N/A | 0.13215543 | 0.159402567 |
| KL(RS,NM) | $3 \times 10^6$ | 10 | 0.13215461 | 0.159402434 |

Convergence of the transmittance mean and standard deviation for increased KL truncation order $K$ towards the CLS solution are plotted in Figures 6.13 and 6.14
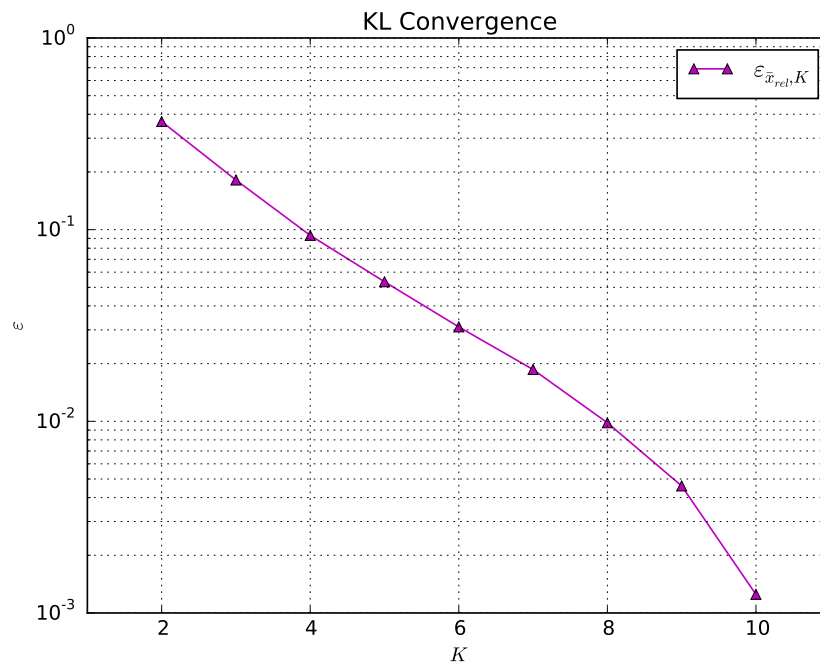


FIGURE 6.13: Uncollided Flux Mean Transmittance Convergence for Karhunen-Loève Truncation for Discontinuous KL Implementation
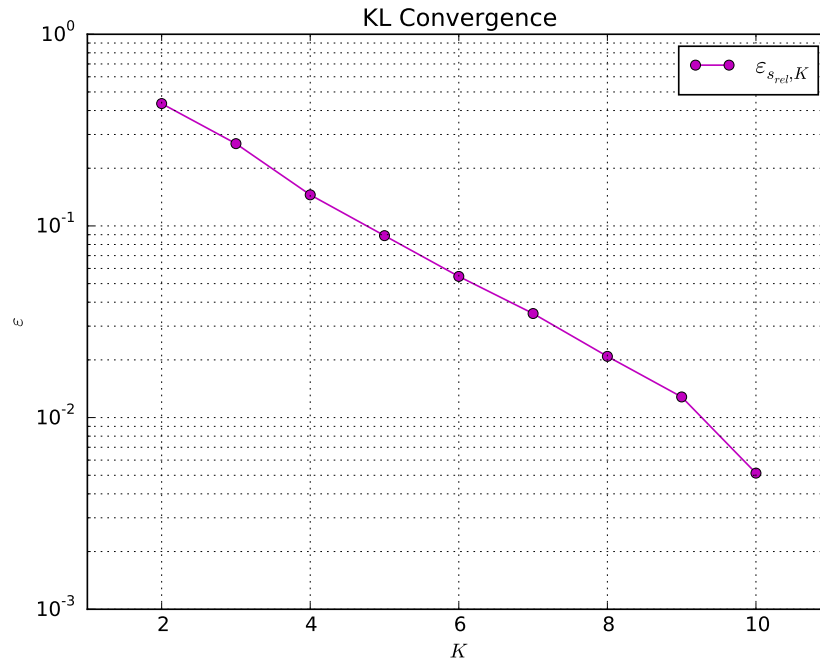
FIGURE 6.14: Uncollided Flux Standard Deviation Transmittance Convergence for Karhunen-Loève Truncation for Discontinuous KL Implementation

The relative error converges monotonically with an increase in KL truncation order $K$ and may be linear in log space. Apparent linear convergence of transmittance values is disrupted as the relative error of the KL truncation approaches the estimated error in the RS ( $1.4 \times 10^{-3}$); to observe the KL truncation convergence further more random samples $R$ should be used. We select a KL truncation order $K = 9$ and estimate the transmittance mean relative error as $5 \times 10^{-3}$ and the transmittance standard deviation relative error as $2.14 \times 10^{-2}$.

### 6.5.5 Nataf and Nyström Discretization Convergence

Error convergence of Nataf and Nyström discretization is observed here for the "discrete" and "linear" Nyström interpolation schemes with $R = 3 \times 10^6$ samples and KL truncation order $K = 10$. With some foresight, the approximated-as-exact solution used is generated for these parameters with the "discrete" interpolation scheme and $N_{Ny} = 300$. The approximated-as-exact solutions and the most converged solutions for which relative error is estimated are provided in Table 6.5.

TABLE 6.5: Uncollided Flux Transmittance Values for Discontinuous KL Implementation - Nataf and Nyström Discretization Solutions

| Solution Method | Disc. Ord. $N_{Ny}$ | $\langle T \rangle$ | $\sqrt{v_T}$ |
|---|---|---|---|
| NM-discrete(RS,KL) | 300 | 0.13296 | 0.16139 |
| NM-discrete(RS,KL) | 100 | 0.13227 | 0.16046 |
| NM-linear(RS,KL) | 100 | 0.13227 | 0.16034 |

Solutions produced with a higher discretization order $N_{Ny}$ were used to approximate the exact solution since the errors are less than the other errors in the system (RS error, KL truncation error)–calculation of error terms through use of the CLS solution is dominated by RS and KL truncation error and does not capture the convergence behavior. The convergence behavior of the relative error is plotted in Figures 6.15 and 6.16.
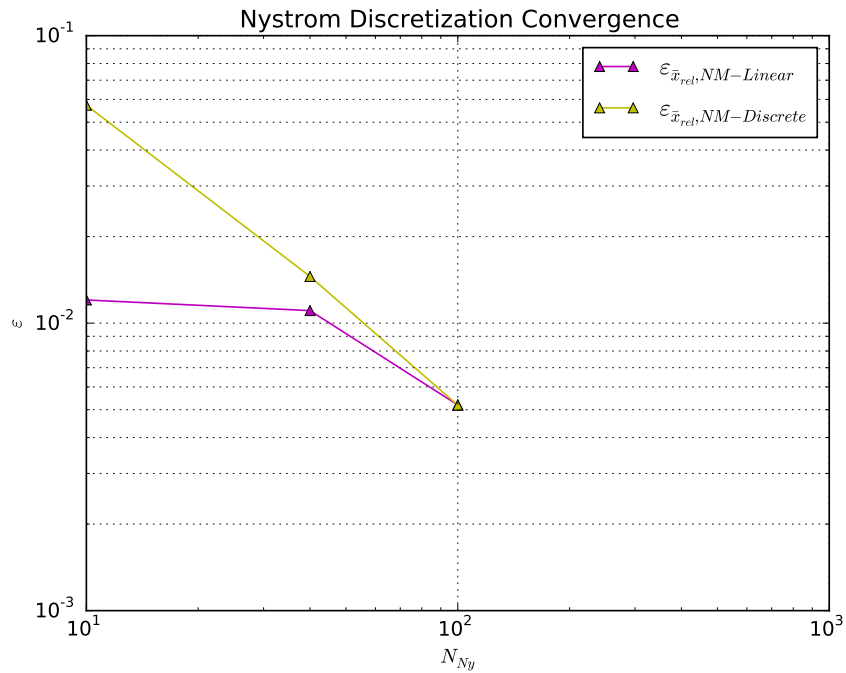


FIGURE 6.15: Uncollided Flux Mean Transmittance Convergence for Nataf and Nystöm Discretization for Discontinuous KL Implementation
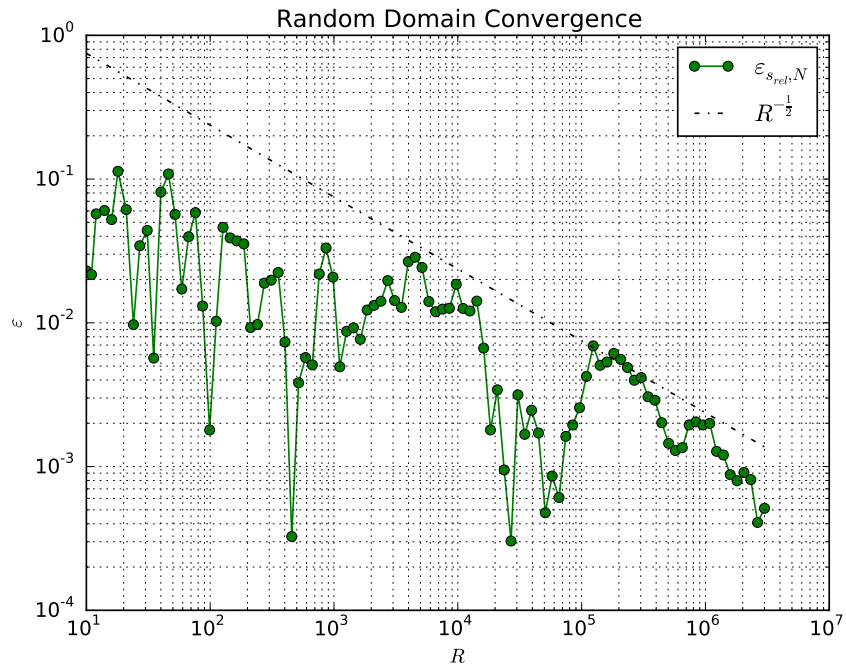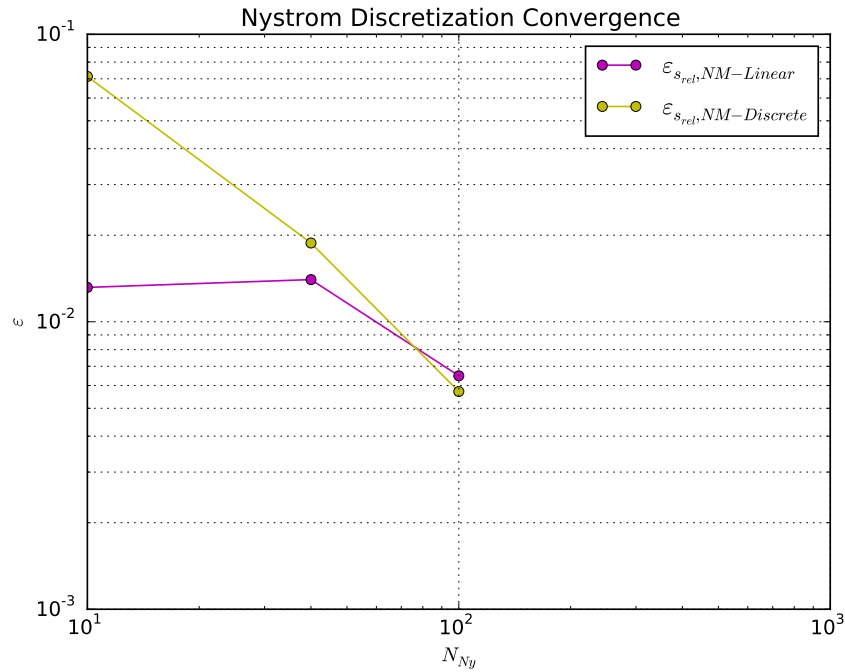
FIGURE 6.16: Uncollided Flux Standard Deviation Transmittance Convergence for Nataf and Nystöm Discretization for Discontinuous KL Implementation

The relative error due to the Nataf and Nyström discretization is converging for each Nyström interpolation scheme, and appears to be about the same, $5 \times 10^{-3}$, for $N_{Ny} = 100$. It is possible that the relative error of the "linear" interpolation scheme is being overestimated by using a "discrete" interpolation scheme to provide the approximated-as-exact solution. Solution of this problem using the "linear" interpolation scheme with $N_{Ny} = 300$ was very expensive, however, so the "discrete" interpolation scheme is used to approximate the relative error of the Nataf and Nyström discretization.

### 6.5.6 Stochastic Collocation Convergence

Stochastic collocation (SC) quadrature order convergence is observed using the chosen KL truncation order $K = 9$ and Nataf and Nyström discretization order $N_{Ny} = 100$ using the "discrete" Nyström interpolation scheme. Transmittance results are solved using isotropic stochastic collocation (iSC) of increasing quadrature order and two anisotropic stochastic collocation (aSC) grids chosen arbitrarily based on intuition. The approximated-as-exact solution is produced using the first Chord Length Sampling ensemble. Transmittance values generated using CLS, iSC, and aSC are shown in Table 6.6.

TABLE 6.6: Uncollided Flux Transmittance Values for Discontinuous KL Implementation - Stochastic Collocation Quadrature Order Solutions

| Solution Method | Quad. Ords. **Q** | $\langle T \rangle$ | $\sqrt{v_T}$ |
|---|---|---|---|
| CLS | N/A | 0.1322 | 0.1594 |
| iSC(KL,NM) | {5,5,5,5,5,5,5,5,5} | 0.1304 | 0.1672 |
| aSC(KL,NM) | {5,4,4,3,3,3,2,2,2} | 0.1301 | 0.1643 |
| aSC(KL,NM) | {6,5,4,4,3,3,3,2,2} | 0.1345 | 0.1589 |

Relative error for the iSC and aSC solutions is shown in Figures 6.17 and 6.18. Isotropic SC relative errors are connected with a line to show the convergence of the iSC solver solutions.
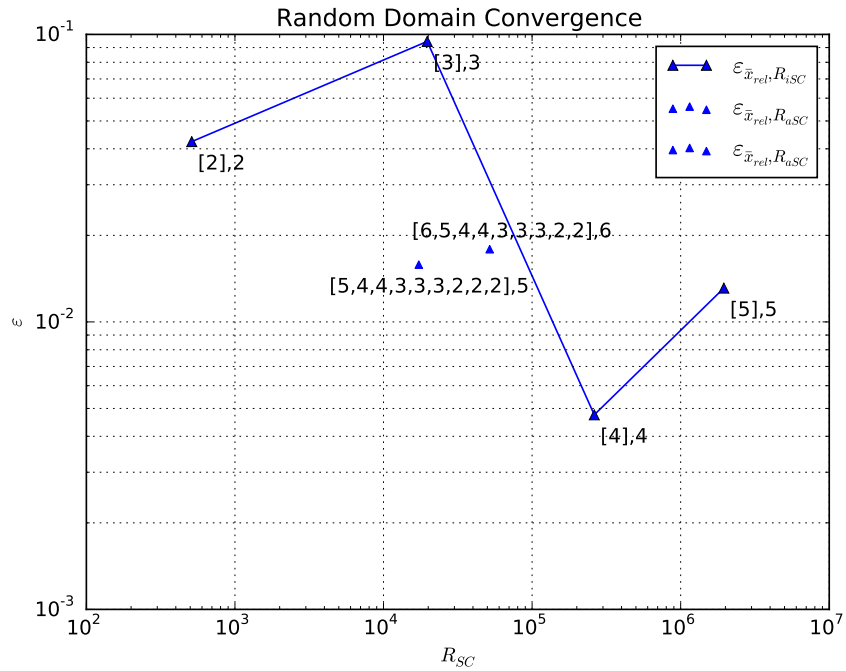


FIGURE 6.17: Uncollided Flux Mean Transmittance Convergence for Stochastic Collocation Quadrature Orders for Discontinuous KL Implementation
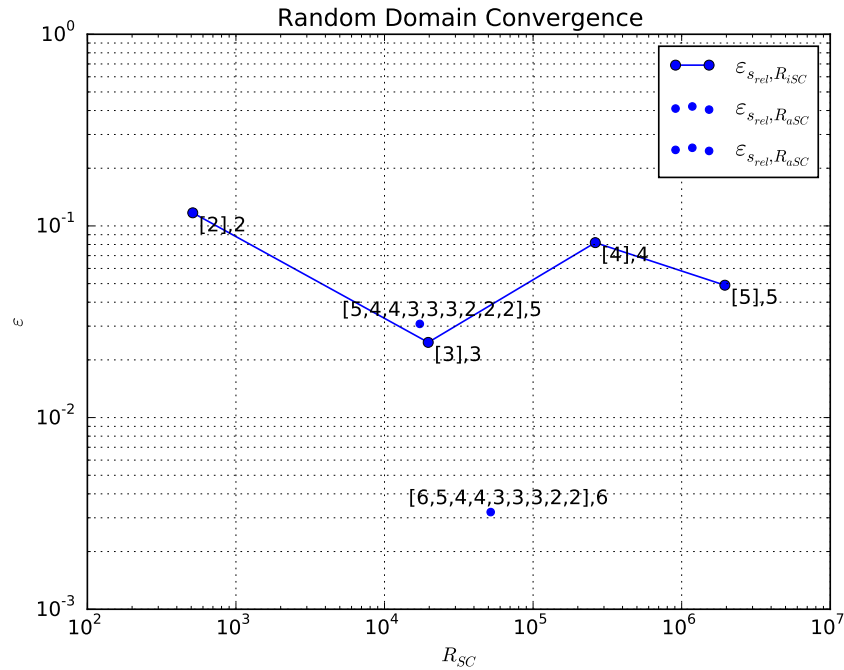
FIGURE 6.18: Uncollided Flux Standard Deviation Transmittance Convergence for Stochastic Collocation Quadrature Orders for Discontinuous KL Implementation

Convergence of the isotropic stochastic collocation transmittance values is not monotonic. This is likely an artifact of integrating a discontinuous function, the transmittance as a function of variation in the stochastic domain, with a quadrature, and the behavior appears to be similar to that of the optical thickness solved by numerically integrating a discontinuous function in Figures 5.5-5.8 in Sections 5.4.2 and 5.4.3. The general trend appears to be one of convergence, though transmittance values solved with higher quadrature orders would be necessary to confirm this. The anisotropic stochastic collocation solutions likely suffer from the same phenomenon such that it is difficult to choose the optimal set of parameters. Their relative errors appear to be less than the relative error of the isotropic SC solutions in three of the four transmittance values shown. We include the relative errors produced using the highest quadrature orders in the error summary in the next section.

We do not include further discussion or analysis of stochastic collocation for this uncollided flux problem, but do present cases for which SC does well using the discontinuous KL approach when solving published benchmark problems later in this chapter.

### 6.5.7 Summary of Convergence Relative Errors

The estimated relative errors for chosen system parameters are summarized in Table 6.7.

TABLE 6.7: Uncollided Flux Transmittance Values for Discontinuous KL Implementation - Summary of Estimated Relative Errors

| Solution Method and Params | $\varepsilon_{\bar{x}_{rel},T}$ | $\varepsilon_{s_{rel},T}$ |
|---|---|---|
| CLS, $R = 10^6$ | $7 \times 10^{-5}$ | $5 \times 10^{-5}$ |
| RS, $R = 3 \times 10^6$ | $1.4 \times 10^{-3}$ | $1.4 \times 10^{-3}$ |
| KL, $K = 9$ | $5 \times 10^{-3}$ | $2.14 \times 10^{-2}$ |
| NM-linear, $N_{Ny} = 100$ | $5 \times 10^{-3}$ | $7 \times 10^{-3}$ |
| Total | $1.04 \times 10^{-2}$ | $2.98 \times 10^{-2}$ |

Based on the parameters we have chosen, we estimate the relative error of the transmittance mean to be about 1% and relative error of the transmittance standard deviation to be about 3%. These parameters are used in the following section when observing the Monte Carlo and random sampling convergence of the transport-with-scattering implementation towards the solutions generated using Chord Length Sampling.

### 6.5.8 Convergence of Scattering Implementation Towards CLS Solution

Error estimates for Karhunen-Loève truncation order $K$ and Nataf and Nyström discretization order with the "linear" Nyström interpolation scheme are provided in the previous sections. The transport-with-scattering implementation is used here and Monte Carlo (MC) and random sampling convergence toward the Chord Length Sampling solutions is observed. Relative error due to the Monte Carlo solve is estimated on a small ensemble of random samples, a number of particle histories is chosen, and random sampling convergence towards the CLS solutions is shown using the number of particle histories chosen. This serves as a verification of the discontinuous KL method by comparing it against numerical results of the same stochastic problem solved in a different way and a verification of the coding implementation.

First the number of Monte Carlo histories required to converge towards the CLS solutions is estimated by solving an ensemble of randomly sampled realizations with $R = 100$ samples using two different random number seeds for the Monte Carlo solver. The approximated-as-exact solution is provided using $N = 10^7$ particle histories on each realization and the relative error against this solution is computed using up to $10^6$ particle histories on each realization. The approximated-as-exact solution for this $R = 100$ ensemble and the most converged solution for the second computation with a different random number seed and solved with less histories are shown in Table 6.8.

TABLE 6.8: Uncollided Flux Transmittance Values for Discontinuous KL Implementation - Monte Carlo Transport with Scattering Solutions

| Solution Method | Num. Part. $N$ | $\langle T \rangle$ | $\sqrt{v_T}$ |
|---|---|---|---|
| MC(RS,KL,NM) | $1 \times 10^7$ | 0.130995 | 0.163030 |
| MC(RS,KL,NM) | $1 \times 10^6$ | 0.131018 | 0.163037 |

Convergence of the transmittance values using the second ensemble towards the solutions provided by the first is plotted in Figure 6.19.
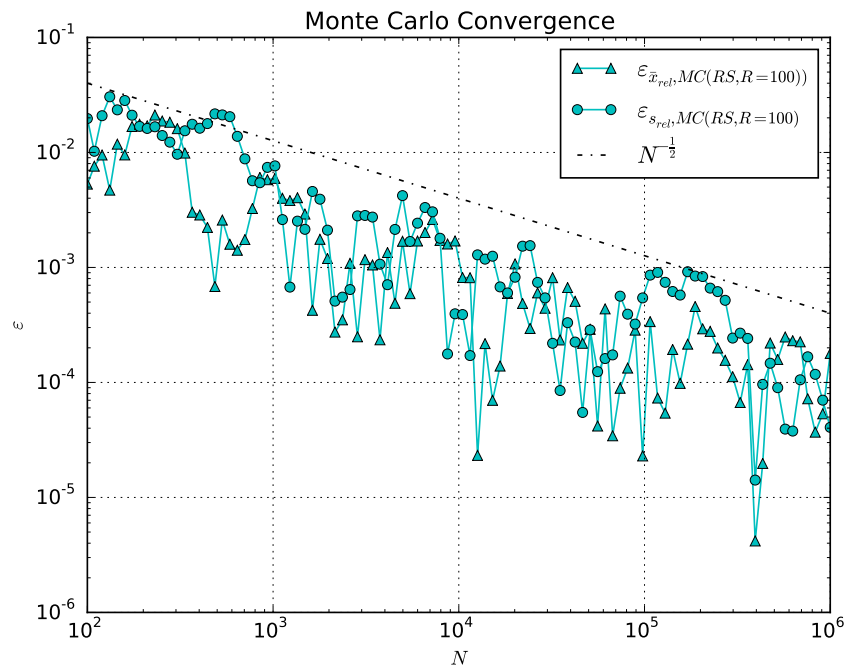


FIGURE 6.19: Uncollided Flux Transmittance Values for Discontinuous KL Implementation - Monte Carlo Transport with Scattering Solutions

We choose $3 \times 10^3$ particle histories on each sample such that the estimated MC relative error for the transmittance mean and standard deviation is less than 1% ( $8 \times 10^{-3}$).

Having selected a number of particle histories with which to solve the stochastic transport equation, random sampling is used to resolve the stochastic domain, and the relative error computed against the CLS solutions in the random sampling solve with successively more samples is plotted. The CLS transmittance values used to approximate the exact solutions along with the most converged transmittance values generated with the transport-with-scattering solve with $N = 3,000$ particle histories, a KL truncation order of $K = 5$, and a Nataf and Nyström discretization order of $N_{Ny} = 100$ are provided in Table 6.9.

TABLE 6.9: Uncollided Flux Transmittance Values for Discontinuous KL Implementation - Karhunen-Loève Truncation Solutions

| Solution Method | Num. Real. $R$ | $\langle T \rangle$ | $\sqrt{v_T}$ |
|:---:|:---:|:---:|:---:|
| CLS | $10^9$ | 0.132155 | 0.159403 |
| RS(MC,KL,NM) | $3 \times 10^6$ | 0.132367 | 0.160813 |

Convergence of transmittance values towards the CLS-generated benchmark solutions is plotted in Figures 6.20 and 6.21.
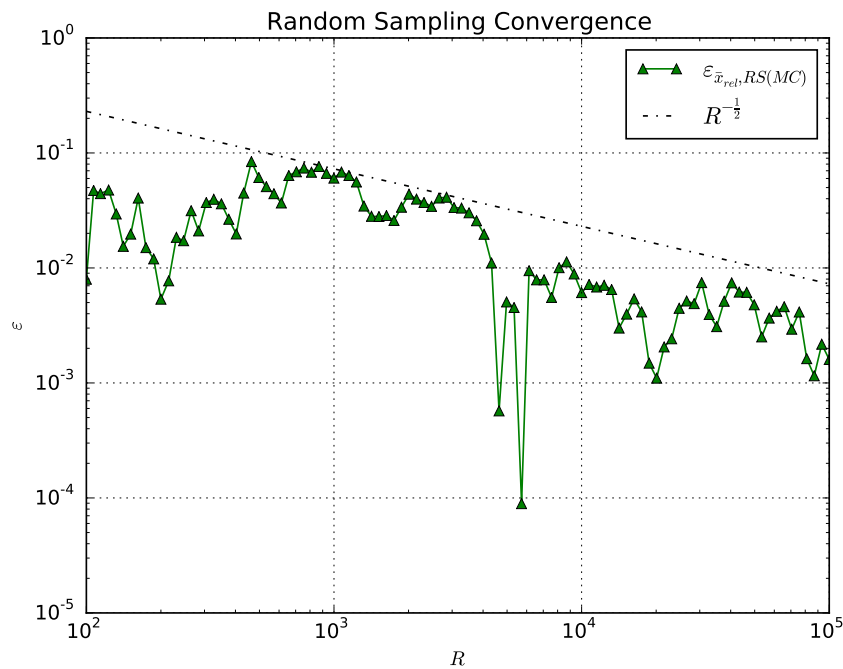


FIGURE 6.20: Uncollided Flux Transmittance Mean for Discontinuous KL Implementation - Random Sampling Transport with Scattering Solutions
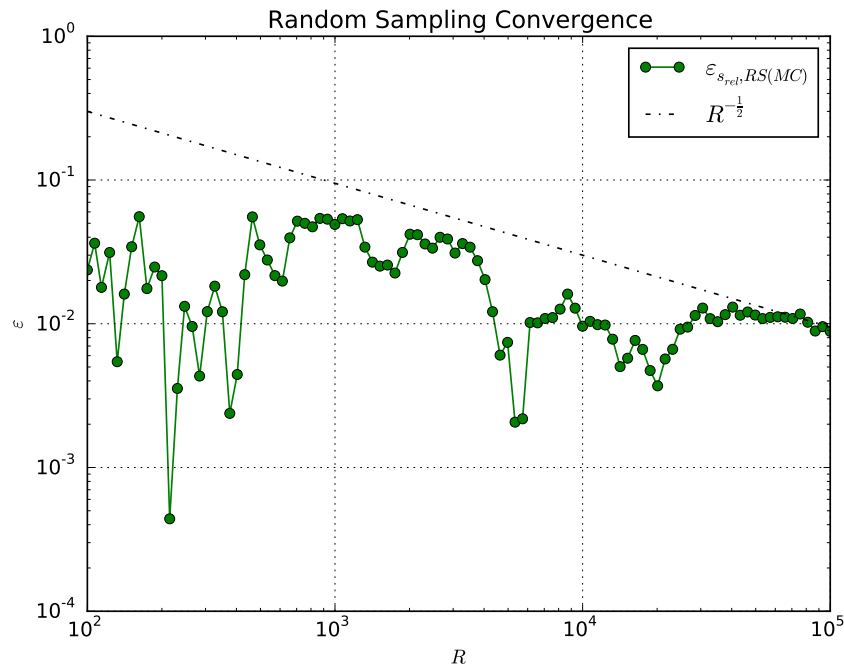
FIGURE 6.21: Uncollided Flux Transmittance Standard Deviation for Discontinuous
KL Implementation - Random Sampling Transport with Scattering Solutions

The expected random sampling convergence of $R^{-\frac{1}{2}}$ is observed for the transmittance mean and standard deviation. Solving with $R = 10^5$ samples contributes a relative error of about $7 \times 10^{-3}$, for a total relative error estimate of about 2.5% for the transmittance mean when solving using the selected parameters ($N = 3,000$, $K = 9$, use of "linear" Nyström interpolating scheme, and $N_{Ny} = 100$). Similarly, $R = 10^5$ samples contributes a relative error for the standard deviation of about $7 \times 10^{-3}$, for a total relative error estimate of about 4.3% for the transmittance standard deviation when solving using the selected parameters. While the expected random sampling convergence rate of $R^{-\frac{1}{2}}$ is observed for the standard deviation, the error computation plateaus at about 1% relative error. The estimated bound on the error from the other solution methods, as seen in Table 6.7 for random material modeling methods and earlier in this section for Monte Carlo particle simulation ( $8 \times 10^{-3}$), is about 3.6%. For relative error values as high as about 3.6% this plateau behavior is expected since errors other than the one being investigated in the convergence plot begin to dominate. It appears that the actual error in this case for the transmittance mean from the other solution methods is not more than about 0.7%, since the error convergence plot did not plateau, and that the transmittance standard deviation relative error from the other methods is about 1%, since the random sampling convergence did plateau here. These errors are less than

the error bounds we estimated for the solution methods. Convergence of these solutions towards the CLS solutions adds confidence in our method and in our transport-with-scattering implementation.

## 6.6   Transport with Scattering - Solving the Adams, Larsen, and Pomraning Benchmark Problems

Not long after interest grew for solving the stochastic transport equation through binary media with Markovian statistics, Adams, Larsen, and Pomraning developed a set of benchmark problems [1]. In that work, they solved a set of problems defined by varying average material chord lengths, cross section values, and slab thickness, using a discrete ordinates solver. They solved approximated-as-exact solutions by randomly sampling realizations and effecting transport on each, estimating that the relative error on their approximated-as-exact solutions is no greater than 1%. They also solved using the Levermore-Pomraning (LP) closure, and compare their benchmark results with their LP results.

More recently this benchmark suite was solved by Brantley [2] with a Monte Carlo solver to lower relative error tolerances and with additional results including atomic mix (AM) solutions. Results generated using a Monte Carlo solve of the LP closure are labeled "Algorithm A" in Brantley's publication.

This benchmark suite serves two purposes for us in this work, the first to benchmark our method and implementation on a problem with scattering, and the second to compare the performance of the method against other solution methods for some problems of interest. The problems in this benchmark suite do not fully characterize the problems on which this method may be applied, but rather focus on binary, stochastic materials with exponential covariances and a large difference in total cross section values. It is a useful set of cases with established value in these types of problems, however, so we seek to produce more accurate transport results than other approximate methods such as the atomic mix (AM) model and the Levermore-Pomraning (LP) closure and be more efficient than the "brute force" method of randomly sampling realizations using the Chord Length Sampling (CLS) method for at least some cases.

### 6.6.1 Problem Statement and Solution Methods

The benchmark suite solves the stochastic transport equation

$$\mu\frac{\partial\psi(x,\mu,\omega)}{\partial x} + \Sigma_t(x,\omega)\psi(x,\mu,\omega) = \frac{\Sigma_s(x,\omega)}{2}\int_{-1}^{1}d\mu'\psi(x,\mu',\omega), \qquad (6.41a)$$

$$0 \leq x \leq L; \qquad -1 \leq \mu \leq 1 \qquad (6.41b)$$

$$\psi(0,\mu) = 2, \quad \mu > 0; \qquad \psi(L,\mu) = 0, \quad \mu < 0 \qquad (6.41c)$$

in which an isotropic source is incident on the left boundary of a slab. The suite contains nine different cases made up of unique combinations of total cross section values $\Sigma_{t,0}$ and $\Sigma_{t,1}$, scattering ratios $c_0$ and $c_1$, and mean material chord lengths $\lambda_0$ and $\lambda_1$. Each of these nine cases is solved on a slab of length, $L$, of 0.1, 1.0, or 10.0 cm. In the Brantley paper, which expands results for this benchmark suite [2], these nine cases are uniquely designated with a number and a letter. Cases with the same case number correspond to those which have the same material chord lengths and total cross section values and cases with the same letter have the same scattering ratios. We adopt this method for labeling the cases, but choose to represent the case parameters using the probability of Material 0 $p_0$ and the process correlation length $\lambda_c$ instead of the average chord lengths for the two materials since these are the parameters the discontinuous KL method uses and the cases are still uniquely and fully identified. The parameters for the nine cases, each of which are solved for slabs of three different lengths, are described in Table 6.10

TABLE 6.10: Benchmark Suite Problem Parameters

| Case # | $\lambda_c$ | $p_0$ | $\Sigma_{t,0}$ | $\Sigma_{t,1}$ | $c_0$ | $c_1$ |
|---|---|---|---|---|---|---|
| 1a | 0.099 | 0.9 | $\frac{10}{99}$ | $\frac{100}{11}$ | 0.0 | 1.0 |
| 1b | 0.099 | 0.9 | $\frac{10}{99}$ | $\frac{100}{11}$ | 1.0 | 0.0 |
| 1c | 0.099 | 0.9 | $\frac{10}{99}$ | $\frac{100}{11}$ | 0.9 | 0.9 |
| 2a | 0.99 | 0.9 | $\frac{10}{99}$ | $\frac{100}{11}$ | 0.0 | 1.0 |
| 2b | 0.99 | 0.9 | $\frac{10}{99}$ | $\frac{100}{11}$ | 1.0 | 0.0 |
| 2c | 0.99 | 0.9 | $\frac{10}{99}$ | $\frac{100}{11}$ | 0.9 | 0.9 |
| 3a | 2.525 | 0.5 | $\frac{2}{101}$ | $\frac{200}{101}$ | 0.0 | 1.0 |
| 3b | 2.525 | 0.5 | $\frac{2}{101}$ | $\frac{200}{101}$ | 1.0 | 0.0 |
| 3c | 2.525 | 0.5 | $\frac{2}{101}$ | $\frac{200}{101}$ | 0.9 | 0.9 |

Transport is effected on individual realizations using Monte Carlo particle simulation (MC) with Woodcock sampling. The random media is modeled using the discontinuous Karhunen-Loève (KL) method presented in this chapter using the Nataf transformation and solving KL eigenvector values using the Nyström method (NM). Once the randomness of the system is characterized by a truncated KL expansion, the solution over the resulting stochastic domain of finite dimensionality is solved either using random sampling (RS) or stochastic collocation (SC). We reserve for future work the use of the polynomial chaos expansion (PCE) on this benchmark suite.

### 6.6.2 Random Sampling and Monte Carlo Convergence

To compare solutions against the benchmark suite the error in the computation must be understood. In this section RS and MC relative error is estimated for benchmark problems using case 3c on a slab of thickness $L = 10.0$ cm. We choose a Nataf and Nyström discretization order, $N_{Ny} = 300$ and Nyström interpolation scheme, "linear", that, based on experience, we expect to produce a relative error smaller than the order of error we are interested in. Random sampling and Monte Carlo error are estimated by solving a problem with two ensembles of randomly sampled realizations for an arbitrarily chosen KL truncation order $K = 7$ and number of MC particles $N = 10^4$. The most converged solution of one ensemble is used to approximate the exact solution and relative errors are computed using the other ensemble. The most converged solutions are shown in Table 6.11.

TABLE 6.11: Most Converged Random Sampling Solutions for Adams Benchmark Cases RS and MC Error Estimating

| Solution Method | Num. Real. $R$ | $\langle T \rangle$ | $\sqrt{v_T}$ | $\langle R \rangle$ | $\sqrt{v_R}$ |
|---|---|---|---|---|---|
| RS(MC,KL,NM) | $1 \times 10^5$ | 0.11234 | 0.24617 | 0.44064 | 0.10178 |
| RS(MC,KL,NM) | $1 \times 10^5$ | 0.11014 | 0.24350 | 0.44152 | 0.10056 |

Random sampling convergence plots are given in Figures 6.22 and 6.23 for leakage value means and standard deviations. Random sampling convergence lines are provided to show the approximate RS convergence.
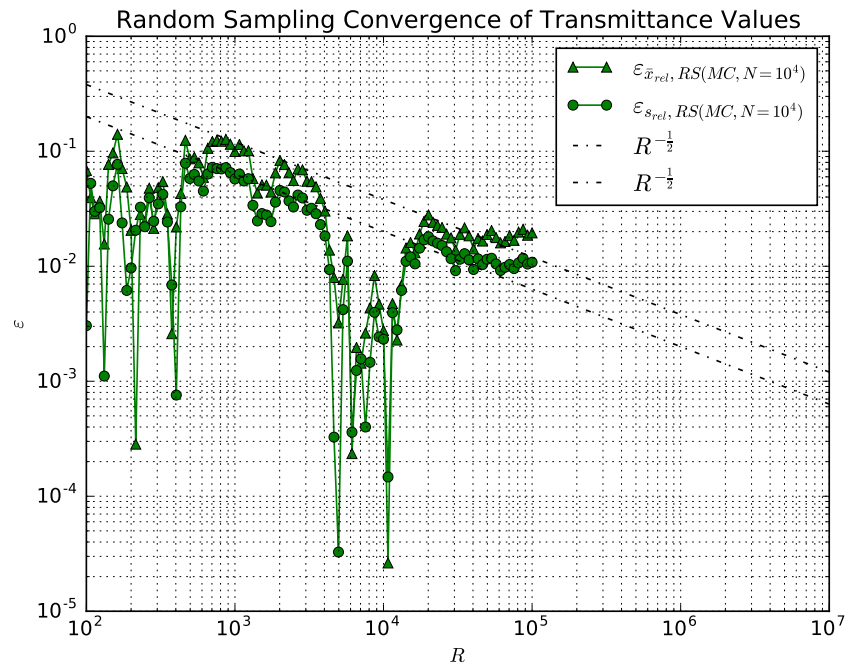
FIGURE 6.22: Uncollided Flux Transmittance Values for Discontinuous KL Implementation - Random Sampling Convergence Estimate Transport with Scattering Solutions
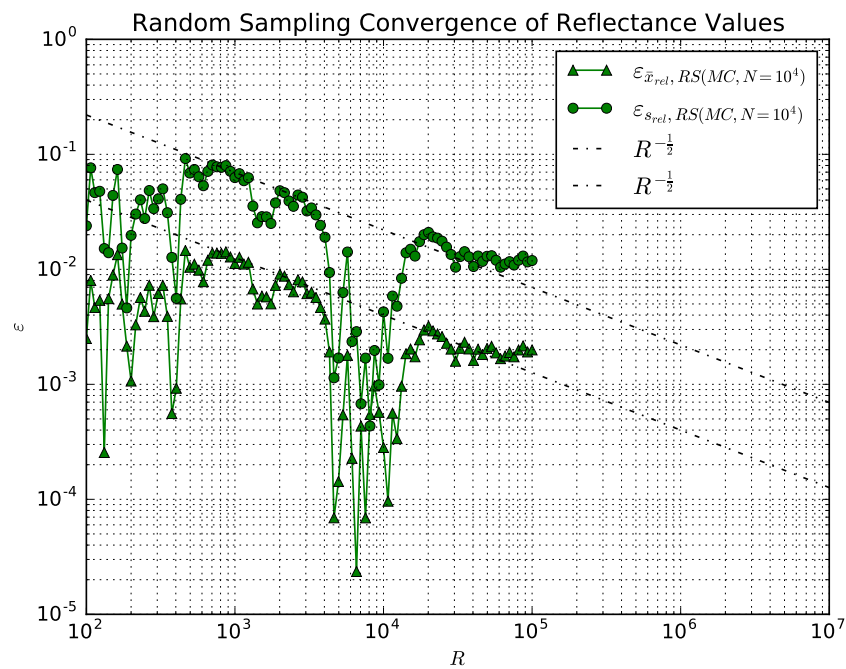


FIGURE 6.23: Uncollided Flux Reflectance Values for Discontinuous KL Implementation - Random Sampling Convergence Estimate Transport with Scattering Solutions

One quickly notes that the relative error values plateau such that the solution has ceased to further converge. This is the error at which the other errors in the system become dominant, and while the random sampling relative error continues to get smaller, this

cannot be seen due to the other errors in the system. Since problem parameters have been chosen such that the Monte Carlo error is expected to be dominant, the Monte Carlo error for the number of particles chosen can be approximated as the relative error at which the RS convergence plateaus. The MC error in these computations is the difference between the leakage values produced with two different sets of particle histories, and thus contains MC error of the same magnitude in the approximated-as-exact solution and the solution used to converge towards that solution. The true MC error for the number of particle histories chosen is thus likely to be about half of the value at which the RS convergence plateaus. We conservatively estimate the MC error on one ensemble as the error at which the plateaus occur, recognizing that the values due to the Monte Carlo solves could, due to statistical variation, be closer together than the sum of the two MC errors. The RS error can be approximated for various numbers of samples for each quantity of interest through extrapolation of the observed convergence.

We estimate RS and MC error and use these estimates to choose the number of random samples $R$ and the number of particle histories $N$ which must be used to yield a desired solution relative error. This provides some confidence that solutions near to or far from benchmark values are not due to statistical happenstance.

We estimate the MC errors for the number of particle histories, $N = 1 \times 10^4$, based on the relative errors at which the RS convergence plateaus, and record these error estimates in Table 6.12.

TABLE 6.12: Monte Carlo Error Estimates for Benchmark Case

|  | $\langle T \rangle$ | $\sqrt{v_T}$ | $\langle R \rangle$ | $\sqrt{v_R}$ |
|---|---|---|---|---|
| Relative Error | $1.8 \times 10^{-2}$ | $1 \times 10^{-2}$ | $2 \times 10^{-3}$ | $1.2 \times 10^{-2}$ |

Extrapolating relative error estimates using the RS error convergence lines in Figures 6.22 and 6.23 and MC relative error estimates in Table 6.12, we choose to use $R = 200,000$ realizations each solved with $N = 100,000$ particle histories for selected benchmark cases and estimate the RS, MC and total relative error for each quantity of interest according to the values in Table 6.13

TABLE 6.13: Random Sampling and Monte Carlo Error Estimates for Chosen Benchmark Solution Parameters

| | $\langle T \rangle$ | $\sqrt{v_T}$ | $\langle R \rangle$ | $\sqrt{v_R}$ |
|---|---|---|---|---|
| RS Relative Error | $8 \times 10^{-3}$ | $5 \times 10^{-3}$ | $1.3 \times 10^{-3}$ | $5 \times 10^{-3}$ |
| MC Relative Error | $5.7 \times 10^{-3}$ | $3.2 \times 10^{-3}$ | $6.3 \times 10^{-4}$ | $3.8 \times 10^{-3}$ |
| Total Relative Error | $1.4 \times 10^{-2}$ | $8.2 \times 10^{-3}$ | $1.9 \times 10^{-3}$ | $8.8 \times 10^{-3}$ |

### 6.6.3 Efficacy and Efficiency of Discontinuous KL method on Benchmark Suite

Use of the discontinuous KL method is investigated against the nine benchmark cases and the three slab lengths presented in the Adams, Larsen, and Pomraning paper. The numerical difficulty present when covariance values are close to 1 presented in Section 6.3.2 was a limiting factor for a significant number of case and slab length combinations. Larger slabs allowed the covariance in the slab to become sufficiently small such that many values of the Gaussian process covariance could be solved, and the rest could be approximated using a polynomial fit. Smaller slabs did not allow the covariance in the slab to become small enough to solve values of the Gaussian process covariance. The lack of ability to solve some of these benchmark cases is not a limitation of the discontinuous KL method, but a technical challenge. A careful examination of numerical evaluation of the Gaussian process covariance $c_g(r)$ based on values of the material index covariance $c_Z(r)$ in Eq. (6.26) such that covariance values closer to one can be solved is a topic of future work. The discontinuous KL method was not able to be used due to this numerical challenge for cases 2a, 2b, 2c, 3a, 3b, or 3c with a slab length of 1 cm or for any of these cases for a slab length of 0.1 cm.

For the remaining case and slab length combinations, convergence towards the benchmark solutions was observed with an increased KL truncation order $K$. Table 6.14 contains the number of terms that was estimated to produce results about as accurate as the Levermore-Pomraning closure using $R = 5,000$ and $N = 5,000$ [2]. It also shows the number of Gaussian process covariance values that were not able to be solved due to the numerical difficulty in the evaluating Eq. (6.26), but were instead approximated through polynomial interpolation.

TABLE 6.14: Number of KL Terms Required to Approximate LP Leakage Values Accuracy

| Case #, L | Case Letter | | | Num. Values |
| --- | --- | --- | --- | --- |
| | a | b | c | Interpolated |
| 1,$L = 1.0$ | $K \approx 7$ | $K \approx 70$ | $K \approx 10$ | 31/300 |
| 1,$L = 10.0$ | $K \approx 70$ | $K \approx 120$ | $K \approx 25$ | 3/300 |
| 2,$L = 10.0$ | $K \approx 7$ | $K \approx 15$ | $K \approx 12$ | 31/300 |
| 3,$L = 10.0$ | $K \approx 3$ | $K \approx 9$ | $K \approx 5$ | 7/300 |

In all cases, we observe less accurate solutions with lower truncation orders $K$ and more accurate solutions with higher truncation orders $K$, such that this discontinuous KL method outperforms the LP closure for values of $K$ roughly larger than those shown in Table 6.14. It is useful to note that the discontinuous KL method provides estimates of quantity standard deviation values whereas the atomic mix and LP approaches provide only mean values. Furthermore, this method enables construction of a surrogate model using the polynomial chaos expansion, whereas the other approximate methods yield only mean values.

We note that the discontinuous KL method produces mean leakage values approximately as accurate as the LP closure, the most accurate commonly used approximate method, with few KL terms for several cases and slab thickness combinations. The two best are case 3a and 3c with a slab thickness of $L = 10$. We demonstrate the accuracy of this method using random sampling (RS) and the efficiency of the method using stochastic collocation (SC) for these two case and slab length combinations. Leakage values are computed using the number of random samples $R = 2 \times 10^5$ and Monte Carlo histories $N = 1 \times 10^5$ such that the RS and MC relative error for each leakage value is estimated as about 1%. When solving using SC, the relative error due to the MC solution method is estimated as less than 1%. We choose to solve these two case and slab thickness combinations using a KL truncation of $K = 5$. Based on Table 6.14, we expect the discontinuous KL method to produce more accurate results than the LP closure for case 3a and results about as accurate as the LP closure for case 3c with this KL truncation order. An anisotropic collocation grid of $\mathbf{Q} = \{5, 4, 4, 3, 3\}$ is chosen based on intuition for the SC solve for each case. Discontinuous KL leakage results are compared against

benchmark solutions, atomic mix (AM) solutions, and LP solutions provided in [2] in Tables 6.15 and 6.16. Relative errors, for which a negative relative error represents an approximate solution smaller than the benchmark solution, are also provided. In these tables $KL_R$ represents the discontinuous KL method solved using random sampling and $KL_S$ represents the discontinuous KL method solved using stochastic collocation.

TABLE 6.15: Transmittance Mean Values

| | $\langle T \rangle$ | | | | | $\varepsilon_{\bar{x}_{rel},\langle T \rangle}$ | | | |
| Case | Bench | AM | LP | $KL_R$ | $KL_S$ | AM | LP | $KL_R$ | $KL_S$ |
|---|---|---|---|---|---|---|---|---|---|
| 3a | 0.16350 | 0.06677 | 0.24038 | 0.17712 | 0.17391 | -0.592 | 0.470 | 0.083 | 0.064 |
| 3c | 0.10457 | 0.00386 | 0.11967 | 0.12063 | 0.12426 | -0.963 | 0.144 | 0.154 | 0.188 |

TABLE 6.16: Reflectance Mean Values

| | $\langle R \rangle$ | | | | | $\varepsilon_{\bar{x}_{rel},\langle R \rangle}$ | | | |
| Case | Bench | AM | LP | $KL_R$ | $KL_S$ | AM | LP | $KL_R$ | $KL_S$ |
|---|---|---|---|---|---|---|---|---|---|
| 3a | 0.69109 | 0.78629 | 0.60759 | 0.67696 | 0.67882 | 0.138 | -0.121 | -0.020 | -0.018 |
| 3c | 0.44516 | 0.47819 | 0.32612 | 0.43617 | 0.43240 | 0.074 | -0.267 | -0.020 | -0.029 |

The discontinuous KL method produces relative errors less than the AM approximation for both leakage values in both cases. For case 3a it produces relative errors of about 7% and 2%, considerably less than the LP method at about 47% and 27%. The discontinuous KL method also does well compared to the LP closure for the 3c case, producing relative errors of about 17% and 3% versus the LP closure's 14% and 27%. For these problems, the discontinuous KL method is a viable option for computing leakage means compared to other approximate methods. It provides additional benefits, including standard deviation estimates and the ability to create a surrogate model of response values over the stochastic domain, further promoting its utility.

While the discontinuous KL method may not be more efficient than random sampling by constructing realizations using the Chord Length Sampling method, it can provide significant efficiency gains when few enough KL terms are required to approximate the solution within a chosen tolerance. For these problems, the discontinuous KL method required about $200,000$ realizations to produce errors of about 2% when using random sampling, but only 1,200 realizations when using stochastic collocation. Since it is reasonable to assume that random sampling using the CLS method required roughly

as many realizations as the discontinuous KL method to achieve a similar error, it is clear that the discontinuous KL method using stochastic collocation is significantly more efficient in this case.

Furthermore, the LP closure and use of the CLS method to create realizations both rely on the Markovian-mixing statistics, producing an exponential covariance function. The discontinuous KL method does not require an exponential covariance.

In conclusion, we present a Nataf transformation of the KL expansion to model discontinuous, random media for radiation transport applications. The numerical evaluation of the Gaussian process covariance needed by the KL expansion in order to use the Nataf transformation contains a numerical challenge in that covariance values near one do not evaluate very cleanly. More work should be done to evaluate the Gaussian process covariance for these values. Solutions using the method do converge towards benchmark values for problems including reflectance on a semi-infinite slab of materials with a constant scattering ratio, computation of transmittance on a slab of absorption-only media, and on the benchmark suite published by Adams, Larsen, and Pomraning. The discontinuous KL method provides advantages over some other approximate methods by providing higher-order statistics on quantities of interest and the ability to create a surrogate model. In some cases the discontinuous KL method is considerably more efficient than random sampling through use of stochastic collocation. In yet other cases, the discontinuous KL method ought to be a viable approach to modeling geometry when there is no other statistically faithful, known method. While the usability of the method may be increased by a more careful approach to solving the Gaussian process covariance, the efficiency may also be improved through use of dimensional reduction techniques or more advanced stochastic collocation grids such as grids that are not only anisotropic but also sparse. The applicability of the method to problems with other covariance functions is a potentially very useful application of the discontinuous KL method, and can be investigated not only in 1D problems, but 2D or 3D.

# Chapter 7

# Conclusions and Future Work

The Karhunen-Loève (KL) expansion has been used to model spatially continuous and discontinuous random media, reducing the stochastic variability from an uncountably infinite set, through truncation of the KL expansion, to a finite set of random variables. Random sampling (RS) and stochastic collocation (SC) were used to solve quantity of interest (QoI) response values over the remaining stochastic domain. Transport was solved over KL realizations created at nodes of RS and SC schemes using Monte Carlo (MC) particle simulation with Woodcock sampling. The polynomial chaos expansion (PCE) was used to create a surrogate model of the QoI response over the stochastic domain, enabling construction of a probability density function (PDF) of the QoI by sampling from the surrogate model cheaply. A lognormal transformation of the Gaussian random process created by the KL expansion was used to model continuous random media, and a Nataf transformation was used on the Gaussian random process created by the KL expansion to model discontinuous random media. KL eigenvalues and eigenvectors were solved numerically using the Nyström method (NM), and several Nyström interpolating schemes were investigated such that KL eigenvectors can be sampled from as eigenfunctions. In these random media cases, and for a purely-absorbing problem with known geometry but uncertain cross section coefficients, the error contribution to the QoI of solver methods was examined, helping provide confidence in transport results and choose solution method parameters for efficient computation.

The error analysis techniques used here enabled a better understanding of the error contributions from each solution method. Such error analysis proved useful in bounding the

total error of the computation and in determining what system parameters to choose in order to solve efficiently. This was especially true when deciding the KL truncation order to select, since the number of terms kept in the Karhunen-Loève expansion determines the resulting number of stochastic dimensions yet to be resolved by RS or SC. The efficiency of the random sampling method, being dimensionally-agnostic, is not significantly affected by the choice of KL truncation order, but the viability of the stochastic collocation method, and the use of the polynomial chaos expansion built using the SC method, hinges largely on the number of stochastic dimensions in the problem. Therefore, especially when using stochastic collocation, it is often advantageous to allow the KL truncation to contribute much of the total system error in an effort to reduce the overall cost, making KL truncation error estimates a quantity of special importance.

The lognormal transformation of the KL-modeled random processes proved useful in modeling continuously varying random media. The prime contributions of this method were having a statistically based approach with which to model spatially continuous media while ensuring that cross section values in realizations are always positive. Additional value to this investigation was that ensembles requiring sufficiently few KL terms can be solved considerably more efficiently using SC than RS, and that the PCE can be used to create a surrogate model which, once built, can populate a response PDF much more efficiently than RS.

The Nataf transformation of the Gaussian random KL expansion was effective in modeling spatially discontinuous random media with Markovian statistical mixing. This method offers an approximate method which, with enough KL terms kept in truncation, is more accurate than the other approximate methods currently used for this problem type. If the number of KL terms required is sufficiently small, the discontinuous KL method can solve quantities of interest more efficiently than random sampling. The benefits of this method extend beyond materials with Markovian statistical mixing, however, since the method is applicable to processes with other covariance functions. The method may therefore be able to provide solutions to mixing problems which currently do not have a statistically faithful solution method.

Though this work has produced useful results, it has also opened up many questions which would serve as worthwhile topics for further investigation.

The error analysis techniques outlined and demonstrated here help invaluably in determining error sources, and total error in a system. The value of this analysis may translate well into development of an adaptive algorithm which takes advantage of error bounds and knowledge of the extra computational cost of changing system parameters to smartly choose which parameters among the various methods being used to increase to most efficiently solve the problem.

The lognormal KL modeling proved effective in modeling many material properties for one material. It may be of interest to model the density profile of, or another quality of, more than one material. It would be easy to model two materials and assume that they are independent of one another, but this is rarely, if ever, true in nature. Development of a way to handle partial or full correlation between two or more random processes using the lognormal transformation would increase the applicability of this method to more problem types.

While the discontinuous KL method has already proved to be useful for 1D problems with Markovian mixing, this method contains perhaps the most obvious next steps for further investigation. First of all, a limiting factor so far has been computing Gaussian covariance values near one. Better ways for computing these values should be investigated, as evaluation of covariance values closer to one would greatly expand the number of problems this method would be effective in solving. Additionally, the problems that would become available for solution are those for which this method tends to excel–problems with large correlation lengths which resultantly require few KL terms. Especially following a better way to evaluate covariance values near one, a more rigorous investigation of solutions using this method against the Adams, Larsen, and Pomraning benchmark suite would be of value. Errors should be more carefully understood, and additional transport results generated for comparison against the benchmark and the other approximate methods. The apparent non-monotonic convergence of solutions generated using stochastic collocation should be investigated further and understood such that the utility of quadrature methods applied over the discontinuous KL random variables can be better understood. The method could be investigated for use with materials mixed according to other material index mixing statistics, and thus be applied to a much wider set of problems. The method could be investigated in 2D or 3D, improving the applicability of the method to more problem types.

Several further investigations of value can be performed over the SC or PCE solution methods and applied to the continuous and/or the discontinuous method. For example, dimension reduction techniques could be applied to the KL terms to determine the error contribution not only of individual terms, but of sets of terms. This may allow for more accurate and therefore efficient truncation. Sparse collocation grids could be used to improve the efficiency of the stochastic collocation implementation. In a related fashion a Lagrange polynomial-based PCE would be of interest, allowing collocation nodes to have much more freedom and thus be able to be more optimally placed. Sometimes quantities of interest are not well characterized by moments of a response, but by values like the maximum or minimum possible value, or other qualities of the response PDF. It may be of value to investigate other QoIs based on qualities of the PDF, and measure convergence error as a function of some measure of PDFs. Additionally, straightforward implementation of the PCE can create surrogate models which allow for negative values, and in some applications this is unphysical. A positive-preserving transformation could be investigated for use with the PCE models of the response such as a lognormal transformation.

The physical solver, Monte Carlo with Woodcock sampling, also provides a potential source for efficiency gains. This algorithm may be able to be made more efficient if distance to collision calculations are limited to portions of the geometry near the particle for which the magnitude of the cross section does not significantly change. This would reduce the number of rejections per accepted particle interaction and improve the efficiency of the implementation.

# Appendix A

# Generation of Gaussian-distributed Random Samples

Different portions of this work were implemented in either Python 2.7 or modern Fortran.

Packages are easily accessible for generating Gaussian-distributed random samples in Python 2.7. We used, at various times, "random.gauss()", available in the standard Python 2.7 distribution or "numpy.random.randn()", available in the "numpy" package.

Packages also exist for generation of Gaussian-distributed random samples in Fortran. Instead of using such a package, we chose to write our own functions for Gaussian-sample generation. We generated Gaussian-distributed variables using the inverse sampling method and a Box-Muller transform. The Box-Muller transform is computationally faster, so in most cases we elect using it, though the derivation of the inverse sampling method is useful in understanding how to sample from a distribution. Additionally, the direct mapping of uniformly distributed variables to Gaussian-distributed variables can be a useful property for applications slightly beyond the scope of this work.

## A.1  Inverse Sampling for Gaussian-distributed Samples

We integrate over the standard Gaussian PDF such that the cumulative probability of the Gaussian distribution to value $z$ is equal to the cumulative probability of uniformly distributed $x$:

$$\eta = \int_{-\infty}^{z} \frac{1}{\sqrt{2\pi}} \exp\left[-\frac{z'^2}{2}\right] dz'. \tag{A.1}$$

We substitute using $t'^2 = \frac{z'^2}{2}$ and re-write Eq. (A.1) as

$$\eta = \frac{1}{2} \frac{2}{\sqrt{\pi}} \int_{-\infty}^{\frac{z}{\sqrt{2}}} \exp\left[-t'^2\right] dt'. \tag{A.2}$$

We integrate for either $\frac{z}{\sqrt{2}} < 0$ or $\frac{z}{\sqrt{2}} > 0$ and discover in each case

$$\eta = \frac{1}{2} \frac{2}{\sqrt{\pi}} \left( -\int_{0}^{-\infty} \exp\left[-t'^2\right] dt' + \int_{0}^{z/\sqrt{2}} \exp\left[-t'^2\right] dt' \right). \tag{A.3}$$

We then utilize the error function and its inverse [74]–

$$\operatorname{erf}(t) = \frac{2}{\sqrt{\pi}} \int_{0}^{t} \exp\left[-t'^2\right] dt'; \qquad \operatorname{erf}(\infty) = 1; \qquad \operatorname{erf}(-\infty) = -1 \tag{A.4}$$

–to solve for the Gaussian-distributed variable $z$ as a function of the uniformly distributed variable $\eta$:

$$z = \sqrt{2}\operatorname{erf}^{-1}(2\eta - 1). \tag{A.5}$$

If we were integrating over the basis function $\exp\left[-z'^2\right]$ instead of a standard normal probability distribution, Eq. (A.1) and the solution for $z$, Eq. (A.5), would instead be:

$$\eta = \int_{-\infty}^{z} \exp\left[-z'^2\right] dz', \text{ and} \tag{A.6a}$$

$$z = \operatorname{erf}^{-1}(2\eta - 1). \tag{A.6b}$$

## A.2   The Box-Muller Transform

The Box-Muller [76] transformation maps a two-dimensional uniform distribution to a bivariate normal distribution. Two psuedo-random numbers generated from a uniform distribution over zero to one can therefore be transformed to two psuedo-random, Gaussian-distributed random variables. Uniformly distributed random samples $\eta_1$ and $\eta_2$ are transformed to Gaussian-distributed random variables $z_1$ and $z_2$ according to

$$z_1 = \sqrt{-2\ln\eta_1}\cos(2\pi\eta_2), \text{ and} \tag{A.7a}$$

$$z_2 = \sqrt{-2\ln\eta_1}\sin(2\pi\eta_2). \tag{A.7b}$$

# Appendix B

# Quadrature Rules

## B.1  Brief Survey of Quadrature Rules

Table B.1 compares several polynomial-based quadrature rules.

Table B.1: Selected Quadrature Rules

| Quadrature Rule | Associated Polynomial | $p(\xi)$ | Support | Nested? |
|---|---|---|---|---|
| Gauss-Legendre (GL) | Legendre | $\frac{1}{2}$ | $[-1, 1]$ | no |
| Gauss-Patterson (GP) | Legendre | $\frac{1}{2}$ | $[-1, 1]$ | yes |
| Gauss-Hermite (GH) | Hermite (physicists') | $\exp[-\xi^2]$ | $(-\infty, \infty)$ | no |
| Genz-Keister (GK) | Hermite (physicists') | $\exp[-\xi^2]$ | $(-\infty, \infty)$ | yes |
| Clenshaw-Curtis (CC) | Chebyshev | variable | variable | yes |

We use GL and GH quadrature rules [77] in this work and introduce them here. We do not use GP [78], GK [79], or CC [80, 81] quadrature, but include them for brief discussion in Section B.2, as any of them would be logical choices for extension of this work.

Gaussian quadratures choose quadrature nodes at roots of Askey polynomials that correspond to the relevant basis function. They integrate polynomials of degree $2Q - 1$ exactly over that density, where $Q$ is the quadrature order. They do not exactly integrate other functions over the basis function, but may still be the preferred option.

174

Quadrature weights sum to a value related to the integral of the basis function, and vary depending on what technique is used to generate the weights.

Gauss-Legendre (GL) quadrature is based on Legendre polynomials and integrates over a basis function which is a uniform probability density function on $[-1, 1]$. Through mapping, GL quadrature can be used to integrate over $[a, b]$. We discuss this mapping in Section B.3.

Gauss-Hermite (GH) quadrature is based on Hermite polynomials and integrates over a Gaussian basis function on $[-\infty, \infty]$. GH quadrature is defined to integrate over a Gaussian basis function often convenient in physics, $\exp[-\xi^2]$, and uses the "physicists'" Hermite polynomials to define quadrature nodes. In this work we integrate over the standard normal Gaussian $\frac{1}{\sqrt{2\pi}} \exp\left[ -\frac{\xi^2}{2} \right]$ basis function. This basis function is based on the "probabilists'" Hermite polynomials. We discuss the required translation of GH quadrature for use over the standard normal basis function in Section B.4.

## B.2 Nested Quadratures

At times it may be advantageous to increase a quadrature order and integrate a function more exactly. This operation is made more efficient if solutions of the underlying problem are reused, which requires reuse of quadrature nodes when increasing the quadrature order. Quadrature rules that reuse quadrature nodes at higher orders are called "nested" quadratures. The Gauss-Kronrod quadrature is a $Q + 1$ point extension to GL quadrature. It reuses all nodes from a $Q$-ordered GL quadrature, and chooses $Q + 1$ new nodes to optimally integrate a polynomial while reusing the existing nodes. It can be used to offer an error estimate of a $Q$-ordered GL quadrature. The Gauss-Kronrod approach has been generalized to add $Q+1$ nodes optimally to Gauss-Legendre or Gauss-Kronrod quadrature of order $Q$. This more general nested quadrature is called either Gauss-Patterson (GP) or Kronrod-Patterson quadrature. Gauss-Patterson quadrature is capable of building on itself and the underlying Gauss-Legendre quadrature an infinite number of times, and is thus a "fully-nested" quadrature rule. Genz-Keister (GK) quadrature is a similar fully-nested extension of Gauss-Hermite quadrature. Fully-nested

quadratures are especially useful for convergence studies in which a quantity of interest is calculated repeatedly with increasing quadrature orders. The reuse of solutions calculated at all existing nodes can save considerable computational time.

Clenshaw-Curtis quadrature is a fully-nested quadrature based on Chebyshev polynomials. Though a given order of GL or GH quadrature integrates polynomials more exactly than CC quadrature of the same order, Gaussian quadratures do not necessarily integrate other functions more exactly. Additionally, CC quadrature does not require an initial quadrature scheme to begin nesting from: Its nodes are always in the same locations whereas the placement of fully-nested GP and GK quadrature nodes rely on initial GL or GH schemes from which to begin the nesting process. In part for these reasons, CC may be the preferred quadrature for an application in spite of an inferior optimality for non-nested, polynomial integration. We do not use CC quadrature in this work, though it may useful, especially if we desire to perform convergence studies on some of the larger problems in this work.

## B.3 Mapping of Gauss-Legendre Quadrature to Arbitrary Finite Support

Gauss-Legendre quadrature nodes integrate over $[-1, 1]$. To integrate over $[a, b]$, we translate the value of each node $\xi^q$ to $\xi'^q$:

$$\xi'^{(q)} = \frac{b - a}{2}\xi^{(q)} + \frac{b + a}{2}. \tag{B.1}$$

The integral of the basis function determines what quadrature weights sum to:

$$\sum_{q=1}^{Q} w^{(q)} = \int_a^b p(\xi)d\xi. \tag{B.2}$$

Gauss-Legendre weights given by Python package numpy.polynomial.legendre.leggauss() are based on the weight function $p(\xi) = 1$ and an integral taken over $[-1, 1]$ and sum to 2. We define our weight function $p(\xi) = \frac{1}{b-a}$ and wish to integrate over $[a, b]$ such that our weights sum to 1 for any choice of $a$ and $b$. We normalize $w^{(q)}$, the weights given by

numpy.polynomial.legendre.leggauss(), to $w'^{(q)}$:

$$w'^{(q)} = \frac{b-a}{2} w^{(q)}. \tag{B.3}$$

## B.4 Mapping of Gauss-Hermite Quadrature to the Standard Normal Basis Function

Gauss-Hermite quadrature integrates function $f(\xi)$ over Gaussian basis function $p(\xi) = \exp[-\xi^2]$:

$$\mathbb{E}[f(\xi)] = \int_{-\infty}^{\infty} f(\xi) \exp\left[-\xi^2\right] d\xi \approx \sum_{q=1}^{Q} w^{(q)} f(\xi^{(q)}). \tag{B.4}$$

We desire integration over $\exp\left[-\frac{\xi^2}{2}\right]$, and choose to multiply our basis function by $\frac{1}{\sqrt{2\pi}}$, yielding $p'(\xi) = \frac{1}{\sqrt{2\pi}} \exp\left[-\frac{\xi^2}{2}\right]$, so that the integral of the basis function is equal to 1:

$$\int_a^b p'(\xi) d\xi = \int_{-\infty}^{\infty} \frac{1}{\sqrt{2\pi}} \exp\left[-\frac{\xi^2}{2}\right] d\xi = 1. \tag{B.5}$$

Since the integral of the basis function is 1, the basis function can also be a probability density. We must map GH nodes and weights defined over basis function $p(\xi) = \exp[-\xi^2]$ and given by Python package numpy.polynomial.hermite.hermgauss(), to GH nodes and weights defined over a standard normal basis function $p'(\xi) = \frac{1}{\sqrt{2\pi}} \exp\left[-\frac{\xi^2}{2}\right]$.

We begin with the integral over which GH quadrature is typically defined:

$$\int_{-\infty}^{\infty} \exp\left[-\xi^2\right] f(\xi) d\xi. \tag{B.6}$$

We substitute $\xi' = \sqrt{2}\xi$:

$$\int_{-\infty}^{\infty} \exp\left[-\frac{\xi'^2}{2}\right] f\left(\frac{\xi'}{\sqrt{2}}\right) \frac{d\xi'}{\sqrt{2}}. \tag{B.7}$$

We normalize the integral to 1 by multiplying by $\frac{1}{\sqrt{\pi}}$:

$$\int_{-\infty}^{\infty} \frac{1}{\sqrt{2\pi}} \exp\left[-\frac{\xi'^2}{2}\right] f\left(\frac{\xi'}{\sqrt{2}}\right) d\xi'. \tag{B.8}$$

We have constructed the form desired for our integration and can apply the same mapping to quadrature nodes and weights:

$$\xi'^{(q)} = \sqrt{2}\xi^{(q)} \tag{B.9a}$$

$$w'^{(q)} = \frac{w^{(q)}}{\sqrt{\pi}}. \tag{B.9b}$$

# Appendix C

# Orthogonal Polynomials and Associated Quadrature Rules

## C.1   Survey of Selected Askey Polynomials

Askey and Wilson [46] identified a large set of orthogonal, hypergeometric polynomials over various basis functions. We display some of them in Table C.1 [44, 46, 74].

TABLE C.1: Example Askey Polynomials and Distributions

| Polynomial $\Gamma(\xi)$ | Distribution $\xi$ | Basis Function $p(\xi)$ | Support |
|---|---|---|---|
| Legendre | uniform | $\frac{1}{2}$ | $[-1, 1]$ |
| Jacobi | beta | $(1-\xi)^{\alpha}(1+\xi)^{\beta}$ | $[-1, 1]$ |
| Laguerre | gamma | $\exp[-\xi]$ | $[0, \infty)$ |
| Hermite (probabalists') | standard Gaussian | $\exp\left[-\frac{\xi^2}{2}\right]$ | $(-\infty, \infty)$ |
| Hermite (physicists') | Gaussian | $\exp[-\xi^2]$ | $(-\infty, \infty)$ |

We note that both forms of the Hermite polynomial have a Gaussian basis function [74]. The probabilists' Hermite polynomial, however, is orthogonal over a standard normal distribution $\left(p(\xi) = \frac{1}{\sqrt{2\pi}}\exp\left[-\frac{\xi^2}{2}\right]\right)$. When the basis function is equal to a standard normal, the basis function is zero mean and unit variance, vis., $\mathbb{E}[p(\xi)] = 0$ and $\mathbb{V}[p(\xi)] =$

179

1. Except as specified, namely in Appendix C, the Hermite polynomials used in this work are the probabilists' form of Hermite polynomials.

## C.2 Askey Polynomial Orthogonality

Each Askey polynomial is orthogonal over its corresponding basis function:

$$\int_{\xi} \Gamma_i(\xi)\Gamma_j(\xi)p(\xi)d\xi = \frac{1}{a}\delta_{ij}. \tag{C.1}$$

As long as the underlying basis functions are independent, multivariate Askey polynomials factor into the product of univariate Askey polynomials as in Eq. (3.41) and we can express the multidimensional Askey polynomial orthogonality as a product of the one-dimensional relationship in Eq. (C.1):

$$\int_{\xi_1}\cdots\int_{\xi_D} \Phi_{\mathbf{i}}(\boldsymbol{\xi})\Phi_{\mathbf{j}}(\boldsymbol{\xi})p(\boldsymbol{\xi})d\boldsymbol{\xi} = \frac{1}{a_{\mathbf{j}}}\delta_{\mathbf{ij}}. \tag{C.2}$$

In this work we utilize Legendre polynomial orthogonality. We write Eqs. (C.1) and (C.2) more explicitly for Legendre polynomials:

$$\int_{-1}^{1} P_i(\xi)P_j(\xi)\frac{1}{2}d\xi = \frac{1}{2j+1}\delta_{ij} = \frac{1}{a}\delta_{ij}; \tag{C.3}$$

$$\int_{-1}^{1}\cdots\int_{-1}^{1} P_{i_1}(\xi_1)P_{j_1}(\xi_1)\cdots P_{i_D}(\xi_D)P_{j_D}(\xi_D)\left(\frac{1}{2}\right)^{D}d\xi_1\cdots d\xi_D$$
$$= \frac{1}{(2j_1+1)\cdots(2j_D+1)}\delta_{i_1 j_1}\cdots\delta_{i_D j_D} = \frac{1}{a_{\mathbf{j}}}\delta_{\mathbf{ij}}. \tag{C.4}$$

We also utilize the probabilists' Hermite polynomials. We write Eqs. (C.1) and (C.2) more explicitly for Hermite polynomials over a standard normal basis function:

$$\int_{-\infty}^{\infty} H_i(\xi)H_j(\xi)\frac{1}{\sqrt{2\pi}}\exp\left[-\frac{\xi^2}{2}\right]d\xi = j!\,\delta_{ij} = \frac{1}{a}\delta_{ij}; \tag{C.5}$$

$$\int_{-\infty}^{\infty}\cdots\int_{-\infty}^{\infty} H_{i_1}(\xi_1)H_{j_1}(\xi_1)\cdots H_{i_D}(\xi_D)H_{j_D}(\xi_D)\left(\frac{1}{\sqrt{2\pi}}\right)^{D}\exp\left[-\frac{\xi_1^2}{2}\right]\cdots\exp\left[-\frac{\xi_D^2}{2}\right]d\xi_1\cdots d\xi_D$$
$$= j_1!\cdots j_D!\,\delta_{i_1 j_1}\cdots\delta_{i_D j_D} = \frac{1}{a_{\mathbf{j}}}\delta_{\mathbf{ij}}. \tag{C.6}$$

Table C.2 summarizes orthogonality parameters used in this work. Note Legendre polynomials are only orthogonal over $[-1, 1]$; GL quadrature can be mapped to $[a, b]$.

TABLE C.2: Legendre and Probabilists' Hermite Polynomial Orthogonality Parameters

| Polynomial | $\Gamma(\xi)$ | $p(\xi)$ | $\frac{1}{a}$ | Support |
|---|---|---|---|---|
| Legendre | $P(\xi)$ | $\frac{1}{2}$ | $\frac{1}{2j+1}$ | $[-1, 1]$ |
| Hermite | $H(\xi)$ | $\frac{1}{\sqrt{2\pi}} \exp\left[-\frac{\xi^2}{2}\right]$ | $j!$ | $(-\infty, \infty)$ |

# Appendix D

# Semi-infinite Slab, Constant Scattering Ratio Reflectance Benchmark Script

```python
#!/usr/bin/env python
import numpy as np
import random


#Input
numParts  = 1000000      #number of particles
scatrat   = 0.5          #constant scattering ratio


#Basic transport driver
i,reflections = 0,0      #initialize counter and tally
while True:              #cycle through particles
    #initialize particle
    x,mu = 0.0,1.0       #initialize particle state
    #simulate particle
    while True:
        dc = -np.log(random.random())       #distance to collision, sig_t = 1.0
        x += dc*mu                          #effect particle streaming
        if x<0.0:                           #tally reflection events
            reflections += 1
            break
        if random.random()>scatrat: break   #if absorb, kill particle history
        else: mu = random.uniform(-1.0,1.0) #if scatter, sample new mu
    #advance to next particle or terminate particle history loop
    if i==numParts: break                   #terminate MC
    i += 1
```

```
#Print reflectance
print 'reflectance: {:14.12f}'.format( float(reflections)/numParts )
```

LISTING D.1: Minimalist Monte Carlo Semi-infinte Slab, Constant Scattering Ratio
Reflectance Python Script

# Bibliography

[1] M. L. Adams, E. W. Larsen, and G. C. Pomraning. Benchmark results for particle transport in a binary Markov statistical medium. *Journal of Quantitative Spectroscopy and Radiative Transfer*, 42(4):253–266, 1989.

[2] P. S. Brantley. A benchmark comparison of Monte Carlo particle transport algorithms for binary stochastic mixtures. *Journal of Quantitative Spectroscopy and Radiative Transfer*, 112:599–618, 2011.

[3] C. D. Levermore, G. C. Pomraning, D. L. Sanzo, and J. Wong. Linear transport theory in a random medium. *Journal of Mathematical Physics*, 27:2526–2536, 1986.

[4] G. C. Pomraning. *Linear kinetic theory and particle transport in stochastic mixtures*. World Scientific Publishing Co. Pte. Ltd., River Edge, New Jersey USA, 1st edition, 1991.

[5] G. C. Pomraning. The variance in stochastic transport problems with Markovian mixing. *Journal of Quantitative Spectroscopy and Radiative Transfer*, 56:629–646, 1996.

[6] A. K. Prinja. On the master equation approach to transport in discrete random media in the presence of scattering. *Annals of Nuclear Energy*, 31:2005–2016, 2004.

[7] M. Kac and A. Siegert. An explicit representation of a stationary Gaussian process. *Annals of Mathematical Statistics*, 18:438–442, 1947.

[8] K. Karhunen. Uber lineare methoden in der wahrscheinlichkeitsrechnung. *Annales Academiae scientiarum Fennicae, Series A. 1*, 37:3–79, 1947.

[9] O. P. Le Maître and O. M. Knio. *Spectral methods for uncertainty quantification with applications to computational fluid dynamics*. Springer, 1st edition, 2010.

[10] E. D. Fichtl and A. K. Prinja. The stochastic collocation method for radiation transport in random media. *Journal of Quantitative Spectroscopy and Radiative Transfer*, 112(4):646–659, 2011.

[11] S. J. J. Ilango, S. Sarkar, and A. Sameen. Reconstruction of 2-D porous media using Karhunen-Lóeve [sic] expansion. *Probabilistic Engineering Mechanics*, 32 (Complete):56–65, 2013.

[12] J. W. Feng, C. F. Li, Cen S., and Owen D. R. J. Statistical reconstruction of two-phase random media. *Computers & Structures*, (137):78–92, 2014.

[13] A. Park, M. M. R. Williams, A. K. Prinja, and M. D. Eaton. Modelling non-Gaussian uncertaintites and the Karhunen-Loève expansion within the context of polynomial chaos. *Annals of Nuclear Energy*, (76):146–165, 2015.

[14] W. Betz, I. Papaioannou, and D. Straub. Assessment of methods for the numerical solution of the Fredholm integral eigenvalue problem. In *11th International Conference on Structural Safety & Risk 2013*, New York, NY, June 2013. International Association for Structural Safety & Reliability.

[15] S. Sun, J. Zhao, and J. Zhu. A review of Nyström methods for large-scale machine learning. *Information Fusion*, 26:36–48, 2015.

[16] D. Ayres and M. D. Eaton. Uncertainty quantification in nuclear criticality modelling using a high dimensional model representation. *Annals of Nuclear Energy*, 80:379–402, 2015.

[17] F. Nobile, R. Tempone, and C. G. Webster. An anisotropic sparse grid stochastic collocation method for partial differential equations with random input data. *SIAM Journal of Numerical Analysis*, 5(46):2411–2442, 2008.

[18] N. Wiener. The homogeneous chaos. *American Journal of Mathematics*, 60:897–936, 1938.

[19] D. Xiu and G. E. Karniadakis. The Wiener-Askey polynomial chaos for stochastic differential equations. *SIAM Journal of Scientific Computing*, 24:619–644, 2002.

[20] L. Mathelin and M. Y. Hussaini. A stochastic collocation algorithm for uncertainty analysis. Technical Report CR-2003-212153, National Aeronautics and Space Administration, 2003.

[21] D Xiu. Efficient collocational approach for parametric uncertainty analysis. *Communications in Computational Physics*, 2(2):293–309, 2007.

[22] A. J. Olson, B. C. Franke, and A. K. Prinja. Scaling of intrusive stochastic collocation and stochastic Galerkin methods for uncertainty quantification in Monte Carlo particle transport. In *Proceedings of the Joint International Conference on Mathematics and Computation (M&C), Supercomputing in Nuclear Applications (SNA) and the Monte Carlo (MC) Method (M&C 2015)*, Nashville, TN, April 2015. American Nuclear Society.

[23] N. Metropolis and S. Ulam. The Monte Carlo method. *Journal of the American Statistical Association*, 44:335–341, 1949.

[24] I. Lux and L. Koblinger. *Monte Carlo particle transport methods: Neutron and photon calculations.* CRC Press, Boca Raton, Florida USA, 1st edition, 1991.

[25] S. A. Dupree and S. K. Fraley. *A Monte Carlo primer: A practical approach to the radiation transport.* Kluwer Academic/Plenum Publishers, New York USA, 1st edition, 2002.

[26] E. E. Lewis and Jr. Miller, W. F. *Computational methods of neutron transport.* American Nuclear Society, Inc., La Grange Park, Illinois USA, 2nd edition, 1993.

[27] E. Woodcock, T. Murphy, P. Hemmings, and T. Longworth. Techniques used in the GEM code for Monte Carlo neutronics calculations in reactors and other systems of complex geometry. In *Proceedings of the Conference on the Application of Computing Methods to Reactor Problems, ANL-7050*, Chicago, IL, May 1965. Argonne National Laboratory.

[28] N. M. Steen. A simple method to improve the efficiency of the $\Sigma_a/\Sigma_t$ estimator in Monte Carlo programs. In *Transactions of the American Nuclear Society*. American Nuclear Society, 1966.

[29] L. B. Miller. *Monte Carlo analysis of reactivity coefficients in fast reactors; General theory and applications.* PhD thesis, University of Illinois, 1967.

[30] W. A. Coleman. Mathematical verification of a certain Monte Carlo sampling technique and applications of the technique to radiation transport problems. *Nuclear Science and Engineering*, 31:76–81, 1968.

[31] L. L. Carter, E. D. Cashwell, and W. M. Taylor. Monte Carlo sampling with continuously varying cross sections along flight paths. *Nuclear Science and Engineering*, 48:403–411, 1972.

[32] R. D. Simon, C. M. J. Baker, A. J. Bird, P. Cowan, N. Davies, G. P. Dobson, T. C. Fry, A. Kyrieleis, and P. N. Smith. MONK and MCBEND: Current status and recent developments. In *Joint International Conference on Supercomputing in Nuclear Applications and Monte Carlo 2013 (SNA + MC 2013)*, Paris, France, October 2013. American Nuclear Society.

[33] B. Forestier, J. Miss, F. Bernard, A. Dorval, O. Jacquet, and B. Verboomen. Criticality calculations on pebble-bed HTR-PROTEUS configuration as a validation for the pseudo-scattering tracking method implemented in the MORET 5 Monte Carlo code. In *International Conference on the Physics of Reactors "Nuclear Power: A Sustainable Resource"*, Interlaken, Switzerland, September 2008. American Nuclear Society.

[34] J. Leppänen. Modeling of nonuniform density distributions in the Serpent 2 Monte Carlo code. *Nuclear Science and Engineering*, 174:318–325, 2013.

[35] B. Forestier. MONTE CARLO techniques implemented in the MORET code. In *MCNEG*, Teddington, UK, March 2007. MCNEG.

[36] B. Forestier et al. Criticality calculations on realistic modelling of pebble-bed HTR-PROTEUS as a validation for the Woodcock tracking method implemented in the MORET 5 Monte Carlo code. In *International Congress on Advances in Nuclear Power Plants*, Anaheim, CA, June 2008. American Nuclear Society.

[37] J. Leppänen. *Development of a new Monte Carlo reactor physics code*. PhD thesis, Helsinki University of Technology, 2007.

[38] J. Leppänen. Performance of Woodcock delta-tracking in lattice physics applications using the Serpent Monte Carlo reactor physics burnup calculation code. *Annals of Nuclear Energy*, 37:715–722, 2010.

[39] A. J. Olson, A. K. Prinja, and B. C. Franke. Woodcock Monte Carlo transport through binary stochastic media. In *Transactions of the American Nuclear Society*, Anaheim, CA, November 2014. American Nuclear Society.

[40] D. R. Reinert, E. A. Schneider, and S. R. F. Biegalski. Investigation of stochastic radiation transport methods in binary random heterogeneous mixtures. *Nuclear Science and Engineering*, 166:167–174, 2010.

[41] F. B. Brown and W. R. Martin. Direct sampling of Monte Carlo flight paths in media with continuously varying cross-sections. In *Proceedings of Nuclear Mathematical and Computational Sciences: A Century in Review, A Century Anew (M&C 2003)*, Gatlinburg, TN, April 2003. American Nuclear Society.

[42] F. B. Brown, D. Griesheimer, and W. R. Martin. Continuously varying material properties and tallies for Monte Carlo calculations. In *Proceedings of PHYSOR 2014 - The Physics of Fuel Cycles and Advanced Nuclear Systems: Global Developments*, Chicago, IL, April 2004. American Nuclear Society.

[43] R. G. Ghanem and P. D. Spanos. *Stochastic finite elements: A spectral approach.* Springer-Verlag New York, Inc., 2nd edition, 2003.

[44] E. D. Fichtl. *Stochastic methods for uncertainty quantification in radiation transport.* PhD thesis, University of New Mexico, 2009.

[45] M. M. R. Williams. The eigenfunctions of the Karhunen-Loeve integral equation for a spherical system. *Probabilistic Engineering Mechanics*, 26:202–207, 2011.

[46] R. Askey and J. Wilson. Some basic hypergeometric orthogonal polynomials that generalize Jacobi polynomials. *Memoirs of the American Mathematical Society*, 54: 1–55, 1985.

[47] L. Mathelin, M. Y. Hussaini, and T. A. Zang. Stochastic approaches to uncertainty quantification in CFD simulations. *Numerical Algorithms*, 38:209–236, 2005.

[48] M. M. R. Williams. Polynomial chaos functions and neutron diffusion. *Nuclear Science and Engineering*, 155:109–118, 2007.

[49] B. C. Franke and A. K. Prinja. Efficient Monte Carlo solution for uncertainty propagation with stochastic collocation. In *Transactions of the American Nuclear Society*, Chicago, IL, June 2012. American Nuclear Society.

[50] B. C. Franke and A. K. Prinja. Monte Carlo solution for uncertainty propagation in particle transport with a stochastic Galerkin method. In *Proceedings of the*

*International Conference on Mathematics and Computational Methods Applied to Nuclear Science & Engineering (M&C 2013)*, Sun Valley, ID, May 2013. American Nuclear Society.

[51] A. J. Olson, A. K. Prinja, and B. C. Franke. Radiation transport in random media with large fluctuations. In *Transactions of the American Nuclear Society*, New Orleans, LA, June 2016. American Nuclear Society.

[52] I. Babuska, F. Nobile, and R. Tempone. A stochastic collocation method for elliptic partial differential equations with random input data. *SIAM Journal of Numerical Analysis*, 45(3):1005–1034, 2008.

[53] F. Nobile, R. Tempone, and C. G. Webster. A sparse grid stochastic collocation method for partial differential equations with random input data. *SIAM Journal of Numerical Analysis*, 5(46):2309–2345, 2008.

[54] X. Ma and N. Zabaras. An adaptive hierarchical sparse grid collocation algorithm for the solution of stochastic differential equations. *Journal of Computational Physics*, (228):3084–3113, 2009.

[55] S. Sankaran and A. L. Marsden. A stochastic collocation method for uncertainty quantification and propagation in cardiovascular simulations. *Journal of Biomechanical Engineering*, 3(133), 2012.

[56] S. Soga and H. S. Abdel-Khalik. Sparse approximation of POD-Galerkin generalized polynomial chaos. In *Transactions of the American Nuclear Society*, San Diego, CA, November 2012. American Nuclear Society.

[57] H. C. Elman and C. W. Miller. Stochastic collocation with kernel density estimation. *Computational Methods Applied to Mechanical Engineering*, (245-246):36–46, 2012.

[58] P. W. Talbot and A. K. Prinja. Sparse-grid stochastic collocation uncertainty quantification convergence for multigroup diffusion. In *Transactions of the American Nuclear Society*, Anaheim, CA, November 2014. American Nuclear Society.

[59] B. M. Adams, M. S. Ebeida, M. S. Eldred, J. D. Jakeman, L. P. Swiler, J. A. Stephens, D. M. Vigil, T. M. Wildey, W. J. Bohnhoff, K. R. Dalbey, J. P. Eddy, K. T. Hu, L. E. Bauman, and P. D. Hough. Dakota, a multilevel parallel object-oriented framework for design optimization, parameter estimation, uncertainty

quantification, and sensitivity analysis: Version 6.1 theory manual. Technical Report SAND2014-4253, Sandia National Laboratories, 2014.

[60] M. S. Eldred and J. Burkardt. Comparison of non-intrusive polynomial chaos and stochastic collocation methods for uncertainty quantification. *American Institute of Aeronautics and Astronautics*, 2009.

[61] M. B. Giles. Multilevel Monte Carlo path simulation. *Operations Research*, 56: 607–617, 2008.

[62] M. B. Giles. Multilevel Monte Carlo methods. In *Proceedings of the Tenth International Conference on Monte Carlo and Quasi Monte Carlo Methods in Scientific Computing (MCQMC 2012)*, Sydney, Australia, April 2012. MCQMC.

[63] T. Gerstner and M. Griebel. Numerical integration using sparse grids. *Numerical Algorithms*, 18:209–232, 1998.

[64] T. Gerstner and M. Griebel. Dimension-adaptive tensor-product quadrature. *Computing*, 71:65–87, 2003.

[65] W. H. Beyer. *Standard mathematical tables & formulas*. CRC Press, Boca Raton, Florida USA, 29th edition, 1991.

[66] R. Vasques. *A review of particle transport theory in a binary stochastic medium*. PhD thesis, Universidade Federal do Rio Grande do Sul, 2005.

[67] P. Switzer. A random set process in the plan with a Markovian property. *Annals of Mathematical Statistics*, (6):1859–1863, 1965.

[68] G. B. Zimmerman and M. L. Adams. Algorithms for Monte-Carlo particle transport in binary statistical mixtures. In *Transactions of the American Nuclear Society*, San Francisco, CA, November 1991. American Nuclear Society.

[69] S. D. Pautz and B. C. Franke. An atomic mix closure for stochastic media transport problems. In *Transactions of the American Nuclear Society*, New Orleans, LA, June 2016. American Nuclear Society.

[70] P. S. Brantley. Modified closures in Monte Carlo algorithms for diffusive binary stochastic media transport problems. In *Transactions of the American Nuclear Society*, New Orleans, LA, June 2016. American Nuclear Society.

[71] R. Vasques, R. N Slaybaugh, and K. Krycki. Nonclassical particle transport in the 1-D diffusive limit. In *Transactions of the American Nuclear Society*, New Orleans, LA, June 2016. American Nuclear Society.

[72] H. Rief. Generalized Monte Carlo perturbation algorithms for correlated sampling and a second-order Taylor series approach. *Annals of Nuclear Energy*, 11(9):455–476, 1984.

[73] H. Rief. A synopsis of Monte Carlo perturbation algorithms. *Journal of Computational Physics*, 111:33–48, 1994.

[74] D. A. McQuarrie. *Mathematical methods for scientists and engineers*. University Science Books, Sausalito, California USA, 1st edition, 2003.

[75] I. S. Gradshteyn and I. M. Ryshik. *Table of integrals, series and products*. New York: Academic Press, New York USA, 1965.

[76] G. E. P. Box and M. E. Muller. A note on the generation of random normal deviates. *The Annals of Mathematical Statistics*, 29(2):610–611, 1958.

[77] O. P. LeMaître and O. M. Knio. *Spectral methods for uncertainty quantification: With applications to computational fluid dynamics*. Sprinter Dordrecht Heidelberg London New York USA, 1st edition, 2010.

[78] T. N. L. Patterson. The optimum addition of points to quadrature formulae. *Mathematics of Computation*, 23:847–856, 1968.

[79] A. Genz and B. D. Keister. Fully symmetric interpolatory rules for multiple integrals over infinite regions with Gaussian weight. *Journal of Computational and Applied Mathematics*, 71(2):299–309, 1996.

[80] C. W. Clenshaw and A. R. Curtis. A method for numerical integration on an automatic computer. *Numerische Mathematik*, 2:197–205, 1960.

[81] L. N. Trefethen. Is Gauss quadrature better than Clenshaw-Curtis? *SIAM Review*, 50:67–87, 2008.